The Effect of Confinement, Surface Chemistry and Topography on Crystallization

Clara Anduix Cantó

Submitted in accordance with the requirements for the degree of
Doctor of Philosophy

The University of Leeds
Faculty of Mathematics and Physical Sciences
School of Chemistry

April 2018

The candidate confirms that the work submitted is his/her own, except where work which has formed part of jointly-authored publications has been included. The contribution of the candidate and the other authors to this work has been explicitly indicated below. The candidate confirms that appropriate credit has been given within the thesis where reference has been made to the work of others.

"Chapter 3: Crystallization of Inorganic Solids in Confinement: Controlled Pore Glass Beads for Highly Soluble Solids" is based on the paper "*Effect of Nanoscale Confinement on the Crystallization of Potassium Ferrocyanide. Clara Anduix-Canto, Yi-Yeoun Kim, Yun-wei Wang, Alexander Kulak, Fiona C.Meldrum and Hugo K. Christenson. Crystal Growth & Design* ***2016,*** *16, (9), 5403-5411*". All the experimental work was done by me, under the supervision of Prof. Fiona Meldrum, except the TEM work which was done by Dr. Yi-Yeoun Kim in cooperation with me.

Acknowledgements

First of all, a huge and sincere thank you goes to Professor Fiona Meldrum, for giving me the opportunity to do my PhD at Leeds and truly inspiring me to become the best researcher that I could. Since I met Fiona, she made me see problems as challenges and questions as exciting mysteries, helping me to develop my confidence and passion for research. I will always be thankful to her for being an endless source of ideas and positive energy, making my PhD always exciting to me. I also owe much gratitude to Professor Hugo Christenson for his essential contribution to all my projects, especially the ones involving CPGs. His always great suggestions and his physical point of view, made me often question things that I had never thought about before.

Moreover, I would like to thank the wonderful people in my group since without them, I would certainly not have arrived this far. Firstly, Dr Yi-Yeoun Kim, one of the brightest people I know, who always gave me the best advice about any problem I could have. And Dr. Alex Kulak, who first put the idea of doing a PhD in my head and who offered me his valuable help and friendly smile since the first moment I stepped a foot in this office. They not only helped me to become a better scientist but also kept the group united and fun with our Monday cakes or wine and gin and tonic evenings in the office, which I will deeply miss. I am also incredibly grateful to my good friend Mark Levenstein, who was always there to help me with my writing and coding, but more importantly, for listening, talking to me and making me laugh when I most needed it. I will never be able to thank him enough for everything he did for me during these 3 years of my life so I can just say that whenever you need me, I will be there with a pint ready for you!

I also want to thank Muling Zeng and Angela Bejarano Villafuerte, for their caring advice during my PhD and personal crisis and their friendly details, which always made me feel much loved. And of course, thanks to Shunbo Li, for being my microfluidics teacher and a great friend, David Green, for the hundreds of useful suggestions throughout my PhD and Steph Foster, Shu

Zhang, Phillip Lee, Joe Marchant and Thembi Gaule for all their help and the fun conversations shared.

I would also like to thank Professor Naomi Chayen and her group members at the Imperial College, Dr. Lata Govada and Sean Kassen for embracing me as if I was a member of their group from the very beginning of my PhD. It was always delightful to come down to London and have Naomi welcoming you with some cake in her office together with some new proteins to crystallize! Also our collaborators in engineering Professor Nik Kapur and Carlos Gonzalez, for all their help with fluid mechanics and those amazing synchrotron times, full with laughter, with the dream-team. Our collaborators in Cardiff, especially, Dr. Colan Hughes for his patience and the fine pints during our NMR time in Warwick. Finally our collaborators in Manchester, especially Dr. Jose Godinho, for spending long hours writing code with me to reconstruct our beautiful tomograms with roses. In addition, thanks to the helpful beamline scientists who make me develop a passion for synchrotron: Dr. Jonathan Wright and Dr. Carlotta Giacobbe (ESRF, ID11) and Dr. Malte Storm and Dr. Andrew Bodey (Diamond, I13). And a special thanks to Dr. Kaz Wanelik (Diamond, I13) for all the patience and wisdom, but also for caring and helping us so much when everything seemed to be going wrong during the long nights of beamtime. Lastly, thanks to Dr. Oscar Cespedes for his help with my Raman experiments and to Dr. Chris Pask for always being happy to share his expertise in X-rays with us.

On a personal level, I would like to thank all my friends in Leeds, especially Jesus, Natalia, Adrià, Mark, Alberto, Claudia and Edu for tolerating my complains and complaining with me during lunch breaks, for all our trips and crazy nights out, and for sharing a million of stories with me. Together, we felt like we had a family here even though we were all far away from home. I would also like to thank Alomgir Ali, for being my rock during these last 4 years. Thanks for believing in me from day 1, for always supporting every decision I made, for spending whole weekends next to me preparing my PhD

presentations, for helping me to be more confident and making me forget everything when I just wanted to disappear.

Finally, a very important thank you to my family, whose support throughout my whole PhD was unimaginable. Thanks to my mum and dad, to Joan, Inma, Ampa, Gonzalo and Pablo and to all my cousins, Marc, Pau, Maria and Pablo, for all the unconditional love, for the skypes, for flying wherever I was every time I had a problem and for the crazy welcomes in the airport. I would have never been able to finish without my family and I feel the luckiest person in the world for having them.

Abstract

This thesis presents an extensive investigation into the effects of confinement, surface chemistry and topography on the crystallization of various inorganic solids and proteins. Firstly, the crystallization of potassium ferrocyanide trihydrate (KFCT), calcium sulfate and calcium carbonate ($CaCO_3$) was studied in nanopores. Remarkably high stabilization of metastable phases was achieved in the pores due to a significant retardation of the crystallization processes in confinement. Indeed, the retardation effects observed here are far greater than any seen before for inorganic solids. The confinement system presented here, controlled pore glass (CPG) rods, also offered the possibility of imaging and characterizing crystals growing in nanopores using *in situ* 3D absorption and diffraction tomography with synchrotron radiation. This provided insights into the crystallization pathways of calcium sulfate and $CaCO_3$ and generated a new understanding of the mechanisms that govern crystallization in confinement. Confinement was also used as a tool to reveal information about the crystallization mechanism of model proteins. All of the proteins studied followed a two-step nucleation pathway involving amorphous precursors. The intermediates could be stabilized in confinement for long periods of time but they readily crystallized in larger spaces. Finally, the nucleation of proteins on chemically modified substrates with topographic defects was also investigated. The proteins adsorbed to the topographic features on the substrates, where an increase of the local supersaturation within the cavities promoted their nucleation. Thus, by simply modifying the surface chemistry and topography of a substrate, amazing control of protein crystallization was achieved, such that control over the location of crystal formation could be achieved.

Table of Contents

List of Tables

List of Figures

Chapter 1: General Introduction

1.1 Introduction

The main goal of the work presented in this thesis is to develop new approaches to gain insight, and ultimately control crystallization processes. A range of novel systems are introduced in this thesis, where confinement, surface chemistry and topography effects are combined to build our understanding of crystal nucleation and control the crystallization processes of various inorganic solids and proteins. The systems and crystallization methods described here helped us to unravel some of the effects that govern crystallization in confinement or within topographic defects and open the door to further *in situ* studies of crystallization in small volumes.

Crystals are an indispensable part of our world and life. From the land where we stand to snowflakes falling down from the sky, we are surrounded by crystals. Since the early times of human history, people have been fascinated by the beautiful crystals found in nature. Stones and gems such as rubies, emeralds and quartz have been used for jewelry and decoration since the times of The Ancient Egyptians.[1] Nowadays, many areas of our everyday life such as food, technology, transport, energy, construction or medicine benefit from crystals, where the ability to control their production to generate crystals with specific properties is essential. Crystals are also an essential part of many organisms present on our planet, constituting teeth, bones, mollusk and egg shells or pearls. As these crystals are often integrated into the body (e.g. the internal skeleton), one can imagine the degree of control involved in the crystallization processes, since any small issue might generate serious medical issues.[1] Additionally, undesired crystallization is responsible for the blocking of pipes, destruction of buildings, bridges and other structures, and also for several human pathological conditions such as kidney stones, cataract formation and even cancer.[2, 3] Given the importance of crystallization in nature and human life, it is not surprising that scientists have developed an increasing interest in understanding crystallization processes and developing new systems and tools to gain control over them.

The formation of a crystal starts with a phase transition called nucleation, which determines many of the important characteristics of the crystal such as

the internal structure, size and purity.[4] Thus, the ability to obtain a crystal with certain properties resides in the facility to control nucleation. Many different approaches have been used over the years to control nucleation, including changes in temperature and solvent, the use of additives and more recently, modifications of the surfaces and size of the environment in which crystallization takes place.[5] In this thesis I study a range of different systems to prove that by simply modifying the crystallization environment it is possible to gain great control over crystallization processes.

The purpose of this chapter is to review recent work devoted to controlling crystallization processes through the use of confinement and chemical and topographical modifications of the surface where a solid nucleates. The chapter starts with a brief introduction to crystallization theory, where the basics of classical and non-classical crystallization are discussed. It continues with a general introduction to protein crystallization, and the main differences between the crystallization of small molecules and macromolecules are examined. This section also includes a range of common methods used for growing protein crystals. Next, a range of confinement systems used to control crystallization in previous studies are described, including relevant findings of crystallization in small volumes. This is followed by a final section focused on illustrating recent discoveries of crystallization on surfaces with different surface chemistries and topographies, and how these can be used to control nucleation.

1.2 Crystallization

1.2.1 The crystalline state

In general, solids can be crystalline or amorphous or a mixture of both, according to the periodicity or long-range order with which their atoms or molecules are arranged.[6] Crystalline solids comprise a regular set of molecules or atoms placed in specific locations and creating a rigid three-dimensional lattice which is characteristic of each substance. Most crystals

are anisotropic (the cubic system is an exception), and as such, their properties can vary according to the direction in which they are measured.

Two types or crystalline materials are usually distinguished, namely single crystals and polycrystalline materials. Ideally, a single crystal would be defined as a crystalline solid with a continuous and unbroken lattice with no grain boundaries. The entire lattice can be subdivided into small groups of atoms or molecules that form a repetitive pattern, where the unit cell is the smallest repeating unit. However, perfect single crystals rarely exist in nature or a laboratory due to the frequent incorporation of impurities or the presence of crystallographic defects within the crystal lattice. Therefore, a more practical definition was given by Meldrum and Colfen: “a single crystal is a solid body with a large coherence length, which shows diffraction behavior characteristic of a perfect three-dimensional alignment of its building units”.[7] Occasionally, crystals show some form of aggregation or intergrowth which might result in random clusters or aggregates with certain degree of symmetry, depending on the aggregation mechanism. Parallel growth and twinning are two types of intergrowth that commonly cause the formation of symmetrical aggregates. In parallel growth, one form of a substance grows on top of another such that their faces and edges are parallel. On the other hand, twinning is a form of intergrowth between two individuals with similar forms, which are joined symmetrically around an axis or a plane.[8] Most crystalline materials are, however, composed of aggregates of many small single crystals (also called grains) at random crystallographic orientations, forming a polycrystalline material.[6] Thus, whereas single crystals have infinite long-range order, polycrystals only present localized periodicity.

In contrast, amorphous solids do not have the structural regularity and translational symmetry of crystalline materials, and therefore could be defined as solids with short-range order.[9] Amorphous solids are isotropic since their properties do not vary with the direction they are measured. Some examples of amorphous materials include glass, many polymers (e.g. cross-linked polymers such as epoxy), metallic and metalloid glasses and some solidified

organic materials such as amber.[9] Amorphous materials find many applications in everyday life, where they are widely used in the construction industry, laboratories, homeware and electronics. Recently, amorphous phases of various inorganic solids including different carbonates, calcium phosphate and iron oxide have been reported.[11,10-12] These amorphous phases were seen to act as precursors to crystalline phases due to their lower stability. They also present the ability to be molded into desirable shapes.[10] This is interesting since it offers the possibility to build crystal morphologies resembling the “crystallization mold” where they grew. These characteristics make amorphous materials a perfect tool for material synthesis and a fundamental element in biomineralization.[7]

1.2.2 Crystal systems

Different crystal structures can be distinguished according to the unit cell configuration or the atomic distribution of a specific crystal. The geometry of the unit cell is described according to its lattice parameters, namely its relative axial length (a, b, c) and the interaxial angles (α, β, γ). 7 different crystal systems arise from the combinations of these parameters as indicated in Table 1.[6, 8]

Crystal system	*Angles between axis*	*Length between axis*	*Examples*
Regular or cubic	α=β=γ=90°	a=b=c	Sodium chloride (NaCl)
Tetragonal	α=β=γ=90°	a=b≠c	Rutile (TiO_2)
Orthorhombic	α=β=γ=90°	a≠b≠c	Silver nitrate ($AgNO_3$)
Monoclinic	α=β=90°≠γ	a≠b≠c	Potassium chlorate ($KClO_3$)
Triclinic	α≠β≠γ≠90°	a≠b≠c	Potassium dichromate ($K_2Cr_2O_7$)
Trigonal or Rhombohedral	α=β=γ≠90°	a=b=c	Calcite ($CaCO_3$)
Hexagonal	α=β=90° γ=120°	a=b≠c	Potassium nitrate (KNO_3)

Table 1. The seven crystal systems.

1.2.3 Polymorphism

Some compounds have the ability to crystallize into more than one crystal structure. This property is known as polymorphism and it is found in many solids such as calcium carbonate, which can crystallize as three polymorphs namely calcite, aragonite and vaterite, or carbon, which can precipitate as graphite and diamond. As different polymorphs have different unit cells and crystal structures, they generally exhibit different mechanical, thermal and physical properties even though they are chemically identical.[13] It is common to find polymorphs existing as different crystal structures and different crystal habits, depending on the atomic occupation of each crystal face and its degree of growth. In this case, microscopy techniques are good tools to rapidly distinguish between different polymorphs. However, polymorphs with the same crystal habit also exist, making it essential to use other characterization techniques such as X-rays to distinguish between them.

As different polymorphs have different properties, they also show different stabilities at certain conditions. The precipitation of one polymorph over

another from solution depends on a variety of factors such as temperature, pressure, solvent and also the presence of additives or stirring speed.[14] Being able to effectively select the formation of a specific polymorph is critical to a wide range of fields such as medicine, pigments, food or agrochemicals, since the properties of the desired product will depend on the polymorph. A clear example of the relevance of polymorph control is seen in the pharmaceutical industry, where different polymorphs often present different bioavailabilities and efficacies.[15] Thus, searching for new approaches to control polymorphism and to increase the stability of specific phases is an important research subject.

Polymorph inter-conversion can follow different paths depending on the system.[16] On the one hand, displacive transformations take place when two polymorphs have similar structures, since they involve minor structural modifications between the phases and no bond breakage.[16] This kind of conversion often takes place during solid-state transformations, when the energy barrier of conversion is low.[17] On the other hand, when polymorphs are very different from each other, they usually convert by reconstructive transformations, which include modifications in their bonding network.[16]

It is important to note that the term polymorph only refers to crystals of identical composition. However, there is a type of polymorphism where a solid incorporates variable amounts of solvent in its crystal lattice with a defined stoichiometry. These compounds are the so called pseudo-polymorphs or solvates and they are very common in pharmaceutical compounds.[18]

1.2.4 Classical crystallization

Crystallization can be defined as a phase transition by which a crystalline phase appears in a supersaturated solution.[1] A solution is supersaturated when the solute concentration is higher than its solubility, which is the concentration at which solute and solution are in equilibrium. The

supersaturation ratio β, depends on the chemical potentials of the molecules in solution according to the following equation,

$$\Delta\boldsymbol{\mu} = \boldsymbol{\mu} - \boldsymbol{\mu_S} = \boldsymbol{k_B T \ln \beta} \quad \text{(Equation 1)}$$

where μ and μ_s are the chemical potentials of the solute molecules in the supersaturated state and the saturated state respectively, k_B is the Boltzmann constant and T is the temperature. A system in equilibrium is characterized by β = 0. If β < 0, a crystal in solution should dissolve and if β > 0, a crystal in solution should grow.[1] The chemical potential can be expressed as a function of the solution activities according to:

$$\Delta\boldsymbol{\mu} = \ln\left(\frac{a}{a_S}\right) \quad \text{(Equation 2)}$$

where a and a_S correspond to the solute activities in solution, and when the system is saturated. When working with dilute aqueous solution, we can consider that the activity coefficients are equal to 1 and therefore, equation 2 can be written in terms of solution concentration, where (C) is the solute concentration in solution and (C_s) its concentration when it is saturated.[1]

$$\Delta\boldsymbol{\mu} = \ln\left(\frac{C}{C_S}\right) \cong {}^{C}/_{C_S} - 1 = \beta - 1 \quad \text{(Equation 3)}$$

In the case of ionic systems, such as the inorganic salts investigated in this thesis, multiple species are often present in solution. Therefore, the concentration or activity of each specie needs to be included in the expression of supersaturation. For a soluble substance AB with solubility product K_{ps}= $a(A)^x \cdot a(B)^y$ and $K_{ps} \approx [A]^x \cdot [B]^y$ in aqueous solutions with low ionic strength. The supersaturation will then be defined as:

$$\boldsymbol{\beta} = \frac{a(A)^x \cdot a(B)^y}{K_{ps}} \approx \frac{[A]^x . [B]^y}{K_{ps}} \quad \text{(Equation 4)}$$

Gaining control over the concentration of the different species in solution is very important for polymorph selection since different polymorphs usually have different solubility products. Once a system is supersaturated, a solid

phase can be separated from solution in a first-order phase transition called nucleation.[19] Many of the basic properties of the new phase are determined during nucleation, which makes it the critical stage of crystallization. During nucleation, molecules, atoms or ions aggregate together due to local fluctuations, giving birth to primary clusters that can either grow to form a nucleus or redissolve.[4] In classical crystallization, a crystal is formed under low reactant and additive concentrations and it is driven under thermodynamic control. When nucleation takes place in a clear solution (without any crystals) it is called primary nucleation and it can be classified as homogeneous or heterogeneous depending on the driving force for nucleus formation.

1.2.4.1 Homogeneous nucleation

Homogeneous nucleation occurs when a stable nucleus forms spontaneously in a supersaturated solution. It is an energy-consuming process where the molecules, atoms or ions assemble and become orientated in a fixed lattice. The Gibbs free energy (ΔG) of a nucleus determinates its stability and it is expressed as a sum of two terms: a volumetric (ΔG_v) and a surface factor (ΔG_s). The volume factor is negative since it expresses the favorable bonding of the atoms, molecules or ions to the cluster, which lowers ΔG. In contrast, the surface factor is positive, because it represents an increase in the Gibbs free surface energy, which is unfavorable. Thus, the free energy for a spherical cluster can be expressed as:

$$\boldsymbol{\Delta G} = \Delta \boldsymbol{G_V} + \Delta \boldsymbol{G_S} = -\left(\frac{\boldsymbol{4\pi r^3}}{\mathbf{3v}}\right) \boldsymbol{k_B T ln S} + \boldsymbol{4\pi r^2 \gamma} \quad \text{(Equation 5)}$$

where r is the radius of the nucleus, v is the volume of a crystal building block, k_B is the Boltzmann constant, T is the Temperature, S is the supersaturation level, and γ is the interfacial free energy between the forming nucleus and the solution. Taking into account both positive and negative contributions, the Gibbs free energy can be represented as a function of the nucleus radius (Figure 1). A first unfavorable step represents the creation of a new surface, where the positive factor dominates, leading to ΔG>0. The curve then reaches a maximum, where a critical radius (r_c) is achieved and the probability of

nucleus formation is minimum.[20] Here, the barrier of nucleation is known as the activation energy, ΔG*. This is followed by a decrease in the free energy as the radius increases and the volume free energy increases in importance.

In a growing cluster, the surface factor usually dominates over the volume factor at early stages and so, most clusters are unstable and redissolve due to the positive contribution to the free energy. Nevertheless, as the volume factor increases faster than the surface term, some clusters can reach certain sizes (r_c), giving rise to a nucleus. Large interfacial tensions (γ) increase ΔG_s and therefore ΔG*, reducing the probability of nucleation.[21] In contrast, high supersaturations decrease ΔG*, promoting nucleation and decreasing the size of the critical nucleus required for crystallization. The size of a critical nucleus can be calculated according to (Equation 5), since it corresponds to a maximum in the free energy of Gibbs and therefore $d\,{}^{\Delta G}/_{dr} = 0$.

$$\boldsymbol{r_c = \frac{2\gamma v}{k_B T ln S}} \quad \text{(Equation 6)}$$

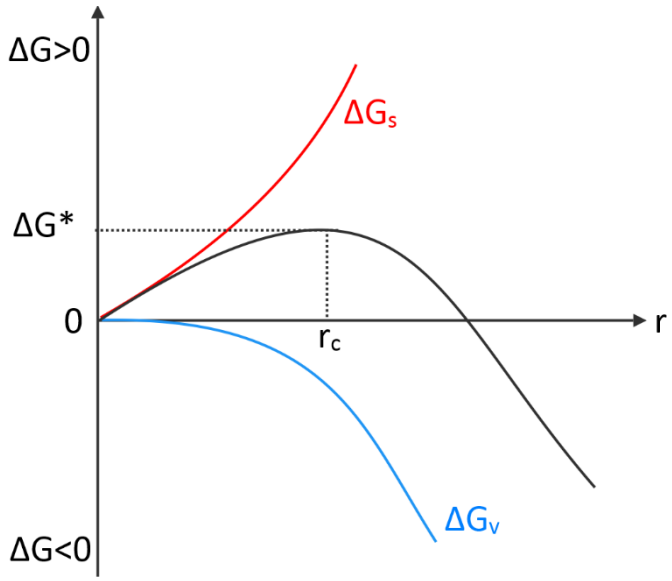

Figure 1. Illustration of the crystal free energy as a function of crystal radius (r). Adapted from ref.[19]

The nucleation rate, *J*, is the number of nuclei that can form in a solution per unit of volume and time and can be calculated as follows:

$$\boldsymbol{J = A\,\exp(-\frac{\Delta G^*}{k_B T})}$$ (Equation 7)

where A is a pre-exponential factor, that is difficult to predict theoretically. It is related to some properties of the solution such as density, viscosity, molecular charge or volume.[22] Moreover, it has been suggested that the nucleation rate also depends on the volume of the system (V). Therefore, *J* and the induction time (τ) can be expressed as:[23]

$$\boldsymbol{J = VA\,\exp(-\frac{16\pi v^2 \gamma^3}{3k_B T ln S})}\ ;\ \boldsymbol{\tau = 1/(1V)}$$ (Equation 8)

1.2.4.2 Heterogeneous nucleation

The fact that homogeneous nucleation is an energetically expensive process makes heterogeneous nucleation the common mechanism in many systems, especially at low supersaturation levels.[8] Heterogeneous nucleation is induced by surfaces, dust or foreign nuclei present in the solution which can provide the starting point for nucleation. The activation energy in heterogeneous nucleation is usually smaller than in homogeneous nucleation since part of the nucleus area is in contact with a surface, decreasing ΔG_s. This decrease is attributed to a lower contribution of the interfacial tension between the nucleus and the solution (γ_{NL}) which can be calculated from the Young equation as follows:

$$\boldsymbol{\gamma_{NS} - \gamma_{LS} = \gamma_{NL}\cos\theta}$$ (Equation 9)

where the new interfacial tension depends on the interfacial energy at the liquid-solid (γ_{LS}) and at the nucleus-solid (γ_{NS}) interfaces, but also on the affinity of the solution for the substrate. This affinity is measured by a parameter named wettability, which is described by the contact angle between the two phases (θ).[24] The activation energy decreases with the contact angle according to:

$$\boldsymbol{\Delta G^*_{het} = \frac{(2+\cos\theta)(1-\cos\theta)^2}{4}\Delta G^*_{homo}}$$ (Equation 10)

Thus, for θ=180°, $\Delta G^*_{het}=\Delta G^*_{homo}$ and for θ=90° or lower, heterogeneous nucleation will be at least twice as favorable as homogeneous nucleation (Figure 2). Very low contact angles are often found when the nucleus presents a high affinity for the surface, which usually happens if they share a similar material and structure. [8, 24, 25] For example, the contact angle between a crystal nucleating on a seed crystal of the same material is θ=0°, and therefore $\Delta G^*_{het}=0$.

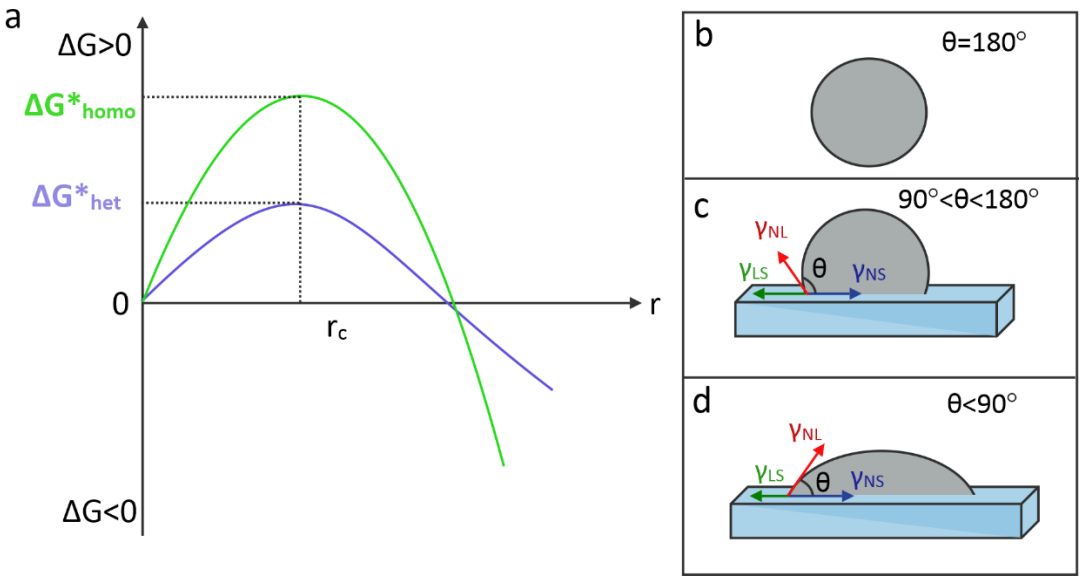

Figure 2. Diagram comparing homogeneous and heterogeneous nucleation (a). (b-d) Contact angle of an emerging cluster in a solution by (b) homogeneous nucleation, and (c,d) heterogeneous nucleation on surfaces with different wettabilities.

1.2.4.3 Crystal growth

When a particle larger than the critical size is formed in a supersaturated solution, it starts to grow into a larger crystal. Crystal growth is a process based on the diffusion of solute molecules or ions from solution to the particle surface followed by an integration process of the ions or molecules into the crystal lattice.[26] Therefore, the two principal steps of the crystal growth are:

- Transport processes: diffusion and/or convection mass transport from the liquid phase to the crystal surface.
- Surface processes: incorporation of material into the crystal lattice. This process starts when a “growth unit” is adsorbed onto the surface

of a particle. Secondly, the solvation shell of the crystal is partially lost and the growth unit diffuses into the adsorption layer. Finally, when the growth unit finds a point to be incorporated into the lattice, the solvation shell is completely lost and the growth unit is incorporated into the lattice.

During the surface processes, the growth units can find three different environments before incorporation: terraces (also known as flat surfaces), step edges and kink sites, with 1, 2 and 3 possible attachment bonds respectively. The fact that kink sites offer more potential for interaction with the incoming growth unit gives a higher probability of the growth unit remaining part of the crystal, and therefore a higher growth rate is expected at the kink sites.[27, 28]

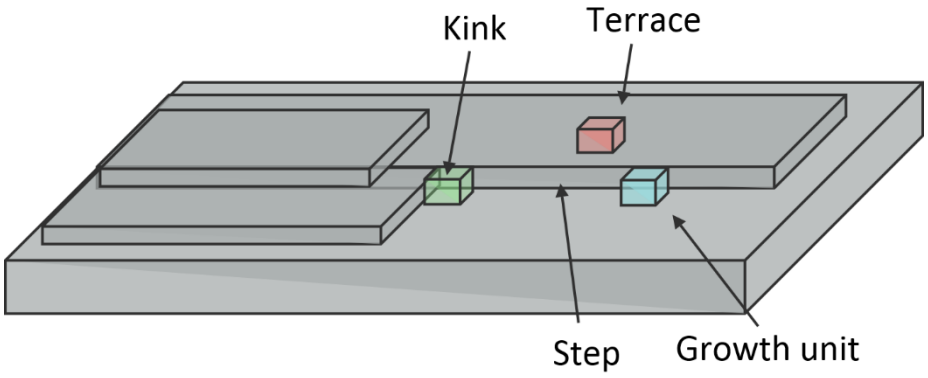

Figure 3. Schematic of the possible environments on a crystal surface where a growth unit can incorporate.

As a growth unit attaches to a kink site, the site will move along the crystal surface, generating new kink sites and steps where new units attach until all kinked or stepped surfaces have been occupied. This explains why most crystals have flat surfaces. Hence, when a specific crystallographic face of a crystal grows quickly, it will gradually disappear, but when it grows slowly, it will remain and dominate the final morphology of the crystal.[1] Different levels of supersaturation will modify the final growth rate and therefore the

crystallographic faces that a crystal will express. Once the supersaturation drops, the system will reach equilibrium and crystallization will be complete.

1.2.5 Non-classical crystallization

Describing crystallization processes with a classical model has the advantage of simplicity, but it does not explain many experimental observations taking place in real systems. Classical nucleation theory is based on a thermodynamic consideration of the process, where crystallization follows an ion-by-ion model. High energy barriers and slow nucleation rates are expected. This is usually valid in systems at low supersaturations, but at higher supersaturations, different polymorphs or intermediate phases might form when kinetic factors control crystallization.[7] The intermediates obtained can transform into more thermodynamically stable phases following different mechanisms such as dissolution-recrystallization, aggregation or solid phase transformations. These observations agree with the principle that Ostwald proposed in 1897, stating that nature does not always start by nucleating the most stable phase, but usually follows a range of phase transitions, starting with the precipitation of less stable intermediates which eventually transform into the most thermodynamically stable phase.[29] Figure 4 shows a schematic of the Ostwald step rule (in blue) with the formation of possible intermediates such as amorphous phases or metastable polymorphs which finally convert into the most thermodynamically stable phase. This behavior has now been reported for different materials such as proteins, colloids, minerals or polymers.[20] Nevertheless, the formation of intermediate phases in solution will always depend on the solution conditions and therefore, different crystallization paths might be found for one compound under different circumstances.

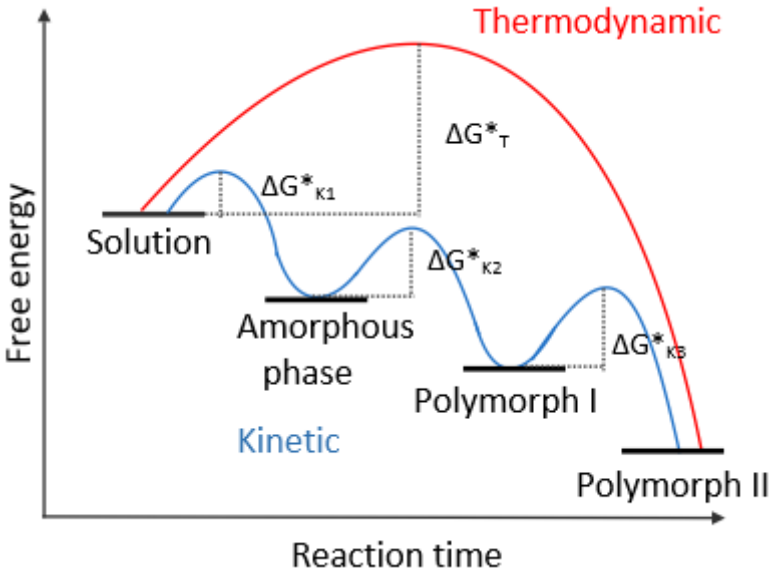

Figure 4. Diagram of the two possible crystallization pathways of a solid under kinetic (several steps) and thermodynamic control (one step).

1.2.5.1 Nucleation theories

Classical nucleation theory encounters some difficulties predicting certain parameters such as nucleation rates. For example, experimentally measured nucleation rates have been proven to be lower than the theoretical values by 10 order of magnitudes.[4] These problems arise from the assumption that some properties such as surface tension, structure and density of microscopic clusters are equivalent to those measured from macroscopic phases. From a classical view of nucleation, a nucleus is expected to have the same interfacial energy as the bulk phase since they maintain the same structure. However, amorphous particles or liquid droplets have been observed as precursors in real systems, confirming that the previous statement is not always true. The observed precursors are in many cases stable with respect to the solution and are named prenucleation clusters (PNC). They are expected to eventually interact, orient themselves and aggregate to form a crystal nucleus (Figure 5).[30] Currently, PNCs have been found in proteins and small organic molecules but also in some inorganic solids such as $CaCO_3$.[4, 31]

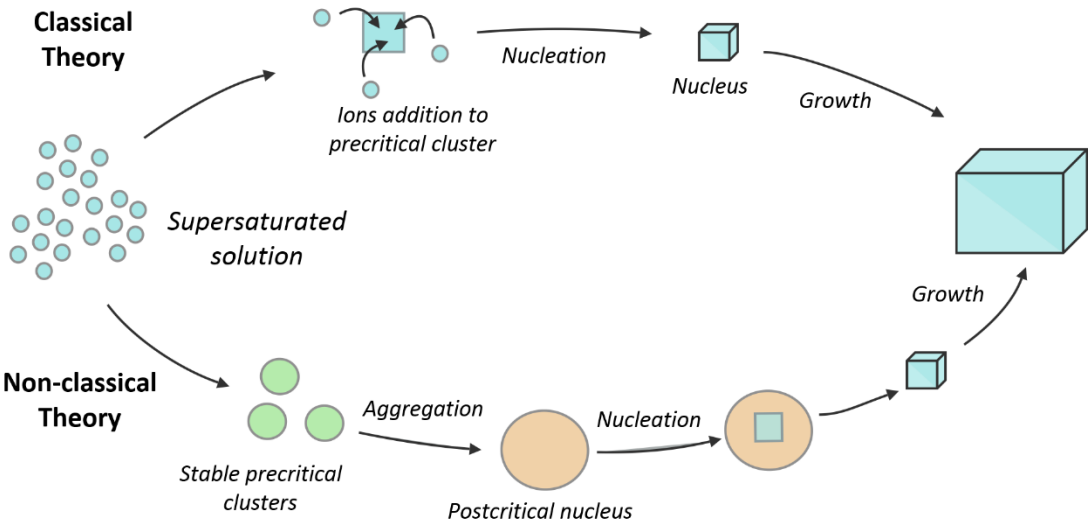

Figure 5. Crystal nucleation pathways according to two different nucleation theories. Adapted from ref.[30]

1.2.5.2 Aggregation-growth theories

As explained previously, crystal growth is described classically by the incorporation of ions or molecules into the crystal lattice after crystal nucleation. However, recent investigations proposed novel growth mechanisms based on the oriented attachment and fusion of nanoparticles (amorphous or crystalline) which can finally form a structure with single crystal characteristics. These non-classical growth pathways were reported especially for the case of biominerals, which typically grow in the presence of organic and inorganic additives.[32, 33] Two different paths are commonly used to describe non-classical growth, which involve the oriented attachment of nanoparticles and the formation of mesocrystals. The two paths are compared with classical growth in Figure 6. Non-classical crystallization starts by the nucleation of stable clusters or other intermediates that form primary nanoparticles which can interact with each other once they are close enough, due to attractive Van der Waals forces. The nanoparticles can then assemble as unit blocks, to reduce their surface energy, and orient themselves into the lowest-energy configuration due to their thermal energy, finally forming an iso-oriented crystal which will fuse into a single crystal.[34]

On the other hand, primary nanoparticles can be stabilized in the presence of additives or polymers, which adsorb to the surfaces of the nanoparticles.

Subsequent oriented attachment of the nanoparticles forms a mesocrystal, which can then fuse to form a product with single crystal properties. Mesocrystals are defined as nanostructured materials which exhibit a well-defined order on the atomic scale and sharp wide angle diffraction patterns, but with clear evidence of its formation through nanoparticle building units.[35] This means that they usually diffract as single crystals, although misalignment issues can be encountered. They usually present higher surface areas than a single crystal of the same volume due to the presence of the iso-oriented units.[36]

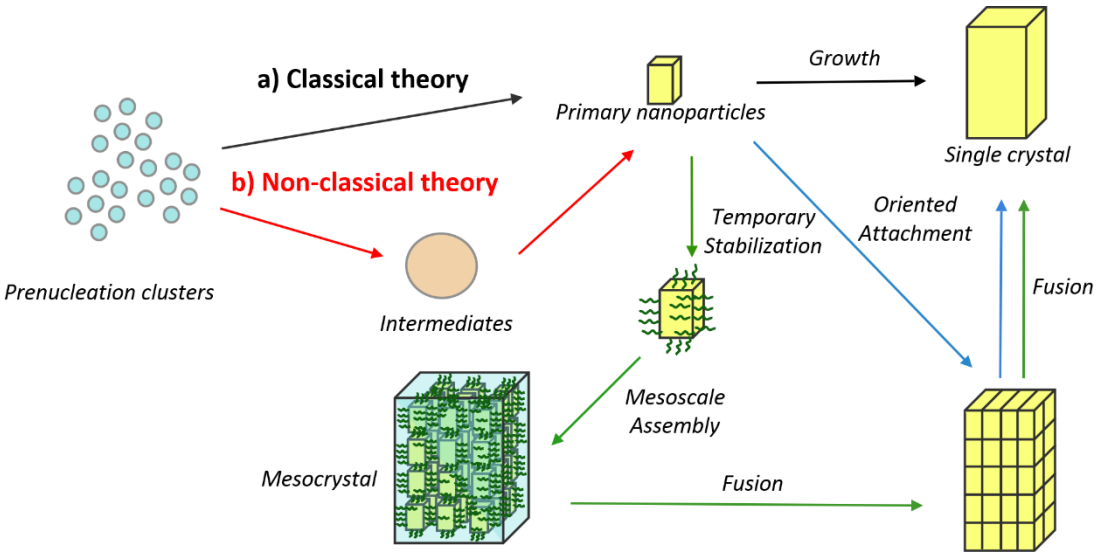

Figure 6. Schematic representation of classical (black) and non-classical (red) crystallization where two growth mechanisms are presented: oriented attachment (blue) and mesocrystal formation (green).

1.3 Protein crystallization

Proteins or macromolecules are polymers of amino acids (between 100-27000 amino acids). They have typical diameters of 30-100 Å, whereas most ordinary molecules have diameters less than 10 Å.[37] The structure of a protein can be described at different levels. The primary structure refers to the sequence of amino acids in the molecule. The secondary structure indicates regions of the long protein chain that are organized into regular structures. The two most common secondary structures found in proteins are known as alpha-helixes and beta-sheets.[38] The amino acids of the protein also interact

with the solvent and with other amino acids in the same chain, depending on their polar and nonpolar characters. These interactions will cause the macromolecule to fold into a three dimensional structure described as the tertiary structure. Thus, the surface of a protein and its charge will not only depend on its internal structure, but also on external factors such as pH and temperature.

Protein molecules are large, complex and chemically and physically unstable as their configurations are easily affected by temperature or solvent modifications in the environment. Changes in the solution conditions or in any experimental parameter such as pH and ionic strength can cause alterations in the protein structure too. Furthermore, every protein presents unique structures and characteristics which are difficult to extrapolate to other proteins, making them a difficult system to study.[37]

1.3.1 Protein crystals

Protein crystallization has been an extensive field of research for over 170 years, since Hünefeld accidentally discovered the first hemoglobin crystal.[39] Hünefeld demonstrated that protein crystals could be obtained by slow dehydration when evaporating a concentrated solution. From that moment, other investigators started to focus their attention on the crystallization of hemoglobin and other proteins such as excelsin,[40] globulin,[41] urease,[42] insulin[43] and lysozyme,[44] and to develop different methods of protein crystal growth.[45] However, despite the large volume of publications about protein crystals, there is still much to learn about the mechanism of crystallization of these biological macromolecules, which is of great importance to the development of more general crystallization methods.

The reason why protein crystallization is studied so widely is due to its important applications. On the one hand, studies of the molecular structure of biological macromolecules are important to understand how these macromolecules operate in biological systems, which is of interest to the pharmaceutical, biotechnological and chemical industries. Currently, only X-

ray diffraction and neutron diffraction techniques are able to provide structural information with atomic resolution. However, these techniques need high quality single crystals which can be obtained from the controlled crystal growth of purified protein samples.[37] Nuclear magnetic resonance (NMR) of protein solutions can also give us information about the structure of some small proteins, but X-ray resolution is needed for many protein samples. As a consequence of this, many recent investigations have focused on the growth of high quality protein crystals and the automation of the crystallization processes in order to obtain well-resolved X-ray diffraction patters in an efficient manner.

Protein crystallization is also of interest from a different perspective. Proteins are very large molecules and their crystallization is slow, which makes them a very interesting subject for crystal growth studies. This novel point of view of protein crystallization could reveal information about the mechanism of crystallization of these macromolecules and other compounds in general, and bring new insights into mechanisms of nucleation. This is the main reason why protein crystallization will be investigated in this thesis.

1.3.2 Principles of protein crystallization

Protein crystals are precious, soft, fragile, sensitive and unpredictable due to the weak interactions that drive the self-assembly of the protein molecules into a protein crystal. These interactions must occur at the right surface locations of the macromolecules and the correct orientations to form an adequate 3D network. Each protein molecule has approximately 15 contact points and a contact surface of 100 to 500 $Å^2$. The solvent in which proteins crystallize is also very important because protein crystals contain a large fraction of disordered bulk solvent that exists in channels throughout the crystals (Figure 7).

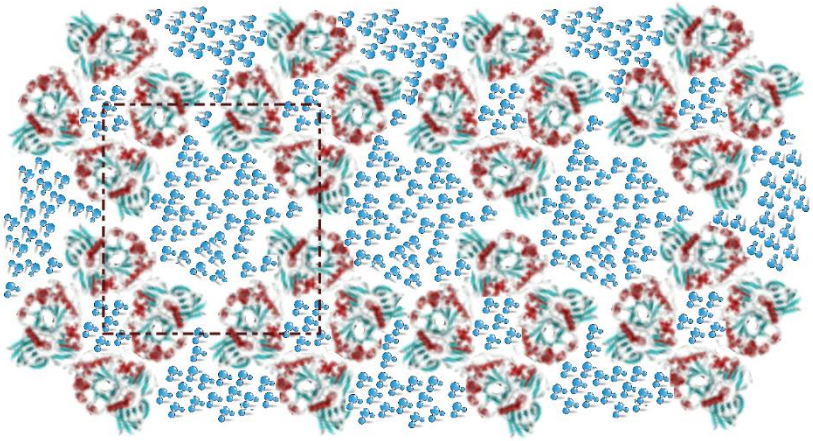

Figure 7. Protein molecules arrangement in a crystal, showing solvent channels in between the macromolecules.

The principles of protein crystallization are identical to those explained previously for smaller molecules, atoms or ions. Theoretically, nucleation and crystal growth will take place in supersaturated solutions. However, many more parameters need to be taken into account when crystallizing proteins experimentally, as suggested by McPherson.[46] For example, whilst ions and small molecules only need low levels of supersaturation to crystallize, particularly high levels of supersaturation are usually needed for the nucleation of protein crystals, due to the high energy barrier that the macromolecules have to overcome.[46] This difference is in a large part the consequence of the solvent interactions with the protein molecules in the dissolved state and in the crystal, and also arises due to the difficulty of arranging proteins into a crystal lattice.

As mentioned previously, water molecules are organized around the proteins in the forming crystal, creating channels. Nevertheless, water also associates with proteins in solution, where the energy of association and dissociation in the phase transition contributes considerably to the overall thermodynamic balance of crystallization.[47] In the formation of a new phase, proteins interact with each other and assemble, giving rise to certain structural rearrangements, the release of the associated water molecules or the trapping of more water molecules. This process involves energy changes in the overall enthalpy of crystallization (ΔH_C), which can be positive or negative, and in the

entropy contribution to the process (ΔS_C).[47] As the solvent molecules play such an important role in protein crystallization, the overall entropy can be divided into two parts: the changes in entropy when the proteins attach to the crystal ($\Delta S_{protein}$) and the changes corresponding to restructuring of the water molecules at the phase transition ($\Delta S_{solvent}$). $\Delta S_{protein}$ will generally be negative due to a decrease in freedom of the molecules when attached to the crystal lattice. However, $\Delta S_{solvent}$ can be positive or negative depending on the balance between the release and the trapping of water molecules during crystallization. This last component is critical in protein crystallization since it is in many cases the driving force for crystallization. The Gibbs free energy of the system can be expressed according to the following equation: [47]

$$\Delta \boldsymbol{G_C} = \Delta \boldsymbol{H_C} - \boldsymbol{T}(\Delta \boldsymbol{S_{protein}} + \Delta \boldsymbol{S_{solvent}}) \quad \text{(Equation 11)}$$

Under satisfactory conditions, proteins can orient and arrange, forming beautiful, high quality crystals which are the target of protein crystallographers. However, the rapid aggregation of protein molecules in a disordered way often results in the appearance of amorphous precipitates or dense liquid droplets, as is frequently observed at high supersaturations.[22] Therefore, the method used to grow protein crystals is usually to initiate their nucleation at the minimum level of supersaturation that allows nucleation. After crystal nucleation, the supersaturation level will decrease, such that the solution enters a metastable zone where the nuclei can grow in the absence of more nucleation. Figure 10 shows a general phase diagram for protein crystallization, which indicates the expected product at different conditions. Drawing a crystallization diagram for each protein helps the crystallographer to interpret the results observed in the crystallization experiments and gives them information about how to modify the parameters such that high quality crystals are obtained.

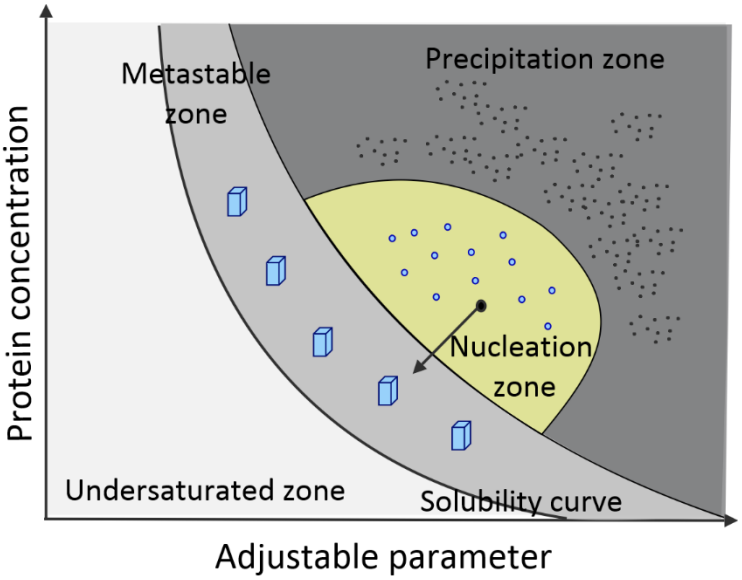

Figure 8. Phase diagram of protein crystallization.

1.3.2.1 Crystal Nucleation

When a solution reaches the necessary level of supersaturation, macromolecules associate, forming disordered clusters. If the radius of the cluster exceeds a critical value (r_c) a crystal nucleus will appear. The critical nucleus size is a function of the supersaturation as described before. Large and well-ordered crystals are expected at low supersaturations while smaller crystals are likely to form at higher supersaturations.[22] How protein nuclei are formed from solution is a question that is currently attracting considerable attention.

While classical or one-step nucleation was traditionally accepted for protein crystallization, recent experimental observations demonstrated the presence of intermediate states, which is indicative of a non-classical behavior.[30, 48, 49] Many simulations and theoretical studies support a two-step mechanism for protein crystallization,[50, 51] in which metastable dense droplets form and act as precursors to crystal formation.[49] The proposed two-step mechanism suggests that proteins assemble in a disordered way, forming clusters of mesoscopic size and the formation of crystal nuclei inside the clusters.[48, 52, 53] Experimental information about these dense protein clusters has been reported over the last decade, with techniques such as dynamic light

scattering, atomic force microscopy, Brownian microscopy and transmission electron microcopy providing information about the nature of the pre-nucleation clusters.[54-58] The clusters were seen to behave as liquids and to be metastable with respect to the protein host solution.[3] Recent attempts to obtain information about the early nucleation stages have used *in situ* techniques such as small-angle X-ray scattering,[59] neutron scattering[60] and liquid-cell transmission electron microcopy, and solid mesoscopic clusters were also observed to act as precursors to protein crystals.[61] However, although a two-step mechanism has now been shown for a range of proteins, many questions remain, such as the liquid or solid nature of the clusters, their characteristics (e.g. shape, size), their role in protein nucleation, under what conditions these clusters appear and if they are identical for different proteins. Increasing our understanding about the nature of these possible nucleation intermediates is of great importance to control their formation and to eventually, control protein crystallization.[62]

1.3.2.2 Crystal growth

Many studies using atomic force microscopy (AFM) have analyzed the growth of protein crystals and revealed a very similar classical growth to inorganic crystals.[63, 64] Crystal growth in proteins is understood as a lateral layer-by-layer growth, resulting in well-defined crystals with flat facets.[65] It is mainly based on an initial diffusion of the molecules from the solution to the crystal interface, where these adsorb and diffuse through the crystal surface until they reach a site that promotes incorporation. Subsequently, the protein needs to achieve the correct orientation to form stable bonds with the other molecules in the lattice. At this stage, partial dehydration or water rearrangement at the protein surface is also expected. Finally, the protein will be incorporated within the crystal lattice, creating additional van der Waals or temporary hydrogen bonds as well as new water channels and water-proteins environments.[46] Possible incorporation of protein aggregates as well as individual macromolecules at the crystal surface has also been considered, although no direct observations have supported this hypothesis.[66, 67] Another interesting fact when studying protein growth is the difficulty in forming pure protein crystals. Macromolecules readily incorporate a greater number and more

diverse impurities into their crystal lattice than small molecules due to the presence of water channels and adsorbed water on their surfaces.[68-70] Special attention must be paid when selecting the crystallization method and precipitating agents to avoid impurity incorporation.

1.3.3 Crystallization methods

Protein crystallization is usually carried out from aqueous solution under controlled conditions in order to avoid protein denaturation (protein unfolding). The most common procedure to induce nucleation is by slow evaporation of the solvent in a process termed “salting out”.[71] In this process, very soluble ionic compounds (typically salts) are mixed with the protein solution, which is then allowed to slowly evaporate. The salt ions strongly interact and bond to the water molecules due to their high solubility, slightly dehydrating the protein and allowing it to crystallize. Organic solvents and some polymers such as poly(ethylene)glycol can also be used as protein precipitants. Crystal growth usually takes place within 1-3 weeks if the crystallization conditions are right, although crystals can sometimes start forming after a few minutes or after a year. The most popular methods for protein crystallization make use of the “salting out” principle to force crystallization and are explained in more detail in the next section.[72]

Other approaches to crystallize proteins include controlled variation in pH or temperature as proteins are strongly sensitive to changes in these parameters. The heterogeneous nucleation of proteins by seeding the solution with pre-existing crystals, or introducing additives or nucleating agents has also proven to be very useful when working with challenging proteins.[73]

1.3.3.1 Vapor diffusion method

The vapor diffusion method allows a protein solution to gradually reach a supersaturated level when the water from the solution is slowly evaporated. In this method, 1-25 mL of precipitant solution of concentration C_1 are deposited in a reservoir close to one or more crystallizing droplets. The crystallizing droplets contain 2-40 µL of a protein solution in buffer, plus 2-40

µL of precipitant of concentration C_1.The final precipitant concentration in the crystallizing droplets is therefore $C_1/2$. The chamber containing the droplets and the reservoir is then sealed and the concentration of precipitant in the solutions is left to equilibrate by diffusion of the volatile species (water or organic solvent). This results in a slow increase of the concentration of precipitant in the crystallizing droplets. This gradual concentration rise can eventually lead to crystallization if the droplet becomes supersaturated. The crystallizing solution can be placed in a hanging or a sitting droplet configuration (Figure 9). The different configurations offer a variation in the distance between the reservoir and the crystallization droplet, which causes changes in the equilibration rate (Figure 9). It is also possible to decrease the rate of crystallization by inserting an oil barrier over the reservoir.

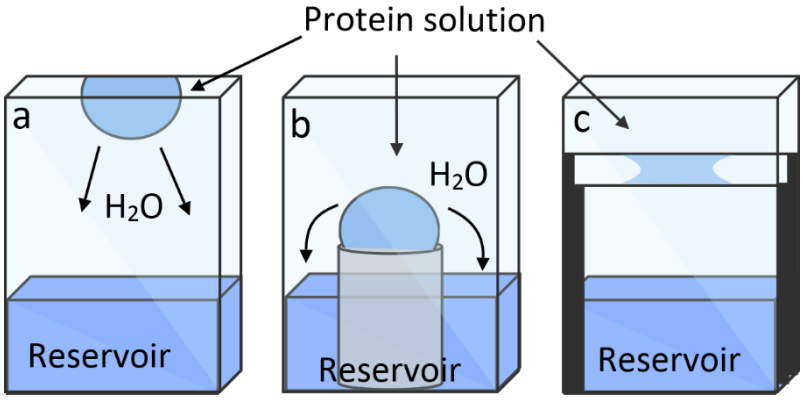

Figure 9. Schematic of the vapor diffusion method for protein crystallization with (a) a hanging drop, (b) sitting drop and (c) a drop between two cover slides.

Protein crystallization by the vapor diffusion method allows the simple integration of different variables to the system and the easy collection of crystals from the crystallization droplet. However, the conditions are continuously changing, making it impossible to know the exact conditions at which crystallization takes place. Also, when supersaturation is reached, both nucleation and fast growth can occur.

1.3.3.2 Batch method

The batch method is the oldest method used to crystallize proteins and it involves the direct mixing of an unsaturated protein solution with a precipitant. [72] Supersaturation with respect to the protein is immediately achieved after mixing and protein crystals will be obtained if the parameters are well selected. The solution is left under oil at all times to prevent solvent evaporation. Using this method, the samples are highly protected from contamination and high quality crystals can be obtained. Different oils can be used in order to control the evaporation rate: paraffin, silicon oil or a mixture of both (Al's oil) are the most commonly used. Frequently, the experiment is carried out in microwell plates which allow the use of very small amounts of protein solution (1-2 μL) and the method is called microbatch (Figure 10).

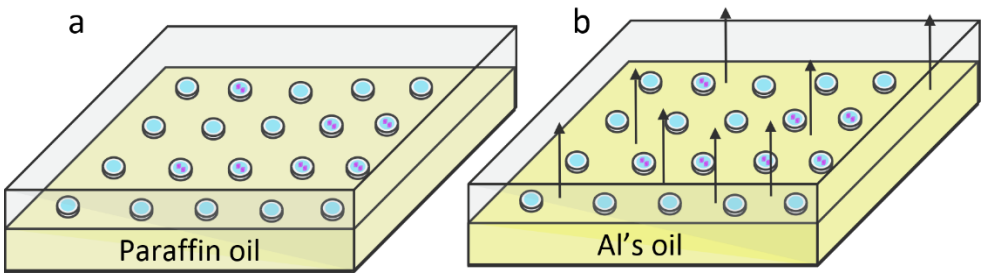

Figure 10. Schematic of the microbatch crystallization method, where different oils modify the evaporation rate.

Crystallization by the batch or microbatch methods allows control of the crystallization conditions and an easy and fast analysis of the crystallization diagram. In one crystallization trial many different protein and precipitant concentrations can be tested. However, it is important to control the mixing of protein and precipitant in every sample in order to achieve reproducible results. The batch method was the preferred method to grow protein crystals in the experiments described in this thesis.

1.3.3.3 Capillary counterdiffusion methods

This method consists of placing a protein and a highly concentrated precipitant solution in opposite ends of an X-ray capillary.[74] Protein crystallization takes place by diffusion of the precipitant agent towards the protein solution, which

creates a supersaturation gradient along the capillary.[75] Due to the differences in concentration, crystals with different sizes and qualities are obtained along the length of the capillary as shown in Figure 11. The counterdiffusion method provides a way of exploring the whole crystallization diagram of a protein in only one experiment. However, it is not possible to know the exact protein or precipitant concentrations at different positions along the capillary.

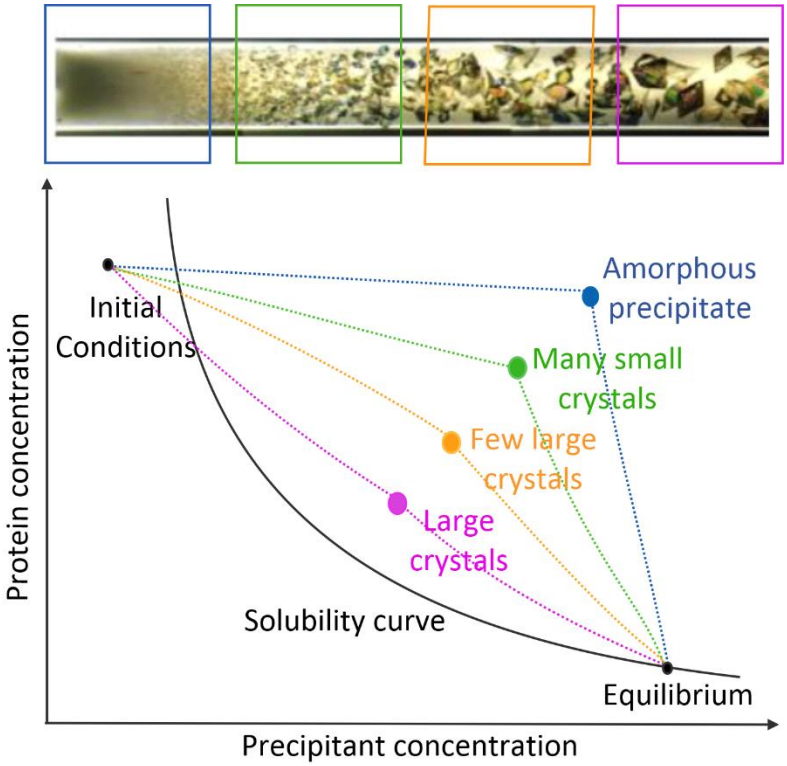

Figure 11. Diagram of the counterdiffusion method for protein crystallization. Figure adapted from ref.[76]

One important advantage of the counterdiffusion method for protein crystallization is that molecular transport by convection is minimized inside the capillaries.[76] A reduction in the convective transport enhances the quality of the crystals, since it assures a steady mass transport of growth units from solution to the surface of a growing crystal.[77] This can be achieved by reducing the size of the capillary or inserting a gel medium into the capillary. The small diameter of the capillaries or the high viscosity of the gel reduces mass transport by convection and increases transport by slow diffusion. It has been

shown that large, high quality crystals with a reduce number of impurities can be obtained using this method.[77]

1.4 Control of crystallization using confinement

The four experimental chapters presented in this thesis describe a wide investigation of the crystallization of various inorganic solids and proteins in confinement and on surfaces with different surface chemistries and topographies. Various crystallization systems are introduced in this thesis, where confinement and surface effects were combined to gain insight into crystallization processes and ultimately control crystal nucleation. Previous systems used to control crystallization via confinement and surface modifications are reviewed in the next two sections.

Changes in the solution composition, temperature, pH or the use of additives are common approaches that are generally used to gain control over crystallization processes in a given solution.[78, 79] The use of soluble additives has been particularly studied since they have the ability to modify crystal morphology, size and polymorph.[7, 80] It has been shown that additives incorporate into the crystal lattice, which allows the alteration of textures and mechanical and optical properties of the crystals.[81-86] In addition, recent studies have demonstrated that the microenvironment in which crystals form affect crystal pathways and products.[87-90] Looking into nature, it is frequently observed that many important processes such as biomineral formation, the templating of nanostructures or degradation of building stones by salt weathering take place in constrained spaces. These can potentially provide environments that enable the controlled formation of crystals.[2, 91-93]

Biomineral formation is an example of crystallization in confinement particularly interesting, and it has been a source of inspiration for material scientists for many years.[1] Organisms have the ability to produce single crystals with complex shapes and curved surfaces which present unique physical properties that are highly difficult to mimic in synthetic systems.[91, 94]

An example of different crystal morphologies observed in synthetic and natural systems is illustrated in Figure 12. Nature also achieves exceptional control over the orientation and polymorphism of crystals. Indeed, nature is able to stabilize crystal phases that are usually transient under ambient conditions.[95] One of the factors offering control over crystallization in natural systems is the interaction of the growing crystals with organic and inorganic additives, which have been shown to alter the morphology and crystal phase of certain minerals.[96] Nevertheless, there is another important factor affecting biomineralization that has not been as well studied: confinement. The small compartments and channels where biomineralization takes place may influence crystal phase, morphology and orientation.[94] Thus, crystals with curved surfaces and complex morphologies are often found within vesicles.[97] Examples include the formation of coccoliths, which occurs within vesicles in the algae cells.[98] Another example is found in the formation of echinoderm spines, which are formed inside a membrane envelope that allows the precipitation of a calcite single crystal by transformation of amorphous calcium carbonate (ACC).[99] The formation of biominerals in enclosed environments provides a regulated ion transport, which offers control over the chemistry and kinetics of crystal growth.[94] These observations suggest that confinement can potentially provide a stand-alone means of controlling crystallization and that similar systems to those observed in nature could be exploitable in synthetic materials chemistry.

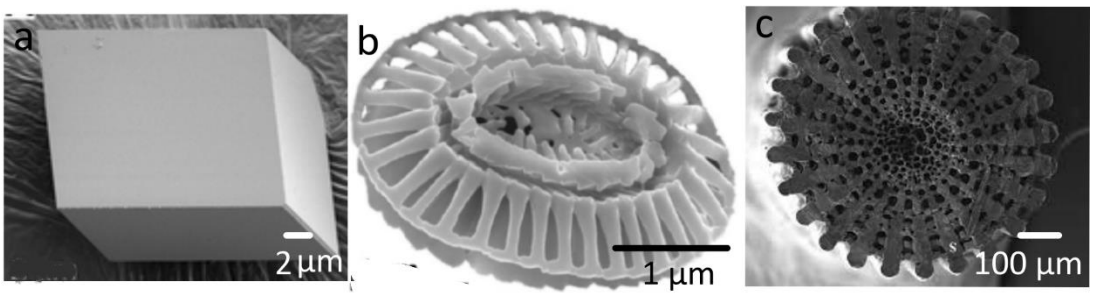

Figure 12. Calcite single crystals under SEM where (a) is synthetically obtained and (b,c) are naturally crystallized by (b) *Emiliania huxleyi* algae (coccolith plate) and (c) sea urchin (crossed-section of the spine).

Another area in which crystallization in confinement is of vital importance is in geology. Salt crystallization in pores and fissures often results in the damage

and breakage of stones, artworks and buildings, causing a huge cultural and economic impact.[100, 101] Similar effects are readily observed in asphalt concrete during frost heave or scale precipitation within porous equipment and pipes. Different factors have been suggested to contribute to the breakage of porous structures, the most relevant being crystallization pressure.[102, 103] Crystallization pressure is the stress that a confined crystal exerts when growing within a constrain space.[104] It can be calculated as a function of the supersaturation of a solution according to:

$$\Delta \boldsymbol{p} = \boldsymbol{p_c} - \boldsymbol{p_1} = \frac{\boldsymbol{RT}}{\boldsymbol{V_m}} \boldsymbol{lnS} \quad \text{(Equation 12)}$$

where p_c is the pressure at a loaded face, p_1 is the ambient pressure, R is the gas constant, T the temperature, V_m the molar volume of the solid phase and S the supersaturation. Other equations have also been proposed for calculation of the crystallization pressure, where these included water activities and crystal size.[104] Nevertheless, none of these theoretical approaches have yet managed to fully explain the different experimental observations of weathering effects with different salts.[103]

Some experimental studies have suggested that a crystal confined between two walls only causes damage if there is a film of solution between the crystal and the walls.[105] This film acts as a diffusion path, allowing continued crystal growth. The presence of the liquid film depends on the interactions between the crystal and the walls. If a crystal presents affinity for the surface, the crystal and the wall can make adhesive contact, avoiding the formation of the liquid film.[106] The absence of the film inhibits extra growth at the faces close to the surface and therefore, no pressure towards the wall can be developed. These observations indicate that crystallization pressure not only depends on the salt concentration, but also on the properties of the specific salt and the surface chemistry of the walls.[103] Understanding the mechanisms involved in the development of crystallization pressure is essential to prevent damaging effects. However, it is a challenging task, due to difficulties measuring such pressures in confined spaces and to the number of variables involved in the process such as evaporation rate, surface chemistry, pore size distribution

and porosity, salt properties and ambient temperature and humidity.[107-110] Recent work has focused not only on calculating crystallization pressures of salt nucleation and growth within porous media, but also on *in situ* imaging crystal formation.[88, 91, 96, 97, 111, 112] A better understanding and prediction of the conditions that govern crystallization in confinement is critical to the development of new strategies to avoid undesired precipitation and breakage in porous media.

A brief review of some of the systems that have been used to study crystallization in confinement are described in this section, together with some significant findings. In general, it has been observed that nucleation and phase transformations in confinement are slower than in bulk solution.[113] This makes confinement a valuable tool for selecting crystallization pathways and products, stabilizing metastable phases,[89, 114, 115] controlling single/polycrystalline structures,[116] crystal orientations[87] and morphologies[117] and even for identifying new crystal phases.[118, 119] However, the mechanisms that govern confinement effects are still unclear due to difficulties of studying *in situ* processes happening in such small spaces.

1.4.1 Synthetic liposomes

Synthetic liposomes are vesicles obtained from the self-assembly of surfactants into bilayer-type structures that can act as small compartments for crystallization.[113, 120] They have been used to study the influence of lipids in the calcification of calcium phosphate and to study the effects of confinement on crystallization.[121-123] Vesicles can exhibit a range of diameters (50 nm-50 μm) and have many similarities to biological systems.[124] Tester et al. showed that $CaCO_3$ nucleation in synthetic liposomes was inhibited, and that ACC was greatly stabilized in vesicles as large as 50 μm.[124] Stabilization in such large vesicles is intriguing. At these dimensions, ACC stabilization by thermodynamic effects is very unlikely and water can move freely from the solution into the vesicle.[124] Thus, the stabilization was rationalized by the lack of heterogeneous nucleation in the vesicles. Influence over crystal size and morphology was also observed using reverse micelles.[125, 126] Nanowires of

calcium and barium carbonates and calcium sulfate were seen to form from the aggregation of primary nanoparticles in vesicles, although their mechanism of formation was not completely understood.[127]

1.4.2 Droplet arrays

A more versatile and accessible system to study crystallization in confinement is the use of small (femto to microliter) droplets, such as droplets on patterned self-assembled monolayers (SAMs) substrates.[128-130] By creating small hydrophilic islands on a hydrophobic substrate, it is possible to direct the solution to the desired sites (Figure 13).[128] The crystallization of different organic[103, 104] and inorganic[128] compounds such as glycine or calcium carbonate and more recently of metal–organic frameworks (MOFs)[131] using these substrates revealed important information about their crystallization. For example, Wu et al. showed that highly oriented single crystals of various MOFs could be obtained by simply allowing femtoliter droplets to evaporate.[131] They also demonstrated that the morphology of the obtained MOF crystals was a consequence of the internal flow of the evaporation droplets, which is of relevance for the future synthesis of functional materials with specific shapes.

Another method that has been recently used to easily deposit picoliter droplets on a substrate is by inkjet printing.[132] This method creates thousands of small droplets on a substrate by acoustic pulses. Again, very low rates of contamination are achieved (Figure 14a). Glycine or perovskite are examples of solids whose crystallization was studied using this system.[133, 134] A decrease of the crystallization rate of the studied solids in the droplets was observed, which allowed the stabilization of intermediate metastable phases that are difficult to obtain in bulk.[128, 133]

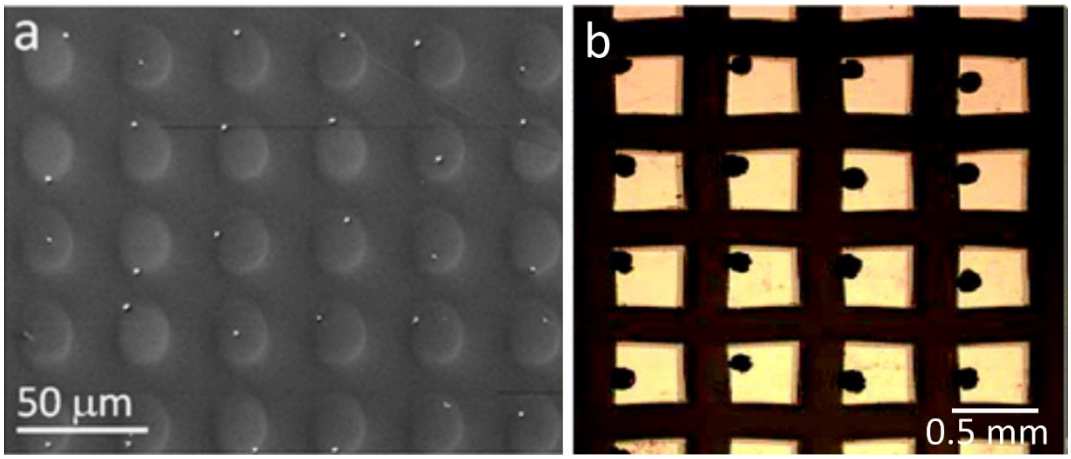

Figure 13. $CaCO_3$ (a) and glycine (b) crystals forming in droplets on patterned SAMs substrates. Figure adapted from ref.[128, 129]

Although droplets sitting on SAMs or deposited by inkjet printing were seen to be useful for studying crystallization in confinement, the solutions were always in contact with the substrates and therefore, possible heterogeneous nucleation from the surfaces cannot be ruled out. Contact-free crystallization has been achieved using levitating droplets (Figure 14b).[135] The crystallization of various inorganic solids and proteins in levitated droplets has been studied using Raman and X-ray diffraction, making this a useful method for obtaining *in situ* information about crystallization processes.[136, 137] For example, potassium hydrogen phosphate (KDP) was observed to nucleate by multiple pathways in evaporating, levitated droplets.[138] The droplets reached high levels of supersaturation before precipitation was ever detected. Interestingly, in these highly supersaturated solutions, new Raman vibrations appeared before crystal formation.[139] This suggested that non-crystalline precursors formed before crystal nucleation, indicating a two-step crystallization pathway.[138] It was also observed that different degrees of supersaturation can lead to the direct formation of the stable tetragonal KDP or it can form via a metastable, monoclinic KDP precursor.[138]

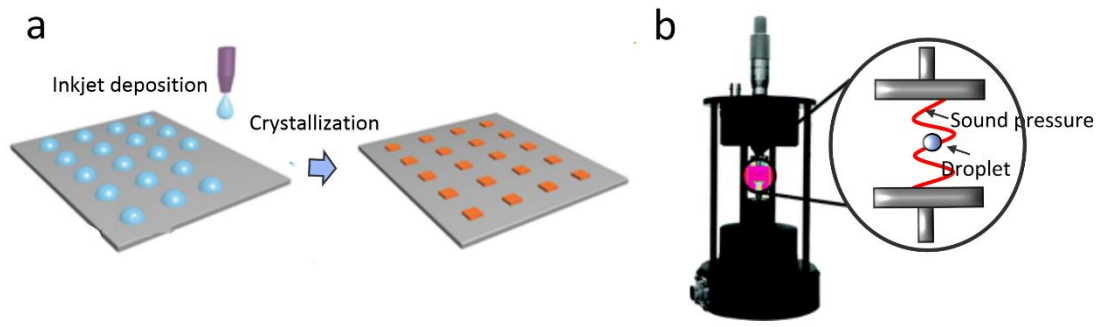

Figure 14. Crystallization in droplets using (a) inkjet printing and (b) a droplet levitation system. Figure adapted from ref.[134, 135]

1.4.3 Microfluidic devices

Microfluidic devices offer another possible means of studying crystallization in small droplets without the presence of surfaces. They present the benefit of producing thousands of isolated reactions in one experiment, allowing the fast screening of crystallization conditions, a nearly homogeneous fluid mixing and a significant reduction in the amount of possible environmental impurities per experiment.[140] Interestingly, microfluidic devices are very versatile, and offer the possibility of adjusting, for example, droplet size by simply modifying flow rates. Many different devices have been built over the last 10 years, where crystallization has been conducted in continuous flow, droplets or in reservoirs of different shapes and sizes, often regulated by a set of valves (Figure 15).[141-145]

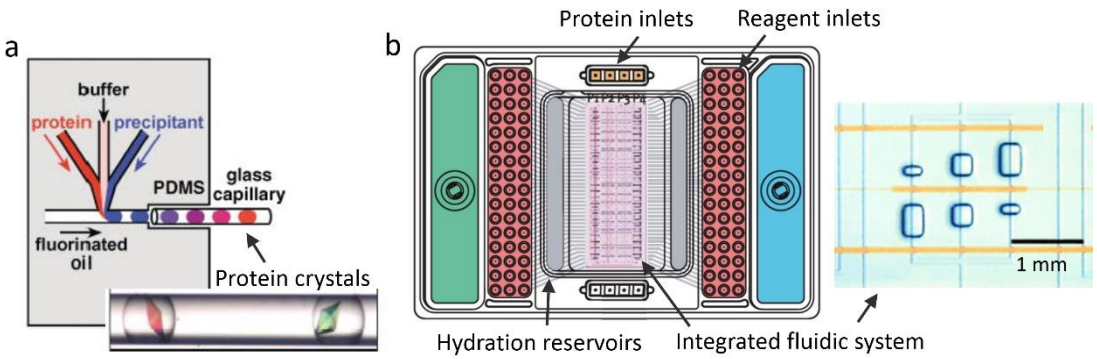

Figure 15. Examples of droplet-based (a) and valve-based (b) microfluidic devices. Figure adapted from ref.[146-148]

Microfluidic devices have been extensively used to identify crystallization conditions for proteins, due to the high throughput nature of these systems and the low amount of sample required.[148, 149] However, they did not have the impact that was expected for crystallization screening as a result of the high cost of the final chips and the equipment required to use them.[147] Also, scaling up the results obtained in the small droplets during the screening was not always possible. Currently, microfluidic systems are largely being exploited for fundamental studies of nucleation and crystal growth, polymorph screening and solubility determination of proteins, inorganic and organic compounds.[141, 147, 150, 151] Confinement effects have often been observed in microfluidic devices. For example, a metastable phase of the protein lysozyme could be isolated and stabilized in droplets created in a microfluidic device.[152] Another relevant example is the crystallization of $CaCO_3$ in a crystal hotel microfluidic device (Figure 16).[87] Direct observation of amorphous calcium carbonate (ACC) transforming into patterned calcite crystals was possible due to a significant retardation of $CaCO_3$ crystallization in confinement.[87] High control over orientation and single/poly crystalline character was also achieved.[87]

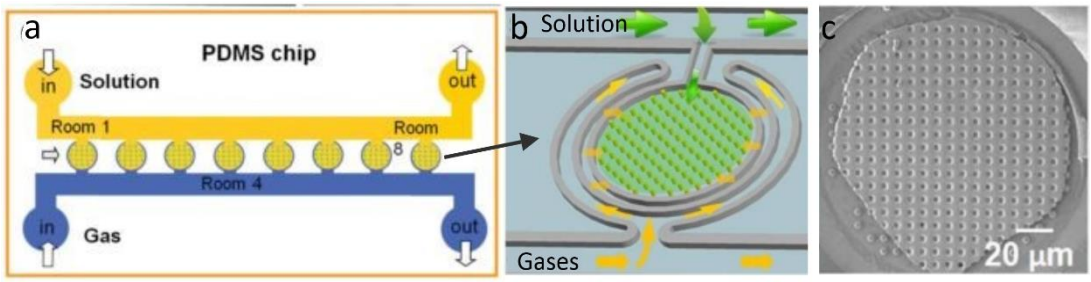

Figure 16. Schematic of a crystal hotel microfluidic device (a,b) and calcite crystal precipitated in one of the chambers (c). Figure adapted from ref.[87]

New advances in microfluidic systems include decreasing the dimensions of the channels to the nanometer scale.[153] The techniques for the fabrication of these small channels are still being investigated but they will certainly be a new and promising area of crystal growth research. Further, the use of additional analytical techniques to characterize the crystals on-chip is currently attracting much interest.[154, 155] Thus, many researchers have

focused on obtaining fast, high resolution Raman and X-ray information of crystals on-chip over the past few years, where these will become extremely useful in the investigation of the formation and stability of different polymorphs, their inter-conversion mechanisms and even the discovery of new phases.

1.4.4 Crossed cylinders

The crossed-cylinder apparatus is based on the injection of a small amount of solution between two crossed cylinders with equal radi of curvature (R). A diagram of this system is illustrated in Figure 17a. An annular wedge is formed between the cylinders, with surface separations that vary from 0 at the contact point to several millimeters. The contact area between the two cylinders is equal to that between a sphere with the same radius R and a flat surface as shown in Figure 17c.

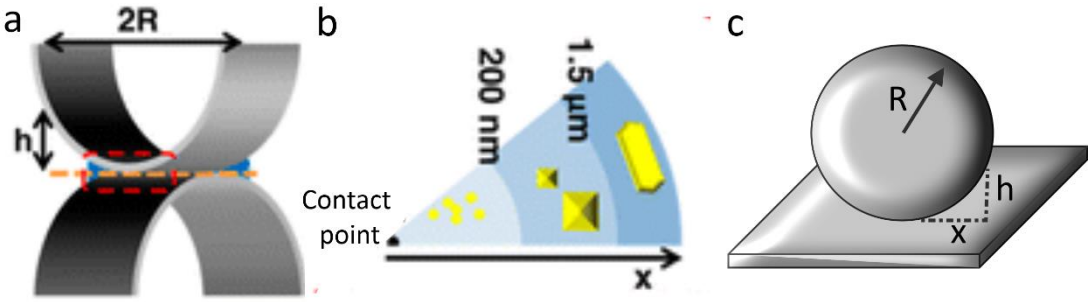

Figure 17. Schematic of the crossed-cylinder apparatus. Adapted from ref.[117, 119]

Using the following equation it is possible to calculate the surface separation (h) at different distances (x) from the contact point:

$$h = R - \sqrt{R^2 - x^2} \quad \text{(Equation 13)}$$

This system has been shown to be very useful for the investigation of crystallization in confinement of a range of inorganic solids.[117] The crystallization of calcium carbonate, calcium phosphate, calcium sulfate and calcium oxalate in the crossed-cylinder system provided insights into the

mechanism of crystallization of these solids.[89, 118, 119, 156] Remarkable stabilization of metastable phases was achieved at low surface separations. With such stabilization, it was possible to observe unusual crystal morphologies and even detect phases that were never observed before in bulk solution, such as amorphous calcium sulfate.[118]

1.4.5 Porous media

The ability to predict and control crystallization in porous media has been, and continues to be, an intense area of research due to its relevance to biological and geological processes.[157-159] Stark differences in crystallization in pores with respect to bulk have been previously reported.[88, 102] However, the general understanding of the mechanisms that govern precipitation in pores and the factors that differentiate it from bulk crystallization, is still poor.[102] A quick review of previous studies of crystallization in porous systems is presented in this section.

1.4.5.1 Polymer sponges

The ability to synthesize porous crystalline structures has attracted significant interest.[160] The internal structure and morphology of these porous crystals can be adjusted by modifying the template in which they form.[160] Porous crystals with interesting characteristics such as high surface areas and high pore volumes can be synthetize and used for many applications such as storage or adsorption materials.[161-163] Many templates have been used as scaffolds over the years, including polymers, biominerals and colloidal crystals.[160] Park *et al.* obtained porous single crystals of calcite by precipitating $CaCO_3$ within polymer replicas of sea urchin plates (Figure 18).[164, 165] The ability to create these complex morphologies by only modifying the crystallization environment, proves that confinement can be a more effective tool to control crystal morphology than the use of additives. Moreover, studying calcite crystallization in these porous systems brought insight into its mechanism of crystallization.[164] Indeed, it was shown that the presence of ACC is not required for the formation of single crystals with complex morphologies as had been suggested in previous studies.[166, 167]

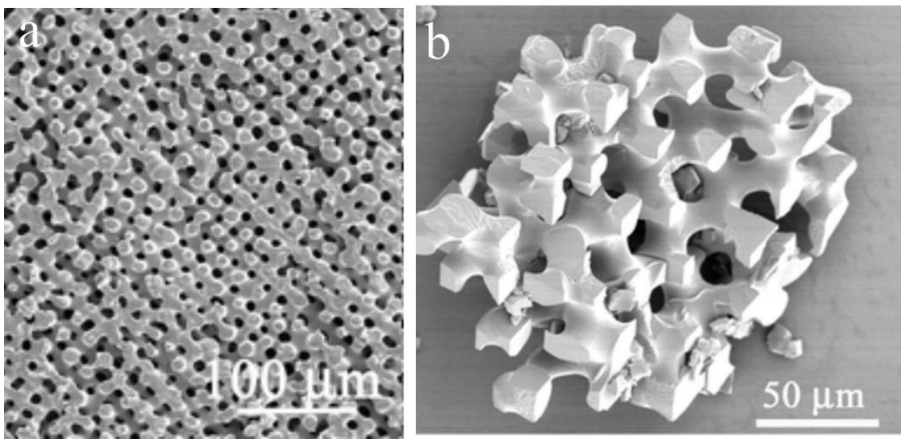

Figure 18. Polymer replica of a sea urchin plate (a) and calcite single crystal formed within the polymer (b). Figure adapted from ref.[164]

1.4.5.2 Porous membranes

Polycarbonate and alumina membranes have also been used to control crystallization.[168, 169] The membranes have thicknesses of tens of microns and contain regular cylindrical pores that cross the membranes. Inorganic solids such as calcium carbonate and calcium phosphate have been precipitated in porous track-etch membranes by placing them between two half U-tube arms, with the reagent solutions in the tubes.[115, 117, 166] In both cases, an amorphous phase formed and was stabilized in the pores, which then converted to a crystalline phase. The morphology of the crystals was also affected by the crystallization environment, resulting in rod-shaped calcite and hydroxyapatite crystals (Figure 19). Confinement also affected the orientation of the crystals, where for example, the orientation of polycrystalline hydroxapatite crystals ($CaPO_4$) in the pores of a track-etch membrane was comparable or even superior to that seen in bone.[115]

Metastable crystalline phases have also been stabilized using this system. Rod-like single crystals of vaterite were stable in the pores of a track-etch membrane for longer than 4 days before converting into calcite.[116] This demonstrated a significant retardation of the crystallization process in small volumes. A more recent study of crystallization within porous membranes also showed that they offer the perfect physical environment for the formation of

high-aspect ratio, CuO_2 crystalline nanorods with entrapped gold nanoparticles.[170] Confinement was in this case used to regulate the encapsulation and assembly of the nanoparticles into the crystals, without the need for organic structure-directing agents.[170]

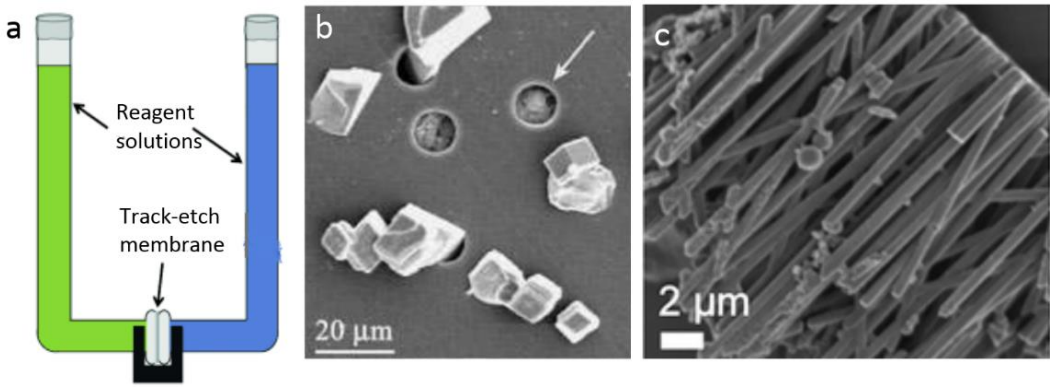

Figure 19. (a) Schematic of a track-etch membrane in a U-tube. (b) and (c) $CaCO_3$ crystals within the membrane and after the membrane was dissolved. Figure adapted from ref.[115-117]

1.4.5.3 Rocks

Recent advances in X-ray techniques, especially in X-ray computed tomography, have made it possible to study crystal growth *in situ* in the interior of rocks.[171] This is important since it allows the simulation and direct observation of mineralization in natural systems, which contain a variety of pore sizes and shapes. Researchers were able to determine changes in porosity when crystals form in the pores of a rock but also, growth and nucleation rates in a variety of porous rocks.[111, 172] Nevertheless, the resolution of these analytical techniques is currently too low to observe processes happening in the smallest pores of a rock: the nanopores. Nanopores are an important part of many rocks since crystals growing in nanopores are expected to exert a higher stress than those growing in macropores.[102, 111] Moreover, Anovitz et al. suggested that nanopores usually predominate in the total porosity of a rock, and play an important role as communication channels between the macropores of a rock.[173, 174] This makes nanopores a critical parameter of investigation.

Attempts to gain insight into processes happening on the nanoscale have involved analytical techniques such as small (and ultra-small) angle neutron

and X-ray scattering.[175] However, *in situ* analysis of large samples is still a challenge.[102] As a consequence, previous work has made use of simplified porous media such as silica aerogels in order to have a better understanding of pore-size dependent precipitation.[176] It was showed that small pores are highly efficient in suppressing nucleation and therefore, higher supersaturations than in bulk or large pores are needed to force precipitation in these confined spaces. Explanations for this phenomenon are still under debate and will be discussed in detail in this thesis. However, general hypotheses involve:[177]

(i) Calculations using classical nucleation theory predict longer induction times and higher supersaturations for smaller pore sizes. This is because the solute transport is slower than in bulk, which causes difficulties in forming clusters with dimensions comparable to the critical nucleus size. Thus, when in competition, nucleation should preferentially take place in large pores.[176]

(ii) A crystal growing in a nanopore will be limited by the size and shape of the pore. This means that crystals growing in nanopores might present a high surface area to volume ratio, making them more unstable than crystals formed in bulk. Thus, confined crystals might have higher solubility than the bulk solubility and therefore a solution could be undersaturated in a pore while it would be supersaturated in bulk.[177]

(iii) Strong interactions between the growing crystals and the pore walls are anticipated. The surface chemistry of the pores will therefore be extremely important for crystallization in confinement.

(iv) As higher supersaturations than bulk are expected in the nanopores, kinetic factors could indeed be dominant in the phase transitions. If the crystallization takes place in a non-classical way, prenucleation clusters and amorphous precursors could form in the supersaturated solutions in the pores. If this is true, the concepts used to define supersaturation at the point of crystal growth should be reconsidered.[177]

1.4.5.4 Controlled pore glass

Controlled pore glasses (CPGs) are a silica material with a refractory nature that contain tortuous pores of defined sizes (Figure 20a). They are usually fabricated via two different methods, namely phase separation of alkali borosilicate glasses and by a sol-gel method (sintered glass).[178-181] The first method consists of heating alkali borosilicate glasses at a desired temperature (usually between 500 – 700 °C) which initiates phase separation. Two interconnected phases are formed which have different solubilities in acidic media: an alkali-rich borate phase and an (almost) pure silica. After the leaching procedure, the borate phase dissolves, resulting in a porous silica structure with a purity of around 96% SiO_2. Porous glass obtained using this method is also known as Vycor and contains pore sizes in the range 1-120 nm. The pore size of the glasses and other structural properties can be tuned by modifying the temperature and time of the heating process and the leaching conditions. Using the second method, the sol-gel process, the use of elevated temperatures is avoided and porous glass can be synthesized at room temperatures by a gelling procedure. A two-phase gel is formed from solution by hydrolysis of an organometallic compound in a water/alcohol mixture. Subsequently, this gel is dried and becomes a porous, hard solid of composition 99.99% SiO_2. In this procedure, the drying process is the critical step which determines the structure of the porous glass.

Numerous studies have used porous glasses to investigate the effects of freezing and melting of pure liquids like water, hydrogen and helium, inert gases and organic liquids in nanoscale pores.[182, 183] These studies showed that melting points and enthalpies of fusion in nanoscale confinement can differ significantly from their counterparts in bulk solution. More recently, CPGs have been used to study the crystallization of organic and inorganic solids in confinement.[24, 184-187] Indeed, the ability to regulate the size or surface chemistry of the pores makes these media very well-suited to these studies. Similar systems that have been used previously as crystallization environments include macroscopic nanoporous poly(cyclohecylethylene) (PCHE) monoliths with ordered cylindrical pores (Figure 20b).[88, 188] However, their surface chemistries cannot be as easily controlled and modified as

porous glasses, making the latter a more convenient system for systematic studies.[185]

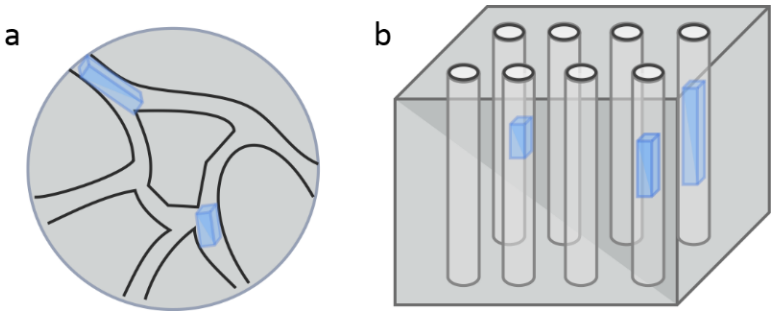

Figure 20. Nanocrystals growing in (a) CPG and (b) PCHE pores. Figure adapted from ref.[185]

CPGs have been used to study the polymorphism of a range of organic compounds.[185] For example, a study of anthranilic acid (AA) crystallization in CPGs of different pore sizes showed a significant stabilization of the metastable phase of AA at room temperature in the smallest pores.[184] This was rationalized by the similar size of the critical nucleus of this phase and the pore.[184] The pore size-dependent polymorphism was also studied for glycine, where the metastable phase (β-glycine) in 55 nm CPG pores only transformed into the most stable phase (α-glycine) in 60 days, as compared with minutes at room temperature.[189] Reducing the pore size to 24 or 7.5 nm stabilized the β- phase for more than one year at ambient conditions.

Another important area of solid precipitation within CPGs is the stabilization of amorphous pharmaceuticals in nanopores.[190] Amorphous drugs have a number of pharmaceutical applications, and are required to remain amorphous for long periods of time. However, many amorphous pharmaceutics show a strong tendency towards crystallization.[190] This problem can be reduced by confining drugs to nanoporous host systems, due to the fact that crystallization is slower in confinement than in bulk solution. Under conditions in which the pores are small, the interaction with the pore walls is strong and the compartments are small and isolated.[190] Thus, to increase the lifetime of the amorphous state, some features like the pore size,

pore topology and surface interactions can be optimized. This effect can also be enhanced in the presence of additives since they confer additional stability on the metastable intermediate phases.

The lack of studies of inorganic solids in CPGs in the literature in spite of the enormous importance of these solids in nature, is interesting. The reason for this is in large part due to the low solubility of many minerals, which makes pore filling difficult as will be discussed in chapters 3 and 4. Stack et al. provided the first attempts to crystallize $CaCO_3$ in CPGs and they showed that it could not precipitate in the nanopores of the CPGs.[186] Pore filling could be promoted by functionalizing the CPGs with carboxyl SAMs. However, analysis of the crystal phases found in the CPGs was still challenging due to the small amount of material in the nanopores. A method of crystallization in CPGs that allows pore infiltration and that can be applied to a large range of inorganic solids is required to gain insight into the effects that nanoscale confinement has on the crystallization of these solids. I describe a solution to this problem in Chapter 4.

1.5 Control of crystallization using surfaces

A solid precipitating in a specific environment is not only affected by the shape and dimensions of the crystallization environment, but also by its surface chemistry and topography. Indeed, as described in section 1.2.4, the activation energy to nucleation can be significantly modified when using different crystallization substrates due to changes in the interfacial free energy of nucleation (γ). Changes to the surface chemistry and the topography of a substrate have been shown to be effective tools to control crystal nucleation.[191-193] A review of relevant studies and findings about how to control crystallization via surface modifications is presented next.

1.5.1 Self-assembled monolayers

In the experiments described in this thesis, confinement, surface chemistry and topography effects were combined with the aim of better understanding

and controlling crystallization. Self-assembled monolayers were widely used to modify the surface chemistry of the different systems.

Self-assembled monolayers (SAMs) have been extensively studied over the last 30 years due to their applications in fields such as electronics, biotechnology and nanotechnology.[194, 195] SAMs are organic molecular assemblies formed by the adsorption and spontaneous organization of an active surfactant onto the surface of a solid. SAM molecules adsorb to the surface through a functional group which has a high affinity for the solid surface (the head group). They are formed by a long alkane chain ending in a terminal group whose functionality can be selected (Figure 21).[196] The most studied types of SAMs are those with thiols or silanes as a headgroup. Alkanethiols adsorb on metals such as gold, silver or platinum while alkylsilanes adsorb on silicon dioxide surfaces such as glass or mica.[197] The packing density of the SAMs depends on different factors including the solvent, temperature, nature of the adsorbate and substrate.

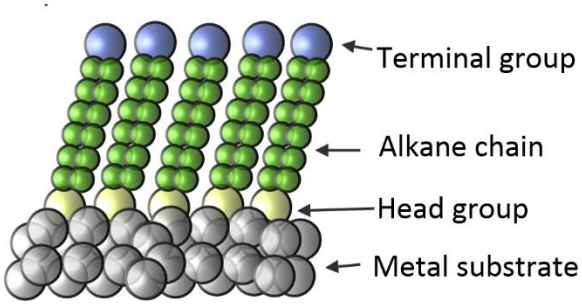

Figure 21. Schematic representation of an ideal SAM of alkanethiols on a metal substrate. Figure adapted from ref.[197]

From the study of biomineralization processes, it has been shown that crystallization takes place within privileged environments, where crystals growth in the presence of organic macromolecules which can modify their crystallization and properties.[198-200] It has been suggested that the organic scaffold where biominerals form is functionalized with active chemical groups, which provide the crystals with great structural control.[94] However, characterization and identification of the organic molecules that regulate crystal nucleation and growth is challenging.[197] Thus, many studies of the

nucleation of biogenic crystals have been carried out using model systems such as SAMs, in order to investigate the interactions between the growing crystals and the organic matrix.[191, 201, 202] These studies showed that the functional groups and the orientation and organization of the SAMs have a large impact on crystallization, affecting crystal density and the size, orientation and polymorphs of the forming crystals.[167, 191]

Currently, many different materials have been crystallized on SAMs, including proteins, semi-conductors and different minerals.[197, 203, 204 205-207] The use of SAMs to study crystallization is very convenient, since it provides a simple, well-characterized system, whose properties can be regulated to effectively study interactions between organic surfaces and inorganic compounds.[196, 197] Furthermore, SAMs are a useful tool for controlling crystallization.[194, 203] Aizenberg *et al*. showed by extensive morphological and XRD analyses of calcite crystals precipitating on SAMs, that highly oriented calcite crystals were obtained on surfaces with COO^-, OH and SO_3^- terminal groups.[202] It was also shown that crystal nucleation was inhibited on CH_3 terminated SAMs, while acidic functionalities induced nucleation.[202]

Another interesting function of SAMs, is the ability to selectively position the organic molecules on specific parts of a surface to create well-defined 2D patterns. Soft lithography techniques such as microprinting or photolithography have been used to create patterns of organic molecules on surfaces.[197] These substrates directed the growth of crystals with specific orientations and spatial distributions.[167, 191] Aizenberg *et al*. used microprinting techniques to create hydrophilic (COO^-) islands where calcite nucleation was induced.[191] The areas of the substrate without carboxyl terminated SAMs can also be functionalized with hydrophobic (CH_3) terminated SAMs, which suppressed calcite nucleation (Figure 22). The results were attributed to mass transport effects from the solution to the carboxyl terminated sites, which promotes the nucleation of the calcium carbonate crystals. Once the crystals start growing, they deplete ions over the hydrophobic region, which impedes nucleation on this area.

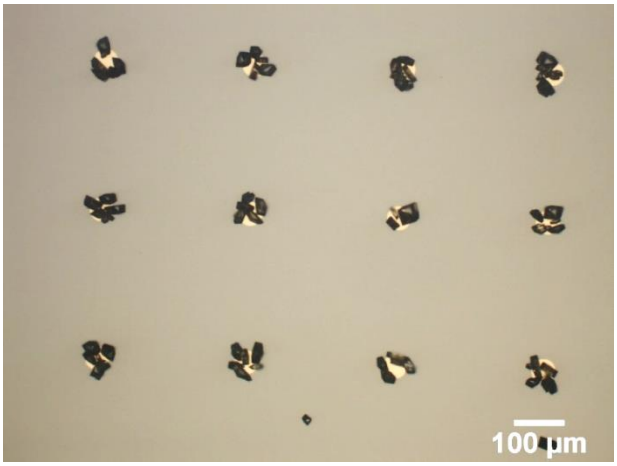

Figure 22. Representative example of calcite crystals growing on a patterned substrate with carboxyl terminated SAMs at the areas with crystals and fluorinate terminated SAMs on the parts of the surface. Image from work undertaken at Leeds.

Other examples of crystallization on SAMs include the work from Hiremath *et al.,* who crystallized 1,3-bis(m-nitrophenyl) urea (MNPU) on different biphenyl thiol SAMs.[208] They observed that different SAMs selectively nucleated specific polymorphs of MNPU and that all the nucleated crystals adopted preferred orientations with respect to the SAM templates.[208] Dressler and Mastai also observed the influence of SAMs on crystal polymorph.[209] They managed to stabilize the metastable α-L-glutamic polymorph by simply modifying the surface chemistry of a glass substrate with SAMs. The observed polymorph stabilizations on SAMs were attributed to the interactions of specific crystal faces with the terminal groups of the SAMs and two-dimensional lattice matching.[194]

1.5.2 Surface topography

Scientists have observed surface topography effects on crystallization for years, for example the formation of crystals on rough materials (such as hair) or on an unintentionally scratched surface.[210, 211] Defects on the surfaces are expected to promote heterogeneous crystallization by decreasing the energy barrier to nucleation.[25] This has been supported by computer simulation of crystallization on surfaces with scratches or pits, which confirmed that nucleation is more favorable at the topographical defects.[212, 213] For example,

Page and Sear showed that nucleation in wedge-shaped grooves is many orders of magnitude faster than on a flat surface and also that the angle of the wedge influences the nucleation rate.[213] This was justified by the competition between the angle of the wedge and the angles of the crystal lattice, which at the same time, might favor the nucleation of specific polymorphs.[213]

Nevertheless, the surface defects that are likely to have a large effect on nucleation are small (nanometric size) and therefore, systematic experimental studies corroborating the mechanisms that govern crystal nucleation in these features are rare.[214, 215] This is due to the difficulties in observing crystal nucleation at very early stages, and also the stochastic nature of crystallization. Furthermore, not every crystal system is affected by the same size or type of features,[216] which makes it challenging to form synthetic substrates with specific defects to promote the nucleation of specific solids. Previous efforts to control crystallization using topography have employed different systems that are summarized next.

Attempts to experimentally investigate the effects of topography on crystallization have been made using rough surfaces with undefined features.[217-219] Keysar *et al.* crystallized calcite on metallic surfaces of varying roughness.[217] They observed an increase in calcite adhesion to the surfaces and morphological changes in the calcite crystals as the roughness increased.[217] Other studies were performed on rough molybdenum, silicon, zinc, copper and iron substrates, where these showed similar effects to those seen by *Keysar et al*.[218, 219] A later study by Holbrough *et al*. showed the differences between crystallizing organic materials on mica and glass substrates before and after being scratched with diamond powders.[192] They showed a huge decrease in the induction time of the studied compounds on scratched mica surfaces.[192] While glass and mica show comparable surface chemistry and wettability, the surfaces of mica often present many nanoscale topographic defects. Flakes with diverse topographic features are formed after rubbing the surface with the diamond powders. Modification of the grain size of the diamond powders used to scratch the mica surfaces also caused

changes in the nucleation density, since different features can be generated in each case. Topographic defects with sharp edges can create wedges with dimensions comparable to the critical nucleus of the organic compounds, which are likely to promote crystal nucleation.

Nevertheless, in order to gain control over crystallization, it is necessary to improve our knowledge of the specific features that promote crystal nucleation. Therefore, investigations of crystal formation in individual features is critical. A first example is provided by the study carried out by Campbell *et al.,* in which organic compounds were precipitated in mica defects.[220] Mica surfaces often present natural features such as step edges or pockets after cleavage, and by comparing these defects before and after crystallization it was possible to predict the most efficient features for crystal nucleation. Preferential nucleation in defects presenting acute wedge geometries was observed for all of the compounds studied and a two-step capillary condensate mechanism of crystallization was proposed. Another relevant study was performed by Lee *et al.* who recently demonstrated that by creating cracks on the surface of PDMS it is possible to effectively guide the nucleation of $CaCO_3$ in association with the cracks.[193] These studies provide the first approaches to directly observe which defects promote nucleation and to guide future research to synthetically create specific features to control nucleation.

Many efforts to promote crystallization using topography have been carried out in protein crystallization as these macromolecules are difficult to nucleate.[221] Mineral surfaces, mica, hair and especially nanoporous materials have proven to be good nucleants for proteins, although as each protein is different, a universal nucleant has not yet been found.[73] Bioglass is a porous material containing a wide pore size distribution which has been shown to be active for the crystallization of a large range of proteins with different critical nuclei.[222] More specific nucleants for proteins are imprinted polymers, which acquire the shape of individual protein molecules (Figure 23).[223] The templates become sites that offer a high probability of nucleation since they

are able to trap proteins in solution. These interact with other proteins, generating a mass transport of the macromolecules towards the polymers.[224]

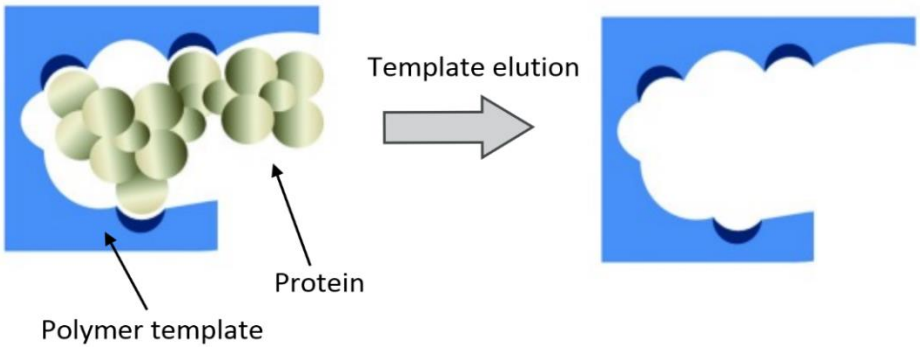

Figure 23. Schematic of polymer templates for protein crystallization. Figure adapted from ref.[224]

Although surface defects have been shown to have a large influence on the crystallization of proteins, [73, 225] recent work has focused on the development of systems that combine surface chemistry and topography to further promote their nucleation.[226, 227] Thus a range of proteins were crystallized on mica, porous polymer templates and carbon nanomaterials whose surfaces had been functionalized with SAMs.[226-230] These studies showed that induction times and crystal densities on functionalized rough substrates were significantly higher than on their respective unfunctionalized counterparts. The effectiveness of these materials is explained through a diffusion-adsorption mechanism in the pores or defects, which is promoted when the surfaces of the pores are functionalized with SAMs with terminal groups capable of interacting with the protein molecules.[216] However, direct observations of protein crystallization in specific features have not been reported yet, and therefore we do not have information about the specific features that are responsible for protein nucleation. Identifying the particular topographic defects that promote protein nucleation in each system is critical for the development of new universal nucleating agents and the crystallization of unresolved target proteins. Chapter 6 presents an investigation of protein crystallization in specific defects of mica and PDMS substrates.

1.5.3 Topics investigated in this thesis

A range of systems are introduced in this thesis to show that confinement, surface chemistry and topography effects can be used to build our understanding of crystal nucleation and to develop new ways of controlling crystallization. A brief description of the main analytical techniques used in the thesis is presented in Chapter 2. Chapters 3 and 4 focus on the crystallization of various inorganic solids in controlled pore glasses, where a new method that can be used to study the crystallization of inorganic solids in nanopores is presented. Surface chemistry modifications of the pores are also discussed. Chapter 5 describes the crystallization of proteins in confinement, where this work brings new insight into the mechanism of nucleation of the proteins studied. Subsequently, chapter 6 describes experiments that combine surface chemistry and topography to promote and control protein nucleation. Evidence for protein crystallization in topographic defects is provided and the most efficient features for crystal nucleation are identified. Finally, chapter 7 summarizes the results and discoveries described in this thesis, and presents new ideas for future work.

Chapter 2: Characterization techniques

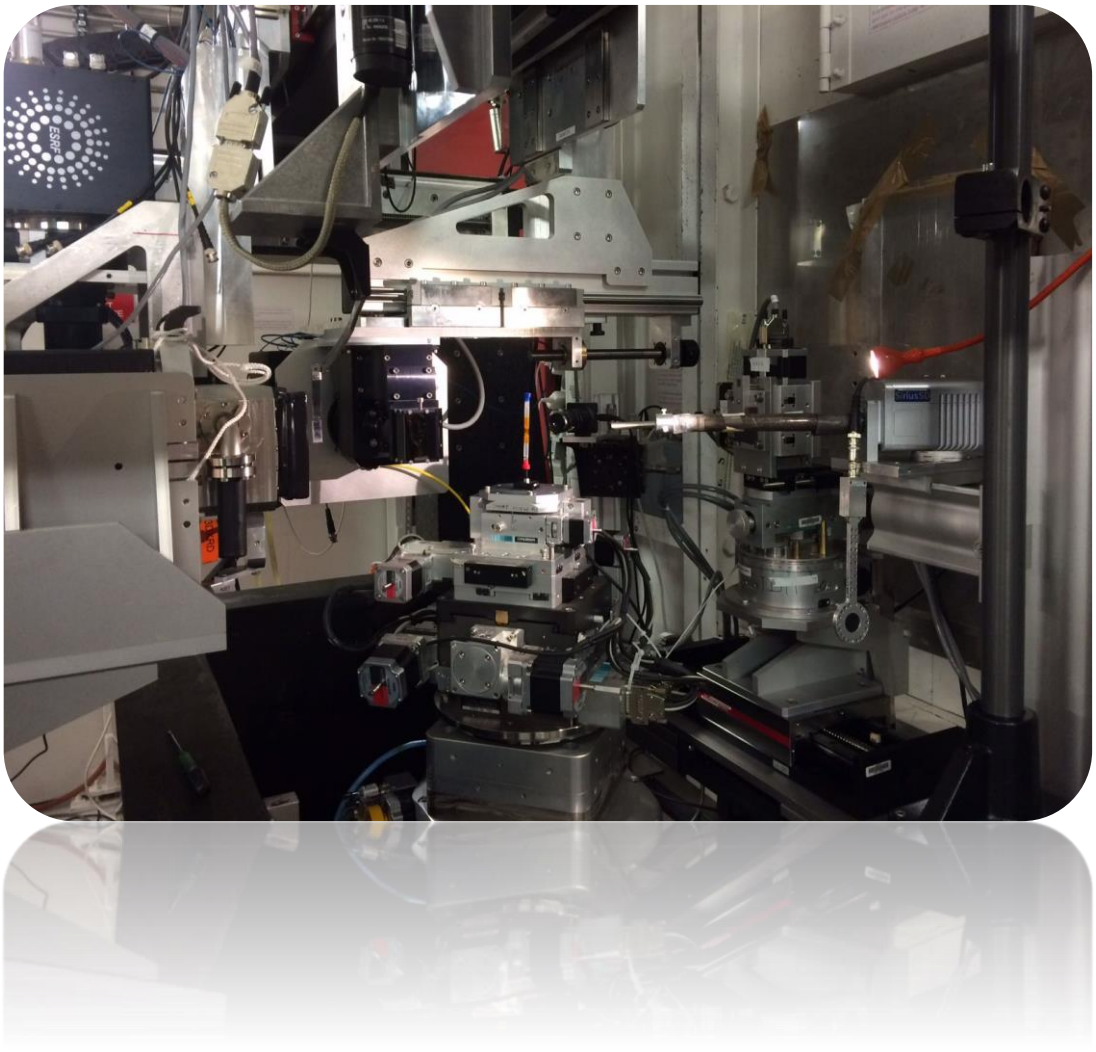

2.1 Experimental methods

2.1.1 General preparation methods

2.1.1.1 Cleaning methods

Before each experiment, extensive cleaning of the apparatus was undertaken since crystallization is affected by the presence of impurities. All basic experimental tools such as tweezers and scalpels were washed with water and ethanol and dried with nitrogen gas. All glassware including microscope slides for crystal growth were cleaned overnight in "piranha solution" (30% H_2O_2 and 70% H_2SO_4), then rinsed with Milli-Q water and stored under Milli-Q water until required. Controlled pore glasses (CPGs) were cleaned by immersing them in a 20% nitric acid aqueous solution at 100 °C for 2 h, then washing with DI water followed by ethanol, in which they were left overnight before drying in the oven at 60°C for 3 h.

2.1.1.2 General crystallization methods

Crystallization of inorganic solids

For the crystallization of highly soluble inorganic solids such as potassium ferrocyanide (II) two methods were employed. Firstly, crystallization by evaporation was conducted by allowing a highly concentrated aqueous solution of the solid studied to evaporate. Variables such as humidity or temperature were regulated as required. The second method used was fast precipitation, where the solid aqueous solution was mixed with a precipitant. The precipitant was a solvent in which the solid of study was insoluble, which causes instant precipitation.

For the crystallization of inorganic solids with poor solubility in water such as calcium carbonate or calcium sulfate a double-decomposition method was used. This method typically consists of mixing equimolar $CaCl_2$ and Na_2CO_3 or $NaSO_4$ aqueous solutions to form a final solution supersaturated in the solid of interest.

Crystallization of proteins

Protein crystallization was mainly carried out using batch and microbatch methods (detailed explanations of these methods can be found in Chapter 1 of this thesis). In this method, the protein in a buffer solution is mixed with a precipitant solution and the mixture is kept under paraffin oil to avoid evaporation.

2.1.1.3 General coating methods

Glass slides, watch glasses, controlled pore glass (CPG) and mica substrates were coated with alkylsilane chains using a chemical vapor deposition method.[231] This method is based on the evaporation of a volatile silane (in the liquid state) using low pressure and/or high temperatures, and its attachment to glass or silicon surfaces (Figure 24). The coating procedure was carried out as follows: the substrates were placed together with 1 mL of the liquid silane in a vacuum chamber for 1h at room temperature. After this, the silane was removed from the chamber and the substrates were kept under vacuum for 1 h at 45 °C in order to evaporate any condensed silane. The substrates were then washed with toluene and ethanol and dried in the oven at 60 ℃ for 2 h.

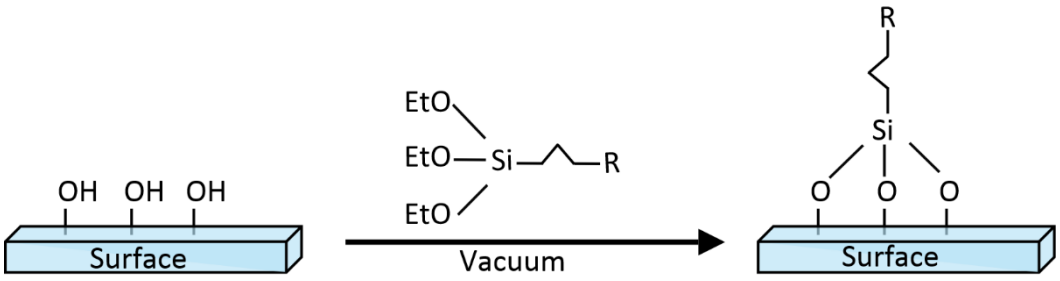

Figure 24. Silane deposition onto a glass or silicon substrate.

The silanes used for coating were purchased from Sigma Aldrich as 3-Aminopropyl-triethoxysilane for amino terminated hydrophilic coating, and triethoxy(1H, 1H, 2H 2H-perfluoro-1-octyl)silane and Triethoxy(octyl)silane for fluorine and methyl terminated hydrophobic coatings, respectively. Successful coating of the substrates was confirmed by contact angle measurements, or by the Ninhydrin test in the case of porous materials.[232] The Ninhydrin test was carried out on amine terminated CPGs beads, where the CPGs were

wetted with 1M ninhydrin/ethanol solution. The ninhydrin solution presents a yellow color but when it reacts with amine groups it forms a purple molecule - called Ruhemann's purple - according to the reaction shown below. The transparent CPGs completely turned purple after ninhydrin contact, proving that they were coated (Figure 25).

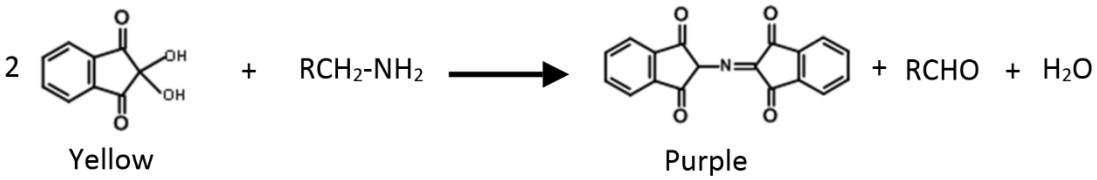

(Equation 14)

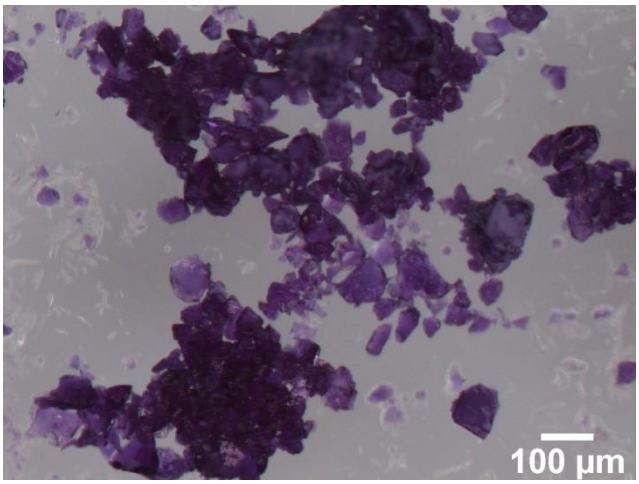

Figure 25. Amine funtionalized CPGs after ninhydrin test.

The amino terminated substrates were converted to carboxyl groups by immersing them in a 10% solution of succinic anhydride and 1% of 4-dimethyl(amino)pyridine in N,N-dimethylformamide (DMF) overnight.[233] After the reaction, the substrates were washed with DMF, water and ethanol and dried in the oven at 60 °C for 2 h. Successful transformation was confirmed by IR (Figure 26).

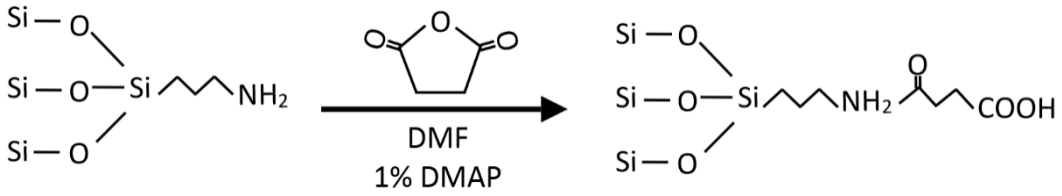

(Equation 15)

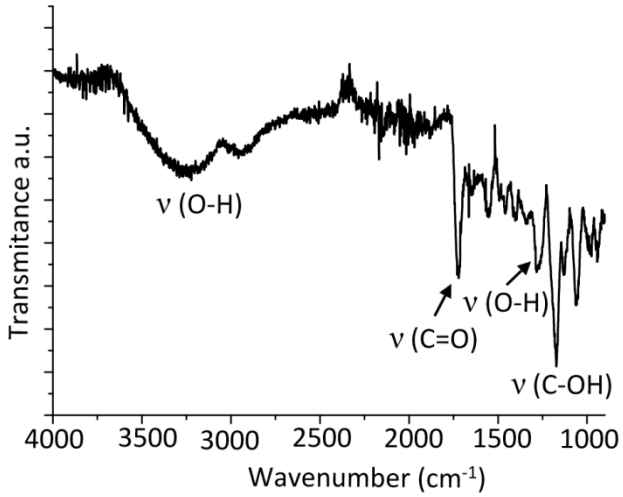

Figure 26. IR spectra of carboxyl functionalized CPG rods.

Other substrates such as polymers (e.g. PDMS) were coated with a 10 nm layer of iridium or gold using a Cressington 208HR High Resolution sputter coater and a Mantis Qprep250 deposition system respectively before SAMs deposition. In the case of the gold coating, 2 nm of chromium were deposited between gold and substrate to improve the metal adhesion. The metal-coated substrates were immediately immersed in a 2mM thiol solution with ethanol as the solvent for 18 h, followed by careful washing of the substrates with ethanol and drying with N_2 gas. The thiols used for PDMS coating were obtained from Sigma Aldrich as 11-Mercaptoundecanoic acid (carboxyl terminated), 11-mercapto-1-undecanol (hydroxyl terminated), 1-hexadecanethiol (methyl terminated) and 1H, 1H, 2H, 2H-perfluorodecanethiol (fluorine terminated).

2.1.2 Analytical techniques

2.1.2.1 Optical microscopy

Optical microscopy is widely used throughout the work presented in this thesis to both image and distinguish between amorphous and crystalline material. The latter is possible thanks to the birefringent properties of most crystals. Birefringence is an optical property by which anisotropic materials refract light differently depending on the angle of the incident light with respect to the crystal lattice. Optical microscopes are often fitted with two polarization filters: a polarizer that only allows the passage of light at a specific orientation and an analyzer oriented at 90° from the polarizer. If the sample of study is isotropic, as in the case of amorphous material, the incident light will not interact with the sample and it will be cancelled by the analyzer. However, in anisotropic crystalline samples, some light will be scattered by the crystal in other directions, travelling through the analyzer and detected in the eyepiece.

2.1.2.2 Confocal microscopy

Confocal microscopy is based on the principle of illuminating a sample point by point, and excluding most of the reflected light from the specimen that is not in the focal plane of the microscope. To do so, a specimen is illuminated at a certain focal plane through a pinhole and the returning light will pass through a second pinhole aperture which will filter the light (Figure 27). Light that is out of focus will be rejected by the pinhole and images will be slowly reconstructed from the light rays of the correct focal plane.

The majority of confocal microscopes are used as fluorescence confocal microscopes and use an intense laser (mainly blue light) as a light source. The laser will excite the specimen for analysis and if it is a fluorophore it will fluoresce. Fluorescein is commonly used in confocal microscopy analysis since it emits green fluorescent light when stimulated with a blue laser. The investigation of fluorescent specimens using confocal microscopy is very useful since only the fluorescent light emitted by the specimen on the focal plane will be observed. The two pinholes of the confocal microscope will strongly reduce the background that is usually observed when using a normal

fluorescent microscope. Using a fluorescent microscope, reflected light from other focal planes is observed which in case of small crystals or cells will be a problem since the images will be blurry and not clear. The confocal microscope will, however, exclude all the reflected light from other focal planes, resulting in images of higher quality. Because it scans thin sections through the sample each time, it is also possible to build clear 3D images of the samples.[234]

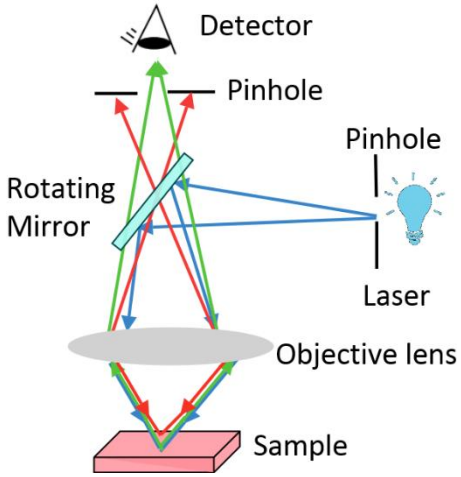

Figure 27. Schematic of a confocal microscope set-up where the light emitted from the sample is represented in green when is on the focal plane and in red when is out of focus.

A Zeiss LSM700 inverted confocal microscope was used in the work described in Chapter 6 to observe proteins labelled with fluorescein. The samples were imaged in solution and ex-situ with 10x and 20x objectives.

2.1.2.3 Scanning electron microscopy (SEM)

SEM is a type of electron microscopy where a beam of electrons is focused on an electrically conductive sample. The electrons are produced and accelerated by an emission gun in a high vacuum column. Subsequently, the electrons pass through condenser lenses and then the beam is focused on the sample. When the electrons interact with the surface of the specimen, different interactions take place between the electron beam and the atoms of the sample. Secondary electrons or back scattered electrons are emitted from the sample and the amount of the electrons detected will depend on the

topography of the sample. These electrons are collected and amplified, generating an image. SEM has a resolution of up to 1 nm and the samples need to be conductive and imaged under vacuum. When the samples are not electrically conductive, they must be coated with an ultrathin layer of electrically conducting material such as gold.

A Nova NanoSEM 450 operating at 1-5 kV with an EDXA (Energy-dispersive x-ray analysis) incorporated, was used in the work described here. The samples for SEM were mounted on SEM stubs using conductive carbon tapes. The samples were usually coated with 2 nm layer of iridium using a Cressington 208HR High Resolution Sputter Coater.

2.1.2.4 Transmission electron microscopy (TEM)

In TEM, a small, coherent electron beam is generated by an electron gun and the electrons are focused on a thin sample (maximum ~100 nm) that allows the electrons to travel through it. Precise focus of the electron beam via condenser lenses is critical to obtain high resolutions down to a few angstroms.[235] The electrons interact with the atoms of the sample as in the case of SEM and the transmitted and scattered electrons are directed using a range of electromagnetic lenses to create an image or a diffraction pattern.[236] When a TEM image is generated from the inelastic and elastic scattered electrons from the sample, the term dark field imaging is used and when the image is generated from the transmitted electrons (most common) it is known as bright field imaging.

Crystalline samples can also diffract electrons. The diffracted electrons can be easily controlled with electromagnetic lenses, which allows very short exposure times of specific areas. This type of diffraction is known as selected area electron diffraction (SAED) and it is very useful to obtain diffraction information of small crystallites or even small areas of a crystal by varying the dimensions of the apertures. TEM is in this way a very effective technique to obtain both morphological and crystallographic information of a sample with high resolution. However, there are limiting factors such as sample thickness

or the need of a vacuum environment for sample imaging, which impede *in situ* experiments. New developments in TEM techniques such as the use of liquid cells or the embedding of samples in amorphous ice (Cryo-TEM) can overcome many of these restrictions.[237, 238]

TEM images for this thesis were recorded with an FEI Tecnai TF20 FEGTEM (high resolution transmission electron microscopy, TEM) operating at 200 kV. Electron diffraction was carried out by selected-area electron diffraction (SAED) using a 0.5 µm aperture.

2.1.2.5 Contact angle measurement

This technique is based on the measurement of the contact angle of a liquid droplet on a substrate. The contact angle of a liquid will vary depending on its wettability, and therefore hydrophobic surfaces show a larger contact angle than hydrophilic ones. Two contact angles are important in each measurement: the advancing contact angle θ_a which is measured when the interface advances over the substrate, and the receding angle θ_r when the interface recedes over the substrate. The advancing contact angle is the biggest angle that the drop can reach on a specific substrate, such that $\theta_a \geq \theta_r$. The difference between these two angles is called the contact angle hysteresis ($H= \theta_a - \theta_r$). This angle gives us information about the chemical heterogeneity, the surface roughness, the contact-line deformation and the adsorption or absorption of the solvent by the substrate.[239] In the work presented here, the contact angle of water droplets on different substrates coated with SAMs were measured in order to obtain information about the wettability of the substrates.

2.1.2.6 Brunauer-Emmet-Teller (BET) and Barret-Joyner-Halenda (BJH) analysis

BET and BJH analysis are gas adsorption techniques that are frequently used to characterize porous materials. Although many gases and vapors can be used as adsorptive in the measurements, nitrogen is most generally used.[240] BET analyses are particularly useful for measuring the surface area of a

material. The sample is first degassed and brought to liquid nitrogen temperature (around 77 K). A controlled amount of N_2 gas is injected in a flask containing the sample and the surface area of the material is calculated by measuring the changes of gas pressure before and after adsorption.[241] BJH analysis, in contrast, is usually used to investigate pore size distributions, porosities and pore sizes. During these measurements, the pores are first filled with N_2 and then pressure is applied, forcing the N_2 to leave the pores in specific steps. The condensed liquid adsorbate in the core of the pore is the first to evaporate at a determined pressure, which is related to the radius of the pore by the Kelvin equation.[242] Subsequently, a layer of adsorbate at the walls of the pores evaporates slowly at different pressures. The thickness of this layer is related to the applied pressure by the thickness equation.[242] Pore volume information is obtained from measuring the pressure at the distinct steps and the range of pore sizes of the sample is estimated. A schematic representation of the different pore zones is shown in Figure 28.

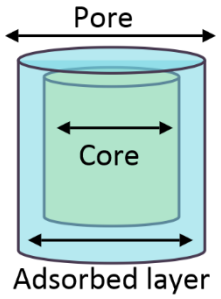

Figure 28. Schematic representation of a pore filled with N_2 gas, where the core is the internal part of the pore containing condensed liquid adsorbate and the adsorbed layer is the external part attached to the pore walls.

In this thesis, BET and BJH analysis were used for surface area, pore size and porosity investigations of controlled pore glasses. The analysis were carried out after degassing for 3 h at 120 °C, using an ASAP 2020 (Accelerated Surface Area and Porosimetry System, micrometrics).

2.1.2.7 Infrared spectroscopy (IR)

When a molecule is irradiated with IR radiation, alterations in the vibrational levels of the molecule occur and so, if the vibrational frequency of a chemical bond is the same as that of the radiation, the chemical bond will absorb energy. The amount of transmitted radiation will therefore decrease in intensity after passing through the specimen. The total decrease depends on the specific frequencies at which individual bonds vibrate after absorbing IR light. These frequencies are characteristic of each bond and therefore can be related to the structure of a molecule. Measurements of the transmitted IR radiation through a sample can be used to characterize not only different materials but also different polymorphs.

IR measurements in this thesis employed a Perkin Elmer Spectrum 100 FTIR with a diamond ATR. A small amount of solid is usually placed on the diamond surface of the instrument and pressure is applied. The samples were scanned 5 times at 4.00 cm^{-1} resolution

2.1.2.8 Raman spectroscopy

Raman spectroscopy is based on the irradiation of a sample with monochromatic light, usually from a laser in the visible, near infrared or near ultraviolet range, which then interacts with the sample causing changes in its photon energies. The intensity of the Raman scattered light depends on the vibrational and rotational modes of the substance which allows its characterization.

In this thesis, both Raman and IR spectroscopies were used to distinguish between the different polymorphs of a solid. The measurements were carried out using a Renishaw 2000 Raman microscope operating with a 785 nm diode laser. The Raman laser was focused on the sample crystals through a microscope objective and the scattered light was collected by the equipment.

2.1.2.9 X-ray diffraction and synchrotron radiation

X-rays were first detected in 1895 by the German scientist Wilhelm Röntgen who researched the nature of this radiation and was able to record the first radiograph of a human being (Figure 29a).[243] Seventeen years later, the physicist Max von Laue suggested that crystalline materias diffract X-rays and together with various colleagues, he recorded the first diffraction pattern of a copper sulfate crystal.[244] Shortly after, Sir William Henry Bragg and his son William Lawrence Bragg discovered how X-rays could be used to elucidate the structure of the crystals following a simple equation known as the Bragg law:

$$n\lambda = 2d\ \sin\theta \quad \text{(Equation 16)}$$

where n is a positive integer number, λ is the wavelength of X-ray incident beam, d is the interatomic spacing between the planes of a crystal and θ is the diffraction and incident angle. Bragg's law predicts when constructive interference between X-rays will occur after the radiation is scattered by the atoms in a crystal lattice, creating peaks at certain diffraction angles (Figure 29b). W. L. Bragg explained how to use these principles to determine the internal atomic structure of the material and also the meaning of differences in the intensity of diffraction spots, launching the field of X-ray crystallography.

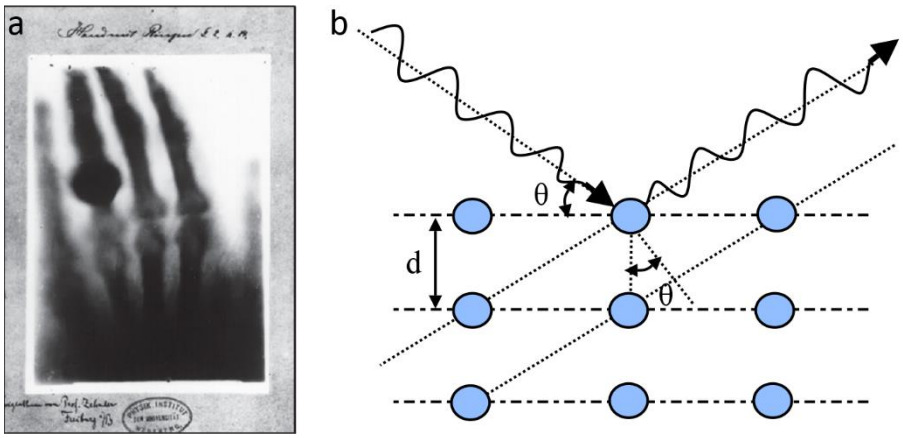

Figure 29. (a) First radiograph of a human being. (b) Schematic of X-ray diffraction according to Bragg's law.

Powder X-ray diffraction (PXRD) measurements in this thesis used an X'Pert Phillips diffractometer with spinner configuration. Samples were placed in a sample holder and PXRD data were collected between 10° and 60° in intervals of 0.033° and a scan rate of 0.119°/min.

The first laboratory X-ray diffractometers produced X-rays by the collision of an electron beam with metal targets, commonly copper, which were then pointed at the sample. Currently, new ways of producing X-rays have been developed where different wavelengths of light and a higher energy beam are achieved at facilities called synchrotrons. In a synchrotron, electrons are accelerated at a maximum speed close to the speed of light which permits the production of narrow X-ray beams of high intensity. The quality of a synchrotron beamline can be designated by the photon flux and the brilliance of the beam, which defines the number of photons that concentrate in a defined area per second.[244] Thus, a requirement for any synchrotron is to achieve low divergent X-ray beams which can be focused in very small spot areas. High brilliances allow short exposure times and low signal to noise ratios which together with modern high quality detectors make fast data acquisition possible for time-resolved experiments.

A synchrotron typically consists of 4 main components, as illustrated in Figure 30. Firstly the electrons are generated in an electron gun and accelerated using linear accelerators (linac). The electrons are then injected into a circular accelerator called the booster, where they are accelerated with a radio frequency voltage source, such that they achieve energies of 6 GeV. The accelerated electrons then pass to a closed storage ring where they circulate following an array of magnets in a vacuum environment. The magnets in the ring guide the electrons, making them follow a circular trajectory. However, as they divert from the straight path, they produce X-ray radiation tangential to the ring. Some radio frequency cavities are usually also found in the storage ring to supply the electrons lost during the emission of X-rays. Finally, the emitted X-rays are directed towards beamlines surrounding the storage ring where the X-ray experiments are carried out.

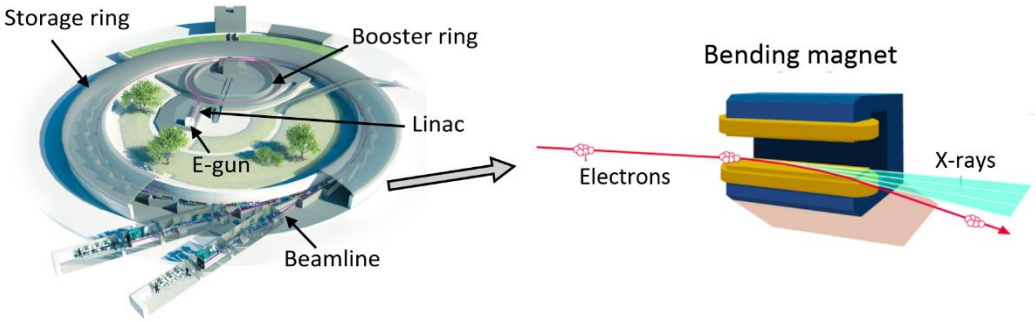

Figure 30. Schematic of a synchrotron facility showing its main components. Inside the storage ring the bending magnets produce the X-rays that arrive to the beamlines. Figure adapted from ref.[245]

Synchrotron radiation is currently used for many applications, from resolving the atomic structure of a protein, to the direct observation of the interior of a cell or even the characterization of amorphous materials. Many novel X-ray analysis techniques have been developed and are now available at these facilities where they benefit from high quality hardware, brilliant high flux and well trained scientific staff.

2.1.2.10 X-ray computed tomography (CT)

X-ray computed tomography is a non-destructive technique which uses X-ray radiation to obtain information about the internal structure of a specimen. Samples can be virtually sliced using this technique and voxels (elements of the topographic reconstruction) are collected with a CCD detector. The principle of CT is that high energy X-rays can penetrate into the material and the amount of X-rays absorbed from the sample vary depending on the electron density of the material. The X-rays transmitted after travelling through the sample form a 2D projection of the object and, as different materials absorb X-rays differently, images with different contrast are expected from different materials. The difference in the contrast between phases creates the projected image. For example, in medical applications, bones or teeth have higher contrast than tissues, making them distinguishable by CT. The observed pixel intensity in the final image is proportional to the intensity of the X-rays after travelling through the object according to Beer's law:

$$I = I_0 \exp(\sum_{k=1}^{M} \mu_k \Delta z) \quad \text{(Equation 17)}$$

where I is the beam intensity and μ is the attenuation coefficient along the path MΔz. 3D imaging of a sample is usually carried out by rotating the sample 180° around an axis perpendicular to the X-rays. For medical applications, the sample (patient) remains still and both X-ray source and detector rotate around the sample. The common set-up used for computed tomography experiments is illustrated in Figure 31, comprising an X-ray source, a sample parallel to the source, a scintillator, magnification optics and a CCD camera.

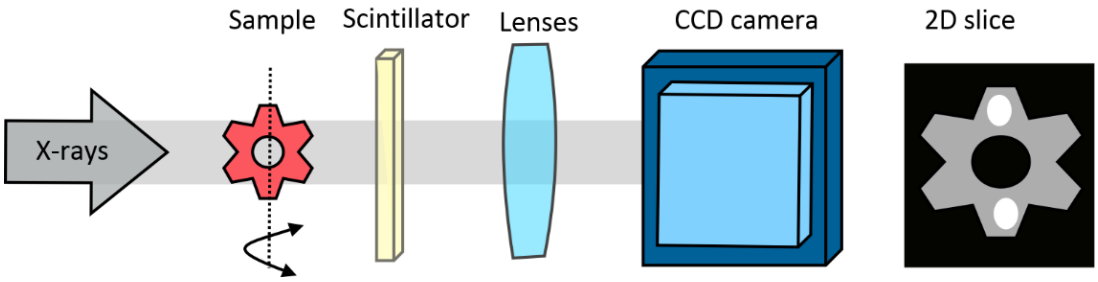

Figure 31. Diagram of the typical set-up for X-ray computed tomography.

2.1.2.11 X-ray diffraction tomography (DCT)

X-ray computed tomography (CT) is a useful technique to obtain time-resolved 3D images of the internal structure of a material. However, it does not allow phase characterization nor does it provide information about crystal orientation or strain. In a multiphase sample (containing different materials or polymorphs), combining imaging with diffraction information is necessary in order to have a complete understanding of the material being studied.

X-ray diffraction tomography (DCT) is based on the same principles as CT but instead of a beam covering the sample, a pencil-shaped X-ray beam moves across the sample, taking diffraction patterns at many different positions and angles.[246] 2D slices are reconstructed for each 2θ angle and then using similar algorithms as those used for CT, diffraction maps can be obtained, allowing materials with similar X-ray attenuation coefficient such as polymorphs to be

distinguished.[247] The use of a pencil beam instead of a full beam has the advantage of avoiding the overlap of diffraction information, but it degenerates into very long scanning times. Furthermore, the resolution of the final image will directly depend on the size of the beam, as well as the sample characteristics, and therefore higher resolution images will require long scans with a small focused beam. Thus, although DCT is a very useful technique since it can provide 3D crystallographic information of a variety of samples, time-resolved studies are still very challenging for this technique.

2.1.2.12 *In situ* solid-state nuclear magnetic resonance (SSNMR)

Nuclear magnetic resonance (NMR) is an analytical technique based on the magnetic properties of atomic nuclei. All nuclei are charged, but in order to be detectable by NMR they must present a non-zero magnetic moment. Nuclei with an odd number of protons or/and neutrons such as ^{13}C or ^{17}O are NMR-active as they show magnetic moment and overall nuclear spin, I different than 0. NMR-active nuclei have randomly oriented spins under normal conditions. However, when a magnetic field is applied, a nuclear energy level diagram is formed, and their spins align into a number of spin states equal to $2I+1$. For example, a nucleus of $I=1/2$ (the most common situation), will have its spins aligned with or against the magnetic field. When the nucleus in then exposed to radiofrequency (RF) radiation, it will resonate at a specific frequency, depending on the energy gap between its spin states.[248] An NMR spectrum can therefore be recorded since different atoms will resonate at different frequencies. This information is very useful to determine the chemical structure of a compound and ultimately for structural determination of unknown samples. The most common nuclei used in NMR are ^{1}H, ^{13}C and ^{31}P due to their spin $I=1/2$ and their relative abundance in nature.

Conventional liquid NMR has been, and still is, one of the most versatile characterization techniques in Chemistry. It has been widely used to study dynamic processes and *in situ* chemical reactions.[249, 250] Solid-State NMR (SSNMR) has also been shown to be very useful to study the structure and properties of solids.[251] However, while in a liquid, unrestricted isotropic

interactions exist between molecules, in a powder, molecules are oriented differently with respect to the magnet. This causes anisotropic molecular interactions which usually result in broad peaks and low resolution spectra.[252] Therefore, *in situ* studies were left behind until very recently. Currently, the development of new methods, new probes and implementation of high magnetic fields are overcoming the problems associated with SSNMR and this technique is becoming a very useful tool to follow crystallization processes.[253] The inclusion of a new method known as magic-angle spinning (MAS) enabled particularly important advances in SSNMS. MAS consists of rapid spinning of a sample at a specific (magic) angle with respect to the direction of the magnetic field. At the magic angle, it is possible to eliminate orientation problems in solid samples by averaging the nuclear anisotropic interactions.[252] The new developments in *in situ* solid-state NMR allow the observation of a solid phase evolution with time, distinguishing for example different polymorphs.[254, 255] It is also possible to obtain information about the evolution of both liquid and solid phases during the crystallization event, providing insight into fundamentals in the crystallization mechanisms.[256]

The *in situ* solid-state ^{13}C NMR measurements presented in this thesis were carried out using a Bruker AVANCE III spectrometer at the U.K. 850 MHz Solid-State NMR Facility at the University of Warwick. The samples were inserted in sealed 4 mm zirconia rotors which were then placed into the probe of the NMR spectrometer and subjected to magic-angle spinning (MAS).

Chapter 3: Crystallization of Inorganic Solids in Confinement: Controlled Pore Glass Beads for Highly Soluble Solids

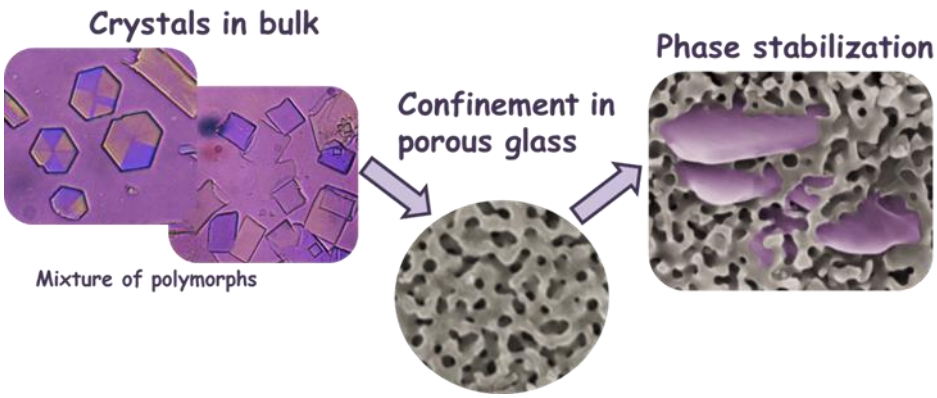

3.1 Introduction

3.1.1 Aims and overview

Many important crystallization processes in nature take place in confined spaces, including the formation of biominerals and weathering or frost heave processes. However, we have a limited understanding of the mechanisms that govern crystallization in confinement from solution. The objective of the work presented in the next two chapters was to develop general methods to crystallize and analyze a wide range of inorganic solids in confinement. Through these methods we aimed to gain insight into the role of confinement on crystallization, and ultimately, to understand and reproduce the formation and stabilization of unique crystals in nature.

This chapter describes an investigation into the crystallization of potassium ferrocyanide, $K_4[Fe(CN_6)]$ under nanoscale confinement. This inorganic compound was chosen as a model solid for study due to its high solubility, rich polymorphism and its attractive physical properties. Controlled pore glass (CPG) was selected as the confining system due to its versatility. CPGs are commercially available in a range of different forms including beads, rods and sheets and they can be obtained with a variety of pore sizes. They are also composed almost entirely of silica, which allows easy modification of their surface chemistry. In this chapter, CPG beads a few hundreds of micrometers in size and with pore diameters of 8, 48 and 362 nm were employed.

First of all, this chapter presents an extensive investigation into the crystallization of potassium ferrocyanide in bulk solution. Crystals with four different morphologies of potassium ferrocyanide were found at room temperature and were analyzed using optical microscopy, SEM, TEM, IR, Raman, XRD and electron diffraction. This combination of techniques allowed each crystal habit to be assigned to its crystal structure. Subsequently, potassium ferrocyanide was crystallized in the nanopores of CPGs and extraordinary differences in the crystallization of this solid in confinement as compared with the bulk solution were observed. A retardation of the crystallization of this solid in the small pores represented a delay of up to 5

orders of magnitude as compared with the bulk solution. These results provide the largest crystallization delay observed for an inorganic solid in confinement and together with the observations from the next two chapters, suggest that confinement effects are universal for all compounds.

3.1.2 Introduction to potassium ferrocyanide

Potassium ferrocyanide usually precipitates from solution as lemon-yellow crystals of $[K_4Fe(CN)_6]\cdot 3H_2O$, (KFCT), which have a solubility in water of 28.9 g/100 mL. The high solubility of KFCT greatly facilitates pore-filling of the CPGs, which makes it attractive as a model solid for the investigation of crystallization in confinement. It can also crystallize as two different polymorphs at room temperature, namely a metastable tetragonal form and a thermodynamically stable monoclinic phase. The structural similarities between the tetragonal and monoclinic phases also leads to the common formation of various twinned crystals.[257, 258] Modifying variables such as temperature, crystallization rate or the solution composition, it is possible to control the relative amounts of each form. However, under practical conditions of crystal growth, a mixture is often found, making their analysis difficult.

KFCT finds many applications in industry. For example, it is used in the food industry as an anti-caking agent for table salt and to precipitate heavy metals from wine.[259] It also has applications as a catalyst, an ion exchanger, photosensitizer and a supramolecular magnetic material.[260, 261] The solid-state transitions of potassium ferrocyanide have attracted significant attention from a fundamental perspective as the room-temperature monoclinic *C*2/*c* phase shows a second-order transition to a second monoclinic *Cc* ferroelectric phase at 249 K.[262-264] Furthermore, on cooling, the metastable tetragonal $I4_1/a$ phase undergoes an irreversible transition to the monoclinic *Cc* modification through an unusual displacive mechanism.

3.1.2.1 General overview of potassium ferrocyanide

In 1869, Wyrouboff was the first to identify monoclinic and tetragonal polymorphs of KFCT by optical microscopy.[265] About 40 years later, Briggs

showed micrographs of KFCT crystals with rectangular, octagonal and hexagonal morphologies.[266, 267] However, it was not until 1960 that Toyoda *et al.* obtained the first diffraction patterns of the different phases of KFCT.[264] More recent investigations have demonstrated the complexity of the KFCT system since its polymorphs are very close in free energy which causes difficulties in isolating the different phases.[257, 258, 262] Kanagadurai *et al*. showed that single monoclinic crystals of KFCT can be grown using the gel method.[268] This method consisted of mixing a KFCT solution with a sodium metasilicate solution and resorcinol in test tubes. Thin, square and transparent crystals were obtained after two weeks as shown in Figure 32a and the structure of a monoclinic KFCT crystal obtained by single crystal X-ray diffraction is shown in Figure 32b.

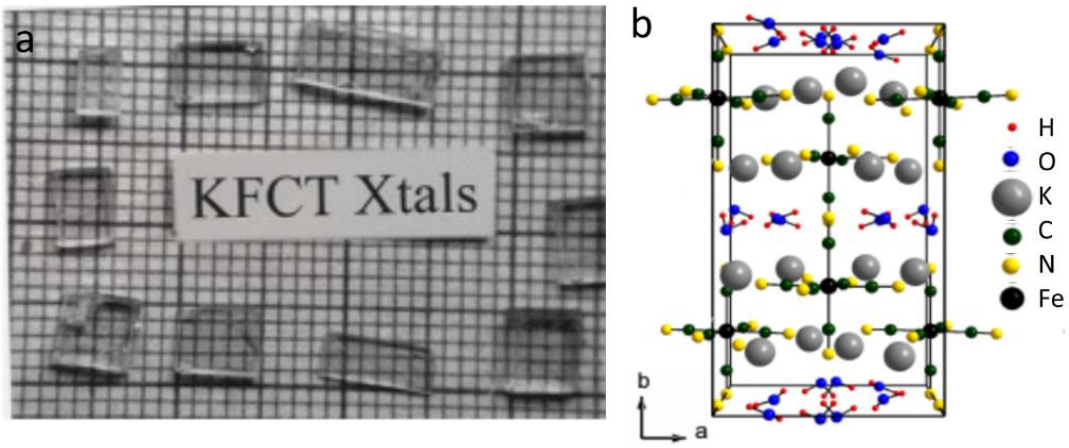

Figure 32. KFCT monoclinic single crystals grown in gel (a) and their crystal structure (b). Figure adapted from ref.[257, 268]

Recently, Geneviciute L. *et al.* investigated the nucleation of KFCT crystals utilizing a microdroplet-based crystallization method.[269] The article analyzed the different crystal habits that formed depending on the temperature and the surfactant choice, where crystals were grown in droplets as a way to control their nucleation. By confining crystallization to a droplet, two different crystal habits were found in the early stages of the crystallization process. The hexagonal habit was more common than the octagonal one (Figure 33) and the proportion of the different crystal morphologies changed with the temperature and the surfactant. However, assignment of each crystal

morphology to a crystal structure was not possible since X-ray diffraction and Raman experiments of the crystals were unsuccessful.

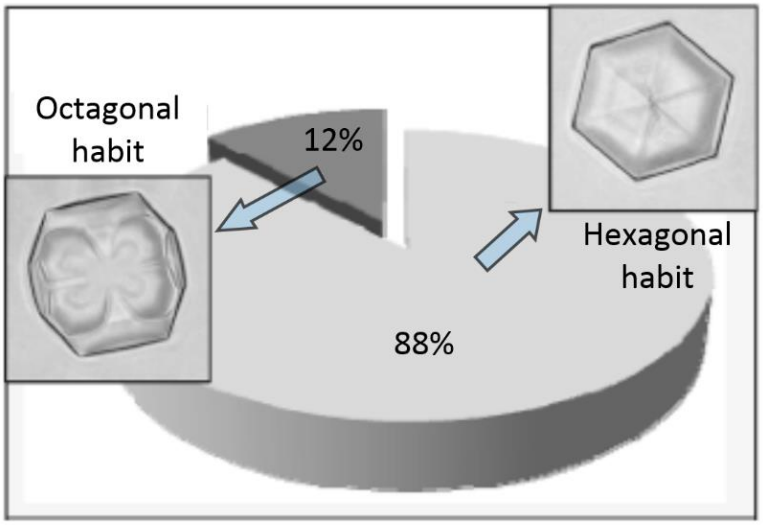

Figure 33. Relative proportion of the hexagonal and octagonal crystal habits of KFCT crystals grown in droplets. Figure adapted from ref.[269]

In summary, although the thermodynamically stable monoclinic polymorph of KFCT has been isolated and characterized,[268] IR or Raman data of tetragonal KFCT crystals have not been reported before. Moreover, X-ray studies undertaken with this solid usually present a mixture of both polymorphs, which has limited the characterization of the tetragonal phase.[257] Complete studies relating crystal morphology with structure were therefore necessary to better understand the crystallization of KFCT from solution.

3.2 Experimental

The crystallization of KFCT was investigated first in bulk solution and then within CPG particles with pore diameters of 362, 48 and 8 nm to study the effect of confinement on its polymorphism. The crystals were imaged by optical microscopy, SEM and TEM and then analysed by Raman and IR spectroscopy, PXRD and SAED. The CPG particles with pore sizes of 362, 48 and 8 nm will be denoted in this thesis as CPG-362, CPG-48 and CPG-8 respectively for simplicity. Unless otherwise indicated, ambient conditions are T = 20 ± 2 °C and a relative humidity (r.h.) of 40 ± 5 %.

3.2.1 Materials

CPG particles were obtained from Millipore as beads with diameters of 10-100 μm for CPG-48 and CPG-8 and of 1-3 mm for CPG-362. Potassium ferrocyanide trihydrate (KFCT) was purchased from Sigma-Aldrich and KFCT solutions were prepared by dissolving this solid in Milli-Q water.

3.2.2 Crystallization in bulk solution

KFCT crystallization in bulk was carried out by two different methods at ambient conditions that allowed slow and fast precipitation. The first method will be denoted as the evaporation method and it consists of evaporating droplets of a concentrated KFCT solution (~20 w/v % in water) on glass slides. This allows the slow crystallization of this solid. Crystals precipitated on the glass slides were characterized after 3, 5, 10 and 30 min and after 24 h, when the solution had completely evaporated. Faster crystallization was induced by adding 50 mL of ethanol to a 10 mL of aqueous more diluted KFCT solution (~2 w/v %). This method will be referred as the precipitant-inducing method. Crystals formed in less than a minute and were collected by vacuum filtration for analysis.

3.2.3 Crystallization in pore controlled glasses (CPGs)

Crystallization of KFCT in the CPG pores was carried out by evaporation. Firstly, the CPG beads were suspended in a 20 w/v% aqueous solution of KFCT and a vacuum was applied for 5-10 min to remove the air inside the pores. Various vacuum sequences were repeated until no more bubbles were observed. Applying sequences of pumping allowed the complete removal of gas in the pores without KFCT precipitation in solution. Subsequently, the CPGs were filtered from solution and left to dry at ambient conditions in the laboratory (slow drying) or under vacuum for 5 h (fast drying). The rapid filtration used in this method resulted in efficient pore-filling, while the surfaces of the CPG beads were clean. Therefore, additional cleaning was not required.

3.3 Results

3.3.1 Crystallization in bulk solution

The experiments carried out in this study generated four crystals with clearly distinguishable morphologies on precipitation of KFCT from aqueous solutions at room temperature. The crystals that initially precipitated from evaporating droplets (after 3 min) were of an hexagonal shape (Figure 34a). After 10 min, crystals of a rectangular, prismatic shape appeared alongside the hexagonal crystals (Figure 34b). A mixture of both crystal habits was always found, although the proportion of rectangular crystals increased with time, growing up to millimeter sizes upon complete evaporation. On rapid precipitation by the precipitant-inducing method at low $K_4[Fe(CN)_6]$ concentrations (2%), needle-shaped crystals were observed immediately after addition of ethanol (Figure 34c). These crystals were unstable and redissolved in less than five minutes if left in the solution. Subsequently, crystals with rounded edges were observed which grew into irregular octagonal prisms (Figure 34d). These crystals either transformed directly into rectangular prisms or redissolved. After time, new crystals nucleated and grew into rectangular prism or hexagons, as found on evaporation of aqueous solutions. Figure 35 shows a sequence of images depicting the evolution of crystal habit after precipitation by ethanol addition. These observations are consistent with morphological descriptions of KFCT crystals in the literature, which previously assigned the monoclinic polymorph to rectangular prismatic crystals.[268]

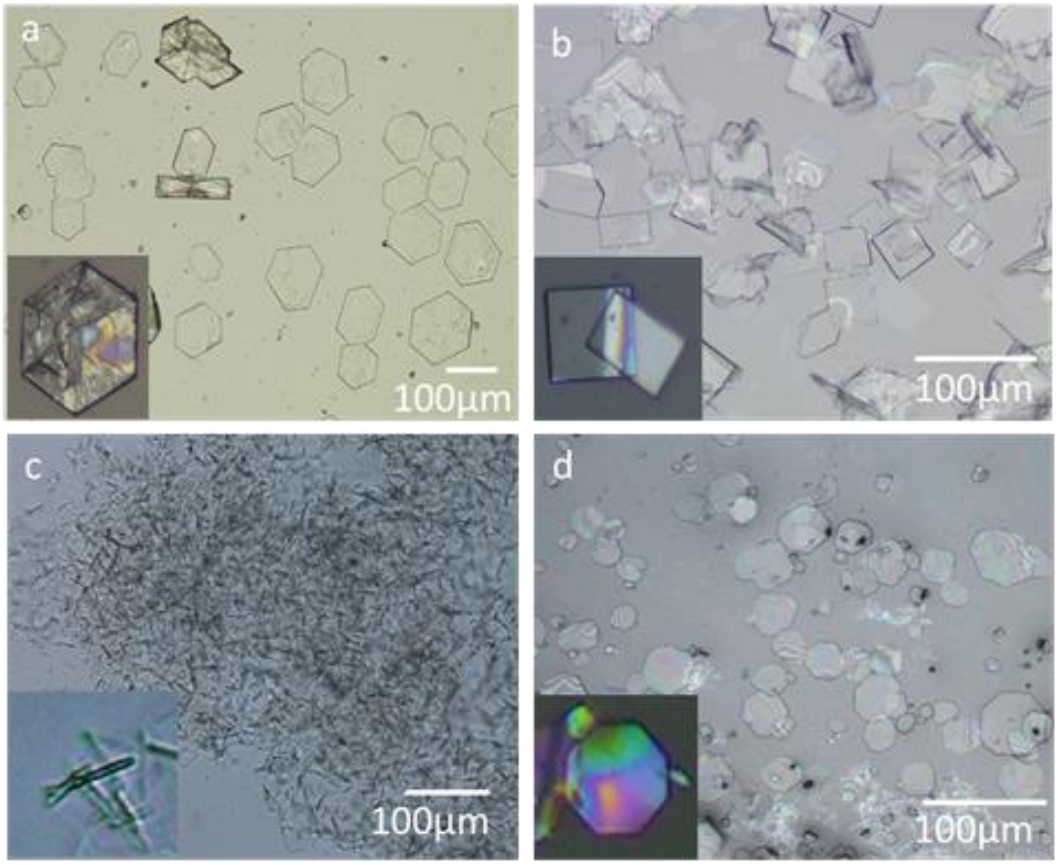

Figure 34. KFCT crystals observed by optical microscopy precipitated by evaporation (a,b) or by ethanol addition (c,d). (a) hexagonal crystals observed after 3 min and (b) rectangular crystals after 10 min. (c) needle-shaped crystals formed immediately after ethanol addition and (d) octagonal prism crystals observed after dissolution of (c).

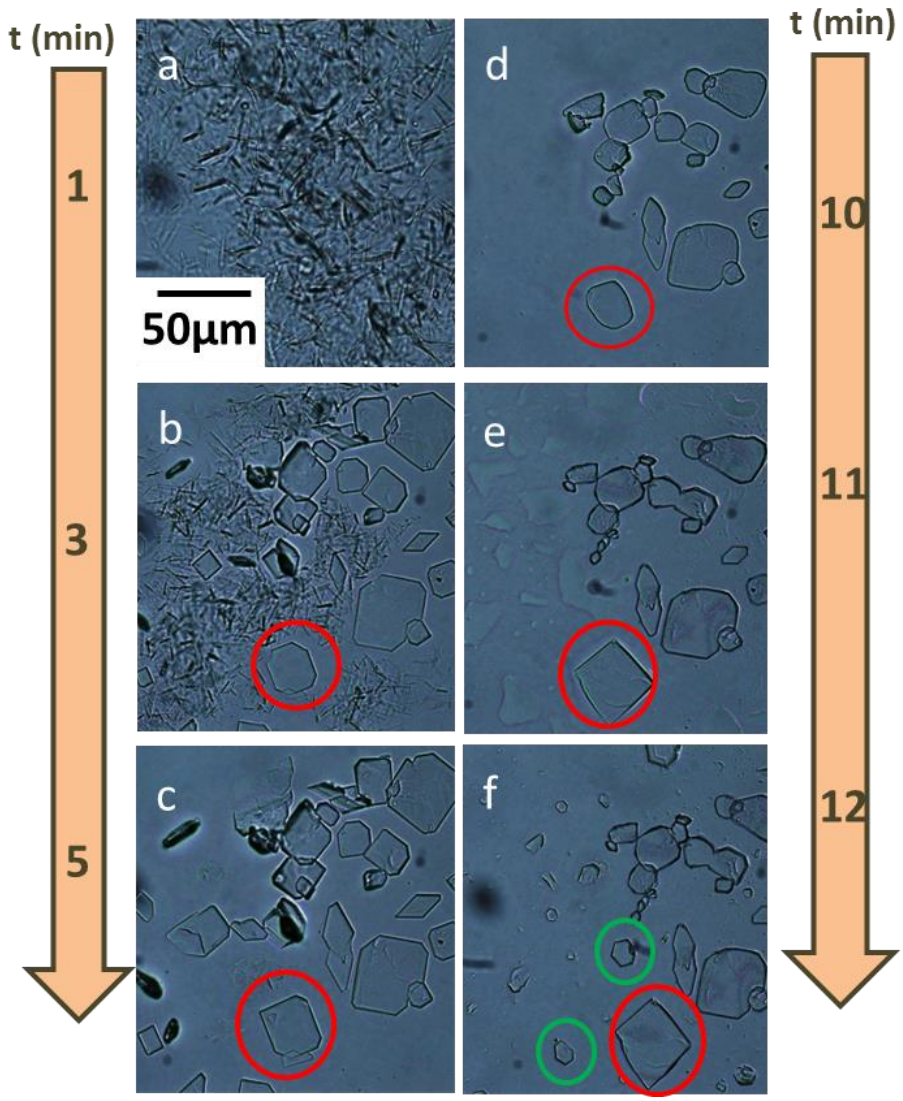

Figure 35. Optical microscopy images recorded during KFCT precipitation using ethanol after: (a) 1 minute, when only needle-shaped crystals are observed, (b) 3 min, when the needles start to dissolve and are replaced by prismatic crystals with different shapes (an octagonal crystal is circled in red), (c) 5 min, when the needles have dissolved and the octagonal crystal in (b) has become more rectangular, (d) 10 min, when most crystals appear to be dissolving, (e) 11 min, when the octagonal crystal in (b) has transformed into a stable rectangular crystal, and (f) 12 min, when new hexagonal crystals have appeared (in green).

The structure of the crystals was then characterized using a range of analytical techniques. IR and PXRD analysis were carried out with bulk samples, where crystals were recovered by filtration. Needle-shaped crystals were filtered from solution 1 minute after adding the ethanol into the diluted KFCT aqueous solution. The other crystal habits were obtained by evaporation and were directly analyzed on the glass slides, which were dried with N_2 flow to stop the

reaction at short times. Hexagonal crystals with a small amount of rectangular crystals (confirmed by optical microscopy) were obtained after 3 min and rectangular crystals with small number of hexagonal crystals were collected after complete evaporation.

3.3.1.1 IR analysis

Samples prepared by evaporation had the same IR spectra at long and short evaporation times (Figure 36a), where the bands at 3587, 3518, 3375, 1647 and 1614 cm^{-1} derive from O-H bond stretching of the water molecules, and 2035 cm^{-1} from the symmetric stretching of the CN group.[268] The IR spectra of samples containing needle-shaped crystals prepared by the precipitant-inducing method was, however, distinct (Figure 36b). The major OH bands in the range of 3300- 3600 cm^{-1} almost disappeared leaving a broad hump at 3300- 3600 cm^{-1}, which can be due to surface water. The 1614 cm^{-1} OH bands also decreased in intensity and new peaks in the CN region at 2093, 2072, 2017 and 2041 cm^{-1} appeared. These data suggested that the needle-shaped crystals correspond to the anhydrous phase (potassium ferrocyanide, KFC), which was confirmed by PXRD.

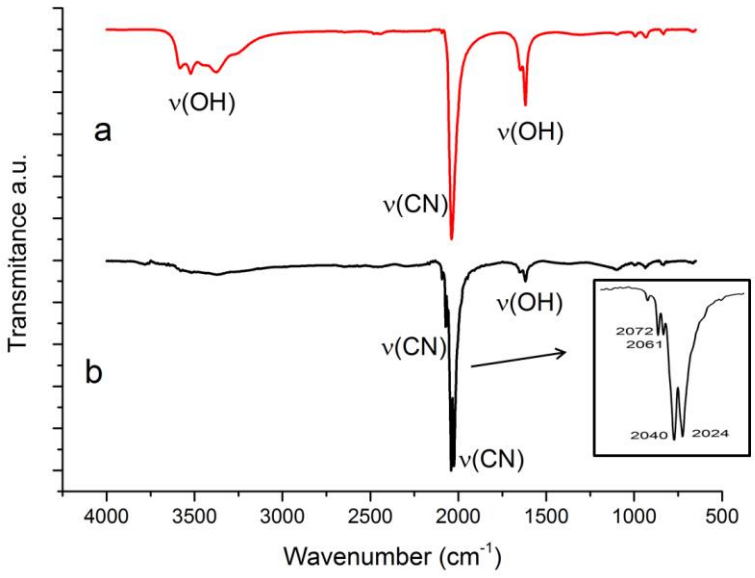

Figure 36. IR spectra of potassium ferrocyanide crystals (a) precipitated by evaporation and (b) isolated after 1 min after ethanol precipitation, where the sample principally contains needle-like crystals, together with some hexagonal and rectangular crystals.

3.3.1.2 PXRD

Samples obtained by precipitation with ethanol contained a mixture of KFCT and KFC when analyzed with PXRD. Crystals isolated after 1 min from solution (mainly needle-shaped crystals) showed weak peaks corresponding to the anhydrous KFC although the dominant phase by PXRD was seen to be KFCT (Figure 37a). That the peaks corresponding to KFCT are more intense than the ones corresponding to KFC can be attributed to their larger size and their orientation due to their plate-like shape. PXRD analysis of the samples prepared by free evaporation did not show any peaks from KFC since needle-crystals were never observed by this method in bulk solution. Figure 37b shows the diffraction pattern of crystals precipitated by evaporation after 3 min, where all the peaks corresponded to hydrated KFCT (monoclinic or tetragonal) crystals.

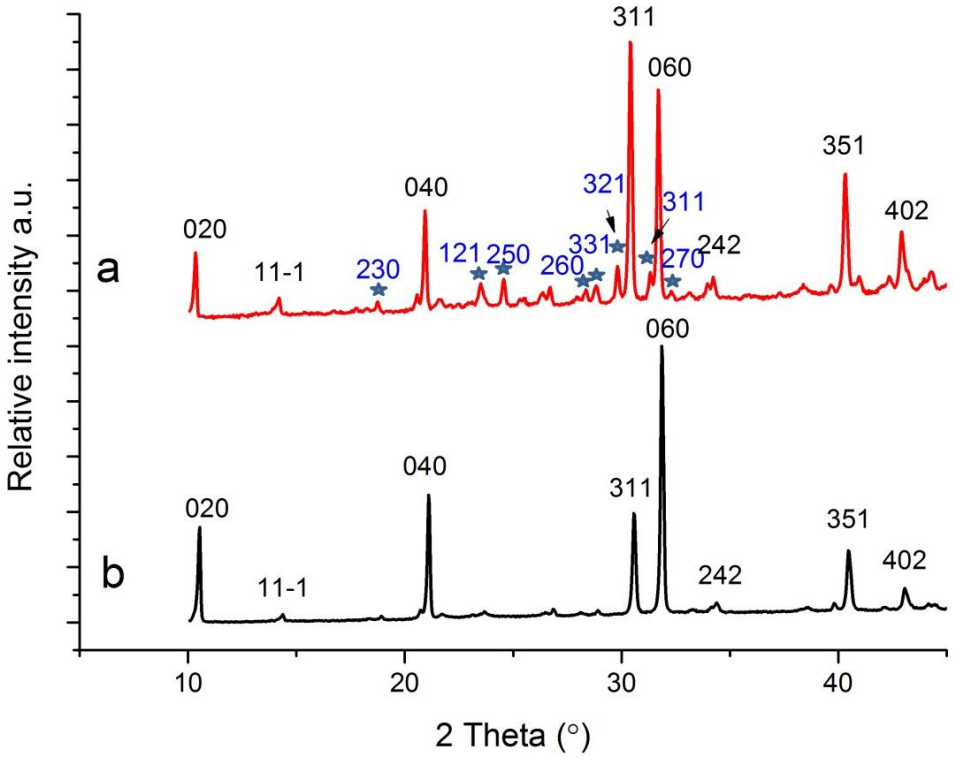

Figure 37. PXRD patterns of (a) samples taken 1 min after ethanol precipitation, where these contain many needle-like crystals. The peaks labelled with a blue star correspond to anhydrous KFC (orthorhombic) and black labelled peaks correspond to the trihydrate, KFCT (monoclinic or tetragonal), without preferred orientation. (b) PXRD pattern of a sample taken from solution after evaporation for 3 min, comprising a mixture of hexagonal (higher proportion) and rectangular crystals with preferred orientation (060) due to platy shape of crystals.

PXRD analysis of the samples prepared at longer evaporation times were also carried out, and yielded very similar diffraction patterns (Figure 38). KFCT crystals showed preferred orientation along (010) planes due to their plate-like shape, making grinding of the large crystals necessary in order to produce a powder and observe peaks of the different crystal planes.

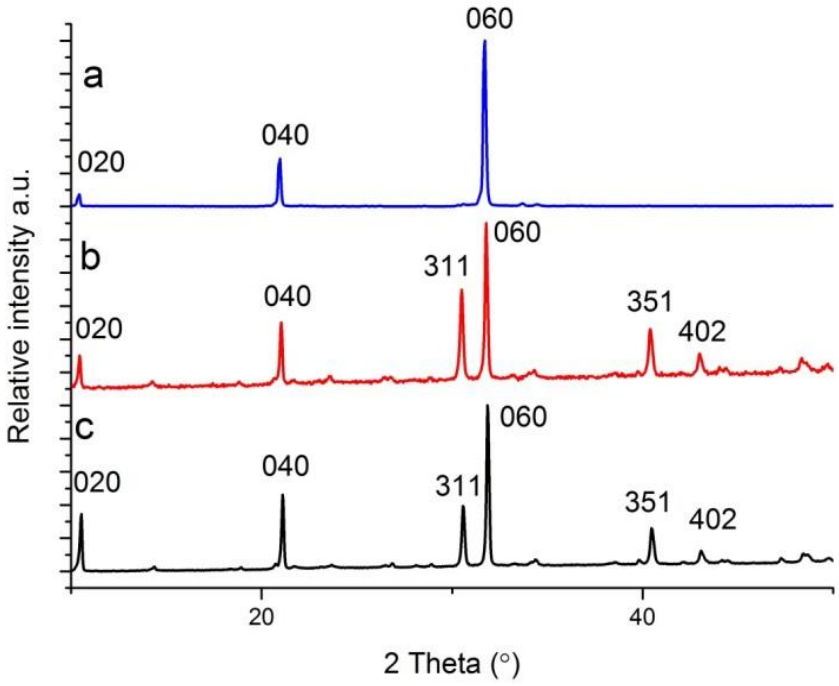

Figure 38. PXRD patterns of (a) large rectangular crystals (monoclinic) precipitated by evaporation in air under ambient conditions. (b) The same crystals as (a) after grinding and (c) crystals precipitated by evaporation after 3 min, where these are a mixture of hexagonal-shaped (tetragonal) and rectangular crystals (monoclinic).

It was not possible to distinguish between the different KFCT polymorphs (hexagonal vs rectangular) by PXRD or IR due to the samples not being pure and them having very similar lattice parameters. These techniques only allowed the assignment of the needle crystals to anhydrous KFC. Single crystal X-ray diffraction was also performed for each crystal habit. Nevertheless, no diffraction data of sufficient quality could be recorded. The crystals were very thin and they quickly became damaged on exposure to the beam. However, other analytical techniques such as Raman and TEM analysis provided an excellent way to determine the polymorph of individual crystals.

3.3.1.3 Raman

Raman analysis of individual crystals yielded a main peak at 2093 cm^{-1} for all the different crystal habits. The rectangular and the octagonal prismatic crystals showed Raman peaks at 2065 cm^{-1} and 2093 cm^{-1}, corresponding to the $\nu_1(A_g)$ and $\nu_3(E_g)$ respectively (Figure 39a,b) in agreement with published Raman spectra for monoclinic KFCT.[268] The hexagonal and the needle-shaped crystals showed three additional peaks at 2024 cm^{-1}, 2040 cm^{-1} and 2071 cm^{-1} (Figure 39c,d), which agrees with previous spectra of hexagonal-shaped KFCT crystals.[269] Raman analysis of octagonal and rectangular shaped crystals were identical. These suggests that these two crystals are different morphological forms of the monoclinic polymorph. This is also supported by in-situ observations during their crystallization by optical microscopy, which shows that the diagonal edge of the octagonal crystals often grew faster than other edges such that the shape evolves to become rectangular. Moreover, needle-shaped crystals showed very similar Raman spectra to the hexagonal crystals. Analysis of anhydrous KFC obtained by heating bulk KFCT crystals confirmed these observations (Figure 39).

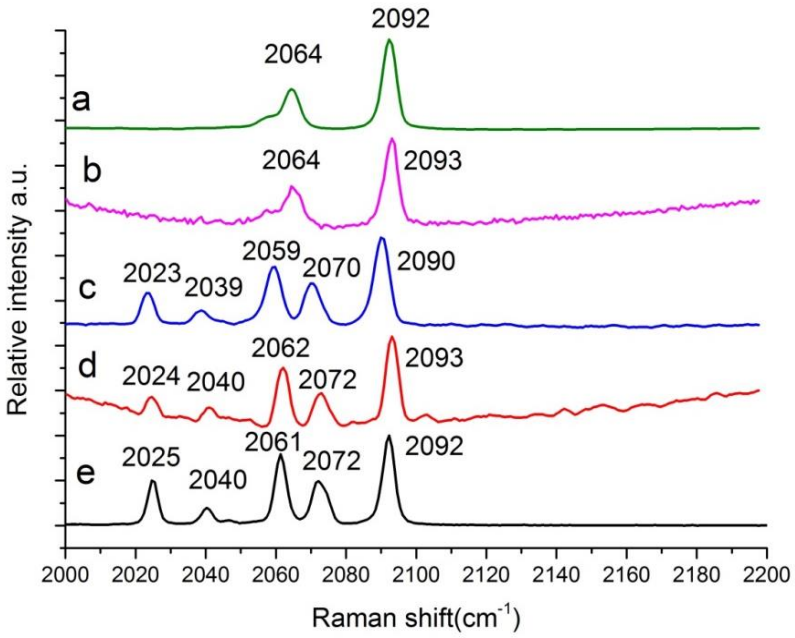

Figure 39. Raman spectra of the (a) rectangular, (b) octagonal and (c) hexagonal-shaped crystals of KFCT, and (d) the needle-shaped crystals in solution or (e) after heating KFCT at 200° C for 2h which correspond to anhydrous KFC.

3.3.1.4 TEM

The small thickness of the crystals allowed their polymorphs to be identified by electron diffraction (SAED) analysis of individual crystals. Both rectangular and octagonal crystals exhibited diffraction peaks corresponding to the monoclinic crystal structure of KFCT[257] (Figure 40 a-d) while the hexagonal-shaped crystals corresponded to the tetragonal structure (Figure 40 e-f). Table 2 shows the measured distances and angles between the observed planes in the diffraction patterns and compares them with the calculated values for both crystal structures.

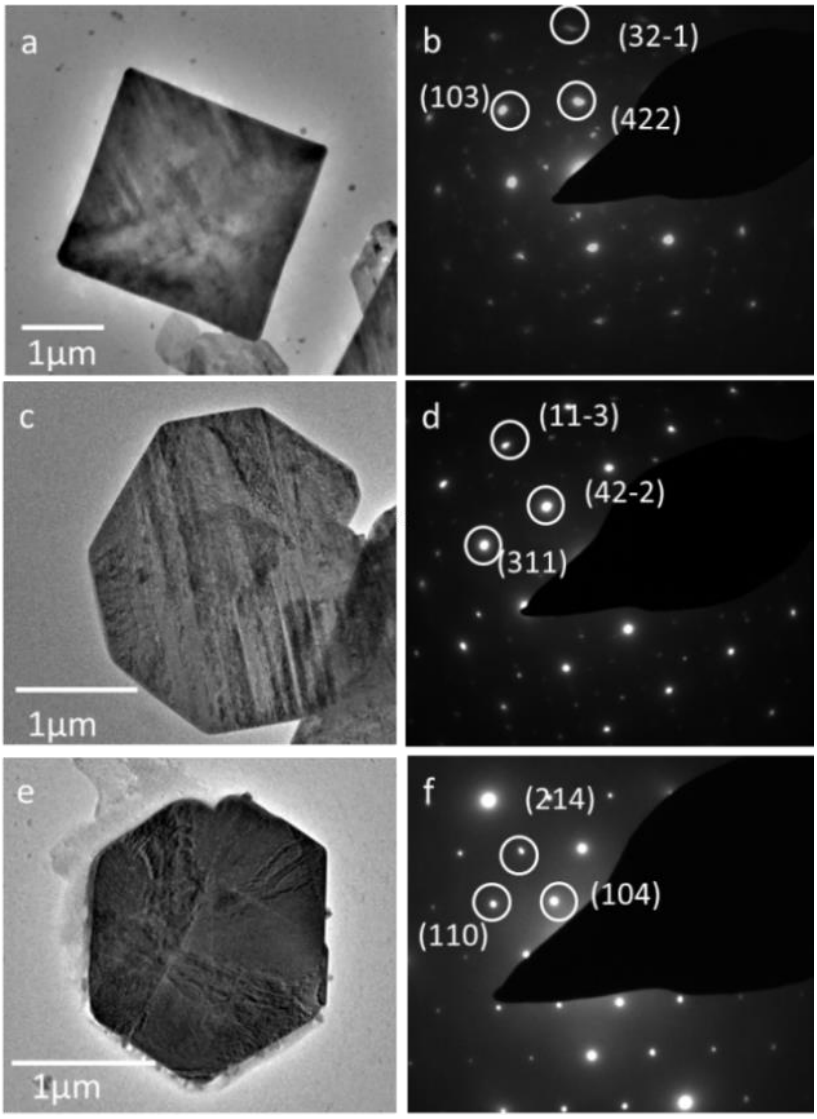

Figure 40. TEM images and corresponding selective area electron diffraction patterns of KFCT crystals. (a) A rectangular prism showing a monoclinic diffraction pattern (b), (c) an octagonal crystal showing a monoclinic diffraction pattern (d) and (e) a hexagonal crystal with a tetragonal diffraction pattern (f).

Crystal shape	Crystal system	Plane	Calculate d(Å)	d(Å) sample	Angles between planes	Measured angles (°)	Calculated angles (°)
Rectangular	Monoclinic C2/c	(103)	2.97	2.90	θ(103/32-1)	90.3	90.0
		(422)	2.04	2.06	θ(103/422)	46.9	46.7
		(32-1)	2.93	2.84	θ(422/32-1)	43.7	43.3
Octagonal	Monoclinic C2/c	(11-3)	2.93	2.93	θ(11-3/311)	88.0	88.3
		(311)	2.93	2.90	θ(11-3/42-2)	43.9	44.1
		(42-2)	2.04	2.01	θ(42-2/311)	43.7	44.1
Hexagonal	Tetragonal I41/a	(104)	6.27	6.25	θ(104/214)	30.1	29.9
		(214)	3.76	3.72	θ(214/110)	30.6	31.8
		(110)	6.64	6.58	θ(110/104)	61.1	61.8

Table 2. Electron diffraction analysis of KFCT crystals. By measuring distances and angles between diffraction spots it was possible to assign crystals with rectangular and octagonal shapes to the monoclinic polymorph and crystals with a hexagonal shape to the tetragonal polymorph.

The use of the different characterization techniques described above allowed the assignment of each crystal shape with a specific crystal system. A summary of the crystal assignments is provided in Table 3.

Morphology	Assignment	Crystal System	Crystallographic parameters	
Needle-like crystals	Anhydrous KFC	Orthorhombic Cmcm	Alpha = beta = gamma = 90 °	a (Å): 4.18 b (Å): 14.01 c (Å): 21.04
Rectangular prism	KFCT	Monoclinic C2/c	Alpha = gamma = 90 ° Beta = 90.69-90.096 °	a (Å): 9.38-9.40 b (Å): 16.84-16.88 c (Å): 9.39-9.41
Octagonal prism	KFCT	Monoclinic C2/c	Alpha = gamma = 90 ° Beta = 90.69-90.096 °	a (Å): 9.38-9.40 b (Å): 16.84-16.88 c (Å): 9.39-9.41
Hexagonal crystal	KFCT	Tetragonal I41/a	Alpha = beta = gamma = 90 °	a (Å): 9.39-9.41 b (Å): 9.39- 0.41 c (Å): 33.67-33.72

Table 3. Summary of the crystals precipitated from bulk solutions of potassium ferrocyanide, where KFC corresponds to the anhydrous form, $K_4Fe(CN)_6$, and KFCT to the trihydrate. Needle-like crystals (yellow) are assigned to orthorhombic KFC, rectangular and octagonal prisms (turquoise) are the monoclinic polymorph of KFCT and hexagonal-shaped crystals (pink) are the tetragonal polymorph of KFCT[257, 264].

3.3.1.5 Effects of humidity on crystals precipitated in bulk

The stabilities of the different crystal polymorphs in air, under controlled humidity levels (open vessels of water were used to maintain the humidity at close to 100%) were investigated. Crystals of the metastable, tetragonal polymorph (hexagonal-shaped crystal) formed by the evaporation method were maintained at 100% humidity. Optical microscopy showed that they transformed into the monoclinic polymorph (rectangular crystals) in 15 mins, which was confirmed by Raman spectroscopy (Figure 41). The effects of the humidity on the orthorhombic metastable KFC phase (needle-shaped) precipitated by ethanol and isolated by filtration were also studied under 100 % humidity. KFC redissolved as water condensate on the glass slide in less than 5 min, and recrystallized into a mixture of monoclinic and tetragonal KFCT crystals as confirmed by optical microscope and Raman. They subsequently transformed into the most stable monoclinic form. It is important to note that once isolated from solution, neither the tetragonal polymorph nor

the anhydrous KFC redissolved or converted into the monoclinic form under ambient conditions (of humidity ≈40 %) for at least 1 month.

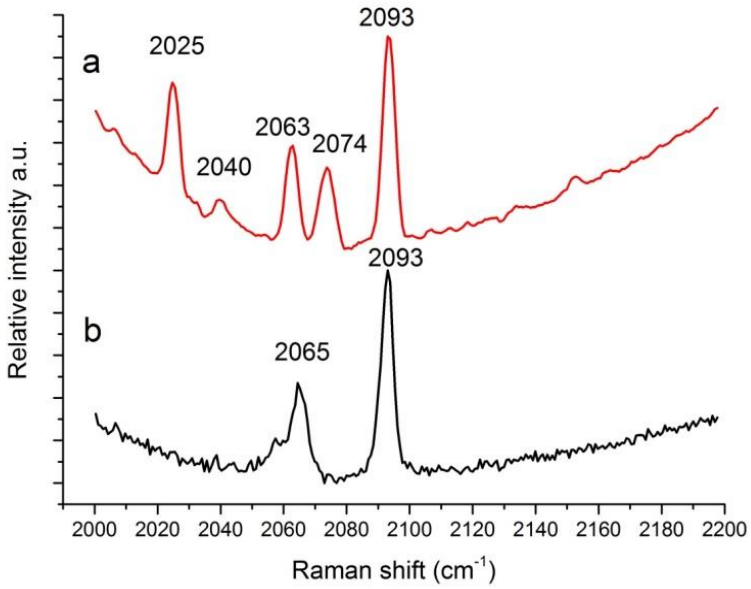

Figure 41. Effect of humidity on the stability of the tetragonal crystals of KFCT in bulk solution when (a) tetragonal crystals were isolated in bulk and (b) after incubating in 100 % humid conditions they converted to the monoclinic polymorph in 15 min.

3.3.2 KFCT crystallization in controlled pore glasses (CPGs)

KFCT crystallization in the pores was achieved by evaporation following the method described in the experimental section. Two different evaporation conditions were applied to remove the solvent from the pores, namely drying in air (at ambient conditions) or under vacuum for 5 h. Both methods allowed crystal formation in the pores and avoided the precipitation of large bulk crystals on the surfaces of the CPGs, or between the CPGs beads. This was confirmed by optical microscopy and SEM (Figure 42). However, at higher magnification under SEM, crystals could be seen emerging from the pores. Pore-filling was also confirmed by BET as shown by a significant decrease in surface area of the CPGs after crystallization (Table 4). The differences in surface area were more appreciable in CPG-48 and CPG-8 than in CPG-362 due to the low surface area of these particles.

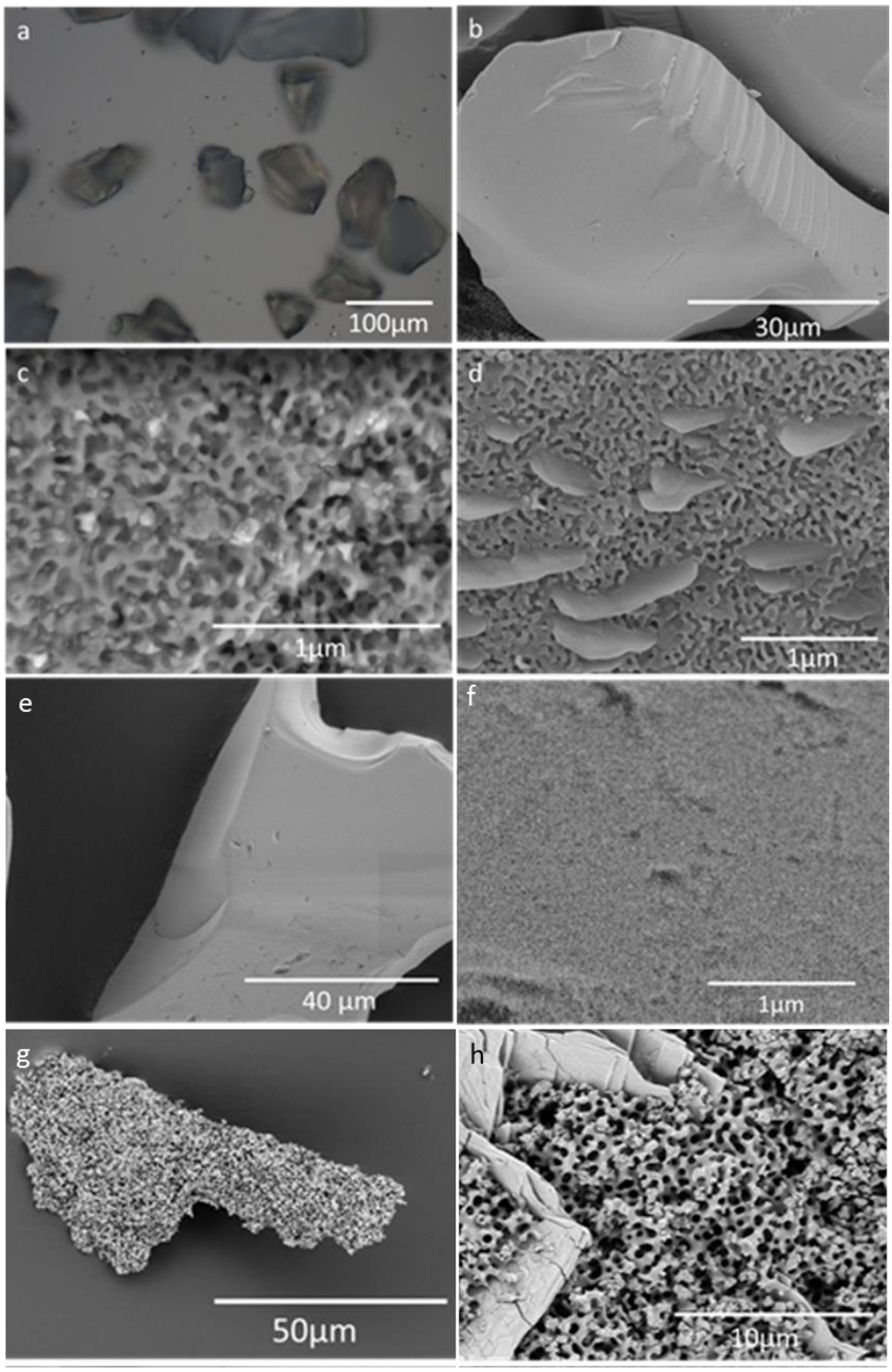

Figure 42. Optical (a) and SEM images of CPG-48 particles after precipitation showing the absence of large crystals on the surface or in between particles (a,b) and higher magnification images of the CPG particles (c,d) showing that the pores are full (c) and that some crystals emerge from the pores during growth (d). CPG-8 particle after precipitation at low (e) and higher magnification (f) and CPG-362 particle after precipitation at low (g) and higher magnification (h).

	CPG-362	CPG-48	CPG-8
Surface area before crystallization (m^2g^{-1})	4.8 ± 0.1	65 ± 1	164 ± 3
Surface area after crystallization (m^2g^{-1})	4.5 ± 0.1	28 ± 1	34 ± 2

Table 4. Surface area BET analysis carried out before and after crystallization in different CPG particles. The data demonstrate the successful precipitation of crystals within the CPGs.

The crystals formed inside the CPG particles were studied at different times using PXRD, Raman and IR spectroscopy, and strong differences were obtained as compared with the bulk crystallization experiments. When the CPGs had been vacuum-dried, KFC crystals precipitated in all three different pore sizes and they remained unchanged for at least 1 year incubation under ambient conditions as confirmed by PXRD (Figure 43).

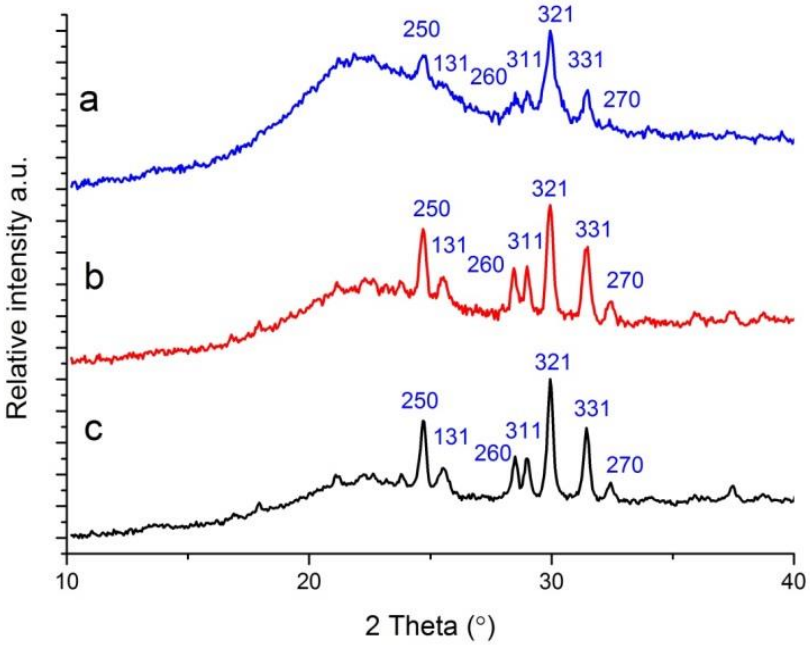

Figure 43. PXRD of crystals in CPGs after vacuum drying the samples for 5h and maintaining them at ambient conditions for 1 year in CPG-362 (a), CPG-48 (b) and CPG-8 (c). All samples contain KFC crystals.

In contrast, air-dried CPGs samples showed different transformation patterns with time. Initially, KFC was formed in all three different pore sizes and the

hydrated KFCT crystals began to appear with time. KFC persisted in the CPG-362 nm and the CPG-48 nm pores after one day, and was still found after a month in the 8 nm pores, according to PXRD analysis (Figure 44, Figure 45 and Figure 46). The glass background intensity in the diffraction patters varies depending on the sample since not all of the CPG beads are the same sizes or shapes. In addition, it was not possible to attribute the intensity of the diffraction peaks to the proportion of material inside the pores due to the small amount of material in these particles.

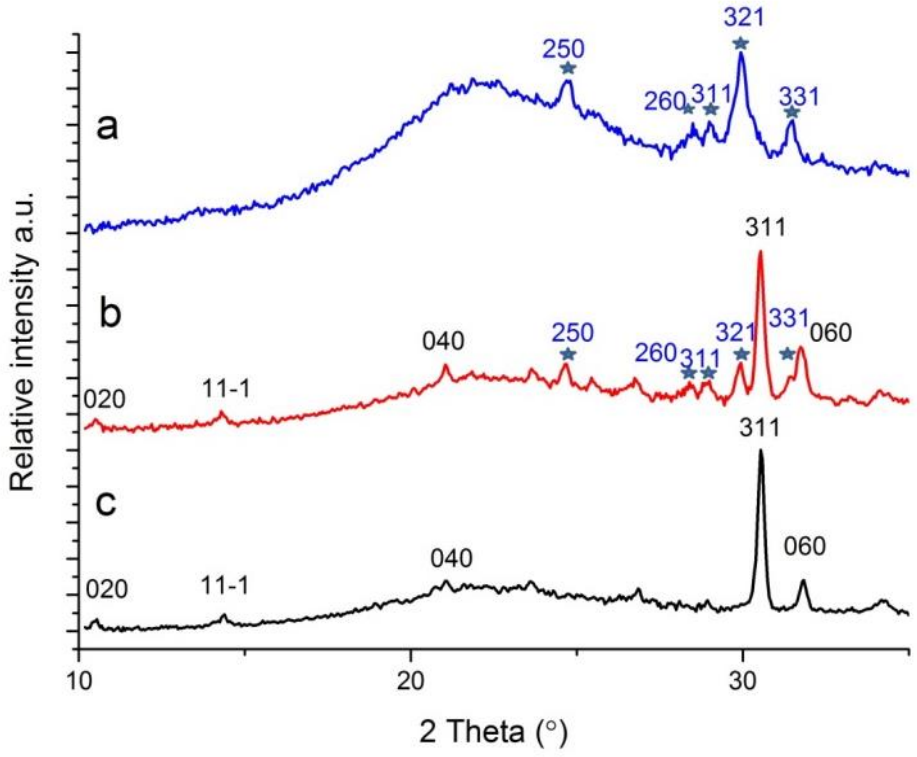

Figure 44. PXRD patterns of crystals precipitated within CPG-362 particles at evaporation times of (a) <24 h (b) 24-48 h and (c) 1 month. Peaks from the anhydrous KFC are indicated in blue, while the KFCT peaks are labeled in black.

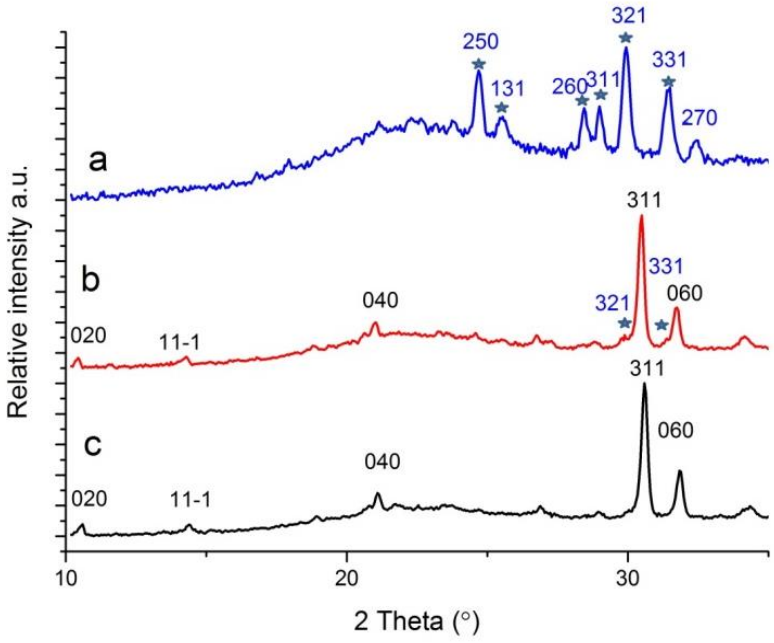

Figure 45. PXRD patterns of crystals precipitated within CPG-48 particles at evaporation times of (a) <24 h (b) 24-48 h and (c) 1 month. Peaks from the anhydrous KFC are indicated in blue, while the KFCT peaks are labeled in black.

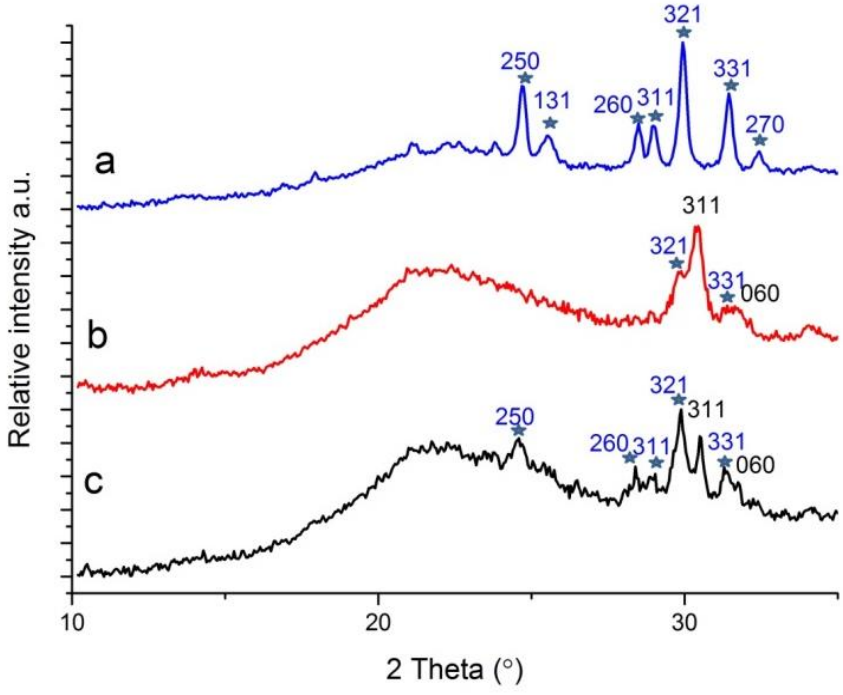

Figure 46. PXRD patterns of crystals precipitated within CPG-8 particles at evaporation times of (a) <24 h (b) 24-48 h and (c) 1 month. Peaks from the anhydrous KFC are indicated in blue, while the KFCT peaks are labeled in black. A mixture of KFC and KFCT is still found after 1 month.

After KFC completely converted to KFCT in the pores (as confirmed by PXRD), the CPG beads were analyzed using Raman in order to evaluate the proportion of monoclinic and tetragonal polymorphs present in the pores. Raman spectra from at least 20 particles per sample were recorded, where the particles would either have spectra with peaks at 2064 cm^{-1} and 2093 cm^{-1} only, demonstrating that significant quantities of monoclinic crystals were present, or peaks at 2024 cm^{-1}, 2040 cm^{-1}, 2064 cm^{-1}, 2093 cm^{-1} and 2071 cm^{-1}, which is indicative of tetragonal crystals. Some particles with overlapping peaks were found and these were not included in the calculated percentages. After 2 days, Raman analysis of CPG-362 and CPG-48 beads showed that the KFCT crystals comprised ≈70% of the monoclinic polymorph and 30% of the tetragonal form (Figure 47). In contrast, only the tetragonal polymorph of KFCT was present in the 8 nm pores after 1 month, when again no KFC peaks were observed by PXRD. Samples analyzed more than 1 month after crystallization, showed mixtures of the monoclinic and tetragonal polymorphs in all three pore sizes. Figure 48 shows the Raman spectra of crystals in CPGs dried by vacuum for 5 h and left at ambient conditions for a month, and crystals in CPGs that had been air-dried. It was also noticed that the CPG particles dried under vacuum were white while those dried under ambient conditions turned from white to yellow with time, reflecting the colors of the anhydrous and hydrated crystals, respectively.

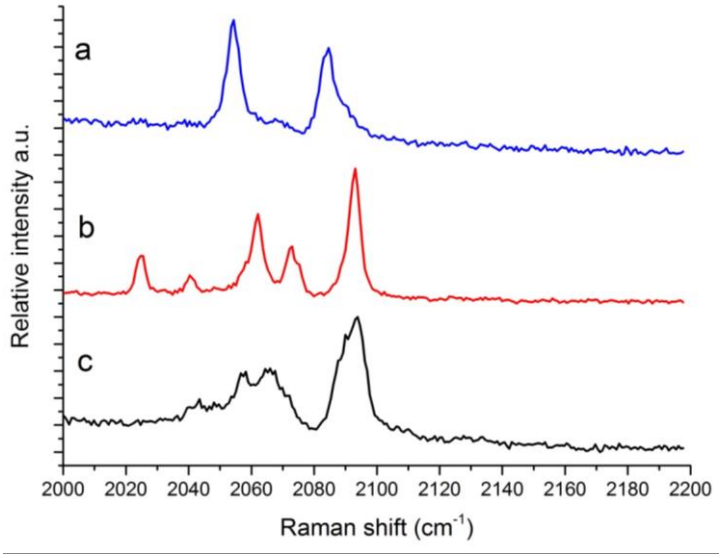

Figure 47. Raman analysis of KFCT crystals in CPG-48 after 2 days evaporation, where a mixture of polymorphs was found. 70% of the particles showed peaks at 2064 cm^{-1} and 2093 cm^{-1} only, showing a high amount of monoclinic crystals (a) while 30% of the particles showed peaks at 2024 cm^{-1}, 2040 cm^{-1}, 2064 cm^{-1}, 2093 cm^{-1} and 2071 cm^{-1} showing mainly tetragonal crystals (b). Particles with overlapping peaks were not included in the percentages (c).

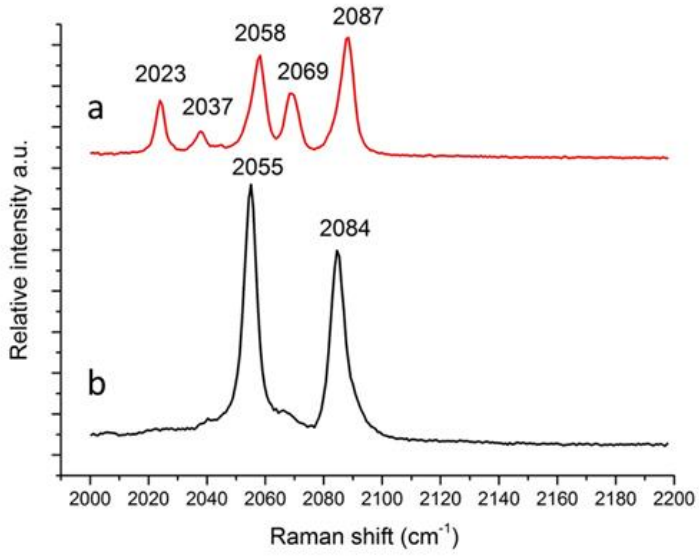

Figure 48. Raman spectra of CPG-48 after (a) vacuum drying and maintaining at ambient conditions for 1 month. Peaks corresponding to anhydrous KFC are seen and no hydrated KFCT was observed. (b) Air-drying and maintaining under ambient conditions for 1 month. Peaks corresponding to KFCT (mainly monoclinic) are seen. Note that the same results were obtained with all three pore sizes.

Table 5 summarizes the results obtained when crystallizing KFCT in bulk solution and in confinement using 3 different pore sizes and 2 different evaporation conditions. Significant differences were observed due to an enormous retardation of crystallization in confinement. The waiting time for nucleation of the tetragonal polymorph of KFCT in CPGs was seen to be 3 or 4 orders of magnitude longer than in bulk. While the waiting time for the crystallization of KFC in CPGs was seen to be retarded by at least 5 orders of magnitude with respect to bulk solution.

	Air-dried				Vacuum-dried
Incubating time	**Bulk solution**	**CPG-362 nm**	**CPG-48 nm**	**CPG- 8nm**	**CPG-362, CPG-48, CPG-8**
1 h to 1 day	KFCT (polymorph mixture)	KFC	KFC	KFC	KFC
2 days	KFCT (polymorph mixture)	KFC + KFCT (polymorph mixture)	KFC + KFCT (polymorph mixture)	KFC + tetragonal KFCT crystals	KFC
3 days to 1 month	KFCT (polymorph mixture)	KFCT (polymorph mixture)	KFCT (polymorph mixture)	KFC + tetragonal KFCT crystals	KFC
>1 month	KFCT (polymorph mixture)	KFCT (polymorph mixture)	KFCT (polymorph mixture)	KFCT (polymorph mixture)	KFC

Table 5. Summary of data obtained on precipitating potassium ferrocyanide in bulk and within CPG particles by solvent evaporation in air or under vacuum. Orthorhombic KFC is represented in yellow, monoclinic KFCT in turquoise and tetragonal KFCT in pink. A mixture of KFCT polymorphs was always found in bulk, while the anhydrous KFC was the first phase to precipitate in the CPGs transforming into KFCT with time. After a month, a mixture of polymorphs (typically ca. 70% monoclinic and ca. 30% of the tetragonal) was found in all three pore sizes. KFC remained stable for at least 1 year when drying the CPGs by vacuum.

3.3.2.1 Effects of humidity on crystals precipitated in CPGs

The influence of humidity on polymorph transformation was investigated by keeping the CPG beads containing metastable phases in an incubator with

100 % humidity and characterizing the crystals over time using IR and Raman. KFC precipitated inside 48 and 362 nm pores after evaporating the solvent with vacuum was seen to hydrate to KFCT after 2 days (Figure 49). In contrast, 8 nm pores containing KFC that was found by drying the solvent under vacuum only showed peaks in IR from the hydrated salt after 2 weeks in humid conditions (Figure 50). The effects of the humidity on air-dried samples were also investigated. CPG-8 beads containing tetragonal KFCT one day after crystallization were place in a humid incubator and Raman spectra were taken over time until the crystals converted to the monoclinic phase. It was observed that tetragonal KFCT crystals remained stable within the 8 nm pores for up to 1 h while tetragonal crystals precipitated in bulk transformed to monoclinic KFCT in 15 mins under the same conditions (Figure 51). A summary of these observations and comparison with bulk solution is given in Figure 52.

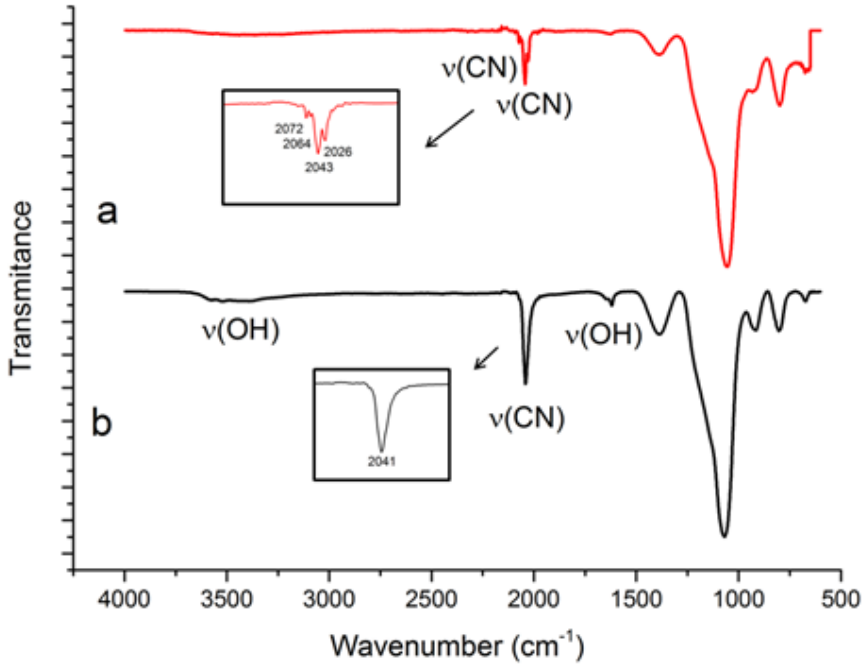

Figure 49. IR spectra of (a) vacuum-dried CPG-48 after crystallization with peaks from KFC at 2072, 2061, 2037 and 2024 cm^{-1} and (b) after incubation in 100% humidity for 2 days. The O-H stretching peak appears at 1614 cm^{-1} and the peaks at 2072, 2061 and 2024 cm^{-1} disappear showing KFCT crystals in the pores.

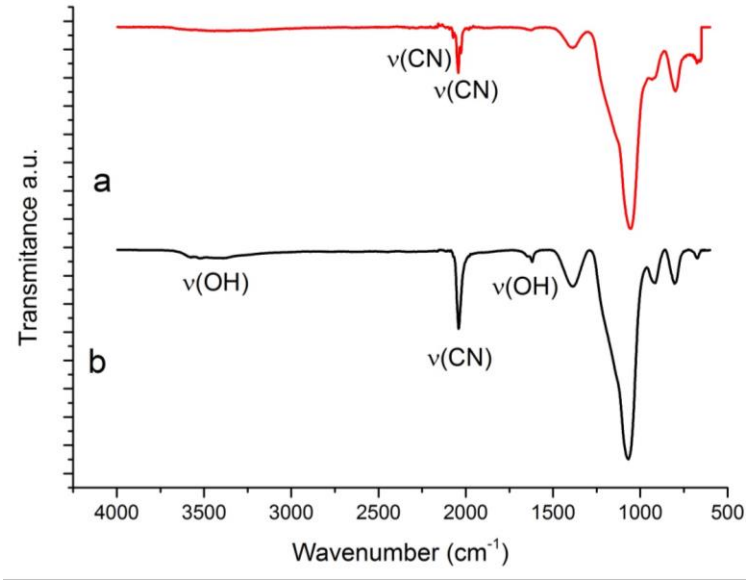

Figure 50. IR spectra of vacuum-dried CPG-8 after crystallization, (a) after incubating in ~100% humidity for 2 days showing KFC crystals and (b) after incubating in 100% humidity for 2 weeks. Peaks from O-H bonds are evident at around 1600 cm^{-1} and the peaks at 2072, 2061 and 2024 cm^{-1} are much reduced since KFCT crystals are not present in the pores.

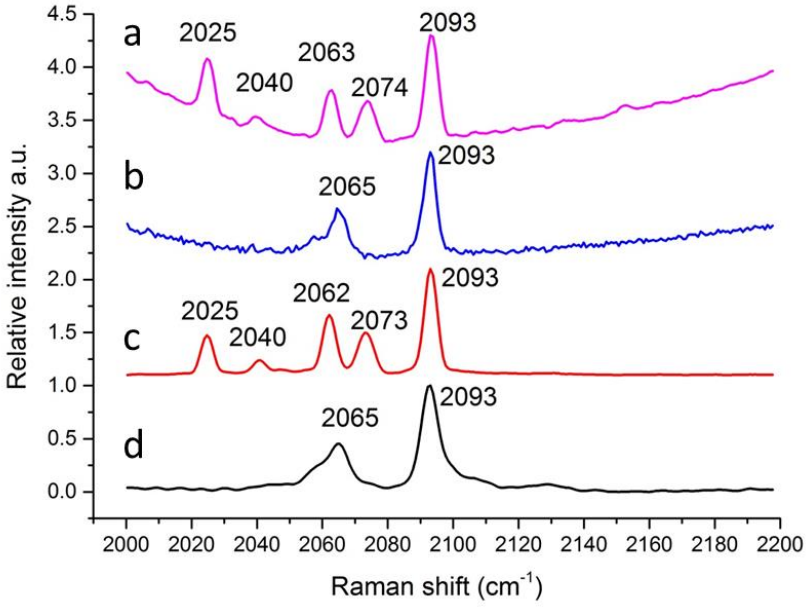

Figure 51. Raman spectra showing the effects of humidity on the stability of the tetragonal crystals of KFCT in bulk solution (a, b) and in CPG-8 (c, d). (a) Tetragonal crystals isolated in bulk converted into the monoclinic polymorph after 15 min in 100 % humid conditions (b). (c) Air-dried CPG-8 containing tetragonal crystals after 2 days and (d) after incubating sample (c) in 100% humid conditions after 1h.

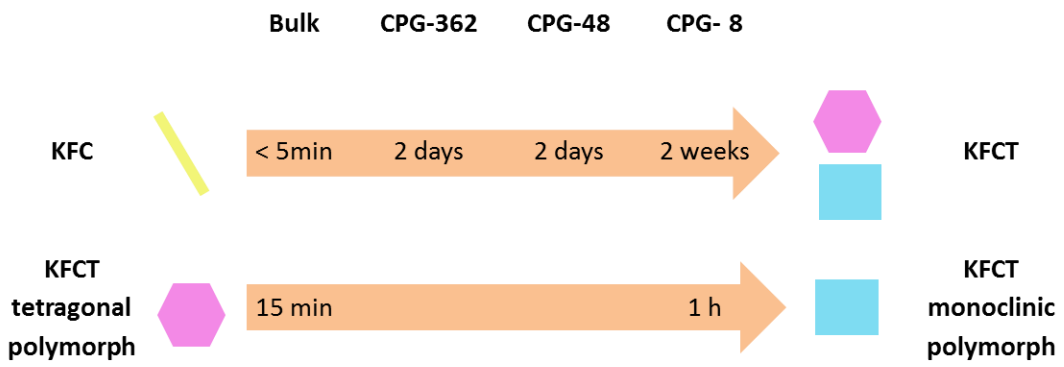

Figure 52. Illustration comparing crystal transformations in bulk and in the CPGs under humid conditions.

3.4 Discussion

This chapter described a study of the crystallization of KFCT in bulk solution and in confinement, clarified polymorph/morphology relationships and brought new insights into its crystallization pathway. Five different forms of KFCT - which are very close in free energy- have been reported in the literature, including a monoclinic and a tetragonal polymorph and three twinned crystals.[257, 258] In this study, 4 distinct-crystal morphologies were observed and characterized. Needle-shaped crystals were assigned to the metastable anhydrous KFC phase, crystals with hexagonal shape corresponded to the metastable tetragonal polymorph of KFCT and rectangular or octagonal shaped crystals were shown to be the thermodynamically stable monoclinic polymorph.

By precipitating KFCT in CPGs it was possible to isolate and therefore characterize the different phases of this solid, while a mixture of phases was always obtained in bulk. The waiting time for KFCT nucleation in confinement was at least 3 orders of magnitude slower than in bulk, which made it easy to track itsphase transformation pathway. These observations are consistent with previous studies of the crystallization of various inorganic solids in confinement.[89, 90, 114] Anhydrous KFC was observed to precipitate as a precursor to KFCT in the CPG pores, and converted with time into the tetragonal and finally monoclinic KFCT. In contrast, KFC was never observed on KFCT precipitation from bulk, aqueous solution. As observed by optical

microscopy, KFC precipitated by fast precipitation with ethanol needs to redissolve to transform into KFCT. The presence of water is therefore essential for the dissolution of KFC and precipitation of KFCT. This might explain the enormous stability of KFC in CPGs after rapid drying. Indeed, drying the CPGs using a vacuum could be a way of removing all of the water from the pores, which would impede the transformation of KFC crystals since the ambient humidity is not sufficient to dissolve them. In contrast, when the CPGs were air-dried (at ambient conditions), some water must remain in the pores, allowing the slow transformation of KFC into KFCT. The transformation from the tetragonal to the monoclinic polymorph was also slower in confinement, and the lifetime of the metastable polymorph was longer in CPG-8. Again, the availability of in the pores is a requirement for polymorph transformation, even though both phases contain the same amount of water in the crystal lattice.

The fact that crystal transformation is slower in confinement (especially in the smallest 8 nm pores) must be due to a combination of different effects. First, it is important to consider that nucleation is a probabilistic phenomenon.[22] Random interactions and collisions between the molecules or ions in a solution produce density fluctuations which play a critical role in cluster formation. The probability for a nucleus of size n to form from a nucleus or cluster of size i can be expressed as:

$$\boldsymbol{N_n = N_i \exp\left(\frac{-\Delta G}{KT}\right)} \quad \text{(Equation 18)}$$

and the number of nuclei that can exceed a critical nucleus size per unit of volume can be calculated as the nucleation frequency, J,[22]

$$\boldsymbol{J = VA \exp\left(-\frac{\Delta G^*}{KT}\right)} \quad \text{(Equation 19)}$$

where V is the volume of the system and A is a preexponential factor related to the kinetics of nuclei formation.[23] The frequency of nucleation in small volumes, such as 7 nm pores, will therefore be significantly lower than in bulk solution. The lower probability of nucleation in small pores might be an

important factor responsible for the overall delay of crystallization in confinement, where higher supersaturations are expected for nucleation.[176, 270]

Moreover,it has been shown that the diffusion rate of ions and water in small pores is slower than in bulk solution.[271] According to the Stokes-Einstein equation, an ion or hydrated ion is transported in aqueous solution with a diffusion rate of,

$$\boldsymbol{D_0} = \frac{\boldsymbol{kT}}{\boldsymbol{6\pi\mu r_0}} \quad \text{(Equation 20)}$$

where k is the Boltzmann constant, T is the temperature in Kelvin, μ is the dynamic viscosity of the liquid and r is the radius of the particle. And the net transfer of ionic species is,

$$\boldsymbol{D_0} = \frac{\boldsymbol{D_1 D_2 (z_1^2 C_1 + z_2^2 C_2)}}{\boldsymbol{D_1 z_1^2 C_1 + D_2 z_2^2 C_2}} \quad \text{(Equation 21)}$$

where D_1 and D_2 are the molecular diffusion coefficients of the individual ions, C_1 and C_2 are the ionic concentrations and z_1 and z_2 are the valences of the ions. However, diffusion in porous media varies from that in the bulk since there are different fluxes in different pores, unknown concentration gradients and lower cross sections available for diffusion. The viscosity of the fluids near solid surfaces has also been shown to change from the values in bulk.[272] An approximation for the solute diffusion in an unsaturated porous media was proposed by Millington and Quirk with the following equation,[273, 274]

$$D_{eff} = \frac{\theta^{7/3}}{\Phi^2} D_0 \quad \text{(Equation 22)}$$

where θ is the volumetric water content and Φ is the porosity. Since CPGs with smaller pore sizes have a higher porosity than those with larger pores, the effective diffusion coefficient of ions in small pores will be lower. Slower ion diffusion through the pores will retard the formation of a stable nucleus and subsequently, this nucleus will grow more slowly. However, it has been

shown that a noticeable decrease in the effective diffusion coefficient only affects pores of a few nanometers.[275, 276] Therefore, this cannot be the only effect directing KFCT crystallization since it would be hardly noticeable in 48 or 362 nm pores. Other possible effects are blockage from crystals growing in the pores which might also cut off various diffusion paths, complicating the necessary ion rearrangement for crystal transformation, especially in small pores, or a decrease in the convective transport of material in the pores. Moreover, adsorption to and ion interactions with the silica pore walls or the tortuosity of the pores might also affect crystallization, although they are unlikely to be major factors in this study.[277]

Other studies of crystallization of inorganic solids in confinement are in agreement with the results discussed here, where confinement effects can operate even on the micro-scale.[118, 156] These observations suggest that there must be a common physical mechanism other than the stabilization of critical nuclei within specific pore sizes, as suggested for many organic compounds.[184, 189, 278] Further investigations with different inorganic solids require *in situ* observations of their crystallization in nanopores in order to provide a new understanding of the confinement effects controlling crystallization.

3.5 Conclusions

This chapter described a study of the crystallization of potassium ferrocyanide in CPGs, and showed that they offer a useful tool to better understand the effects of nanoscale confinement on crystallization and to observe and stabilize polymorphs that are short-lived in bulk solution. Precipitation of $K_4Fe(CN)_6$ from aqueous solution follows a markedly different pathway in the confinement of controlled-pore glasses of pore diameter d = 8, 48 and 362 nm as compared to bulk solution. The first phase to crystallize from aqueous solution in confinement is the anhydrous salt, KFC, which was not observed when precipitating by evaporation of a bulk aqueous solution. KFC confined to the pores transforms slowly to the trihydrate under ambient conditions (r.h. = 40%), whereas the conversion in bulk takes less than 5 minutes. The

metastable tetragonal polymorph is the only phase present in CPG-8 for over two months, while in bulk solution, it only remains stable for 15 min in humid conditions or as a mixture with the monoclinic phase at ambient conditions. Confinement is therefore responsible for a significant decrease of the waiting time for nucleation of the metastable phase of KFCT and KFC (by 4 or 5 orders of magnitude in CPG-8) which enables the investigation of the mechanism of crystallization of this solid.

Chapter 4: Crystallization of Inorganic Solids in Confinement: Controlled Pore Glass Rods for solids of low solubility

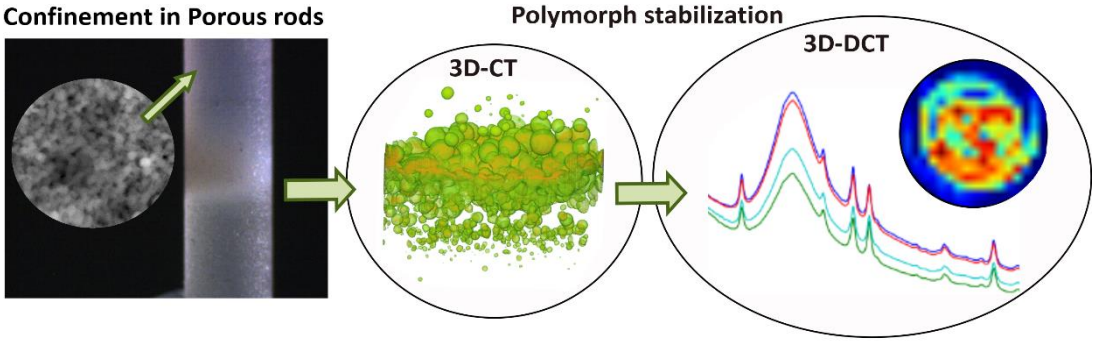

4.1 Introduction

4.1.1 Aims and overview

Having demonstrated the enormous potential effect of nanoscale confinement on the crystallization of a model inorganic solid and the efficacy of CPGs as a confinement system, other solids of greater abundance in nature and importance were investigated. Calcium sulfate and calcium carbonate are both important solids in industry and in biomineralization processes. Their polymorphism and mechanisms of crystallization have been areas of significant interest in recent years, where confinement has proven to be a helpful tool to gain insight into these processes.[114, 118, 156] However, the majority of studies of the crystallization of calcium sulfate and calcium carbonate in confinement have used systems with micron-size confinement.[117, 118, 156] It is clearly important to extend the investigations to nanoscale confinement in order to increase our understanding of the crystallization pathway of the investigated solids and, to determine the effects that govern crystallization in confinement.

This chapter presents the first study of the crystallization of calcium sulfate and calcium carbonate in nanopores and the *in situ* characterization of the crystals in the pores using synchrotron radiation. The poor solubility of these solids in water causes difficulties in achieving pore filling, which might explain the lack of previous successful studies in the literature. In order to solve these issues, macroscopic CPG rods with pore diameters of 7 nm were used here, instead of the microscopic CPG beads utilized in the previous chapter. The differences between these systems will be explained in this chapter. 3D synchrotron diffraction and absorption tomography of the crystals in the pores was used to gain information about the development of their morphology and polymorphism as a function of time, their position within the rod and the effect of the surface chemistry. CPG rods serve as exceptional systems for this study, since they exhibit uniform X-ray absorption, which allows high resolution images of the crystals growing in the pores to be recorded. Further, in contrast to natural samples, they present a homogeneous pore size and

shape distribution, providing an excellent model for the study of crystallization specifically in nanopores.

The results showed an enormous retardation of crystallization in the nanopores and a significant stabilization of metastable phases. These retardation effects allowed us to gain insight into the precipitation pathway of calcium sulfate, enabling, for example, the observation of an amorphous phase, whose existence has been considered controversial. In addition, direct monitoring of the crystallization of inorganic solids in nanopores revealed new insights into how crystallization occurs in small volumes, bringing us a step closer to understanding the role that confinement plays on crystallization.

4.1.2 Introduction to calcium sulfate

Calcium sulfate is an inorganic solid of great significance due to its abundance on Earth[279] and on Mars[280, 281] and its environmental and industrial applications. It is well known that calcium sulfate can be found in three different phases depending on its hydration level, namely, gypsum ($CaSO_4 \cdot 2H_2O$), bassanite ($CaSO_4 \cdot 0.5H_2O$) and anhydrite ($CaSO_4$). Gypsum and anhydrite are stable at room temperature and are usually used after extraction from their natural resources. However, gypsum is also commonly found in pipes, equipment in desalination plants and buildings, where its undesired precipitation causes an enormous economic impact.[282, 283] The development of new approaches to prevent gypsum crystallization is critical and can only be solved by a better understanding of the crystallization system.

Bassanite is the metastable phase of calcium sulfate, and is rarely found as a natural deposit on Earth. However, it is one of the most used inorganic compounds in the construction industry since it is one of the main components of cement. In industry it is known as plaster of Paris and it is produced by thermal conversion of gypsum in a cost and energy expensive process[284]. Recent investigations have revealed the existence of bassanite deposits on the surface of Mars, the formation mechanisms of which are still being discussed.[281, 285] Moreover, calcium sulfate has a range of clinical and medical

uses due to its biocompatibility and rapid resorption.[286] The extensive uses of this solid make it essential that we increase our understanding of its mechanisms of crystallization in order to obtain efficient strategies for better control over crystal phase, size and morphology.

4.1.2.1 General overview of calcium sulfate

Gypsum, the thermodynamically stable phase of calcium sulfate, readily precipitates from aqueous solution at temperatures up to 90 °C. It belongs to the monoclinic system (*I2/a*) and its structure comprises double layers of Ca^{2+}/SO_4^{2-} tetrahedra parallel to (010) that are separated by sheets of water as shown in Figure 53a. Perfect cleavage is obtained along 010 faces due to this layered structure.[287] Above 90 °C, gypsum starts losing its crystalline water and dehydrates first to bassanite and then anhydrite. Bassanite can crystallize as two different forms depending on the method of production, namely α-hemihydrate and β-hemihydrate. They differ from each other in their crystal shape, reactivity with water and mechanical properties, although structural differences are still being disputed.[288] Bassanite crystals have a monoclinic structure with lower symmetry than gypsum due to the presence of water channels in between the tetrahedra, instead of layers (Figure 53b). Bassanite is metastable in water and easily converts to gypsum at room temperature or completely dehydrates at temperatures >100 °C. Finally, the anhydrous form of calcium sulfate comprises three different polymorphs which can be prepared from heating gypsum or bassanite at different temperatures. Anhydrite III belongs to the orthorhombic system (*C222*) and it is difficult to obtain as it is metastable in dry air. Anhydrite II (Figure 53c), with orthorhombic symmetry (*Amma*) is obtained at temperatures >100 °C and it is stable up to 1180 °C. Above this temperature, anhydrite I replaces anhydrite II as the stable phase.[289, 290] Table 6 describes the different phases found for calcium sulfate together with some properties and crystallographic data.

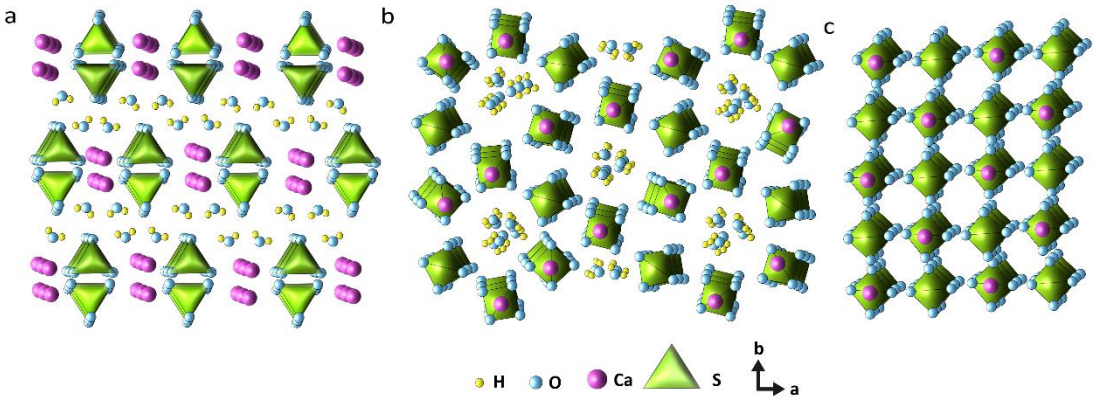

Figure 53. The crystal motifs of (a) gypsum ($CaSO_4 \cdot 2H_2O$), (b) bassanite ($CaSO_4 \cdot 0.5H_2O$) and (c) anhydrite II ($CaSO_4$).

Phase	*Formula*	*Crystal system*	*Lattice parameters (Å)*	*Solubility in H_2O at 20 °C (g/100mL)*	*Stability and abundance*
Gypsum	$CaSO_4 \cdot 2H_2O$	Monoclinic *I2/a*	a=5.679 b=15.202 c=6.522 β=118.4°	0.21	Common <90°
Bassanite	$CaSO_4 \cdot 0.5H_2O$	Monoclinic *I121*	a=12.028 b=6.931 c=12.692 β=90.2°	0.6-0.88	Rare Metastable in H_2O
Anhydrite III	γ-$CaSO_4$	Orthorhombic *C222*	a=12.078 b=6.972 c=6.304 α=β=γ=90°	Hydrates to bassanite	Rare Metastable in H_2O and air
Anhydrite II	β-$CaSO_4$	Orthorhombic *Amma*	a=7.006 b=6.998 c=6.245 α=β=γ=90°	0.27	Artificial <1180°
Anhydrite I	α-$CaSO_4$	Cubic *P31c*	a=b=5.064 c=7.978 γ=120°	-	Artificial >1180°

Table 6. Properties and crystallographic data of the different phases of calcium sulfate.[282, 288, 289]

4.1.2.2 Calcium sulfate phase transitions

Gypsum readily loses crystalline water on heating to form partially or completely dehydrated gypsum, which in contact with water reverts to the original dihydrate. This process makes it a suitable industrial material, where it is possible to tune the hardness of the solid. Bassanite rapidly loses water, and converts into anhydrite due to the relative ease of escape of the water trapped in the channels of its structure.[289]

$$\boldsymbol{CaSO_4 \cdot 2H_2O + heat \rightleftarrows CaSO_4 \cdot \frac{1}{2} H_2O + \frac{3}{2} H_2O} \quad \text{(Equation 23)}$$

$$\boldsymbol{CaSO_4 \cdot 2H_2O + heat \rightleftarrows CaSO_4 + 2H_2O} \quad \text{(Equation 24)}$$

Another important approach for phase selection is by modifying the crystallization solvent. By tuning the proportion of water in the medium by adding ethanol or dry methanol, it is possible to change the phase from gypsum to anhydrite. Tritschler et al. showed that pure anhydrite forms at room temperature at water contents <0.2 wt%, pure bassanite at water contents between 2-30 wt% and finally gypsum at water contents higher than 50 wt%.[291, 292] These studies provided the first method to obtain the different phases of calcium sulfate at room temperature, although they require large amounts of organic solvent.

4.1.2.3 Crystallization pathway of calcium sulfate

The mechanism of crystallization of calcium sulfate has been under intense debate for the last 5 years due to the difficulties in tracking the early stages of nucleation of this solid from solution. Direct observations of the nucleation and evolution of the relevant phases is necessary to gain insight into the crystallization pathways. Moreover, calcium sulfate polymorphism has been shown to be affected not only by temperature, but also by reagent concentration, nucleation time, solution solvent, crystallization environment, water availability or through the use of additives.[118, 291-293]

The crystallization of calcium sulfate was for a long time assumed to follow a classical, one-step mechanism.[294] However, recent studies at the early stages

of crystallization of this solid suggested that the formation of gypsum from solution proceeds through the nucleation of metastable precursors instead of being a single-step process.[118, 295-298] Wang *et al.* studied the mechanism of crystallization of calcium sulfate by quenching a low concentrated solution with ethanol at the early stages of crystallization. The formation of bassanite as a precursor of gypsum was observed, and also, the presence of an amorphous phase, which was stabilized by the use of additives.[293, 298] Wang *et al.* also studied calcium sulfate precipitation using a crossed-cylinder apparatus, where the amorphous phase was stabilized by confinement effects.[299] Jones[297] and Saha *et al*.[300] also suggested the presence of a disordered phase before bassanite and gypsum formation. Nevertheless, the existence of this amorphous precursor is still disputed by some. Van Driessche *et al.* suggested, based on TEM analysis of cryo-quenched samples, that gypsum did not crystallize through an amorphous precursor but through the nucleation, growth and oriented self-assembly of nanocrystalline bassanite.[296]

These observations have been recently called into question by *in situ,* synchrotron SAXS/WAXS studies of the early stages of cacium sulfate precipitation.[295] Stawski *et al.* showed that sub-3nm primary species formed by anhydrous Ca-SO_4 cores initially aggregated, and then coalesced to form larger gypsum particles. No diffraction patterns corresponding to bassanite were obtained in this case.[295, 301] The discrepancies in whether amorphous particles or bassanite are precursors of gypsum crystallization were attributed to the instability and short lifetimes of the precursor phases and also to the differences in experimental conditions used to capture the early stages of the reaction. Indeed, quenching the particles after crystallization might cause changes in the crystallization pathway.[291, 295] Rapid, high resolution, *in situ* analytical techniques are therefore critical to study the mechanism of crystallization of calcium sulfate.

4.1.3 Introduction to calcium carbonate

Calcium carbonate ($CaCO_3$) is an important and well-studied mineral due to its abundance in nature, where it is one of the main components of

sedimentary rocks, limestone and biominerals. In addition to its abundancy in nature, it has many applications in food, medicine and the construction industry. It is also used for environmental purposes, where $CaCO_3$ deposits can be used to neutralize acid water, or as a technique to capture CO_2.[302, 303] $CaCO_3$ is only slightly soluble in pure water and its solubility is strongly influenced by the presence of CO_2 by the generation of bicarbonate:

$$\boldsymbol{CO_2 + H_2O \rightleftarrows HCO_3^- + H^+} \quad \text{(Equation 25)}$$

$$\boldsymbol{Ca^{2+} + 2HCO_3^- \rightleftarrows Ca^{2+} + CO_3^{2-} + CO_2 + H_2O} \quad \text{(Equation 26)}$$

4.1.3.1 Calcium carbonate polymorphism

$CaCO_3$ precipitates in nature as three anhydrous polymorphs namely calcite, vaterite and aragonite, two hydrated forms ($CaCO_3{\cdot}6H_2O$ and $CaCO_3{\cdot}H_2O$) and an amorphous phase. Control over crystal phase, crystal size and morphology is very important in industry as $CaCO_3$ crystals with different properties are used for different applications. Furthermore, this solid has often been used as a model solid for crystal growth studies due to its abundance, easy production and its non-toxic character.[7]

Calcite is the most common and thermodynamically stable polymorph of $CaCO_3$, where it has a rhombohedral crystal structure with space group *R*-3*c*. Its unit cell resembles the face-centered cubic NaCl unit cell, with Ca and CO_3 groups instead of Na and Cl. The unit cell is distorted however, due to the large CO_3 groups, such that it has a face-centered rhombohedral unit cell.[304] Aragonite is considered a metastable phase although the difference in standard free energy with respect to calcite is only around 1.1 kJ/mol. It is expected to eventually convert to calcite under ambient conditions.[305] Aragonite presents an orthorhombic crystal structure with space group *Pmcn*. Vaterite is the least stable crystalline polymorph of $CaCO_3$ and should transform under standard conditions into calcite or aragonite. It presents a hexagonal structure with space group $P6_3$.[306]

Calcite and aragonite are both commonly found in skeletons or shells of many marine organisms such as corals, sea urchins or abalones, while vaterite is rarely found as a biomineral apart from a few exceptions.[307] All three polymorphs are selectively found in nature and often exhibit amazing morphologies, where organisms have achieved high degrees of control over crystal size, shape and orientation. Comparable control over crystallization is very difficult to achieve in the lab, where the use of additives and more recently, modifications in the crystallization environment are the main approaches to control crystallization.[7, 84, 88, 96, 158]

Finally, calcium carbonate also exists as an unstable amorphous phase known as amorphous calcium carbonate (ACC) which often acts as a precursor to crystalline $CaCO_3$ biominerals. ACC is isotropic and has no defined morphology. It precipitates as spheres in solution to reduce its interfacial free energy, but it can also be easily molded into more complex structures by modifying the local environment.[308] This property is very important since the anhydrous crystalline phases forming through ACC may preserve the shape of the deposited precursor. This means that ACC can ultimately be used as a tool to control crystal morphology and orientation. As a consequence, researchers have shown increasing interest in stabilizing and controlling ACC precipitation by using confined environments, additives and surface modifications.[114, 167, 198, 309]

The transformation from ACC to any of the anhydrous polymorphs of $CaCO_3$ was traditionally known to occur via a dissolution-reprecipitation mechanism. However, recent studies have also observed the direct nucleation of aragonite or vaterite on the surface of ACC particles, leading to their direct conversion.[310] Furthermore, different types of ACC have been proposed in the literature, namely an hydrated amorphous calcium carbonate (ACC-H_2O) and anhydrous ACC.[311] Both phases have been found in corals and in sea urchin larval spicules. It was shown that ACC-H_2O was the most metastable phase, converting into ACC prior its crystallization into calcite or aragonite.[311, 312] Other forms of ACC have also been proposed, where short-range internal

order may act as a blueprint for the final crystal structure. Recent observations of poorly crystalline or proto ACC structures of calcite, vaterite[313] and aragonite[157] open the door to new means of polymorph selectivity through the control of the precipitating amorphous precursors.

4.2 Experimental

The crystallization of calcium sulfate and calcium carbonate ($CaCO_3$) was first carried out in CPG beads and CPG rods of 10 mm in length and 1 mm and 2.8 mm diameters. Subsequently, the crystallization of both solids within the CPG rods was followed by *in situ* synchrotron 3D absorption and diffraction tomography and compared with crystallization performed in 1 mm glass capillaries. All the experiments were carried out under ambient conditions which, unless otherwise stated, are T = 20 ± 2 °C and a relative humidity (r.h.) of 40 ± 5 %.

4.2.1 Materials

All the chemicals including calcium chloride, ammonium sulfate, sodium carbonate, succinic anhydride, 4-dimethyl(amino)pyridine and N,N-dimethylformamide were obtained from Sigma-Aldrich, while the CPG rods were obtained as Varapor100 from Advanced Glass & Ceramics (St. James, NC, USA) as rods of 1 or 2.8 mm in diameter and 10 mm in length. They possess a narrow pore size distribution with mean pore size of 7 nm. Controlled pore glass beads were obtained from Millipore as particles of diameter 10−100 μm with pore size of 8 nm.

4.2.2 Crystallization in Glass Capillaries

Equimolar solutions of $CaCl_2$ and $(NH_4)_2SO_4$/Na_2CO_3 were injected into plastic tubes connecting a glass capillary of 10 mm in length and 1 mm diameter filled with Milli-Q water. Figure 54a illustrates the set-up employed. Crystallization in the glass capillary was followed by optical microscopy at two different concentrations: 3M and 250 mM for $CaCl_2$/$(NH_4)_2SO_4$ and 1M and 250 mM for $CaCl_2$/Na_2CO_3.

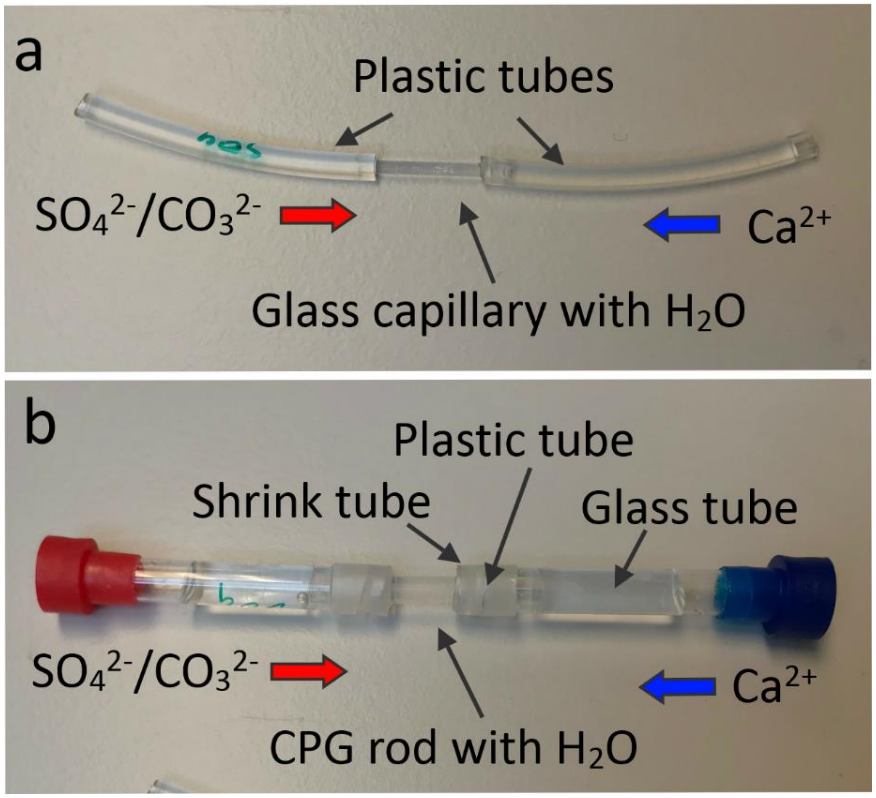

Figure 54. Set-up of $CaCO_3$ and calcium sulfate crystallization in (a) glass capillaries and (b) CPG rods.

4.2.3 Crystallization in Controlled Pore Glass (CPG) Beads

Crystallization in the CPGs beads was carried out by two different methods following previous studies of crystallization in CPG beads.[187, 189, 314] The first method is described as the “filtration method”. It consisted of suspending the porous glass particles in a calcium sulfate or $CaCO_3$ solution and applying a vacuum to remove the gas present within the pores until no more bubbles were observed. The bulk solution was then removed by filtration and the particles were dried at room conditions. The second method will be referred as the “impregnation method”. It consisted of successive impregnations of CPGs with a small amount of calcium sulfate or $CaCO_3$ solution and leaving them to dry at ambient conditions. In both cases calcium sulfate or $CaCO_3$ crystallization was achieved by evaporation and no cleaning of the particles could be carried out.

4.2.4 Crystallization in Controlled Pore Glass (CPG) Rods

The CPG rods were kept in Milli-Q for 4h prior to crystallization in order to fill the nanopores with water. The ends of a CPG rods were then inserted into two pieces of plastic tubing, which were in turn inserted into glass tubes closed with plastic lids. The plastic and glass tubes were sealed with 3:1 ratio shrink tubes obtained from Hellermmann Tyton (Figure 54b). Crystallization in the pores was achieved by counterdiffusion of Ca^{2+} and SO_4^{2-} or CO_3^{2-} ions. Equimolar solutions of $CaCl_2$ and $(NH_4)_2SO_4$/Na_2CO_3 were injected into the two glass tubes. Two different initial concentrations were tested, 3M and 250 mM for $CaCl_2$/$(NH_4)_2SO_4$ and 1M and 250 mM for $CaCl_2$/Na_2CO_3. 1 mm CPG rods were wrapped in a Kapton film or coated with paraffin wax to avoid evaporation from the open pores. For wax coating, the rods were rolled onto hot wax, where this created a thin homogeneous film on the glass rod.

For *ex situ* studies, the rods were first immersed in H_2O for 5 min followed by ethanol for 30 min. The rods were then left to dry at ambient conditions. CPG rods were functionalized with carboxyl-terminated self-assembled monolayers by a chemical vapor deposition method. The procedure followed for the coating is described in the general preparation methods (2.1.1.3).

4.2.5 Characterization Methods

The crystals growing in the nanopores were imaged over time using computed micro-tomography (µ-CT) and diffraction contrast tomography (DCT) at the European Synchrotron Radiation Facility (ESRF), at beamline ID11. The growing crystals were characterized by alternating between a diffraction and an imaging detector, which gave us information about crystal phase and morphology at different positions of the rod. Although DCT is a slow technique, fast scans are necessary for *in situ* measurements, which required a compromise on resolution. For synchrotron experiments, the ends of a wet CPG rod were inserted in plastic and glass tubes as described previously and the lid closing the $CaCl_2$ reservoir was glued to an M4 screw attached to a rotating stage (Figure 55). The system was mounted perpendicular to the

detectors with the reservoir containing the $(NH_4)_2SO_4/Na_2CO_3$ solution at the top.

DCT was performed by recording 2D diffraction patterns at different heights of the samples with a 50 x 50 μm^2, 40 keV beam. A 100 x 100 μm^2 beam was also used for faster scans when samples were changing very fast. DCT data was collected at 86 positions in 2.8 mm CPG rods and 22 in 1 mm CPG rods with a FRelon 4M detector. 2D diffraction patterns were recorded every 37.5 µm along y axis, and from 0° to 180° and from 180° to -180° in 5° rotation step (w) size, 1 s expose time. 2D X-ray diffraction patterns (XRD) were also recorded using a larger beam (0.4 x 0.4 mm^2) in order to take average diffraction patters of the crystals present in specific samples in a rapid manner. 1D diffraction profiles were obtained by Azimuthal integration of 2D diffraction patterns and reconstructed into 2D maps using an iPython command shell. In the spatial diffraction maps, areas of high intensity correspond to the position of the crystals within the rods. The beam was calibrated with a CeO_2 standard. A diffraction pattern of a CPG rod filled with water was used to substract the glass background from the diffraction patterns of the CPG rods with crystals.

The crystals were also imaged by µ-CT, where 3D images were obtained from 2D slices. The samples were scanned over 180° with a field of view of 1.4 x 1.4 mm and a voxel size of 0.1 µm. Two-dimensional CCD area detector (FReLon 4M) coupled with a microscope objective and high resolution scintillator was used for µ-CT. Figure 55 shows a schematic of the procedure followed at the synchrotron source.

Due to the size of the beam, CPG rods of diameter >1.4 mm could not be imaged by µ-CT at the ESRF. Nevertheless, high resolution µ-CT scans of CPG rods of 2.8 mm in diameter could be obtained at Diamond Light Source, beamline I13-2. The larger beam size allows larger objects to be scanned with a field of view of 3.5 x 3.5 mm. The voxel size was in this case 1.6 µm over 180° with a total of 2000 projections and 0.1 s exposure time. High resolution

is achieved by the use of a high resolution pco edge 5.5 camera. The images were processed with Avizo 8 and Image J software.

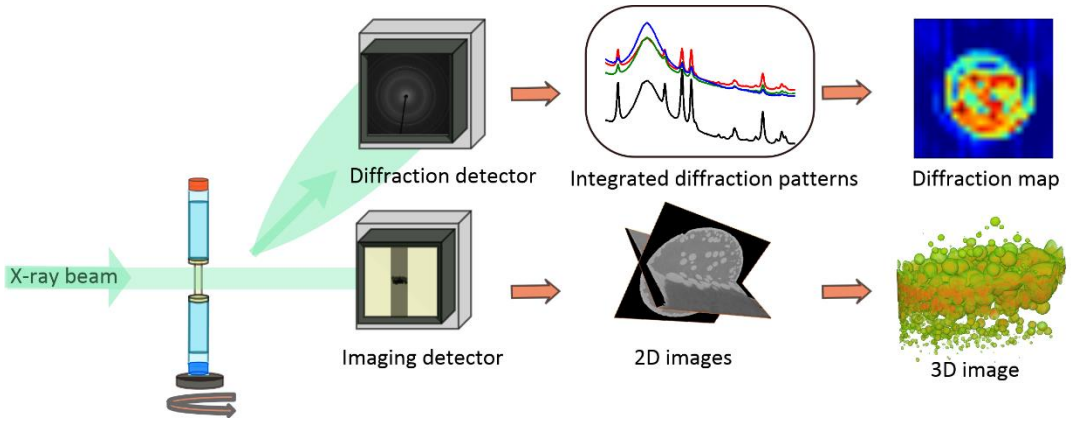

Figure 55. Diagram showing the in situ characterization of calcium sulfate crystals in CPG rods by synchrotron DCT and μ-CT. The CPG rod is connected to a Ca^{2+} and a SO_4^{2-} reservoirs and mounted perpendicular to a 40 keV. By rotating the sample and alternating between diffraction and imaging detectors, 3D diffraction and imaging information of the crystals in the pores is acquired.

The commercial simulation software, COMSOL Multiphysics, was employed to model the variations in the ion concentration through the 7 nm pores over time. A 2D model was applied, and no evaporation was assumed. The rods were considered perfect sealed cylinders of dimensions 10 mm in length and 1 mm or 2.8 mm in diameter, porosity of 25% and tortuosity, τ=1.4. Any adsorption of the ions to the pore walls, dispersion or ionic flux in the pores were considered negligible. The diffusion coefficients of the ions implemented in the model were $D_{Ca} = 7.9 \cdot 10^{-6}\, cm^2/s$, $D_{SO_4} = 1.07 \cdot 10^{-5}\, cm^2/s$ and $D_{CO_3} = 9 \cdot 10^{-6}\, cm^2/s$.[315]

4.3 Results

4.3.1 Calcium sulfate crystallization

4.3.1.1 Crystallization in glass capillaries

Calcium sulfate was first crystallized in a 1 mm capillary by counter diffusion of the SO_4^{2-} and Ca^{2+} ions and the crystals were analyzed by optical microscopy and Raman spectroscopy. At high initial reagent concentrations (3 M) large gypsum clusters were observed after 2 min and at lower concentrations (250 mM), gypsum crystals were observed after 1 h (Figure 56). Amorphous intermediates or bassanite were not detected at these concentrations.

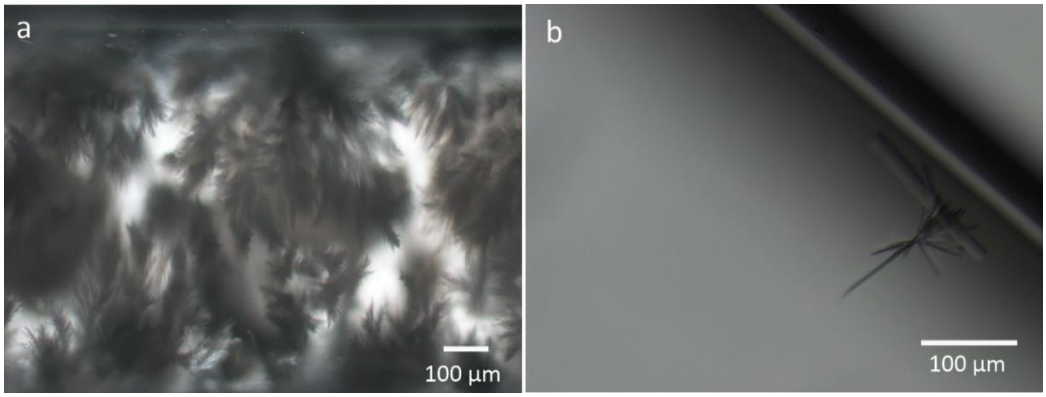

Figure 56. Gypsum crystals in a 1 mm glass capillary at (a) 1.5 M calcium sulfate concentration after 2 minutes and (b) 250 mM calcium sulfate after 1 h.

4.3.1.2 Crystallization in CPG beads

Calcium sulfate crystallization in CPG beads with 8 nm pore sizes was carried out evaporation of a calcium sulfate solution by two different methods: filtration and impregnation. The filtration method was successfully used to crystallize soluble inorganic solids (KFCT) in the previous chapter. As discussed before, clean outer surfaces of the CPGs beads can be achieved by filtering the beads after immersion in the reagent solution (Figure 57a). After immersing the CPG beads in a slightly undersaturated calcium sulfate solution, a vacuum was applied and the beads were filtered. Both normal and vacuum filtration were tested, but not enough material remained in the pores to be characterized by powder X-ray diffraction (PXRD), IR or Raman. The low amount of material in

the pores is due to the lower solubility of calcium sulfate in water (compared to KFCT), which causes difficulties with pore filling.

With the objective of achieving a larger amount of crystals in the pores, successive impregnations of the CPGs with small amounts of solution were carried out. The solution was allowed to evaporate at ambient conditions in between impregnations. This method presented a cleaning problem. Large calcium sulfate crystals usually precipitated in between the CPG particles (Figure 57b) and on their surfaces (Figure 57c). PXRD analysis of the CPG beads only revealed the presence of gypsum crystals (Figure 57c), which most probably correspond to bulk crystals rather than crystals in the pores. When the CPG beads were washed with water or mixtures of water/ethanol, bulk crystals dissolved and no clear signal from the crystals was detected by any of the analytical techniques used. The crystals in the pores either redissolved after washing or were again too small/few to be characterized. Another possibility could be that the techniques used during these analyses were not sensitive enough to characterize the crystals within 8 nm pores. Nevertheless, we successfully characterized KFCT crystals in the pores as described in the previous chapter and therefore, this is not likely to be a major problem.

An important advantage of using controlled pore glass as a confinement system is the variety of manufacturing possibilities. CPGs with different shapes and sizes are commercially available and can be customized as desired. CPG rods with larger dimensions than the CPG beads were easier to wash and manipulate, making it possible to crystallize poorly soluble inorganic solids such as calcium sulfate in a controlled way.

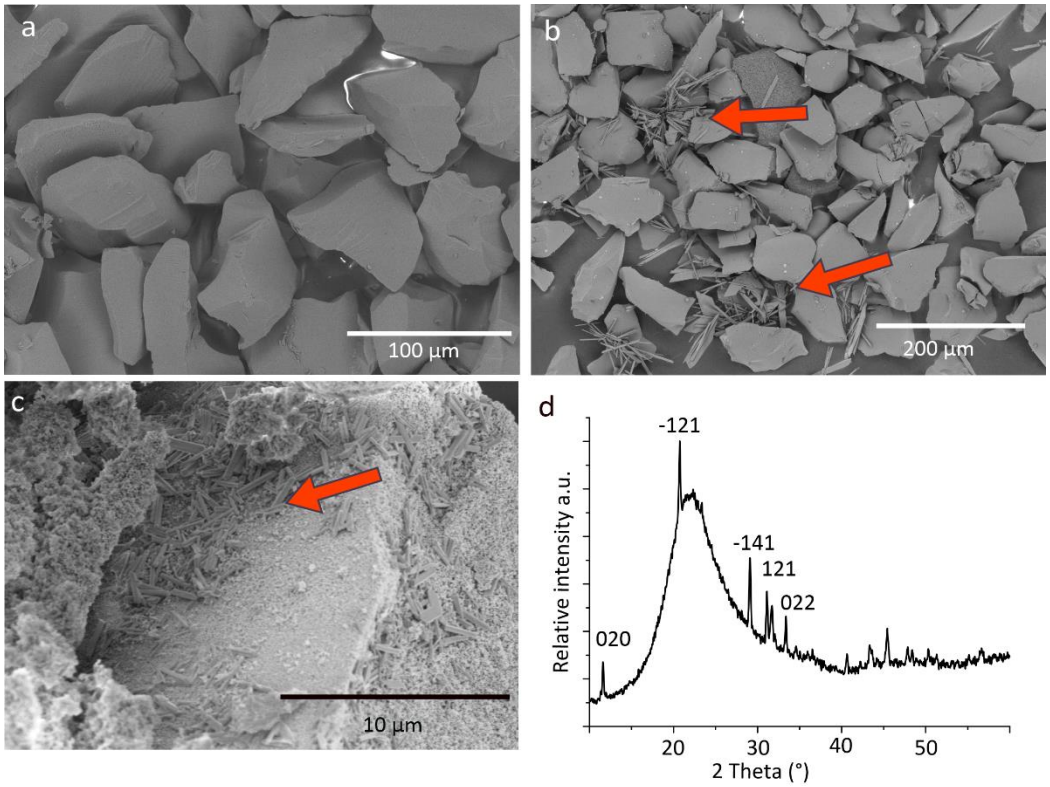

Figure 57. CPG beads after calcium sulfate crystallization by the filtration method (a) where the surfaces are clean but crystals in the pores are not detected and by the impregnation method (a-d), where gypsum crystals (indicated with red arrows) grow in between or on the surfaces of the particles, therefore preventing crystals growing from the pores.

4.3.1.3 Crystallization in CPG rods

Macroscopic CPG rods of 10 mm in length and diameters of 1 or 2.8 mm were employed for the crystallization of calcium sulfate in 7 nm pores (Figure 58a). Figure 58b shows an SEM image of the internal structure of the rods manufactured by the sol-gel method.[316] Calcium sulfate crystallization in the pores was achieved by inserting the ends of a wet CPG rods between two tubes containing aqueous $CaCl_2$ and $(NH_4)_2SO_4$ solution reservoirs. A diagram of the set up can be found in Figure 58c. Counter-diffusion of the Ca^{2+} and SO_4^{2-} ions through the pores leads to an increase of calcium sulfate supersaturation over time, and precipitation takes place when a threshold of supersaturation has been exceeded. As with the glass capillaries, 2 different initial ion concentrations were tested, namely 3 M and 250 mM.

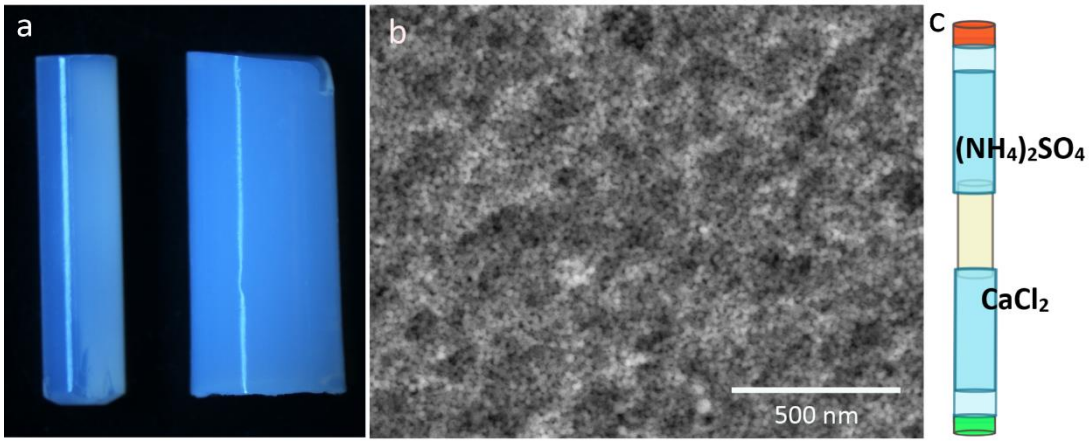

Figure 58. CPG rods of 1 and 2.8 mm in diameter (a) and the internal structure of the rods imaged by SEM (b). (c) Schematic of calcium sulfate crystallization in the CPG rods where the two reagents are injected in tubes connected to the rod.

CPG rods characterization

CPG rods with a chemical composition of 99.99% SiO_2 were manufactured by the sol-gel process by Advanced Glass & Ceramics. Analysis of pore size, porosity and surface area of the CPG rods were carried out using Brunauer–Emmett–Teller (BET) and Barrett-Joyner-Halenda (BJH) analysis. From BET and BJH analysis the surface area is obtained, together with pore volume information, which gives us information about the average pore size. The area under the graph obtained when plotting pore radius vs incremental pore volume corresponds to the total porosity of the sample as shown in Figure 59. The rods contained narrow pore size distributions of around 7 nm, the surface area was 120 $\pm$ 10 m^2/g and the porosity was 25 $\pm$ 4 %. CPG rods with 20 and 4 nm pores were also analyzed but both were too fragile for the experiments proposed here. CPG rods with 20 nm pore sizes presented a porosity of 70% and easily fragmented during crystallization. CPG rods with 4 nm pore sizes showed a porosity of around 50% and they broke during washing treatments before crystallization.

a

Average Radius (Å)	Incremental Pore Volume (cm³/g)	Cumulative Pore Volume (cm³/g)	Incremental Pore Area (m²/g)	Cumulative Pore Area (m²/g)
228.8236	0.000553	0.000553	0.048365	0.048365
162.1183	0.005149	0.005703	0.635234	0.683599
119.2711	0.019186	0.024889	3.217237	3.900836
91.85444	0.035991	0.06088	7.83662	11.73746
15.23974	0.003219	0.273157	4.224174	121.784
13.74696	0.002332	0.275489	3.392042	125.1761
12.34919	0.002177	0.277666	3.5257	128.7018
11.08526	0.001781	0.279447	3.213891	131.9157
10.32106	0.000729	0.280177	1.413537	133.3292
9.849761	0.000598	0.280774	1.213501	134.5427
9.380242	0.000875	0.281649	1.865527	136.4082

b

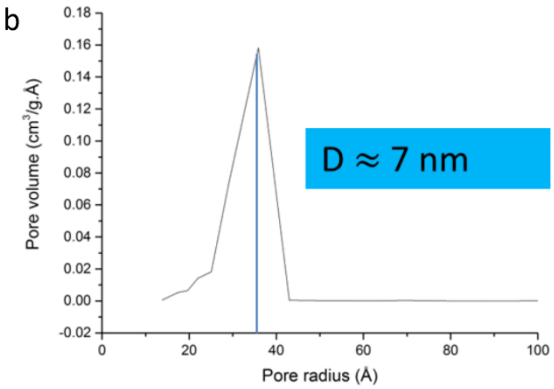

Figure 59. Example of data obtained from BJH analysis. Pore size and pore volume information (in green) can be plotted to obtain the porosity (in pink), from the area below the graph in (b) and the average pore size of 7 nm.

Simulations of the ion diffusion through the rods

In order to estimate the ion concentration at any position along the rods over time before crystallization, the diffusion rate of the ions through the porous network was modelled using computer simulations. The concentration gradient of the ions in the pores is dependent on the porosity, pore geometry (tortuosity) and dimensions of the rod. This model permitted us to calculate the time at which crystals should nucleate in the pores. It is important to note that the model assumes no evaporation from the pores, and the rods act like sealed systems. However, the rods employed in the experiments contained open pores in all directions and possible evaporation effects need to be taken into account.

If evaporation effects are an important factor in this system, it is assumed that crystallization on the surface of the rods will be favored, generating a flow of ions from the pores to the surface and therefore a concentration gradient from the core of the rod to its surface.[317] This velocity field within the rod will cause a competition between diffusion and advection effects. If diffusion effects dominate in the system, our model will be valid, but if advection is the dominant force, the model cannot be used. This competition can be estimated by the Péclet number, $Pe = \frac{uL}{\varepsilon D_s^*}$, where *L* is the length of the porous rod (10

mm), D_S^* is the effective diffusion coefficient of the ions through the pores, ε is the porosity of the rod (0.25) and *u* is the velocity of the salt in the porous media.[318] The velocity is related to the evaporation rate according to the following equation: $u = \frac{J}{A\rho}$, where *J* is the evaporation rate, *A* is the exposed surface area and ρ is the density of the liquid. The effective diffusion coefficient of the ions in the pores is $D_S^* = \frac{\varepsilon}{\tau} \cdot D_S$ where (τ) is the tortuosity, which is the degree of curvature or 'tortuousness' of a porous medium. The tortuosity of the system presented here is calculated with the equation $\tau = \varepsilon^{-0.25}$, where the internal structure is assumed to be a three-dimensional network of overlapping spheres.[319]

The obtained Péclet numbers for rods with different diameters are illustrated in Table 7, where these were calculated using the parameters $\tau = 1.4$, $D_{Ca}^* = 1.25 \cdot 10^{-6}\, cm^2/s$ and $D_{So4}^* = 1.79 \cdot 10^{-6}\, cm^2/s$. According to Huinink *et al.*, convection will dominate over diffusion at Pe > 1, when the ions are highly attracted to the surfaces of the system.[318] As shown in the table below, in rods of 1 mm diameter, Pe > 1 and therefore the model chosen here would not be valid. Coating the surfaces of these thin rods with wax solves this issue since it reduces the evaporation rate by one order of magnitude, resulting in a Pe < 1. For rods of thicker diameter (2.8 mm), both coated and non-coated rods presented Pe < 1, resulting in diffusion-driven processes.

Rod	R (cm)	A (cm^2)	u (g/s)	h (cm/s)	Pe (Ca)	Pe (SO_4)
1mm	0.05	0.329867	2.58E-06	7.82E-06	6.26E+00	4.13E+00
1mm coated	0.05	0.329867	2.86E-07	8.67E-07	6.94E-01	4.58E-01
2.8mm	0.14	1.002796	1.00E-06	9.97E-07	7.98E-01	5.27E-01
2.8 mm coated	0.14	1.002796	9.40E-07	9.37E-07	7.50E-01	4.95E-01

Table 7. Summary of calculated Péclet numbers of CPG rods with diameters of 1 and 2 mm before and after coating their surfaces with paraffin wax.

Once the validity of the model was verified for CPG rods of 2.8 mm, the ion diffusion through the pores was simulated, and the concentration gradient of

ions through the rods were plotted over time (Figure 60). From the ion concentration at the center of the rod it is then possible to calculate the supersaturation of the solution in the pores at a given time. Thus, the system reaches supersaturation with respect to gypsum in around 40 min after 3 M reagent injection and in 1 h 30 min for 250 mM (Figure 60 a,b,c). For lower concentrations, e.g. 50 mM, the solution in the pores is supersaturated at times > 7h (Figure 60 d). Supersaturations were calculated with values of ion activity using Visual Minteq.

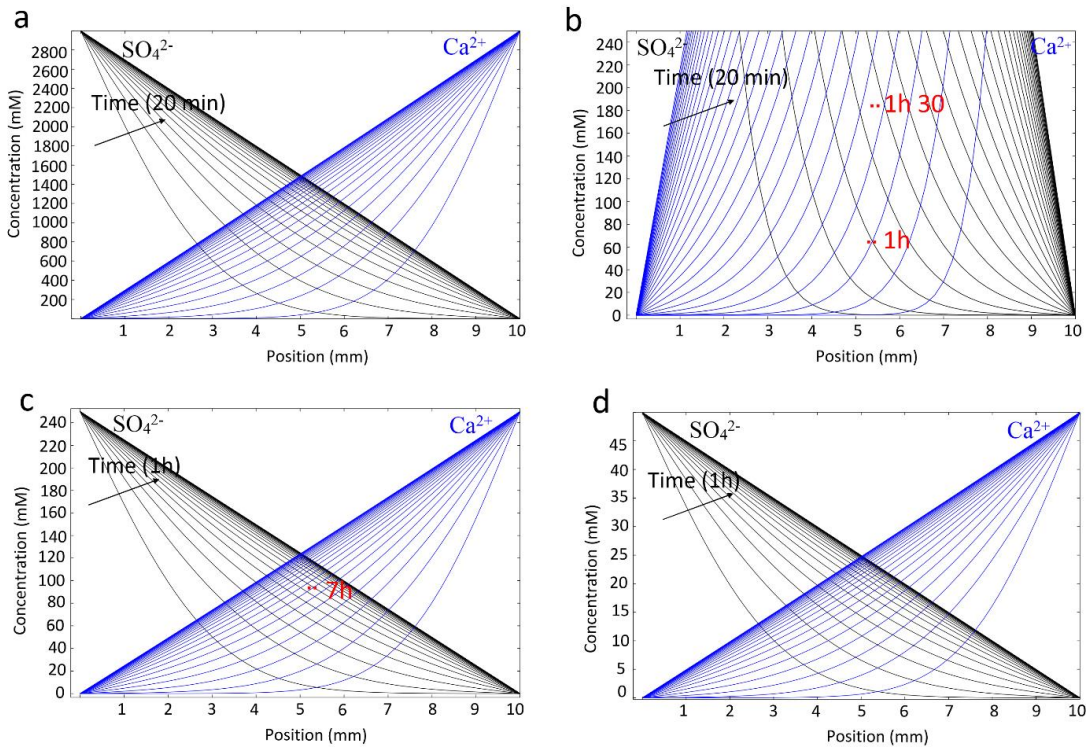

Figure 60. Graphs of ion concentration profiles as a function of the position along the CPG rods and time at 3 M (a,b), 250 mM (c) and 50 mM (d) initial reagent conditions. The concentration of calcium and sulfate ions is represented in blue and black respectively and the concentration lines are separated by 20 min (a,b) and 1 h (c,d). After 1 h from 3 M reagent injection (a,b), the ion concentration is around 65 mM at the centre of the rod and almost 180 mM after 1 h 30 min. After 7 h from 250 mM from reagent injection, the concentration of the ions at the centre of the rods is around 90 mM.

The ion diffusion through the pores dramatically changes as a function of the porosity according to our model (Figure 61). Thus, as porosity increases, ion

diffusion is faster and therefore, nucleation should be expected at earlier times.

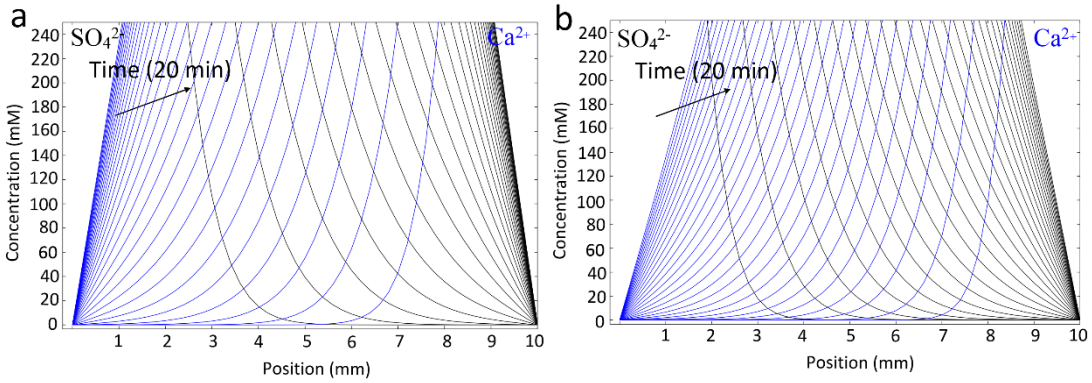

Figure 61. Graphs of ion concentration profiles as a function of time and position along CPG rods with (a) 50% and (b) 10% porosity at 3 M initial reagent conditions. The ion concentration in the pores at the centre of the rod after for example 1 h, is expected to be (a) 85 mM and (b) 18 mM.

In situ characterization of calcium sulfate crystallization in 7 nm CPG rods

Precipitation of calcium sulfate within 2.8 mm CPG rods was first observed with the formation of a 3 mm, cloudy, white band in the middle of the rod 1h after 3 M reagent injection (Figure 62a,b). XRD at the center of an intact rod using a 0.4 mm beam showed a broad band ≈ 3 Å only (Figure 62d, black). This confirmed that the material in the pores exhibits no long-range order and is an “amorphous calcium sulfate” (ACS) phase. The transparency of the rods started to recover after 2 h and a well-defined band of around 0.5 mm began to form in the middle of the rod (Figure 62c). XRD showed that ACS was still present, together with bassanite crystals (Figure 62d). The band became more defined with time, reaching a thickness of around 1 mm. Sharp peaks corresponding to bassanite were observed after 7 h, showing an increase in crystallinity and in the amount of crystals in the pores (Figure 62d, green). The diffraction patterns at short times showed various broad peaks which turned into sharp individual peaks with time (Figure 62d). These peaks might indicate differences in the amount of crystalline water in bassanite. There has been much debate about the correct description of water in the crystalline structure of calcium sulfate hemihydrate, where discrepancies involving $CaSO_4 \cdot xH_2O$ with $0.5 \leq x \leq 0.8$ have been found.[320] Slight shifting and splitting of some

reflections have been observed when comparing the diffraction patterns of $CaSO_4 \cdot 0.5H_2O$ and $CaSO_4 \cdot 0.625H_2O$.[320]

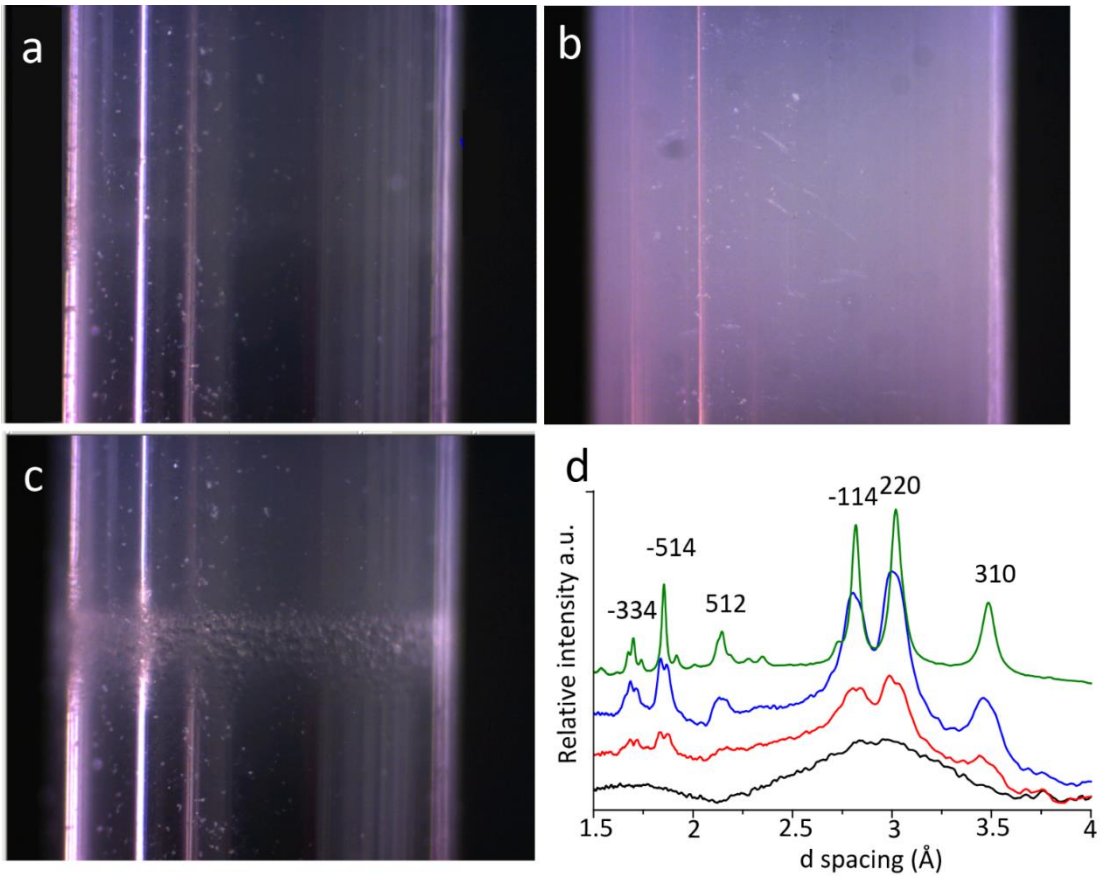

Figure 62. 2.8 mm CPG rod (a) 10 min, (b) 1h and (c) 2h after 3 M solution injection. (d) Diffraction patterns of the rod at different time points after 1h (in black), 1h 30 min (in red), 2h (in blue) and 7h (in green). Note that the diffraction patterns are plotted after background subtraction (from a rod filled with H_2O). Small "particles" observed on the surfaces of the rods are defects on the glass and therefore remain unchanged with time.

Observations of the band at the center of the rod after 24 h with optical microscopy revealed the presence of spherulitic crystals several hundreds of microns in size (Figure 63a). Intact rods were characterized by Raman, where this allowed us to study polymorph development *in situ* for longer periods of time. As the rods are optically transparent, the laser can be focused on individual crystals at different positions and depths in the rods. Characteristic peaks of bassanite ($CaSO_4 \cdot 0.5H_2O$) at 430 cm^{-1} $\nu_2(SO_4)$ (bending) and 1014 cm^{-1} $\nu_1(SO_4)$ (symmetric stretching) were observed after 4h, and no transformation to gypsum was detected over a period of 3 weeks. (Figure

63b). However, the Raman signal of small crystals was often too weak to determine the polymorph.

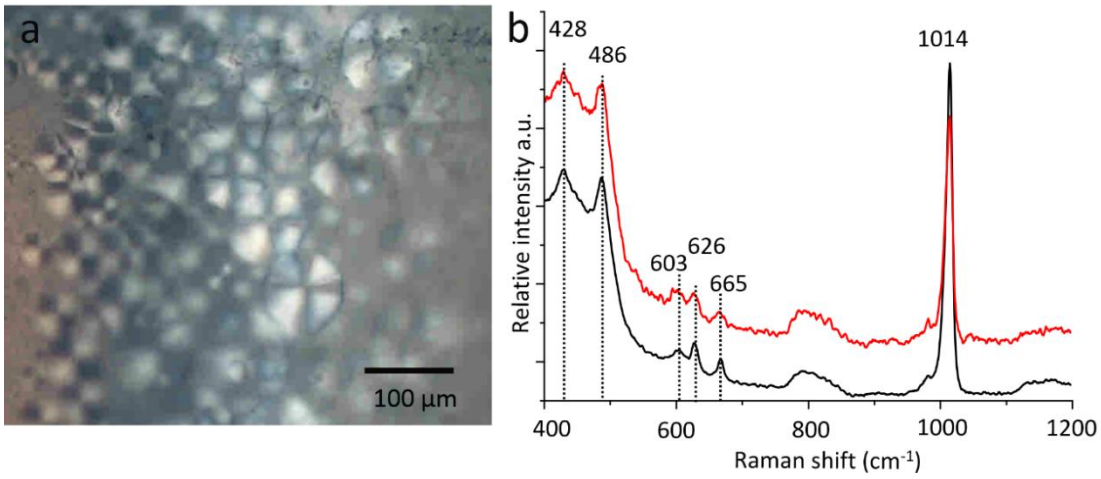

Figure 63. (a) Optical micrograph of calcium sulfate crystals inside 7 nm pores in a CPG rod under polarized light after 24 h from 3 M reagent injection. (b) Raman of the crystals in the pores after 4 h (in black) and 3 weeks (in red) showing characteristic peaks from bassanite at 430 cm^{-1} and 1014 cm^{-1}.

Calcium sulfate crystallization was then followed over time by µ-CT and DCT in order to obtain 3D information about the development of the crystals inside the porous rod. µ-CT showed the presence of large spheroidal crystals between tens to hundreds of hundreds of microns in diameter after 3 h (Figure 64 a,c). Further crystal nucleation and growth was observed over time, resulting in a continuous band that blocked the majority of the rod after 24 h (Figure 64 b,d). DCT was performed over a 0.6 mm height in the middle of the rod, and as previously observed by XRD, bassanite was the only polymorph detected in the rod after 7 and 24 h (Figure 64 e,f,g). The diffraction maps were obtained by selecting a range of 2θ where a specific peak of bassanite was present (110). The pixels with high intensity in the diffraction map correspond to the positions of the bassanite crystals. A specific diffraction peak from gypsum, (020), was also selected and a diffraction map was plotted, which showed that no gypsum crystals were present in the rod (Figure 64 h). Minor evaporation at the surfaces of the rods cannot be ruled out since they contain open pores in all directions. However, from the tomograms and

diffraction maps it is clear that crystals grow both within the rods and adjacent to their surfaces. These results show amazing differences between crystallization in bulk and in confinement since neither ACS or bassanite were observed in bulk under the same conditions.

Calcium sulfate crystallization in the 7 nm pores was also carried out at lower concentrations. Bassanite was detected within the CPGs 7 h after injecting 250 mM reagents, in comparison to 1 h 30 for the 3 M reagents (Figure 65). Bassanite was again stable for longer than 3 weeks in the pores while this phase was never observed in the glass capillaries at the same concentrations. On further reduction of concentrations to 50 mM, no crystals were observed to form within the CPG rods.

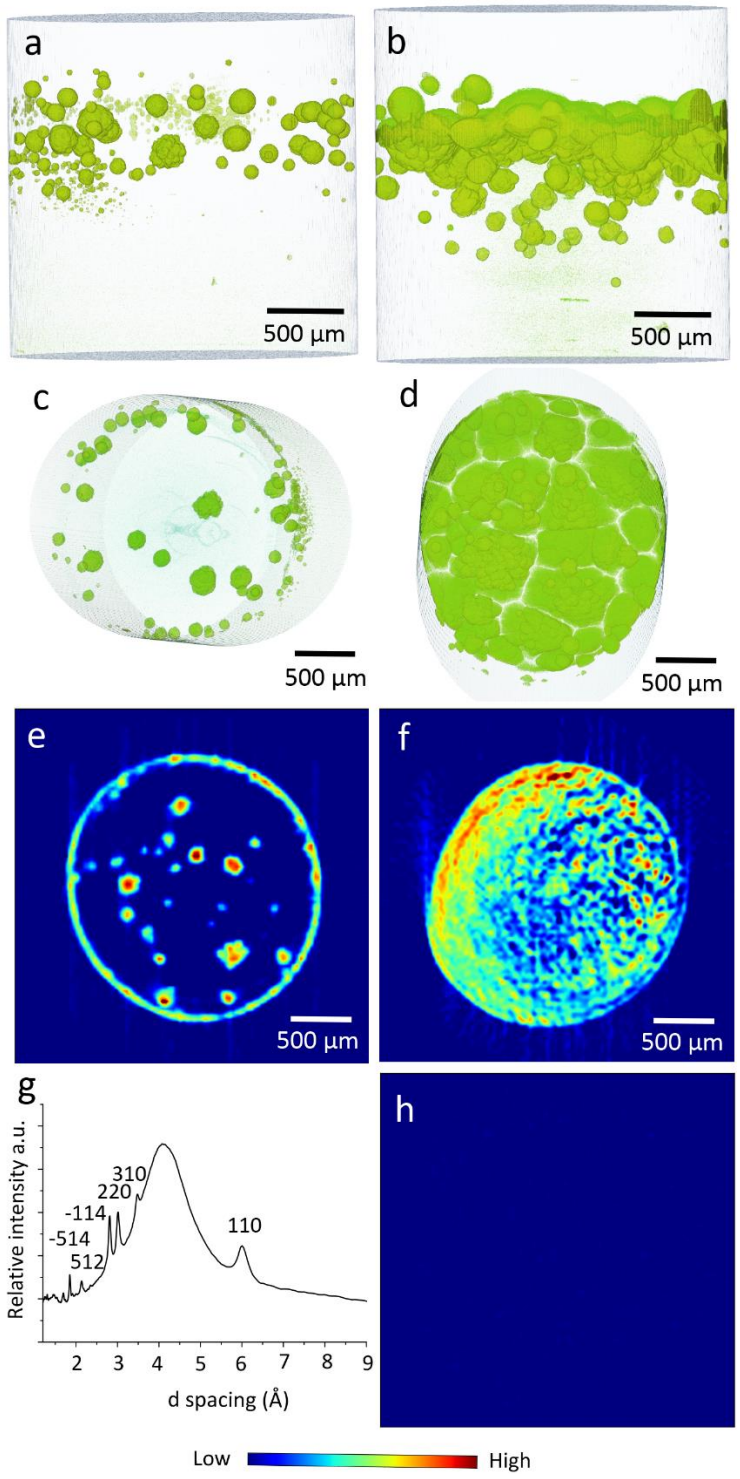

Figure 64. 3D tomogram of bassanite crystals growing from 3 M reagents in a 2.8 mm CPG rod after 3 h (a,c) and 24 h (b,d). 2D spatial diffraction map of the crystals in the rod recorded with a 50 µm beam after 7 h (e) and 24 h (f). The peak (110) was selected from the diffraction patters of the crystals (g).[321] Low and high intensities of the (110) peak are illustrated in blue and red respectively. (h) (020) peak from a gypsum reference[322] diffraction pattern was selected and plotted as a diffraction map, highlighting the absence of gypsum throughout the sample.

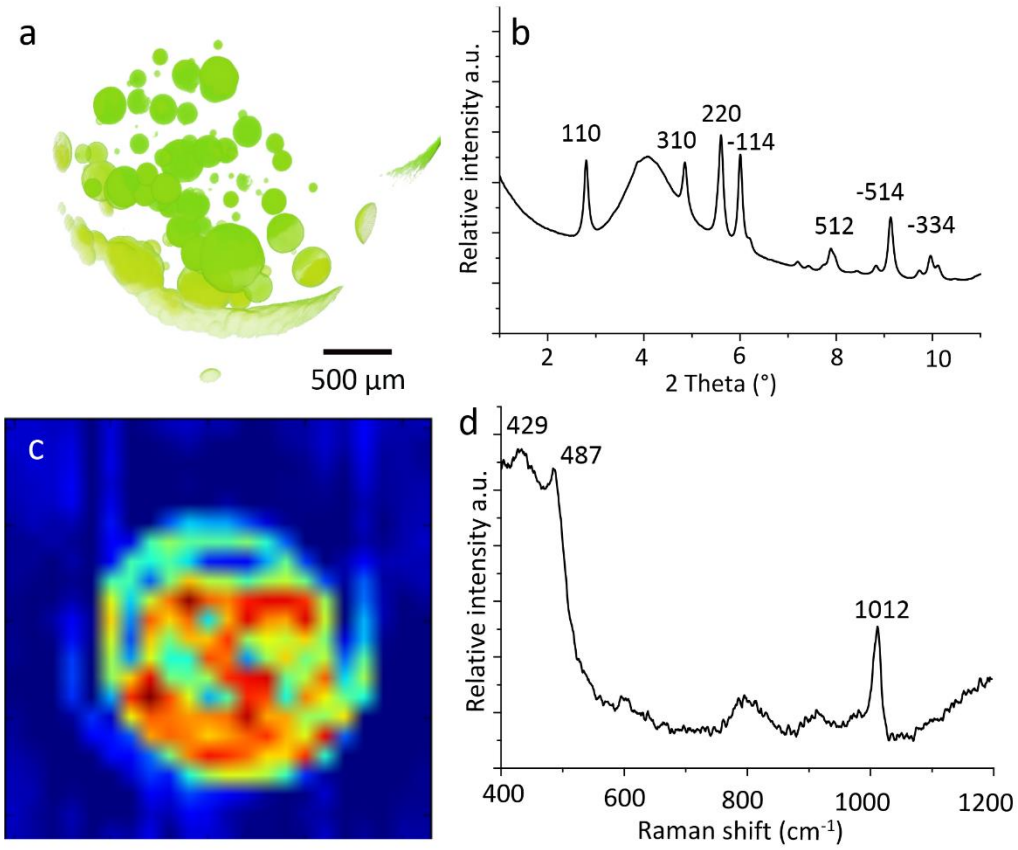

Figure 65. (a) 3D tomogram of bassanite crystals growing in a porous glass rod with 7 nm pore sizes at 250 mM after 18 h from solution injection. (b) Diffraction pattern of the crystals in the pores and (c) 2D spatial diffraction map of the crystals after plotting the peak 110 with a 100 µm beam. (d) Raman spectra of bassanite crystals in the rod after 3 weeks from 250 mM solutions injection.

In order to obtain more information about the stability of bassanite crystals in the pores, dry CPG rods were heated after crystallization at 200, 300 °C for 12 h and 400 and 700 °C for 4 h. The results were compared with a solid sample of bassanite heated at the same temperatures. As described in the introduction to this chapter, gypsum starts to lose structural water and converts into bassanite around 45 °C and bassanite into anhydrite ($CaSO_4$) at temperatures above 110 °C. [290, 323, 324] XRD analysis of the crystals in the CPG rods showed no evidence of bassanite transformation at temperatures up to 400 °C and anhydrite II was the sole product observed at 700 °C (Figure 66). In contrast, anhydrite II started to form when heating bassanite powder at 200 °C and it was the only phase present at higher temperatures.

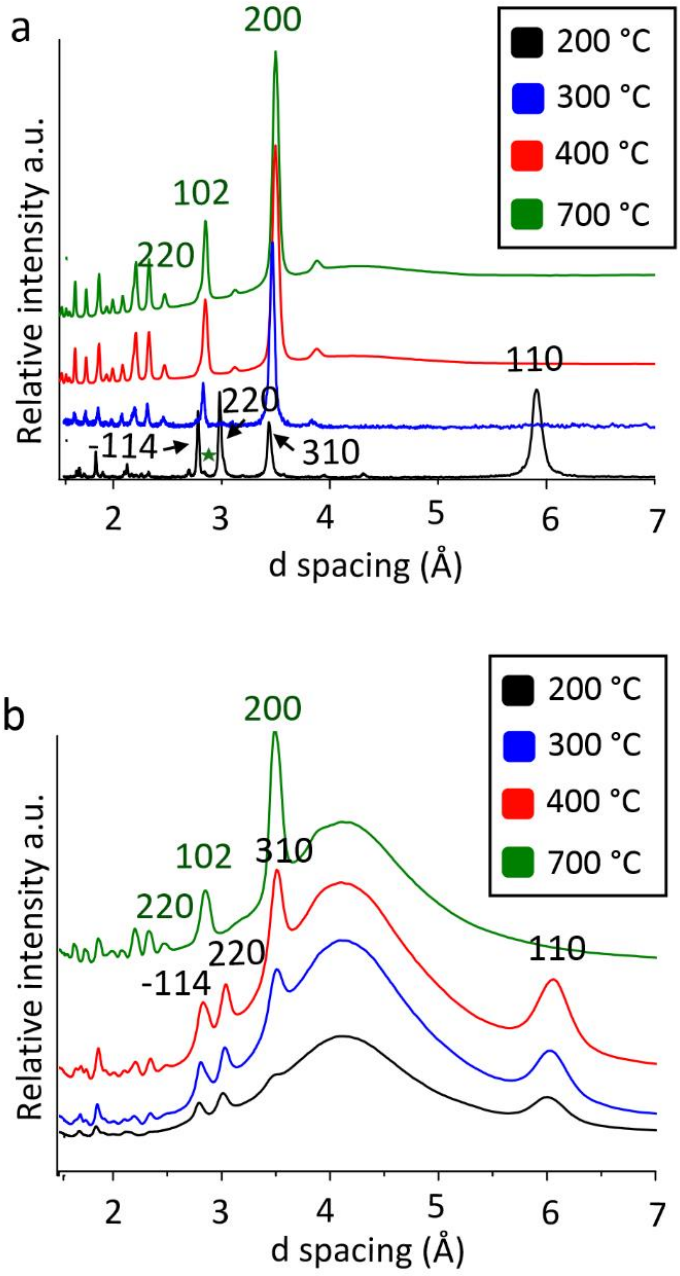

Figure 66. XRD diffraction patterns recorded at room temperature with a 0.4 mm beam of a bassanite powder (a) and bassanite within a CPG rod (b) at different temperatures. Anhydrite peaks are represented in green (and green stars) and bassanite ones in black. (a) Bassanite starts transforming into anhydrite in bulk at 200 °C as shown by the appearance of the (102) reflection (indicated with a green star) and anhydrite is the only phase observed in bulk at higher temperatures. (b) Bassanite is stable in CPGs up to 400 °C and completely transforms to anhydrite on heating at 700 °C. The intensity of the diffraction patterns in (b) is relative since the patterns were recorded at different positions along the rod.

In addition, as CPG samples containing bassanite were heated, a slight shift of the peaks of around 0.02 Å was observed (Figure 67). The shift could be due to slight loss of crystalline water from $CaSO_4 \cdot 0.5H_2O$ to $CaSO_4 \cdot xH_2O$ where x <0.5.

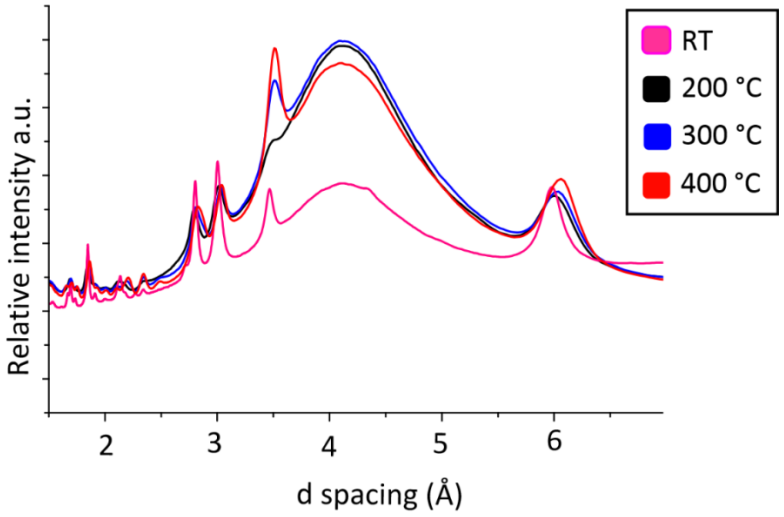

Figure 67. XRD diffraction patterns recorded at room temperature with a 0.4 mm beam after heating a CPG rod containing bassanite at different temperatures. A shift of around 0.02 Å is observed when increasing temperature.

Ex situ characterization of bassanite crystals within CPG rods

Further information about the crystals in the 7 nm pores was obtained using electron microscopy. The rods were first removed from the reservoirs, immersed in ethanol for 30 min and then dried at room temperature. Finally the rods were fragmented and imaged using SEM after 5 h reaction time with 3 M reagents. Under SEM, calcium sulfate crystals showed darker contrast than the glass as observed in Figure 68 and confirmed by EDAX (energy dispersive X-ray analysis) mapping (Figure 68). Importantly, electron microscopy allowed us to confirm the integrity of the porous glass matrix on the mesoscale. Thin sections of the CPG rods were prepared by FIB milling (FIB was carried out by Dr. Alex Kulak) and they were imaged by TEM in order to characterize the crystals on the nanoscale(Figure 69). Bright field imaging confirmed that the porous network was intact after crystallization and no sign of breakage was found (Figure 70a). The crystallites observed by TEM were

confirmed to be bassanite by selected area electron diffraction (SAED) (Figure 70c). Scanning TEM (STEM) and EDAX mapping at high resolution verified that the crystals grew through the interconnected pores (Figure 70d).

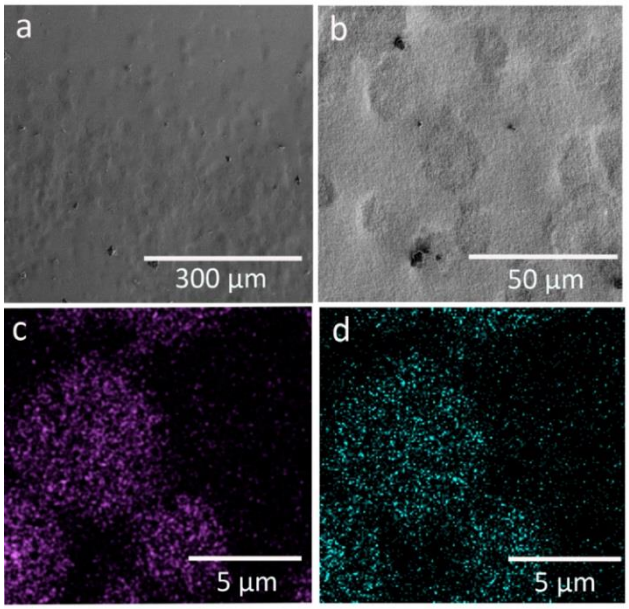

Figure 68. (a,b) SEM images of a fractured porous glass rod after 7h crystallization with 3M reagents. Calcium sulfate crystals present higher contrast under SEM. Corresponding EDX mapping showed these areas to be rich in Ca (c) and S (d).

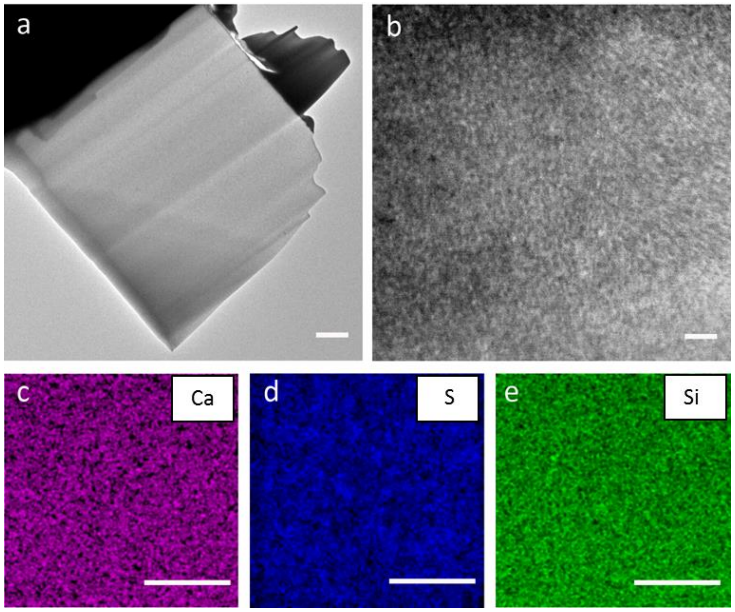

Figure 69. (a,b) TEM images of a cross-section of a CPG rod containing calcium sulfate crystals as confirmed by STEM elemental mapping (c,d,e).

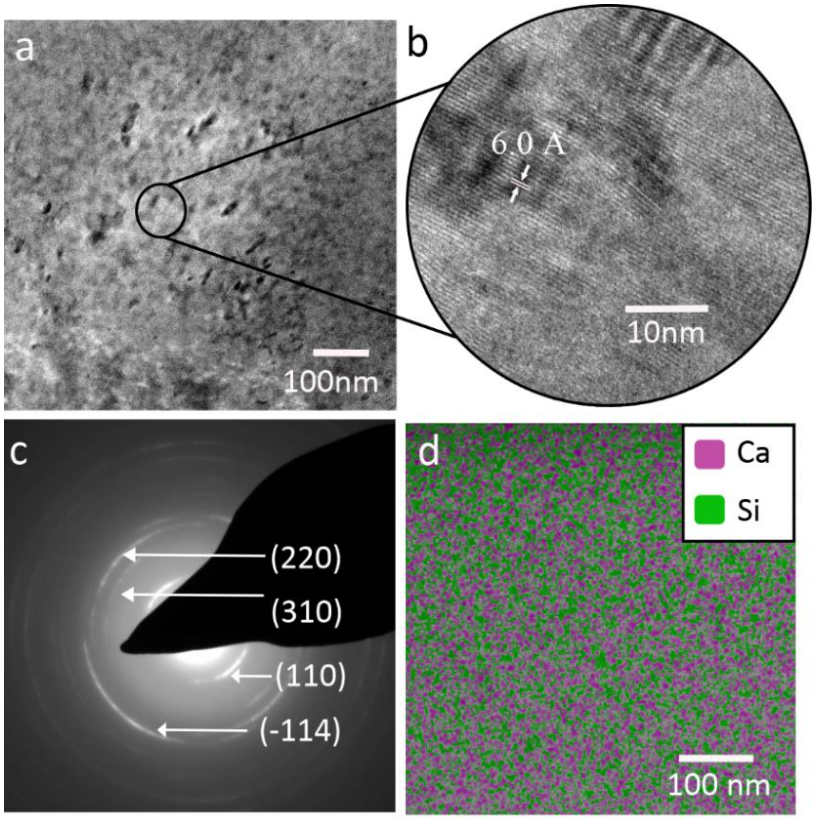

Figure 70. TEM images of calcium sulfate crystals within 7 nm pores of a thin section of dry CPG after 5 h reaction using 3 M reagents (a). The crystal lattice is observed at high magnifications where 6 Å corresponds to the (110) plane (b) of bassanite. The presence of bassanite in the pores was confirmed by electron diffraction (c). (d) EDAX mapping at high resolution where the porous structure is shown in green and the crystals following the pores in pink.

Bassanite Transformation to Gypsum

ACS was observed to be a precursor to bassanite crystallization in the pores at high concentrations, but is gypsum the product of bassanite crystals? Previous studies universally reported a rapid transformation from bassanite to gypsum in aqueous solution under ambient conditions.[118] However, we observed an extraordinary stabilization of bassanite in the pores, greater than any observed before with other systems. Indeed, gypsum formation in the pores was not detected in the whole period of study (3 weeks).

Interestingly, transformation to gypsum can be immediately induced by simply breaking the rod. When the porous structure is broken, the solution in the pores and bassanite crystals adjacent to the fracture are not confined

anymore and large gypsum clusters form, emerging from the surfaces of the rod (Figure 71 a,b,c). The phases were characterized by Raman spectroscopy and by DCT (Figure 71 e,f). Both techniques showed that crystals inside the rods were bassanite, but the ones at the rod fracture surface were gypsum.

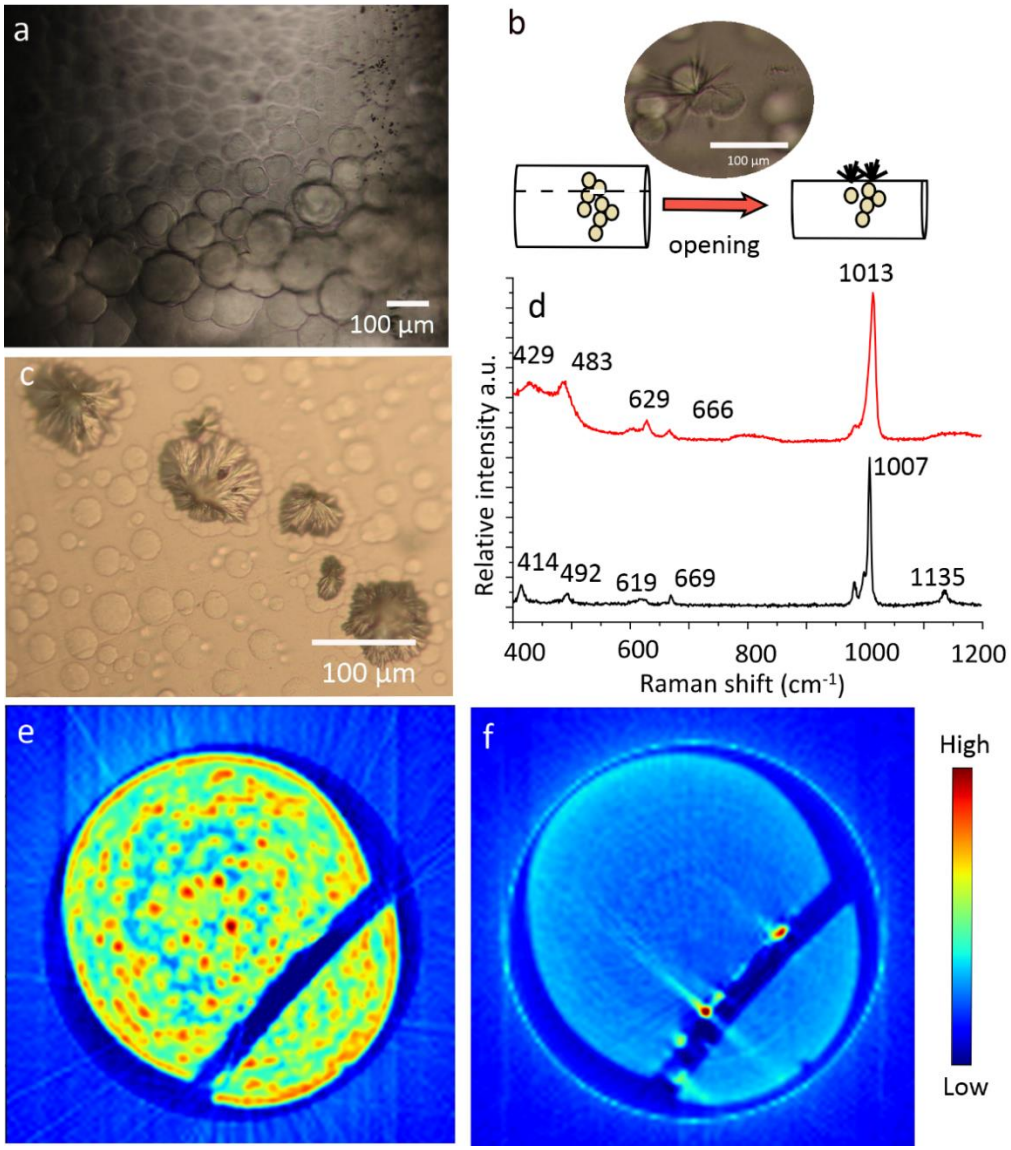

Figure 71. Micrographs of bassanite crystals precipitated from 3 M reagents inside a CPG rod after 5 h (a) and gypsum clusters growing on the surfaces immediately after rod breakage (b,c). The crystals were characterized by Raman, showing broad peaks at 429 cm^{-1} and 1013 cm^{-1} for bassanite (in red) and peaks at 414 cm^{-1}, 1007 cm^{-1} and 1135 cm^{-1} for gypsum (in black) and by DCT (e,f) where bassanite crystals are present all throughout the sample (e) and gypsum crystals only at the crack area (f). Note that the peaks selected for the diffraction maps are (110) for bassanite and (020) for gypsum.

The transformation from gypsum to bassanite was also induced by experimental conditions that facilitated crystallization on the surfaces of the rod, such as a humid environment. A humid environment was created prior to or after crystallization by either placing the rods in a desiccator with water vessels or by wrapping them with a Kapton film. Kapton was selected for synchrotron experiments since this material is gas-permeable and it has low X-ray attenuation and scattering.

When the CPG rods are placed in a humid environment prior crystallization, water condenses on the surfaces of the rods and evaporation of the condensed water is prevented. Under these conditions, large gypsum crystals nucleate on the surfaces of the rod and grow towards the interior, eventually leading to cracking of the rod. The rods completely break within 4 h as shown by µ-CT (Figure 72 a,b) and large gypsum crystals are found growing from the surfaces and along the cracks (Figure 72 c,d).

A CPG rod can also be placed in a humid environment after bassanite crystallization in the pores. In this case, large gypsum crystals also nucleate on the surfaces of the rod, consuming the ions from the pores and eventually dissolving the bassanite crystals (Figure 73). In order to avoid breakage of the rod, the surfaces were wiped every 15 min and the rod was placed again in a desiccator with water vessels. Bassanite crystals completely dissolved after 3 h.

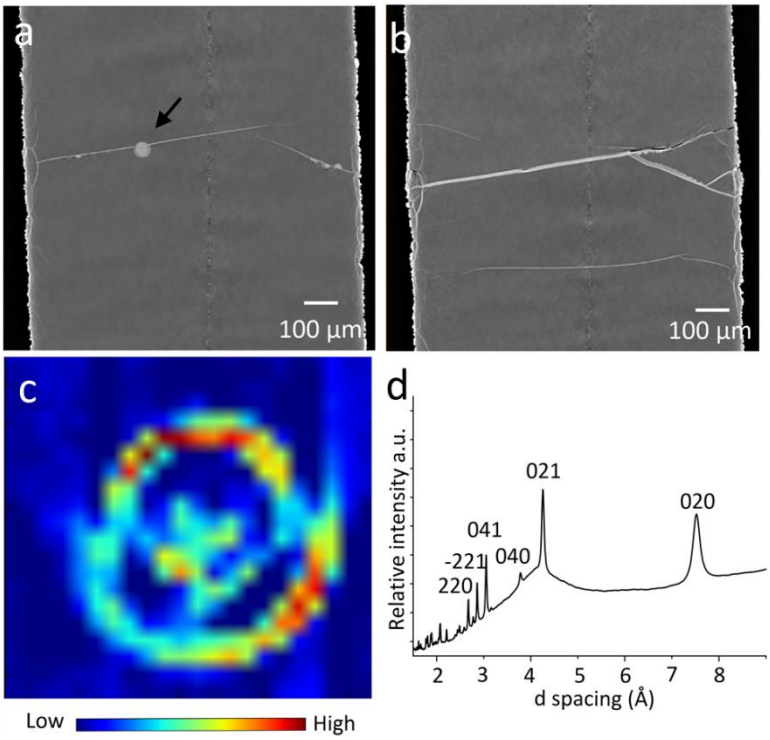

Figure 72. 2D tomography slices of calcium sulfate crystals growing within a 1 mm CPG rod inserted into a Kapton film (a) 2 h 30 min where a few cracks and a bassanite crystal is indicated with an arrow are observed and (b) 3 h 30 min after reagent injection, where only large cracks are observed and no internal crystals. (e) Diffraction tomography recorded with a 100 x 100 µm^2 beam after 5 h shows that the crystals adjacent to the cracks are gypsum (d), where the (202) reflection of gypsum was used to generate the image.

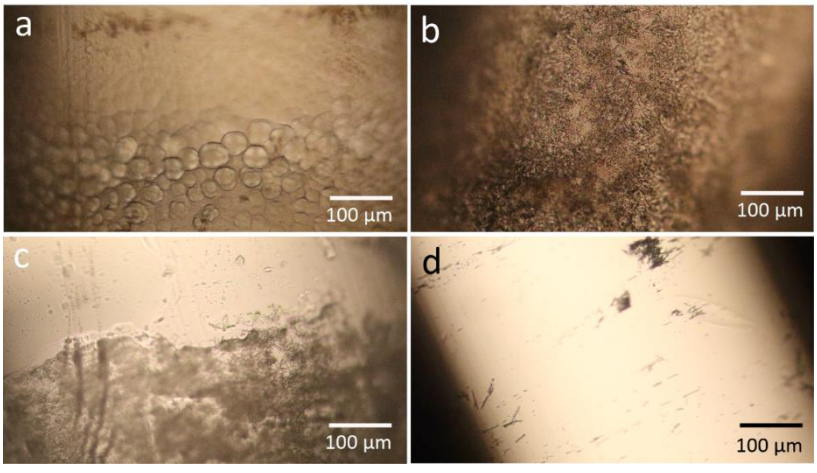

Figure 73. Optical micrographs of a CPG rod after (a) bassanite crystallization and (b,c) placing the rod in humid conditions for 3 h. Gypsum crystals form on the surfaces of the rod and bassanite crystals dissolve, as observed after wiping the gypsum crystals from the surface (d).

The effects of the surface chemistry

The crystallization of calcium sulfate was also studied in functionalized CPG rods. The surfaces of the pores were coated with a carboxyl-terminated silane group following the general procedure described in Chapter 2. The crystals inside 7 nm functionalized CPG rods were analyzed by synchrotron μ-CT, DCT and Raman over a period of 3 weeks. Small differences (around 15 min) were detected in the induction time from 3 M reagents as compared with unfunctionalized CPG rods. Nevertheless, while gypsum was never seen to nucleate in the unfunctionalized pores within 3 weeks, after 1 h 15 min, both gypsum and bassanite were present in the carboxyl-terminated CPG rods. Both phases could be differentiated by μ-CT due to their different contrast. The higher density of bassanite with respect to gypsum implies a greater X-ray absorption and therefore a higher contrast than gypsum with respect to the glass framework (Figure 74a). The two calcium sulfate phases also presented distinct morphologies, comprising spheroidal bassanite crystals and dendritic gypsum crystals. The assignment of both crystal phases was confirmed by DCT (Figure 74 b-d).

At lower concentrations (250 mM) the crystallization of calcium sulfate was significantly faster in the functionalized CPG rods. Crystals were observed in the pores after 5 h, in contrast to 7 h in the non-coated rods. Bassanite crystals formed first and gypsum crystals started to be detected after 24 h by Raman (Figure 75).

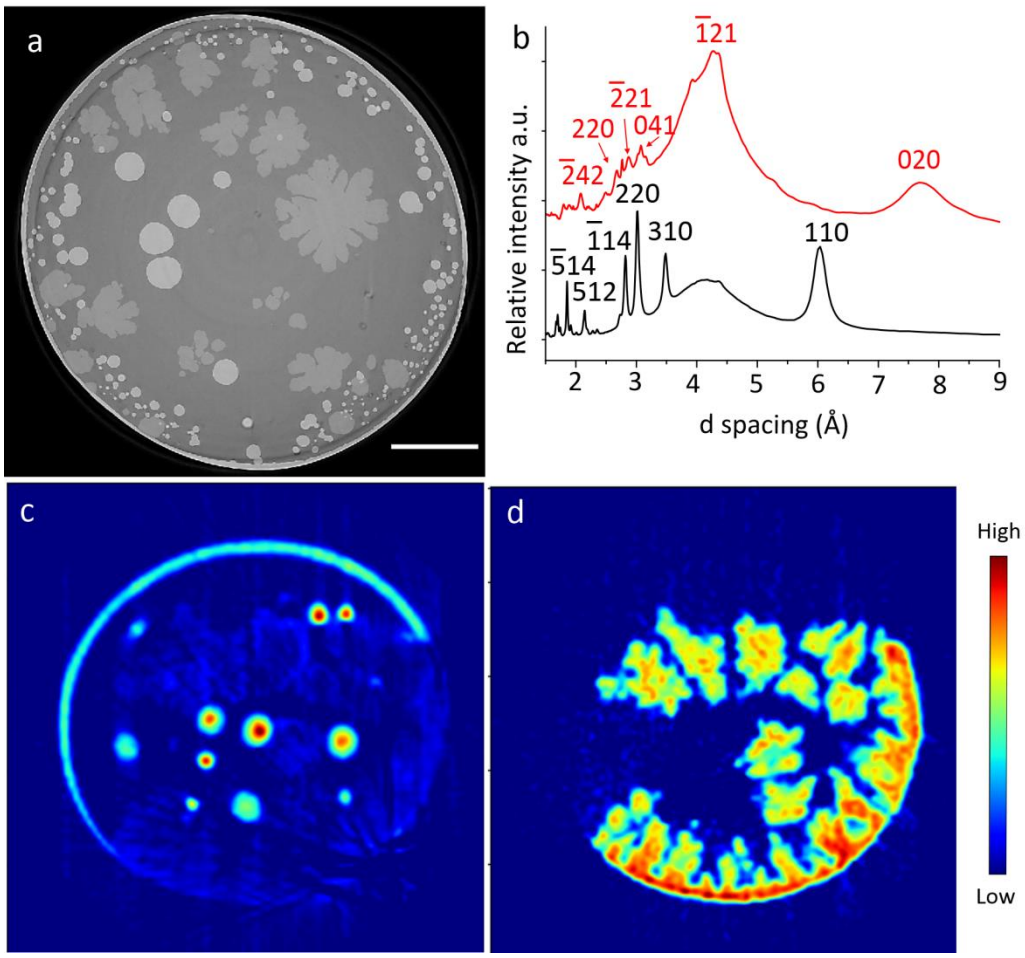

Figure 74. (a) 2D tomogram of calcium sulfate crystals in a carboxyl-terminated CPG rod 2h 30 min after of 3 M reagents injection. Circular light crystals are bassanite and dendritic darker crystals are gypsum. (b) The presence of both phases was confirmed by diffraction where the red spectrum corresponds to gypsum and the black to basanite. The assignment of the phases was made by DCT when plotting the (110) peak from bassanite (c) and the (020) peak from gypsum (d). Note that different samples were used for the μ-CT and DCT measurements. The scale bar is 500 μm.

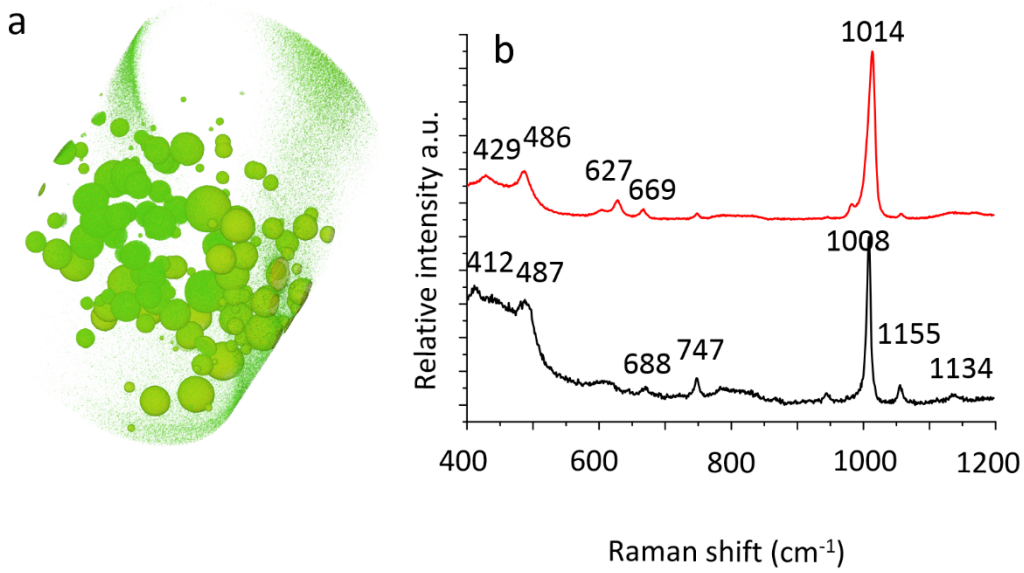

Figure 75. (a) Calcium sulfate crystals in a carboxyl coated porous rod after 15 h at 250 mM. (b) Raman spectra showing that the crystals were bassanite (red) after 8h and gypsum (black) after 1 day.

How does gypsum nucleate?

The evolution of the calcium sulfate crystals in the pores was also studied over time (Figure 76). Two different mechanisms of gypsum formation were observed in the pores. Direct nucleation of gypsum was often observed in the glass matrix, even when bassanite crystals were present in close proximity (Figure 76 e-h). Nevertheless, gypsum crystals often formed very close to existing bassanite crystals, which seemed to act as heterogeneous nucleation sites for gypsum crystallization (Figure 76 i-l). Interestingly, bassanite crystals present in the pores did not dissolve or convert to gypsum, but remained stable throughout the period of study. Large gypsum crystals blocked the rod after 4 h and no more changes were observed by either µ-CT or DCT (Figure 77).

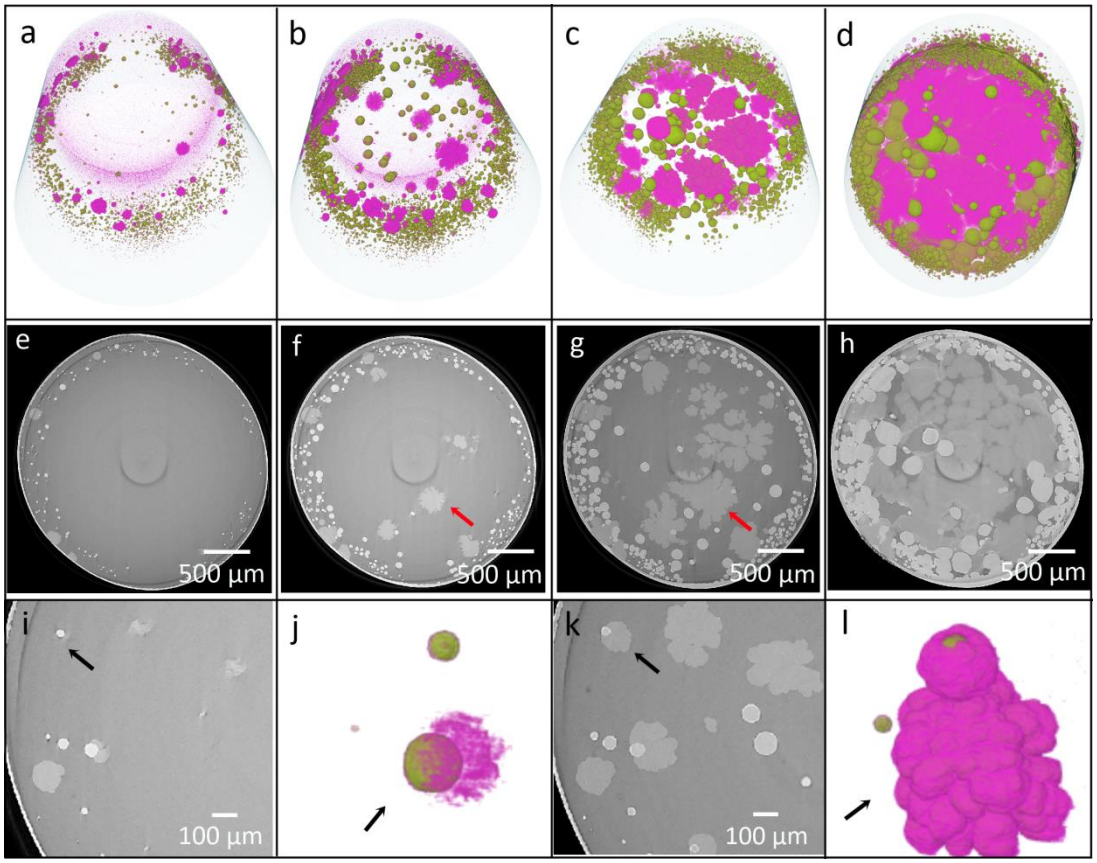

Figure 76. 3D images (a,b,c,d) and 2D tomograms (e,f,g,h) of calcium sulfate crystals in a carboxyl-coated CPG rod after 1h 45 min (a,e), 2 h (b,f), 2 h 30 (c,g) and 4 h (d,h). In the 3D images, bassanite is represented in green while gypsum is shown in pink. After 1 h 45 min from 3M reagent injection, both bassanite and gypsum are already found in the pores (a,e). Nucleation and growth of both phases are observed with time until the rod gets blocked after 4 h (d,h). Direct nucleation of gypsum was frequently observed (red arrows), together with gypsum growing from or very close to bassanite crystals (black arrow) as shown by high magnification 2D (i,k) and 3D tomograms (j,l) after 2 h (i,j) and 2 h 30 (k, l).The pink specks found on the background of the 3D tomograms (a,b) are due to noise.

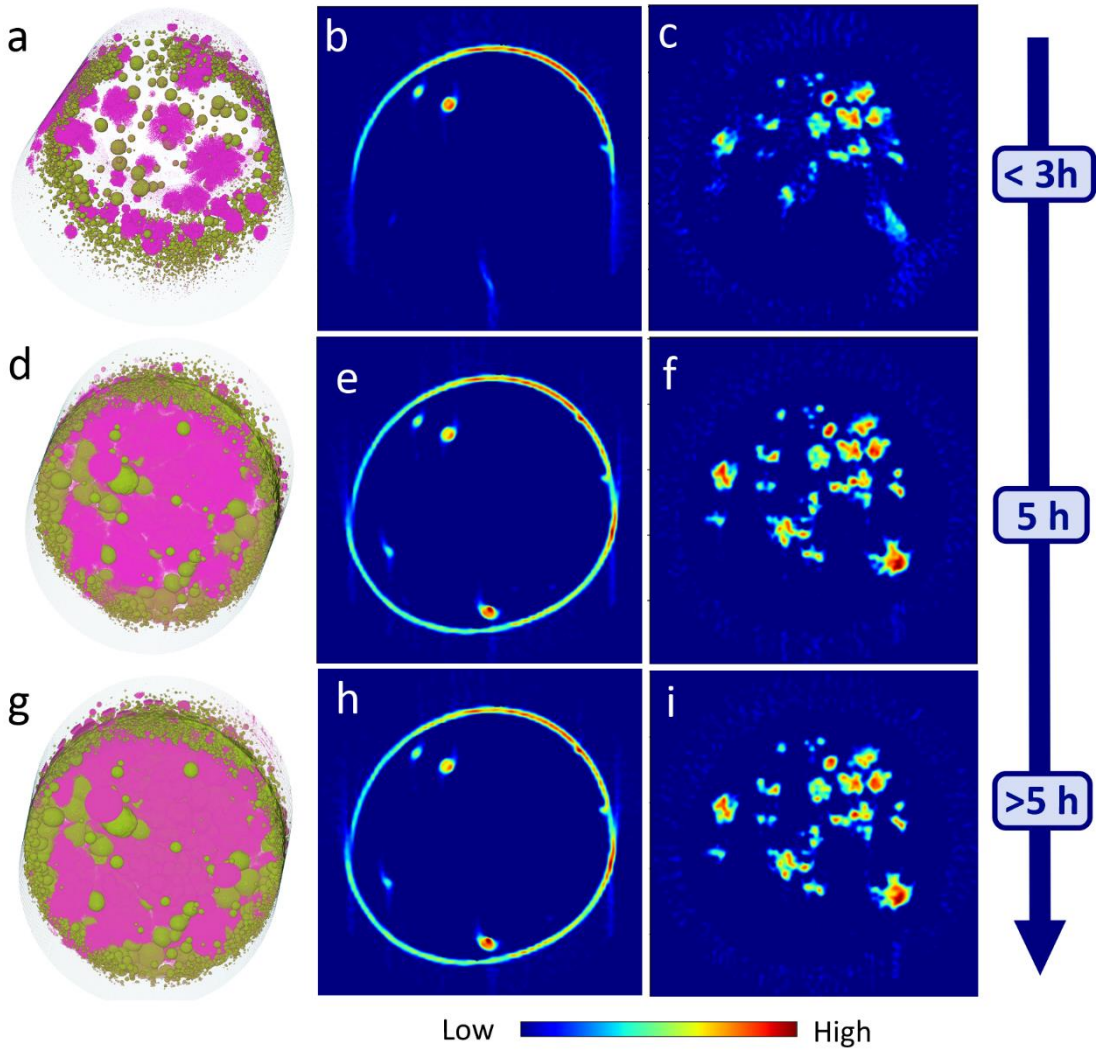

Figure 77. 3D images (a,d,g) and 2D diffraction maps (b,c,e,f,h,i) of calcium sulfate crystallization from 3M reagents in functionalized CPG rods over time. In the 3D images bassanite crystals are shown in green and gypsum in pink. DCT shows the presence of bassanite (b,e,h) and gypsum (c,f,i) over the whole period of study. After 4 h from reagent injection rods get blocked and no more changes were observed by either µ-CT or DCT.

Further insight into the transformation of bassanite into gypsum was achieved by exchanging the reagent solutions for water 2 h after solution injection. Phase conversion was followed over time by µ-CT, where direct solid-state transformation from bassanite to gypsum was observed after 5-8 h (Figure 79). Gypsum crystals maintained the same morphology as the original spherical bassanite crystals rather than acquiring the dendritic morphologies that had been previously observed. Bassanite crystals were never seen to

dissolve, but rather they slowly hydrated into gypsum. 3D images of the transformation over time are shown in Figure 79.

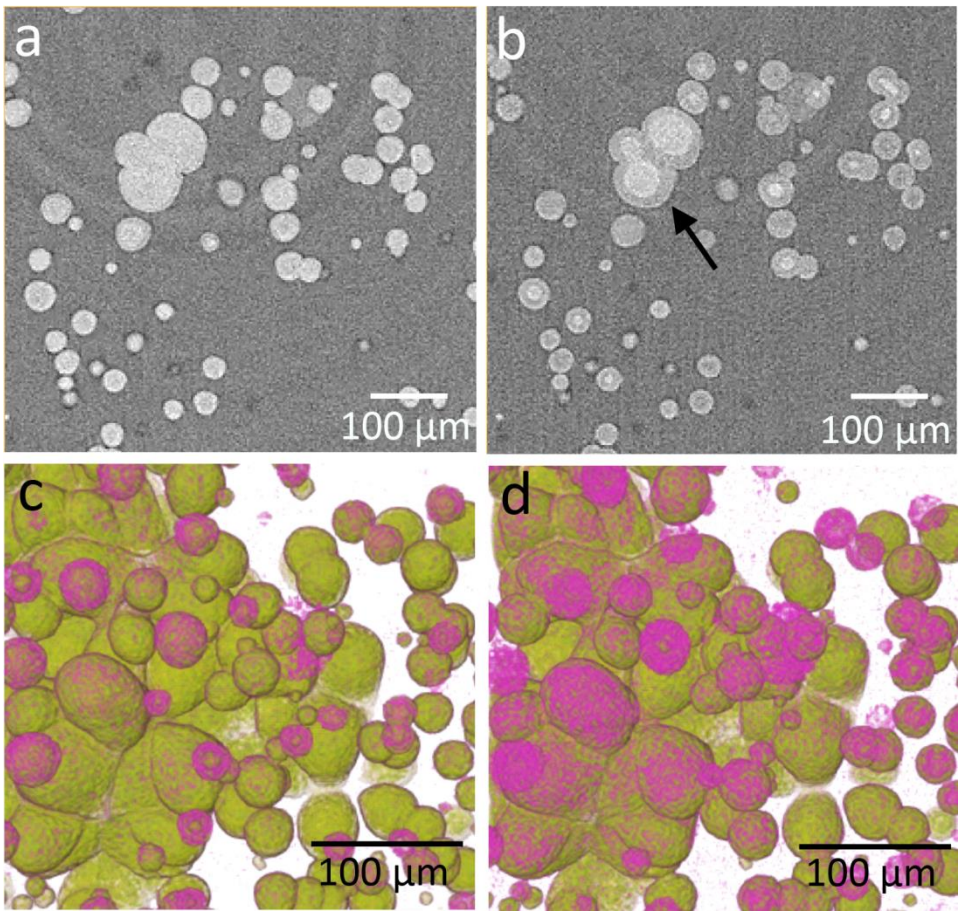

Figure 78. (a,b) 2D Tomograms and (c,d) 3D images of bassanite to gypsum transformation over time 5 h (a,c) and 8 h (b,d) after the 3M reagents are replaced by H_2O. The bassanite crystals can be seen to be transforming to gypsum with retention of morphology, as shown by the dark halo surrounding a bright core (arrowed). This is also seen in (d) where bassanite is represented with green and gypsum with pink.

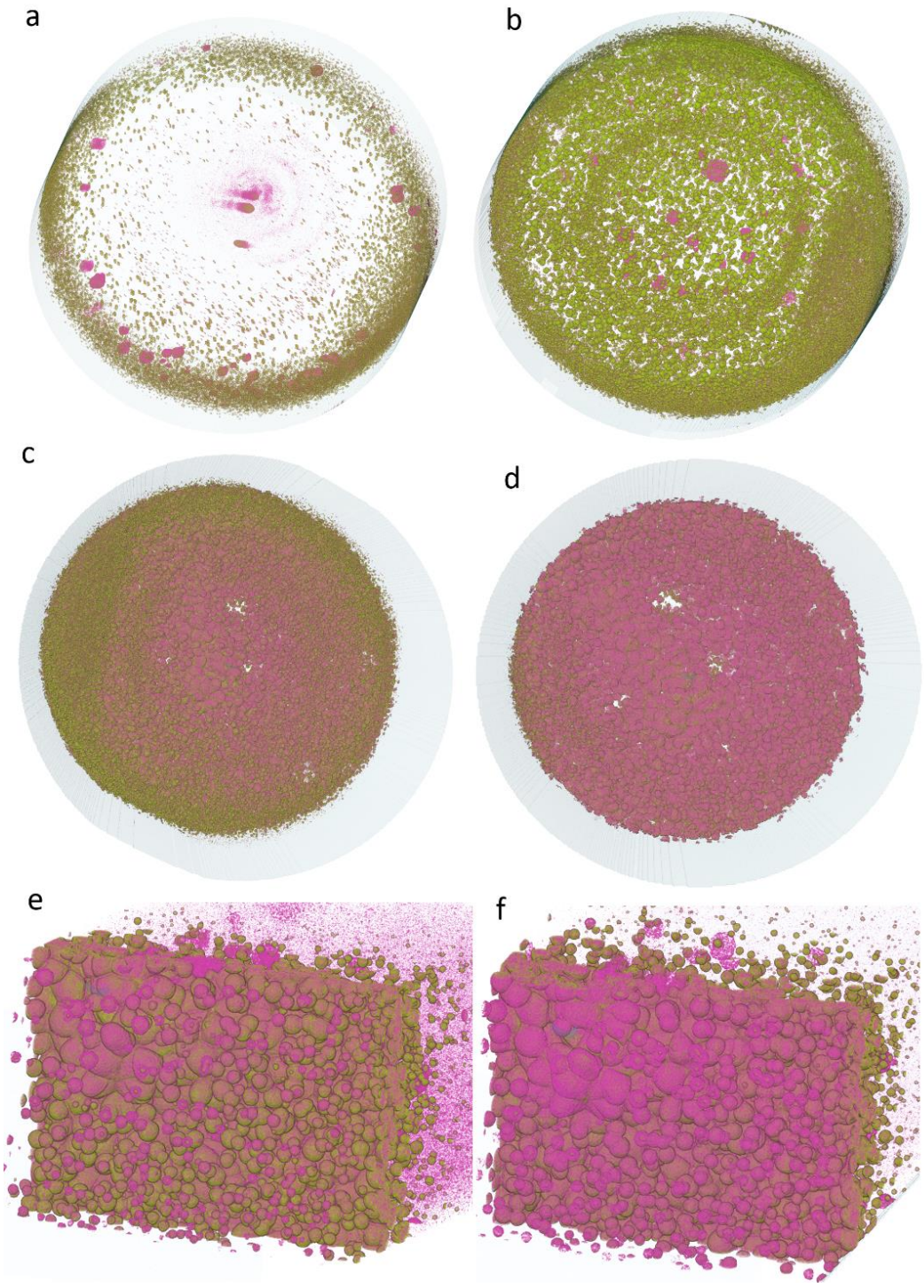

Figure 79. 3D images of calcium sulfate crystals forming in functionalized CPG rods after (a) 1 h 15 min and (b) 1 h 30 min from reagent injection. 3D images of the crystals when the reagents were replaced by H_2O after 5 h at low (c) and high (e) magnification and after 8 h at low (d) and high magnification (f).

4.3.1 Calcium carbonate in CPG rods

4.3.1.1 Crystallization in bulk solution

$CaCO_3$ crystallization was first investigated in bulk solution by counter diffusion of CO_3^{2-} and Ca^{2+} ions through 1 mm capillaries. 1 M and 250 mM solutions were tested. The first phase to precipitate in the capillary at both concentrations was amorphous calcium carbonate (ACC), followed by calcite and vaterite after <5 min. For both conditions, ACC completely dissolved within 2 h (Figure 80).

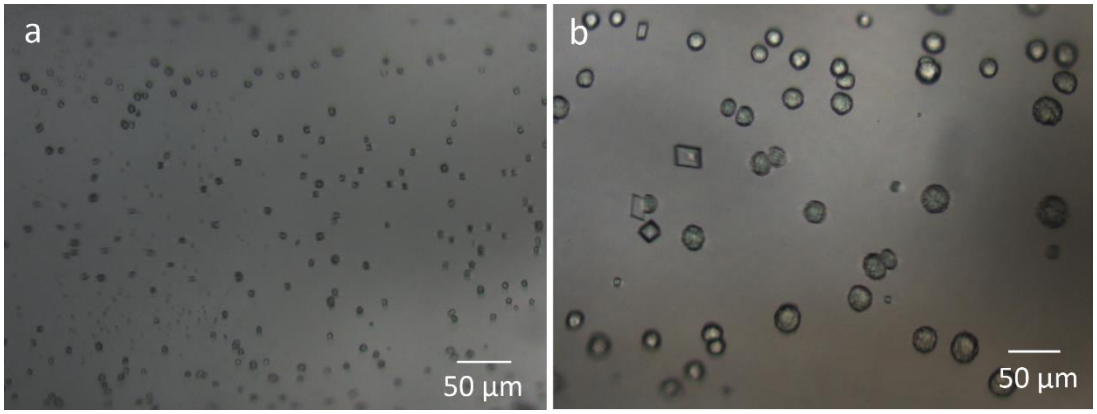

Figure 80. $CaCO_3$ crystallization achieved by counter diffusion of CO_3^{2-} and Ca^{2+} ions in a 1 mm glass capillary 2 h after injecting (a) 1 M and (b) 250 mM reagents.

4.3.1.2 Crystallization in CPG beads

The crystallization of $CaCO_3$ in CPG beads presented the same problems previously described for calcium sulfate: the low solubility of these inorganic solids makes it difficult to fill the nanopores. This promoted $CaCO_3$ crystallization on the surfaces or in between CPG particles which made it impossible to characterize the crystals formed within the pores. Calcite was the only phase detected when using CPG beads (Figure 81).

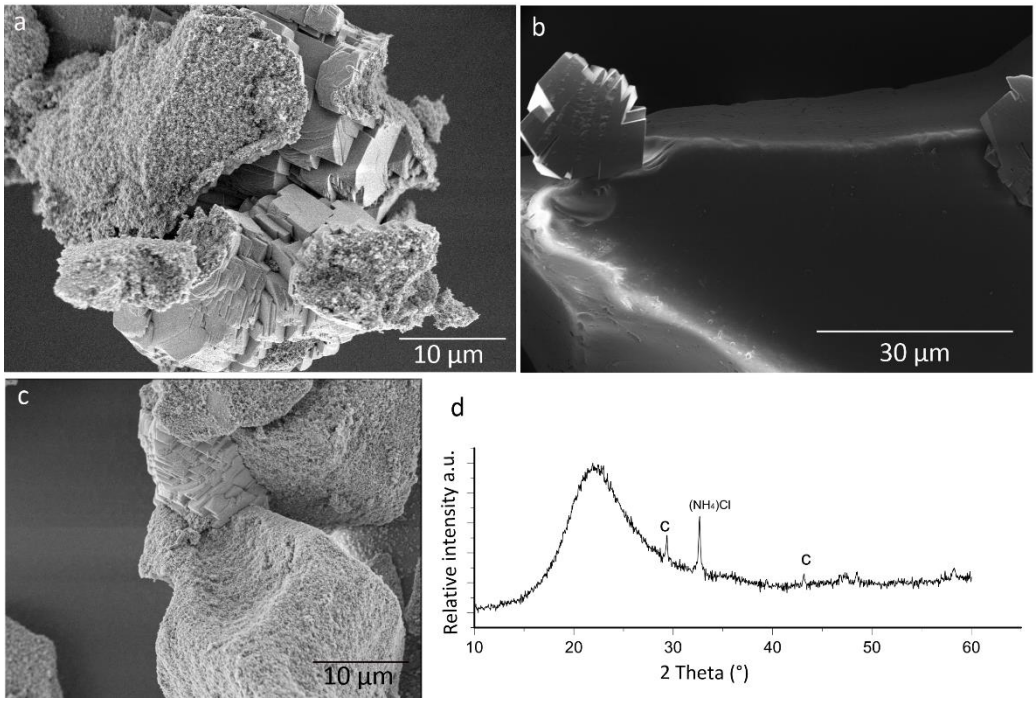

Figure 81. (a-c) SEM images of $CaCO_3$ crystals within CPG beads and (d) diffraction pattern showing the crystals to be calcite (c) and some precipitated salt.

4.3.1.3 Crystallization in CPG rods

The crystallization of $CaCO_3$ in 1 mm and 2.8 mm diameter CPG rods with 7 nm pore diameters was achieved by counter diffusion of Ca^{2+} and CO_3^{2-} ions at two different initial concentrations, 1 M and 250 mM. The ends of wet CPG rods were inserted between two tubes containing aqueous $CaCl_2$ and Na_2CO_3 solution reservoirs. The set-up was the same as the one previously described for calcium sulfate (Figure 58). The crystals in the nanopores were imaged *in situ* by optical microscopy and computed tomography (CT). Additional characterization to determine the polymorphs of the crystals forming in the pores was performed over time by *in situ* diffraction tomography (DCT) and solid-state NMR and *ex situ* Raman spectroscopy.

Imaging of $CaCO_3$ crystallization in CPG rods over time

Precipitation within 1 mm diameter CPG rods started with the formation of a 2 mm thick, cloudy white band at the center of the rod 10 min after injection of 1 M reagents (Figure 82a). XRD of this band showed two broad humps around 2 Å and 2.9 Å (Figure 82d, in black). These reflections were identical to those

reported in the literature by Faatz *et al.* and Rodriguez-Blanco *et al*., which confirmed that the material in the pores was amorphous calcium carbonate (ACC).[325, 326] Over time, the band divided into two, thinner (~0.5 mm) bands which seemed to “move” across the rod (Figure 82b). The “movement” of the bands within CPG rods was due to Ostwald ripening effects as will be explained next. Diffraction peaks could be observed from the upper band after 1 h when ACC was still present (Figure 82d, in red). The lower band dissolved within 4 h and the upper band became more defined (Figure 82c).

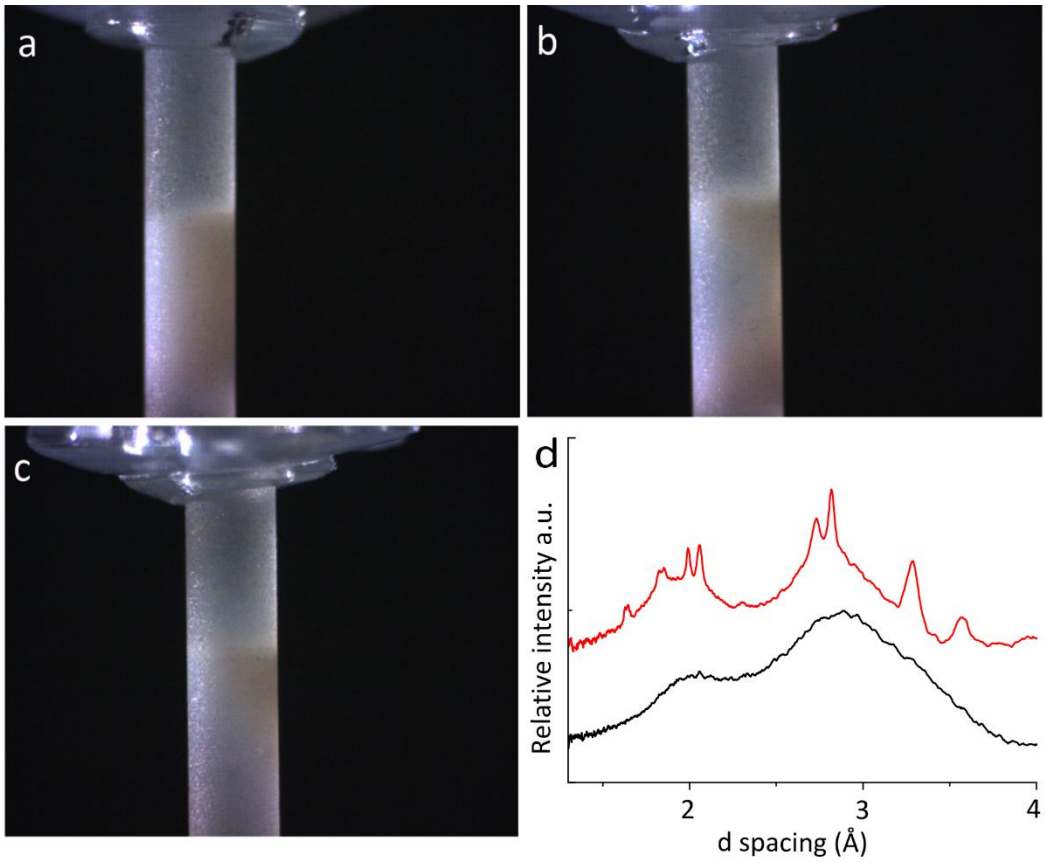

Figure 82. Optical images of $CaCO_3$ precipitation in 1 mm CPG rods (a) 10 min (b) 15 min and (c) 4h after injection of 1 M solutions. (d) Diffraction patterns of the rod after background subtraction (from a H_2O filled rod), after 10 min (in black) and 1 h (in red).

As previously discussed, evaporation effects cannot be disregarded when using 1 mm CPG rods. Indeed crystals preferentially nucleated at the

perimeter of the rod and crystals inside the rod were rarely observed (Figure 83). Moreover, the surfaces of the rod often cracked.

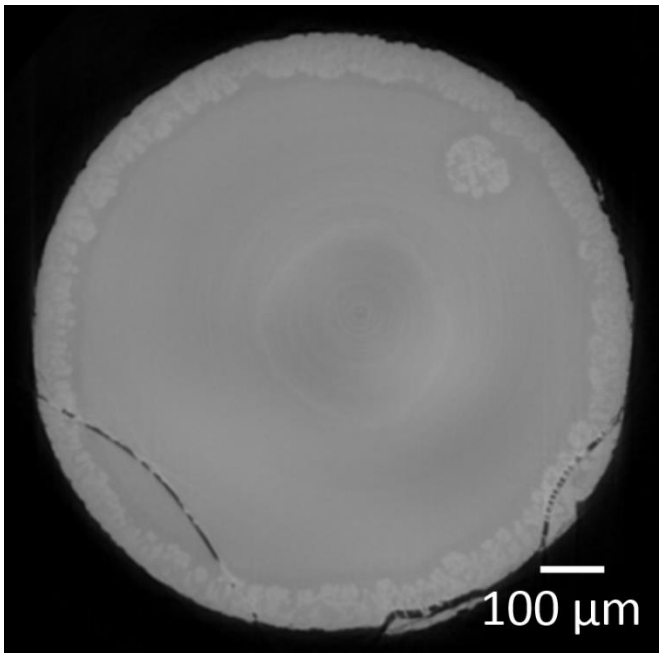

Figure 83. 2D tomogram of $CaCO_3$ crystals within 1 mm CPG rod 2 h after injection of 1M solutions. Crystals mainly nucleate at the surfaces of the rod.

Reduced evaporation through the open pores could be achieved by coating the surfaces of the rods with paraffin wax. However, obtaining a very thin, uniform layer of wax around the rod was challenging and very intense diffraction peaks from the wax were always observed in the diffraction patterns. $CaCO_3$ crystallization in the pores was therefore analyzed using 2.8 mm diameter rods and 1 mm diameter rods wrapped with a Kapton film. In both cases, crystals nucleated within the rod, although different nucleation times were observed. A schematic of the three scenarios tested is shown in Figure 84.

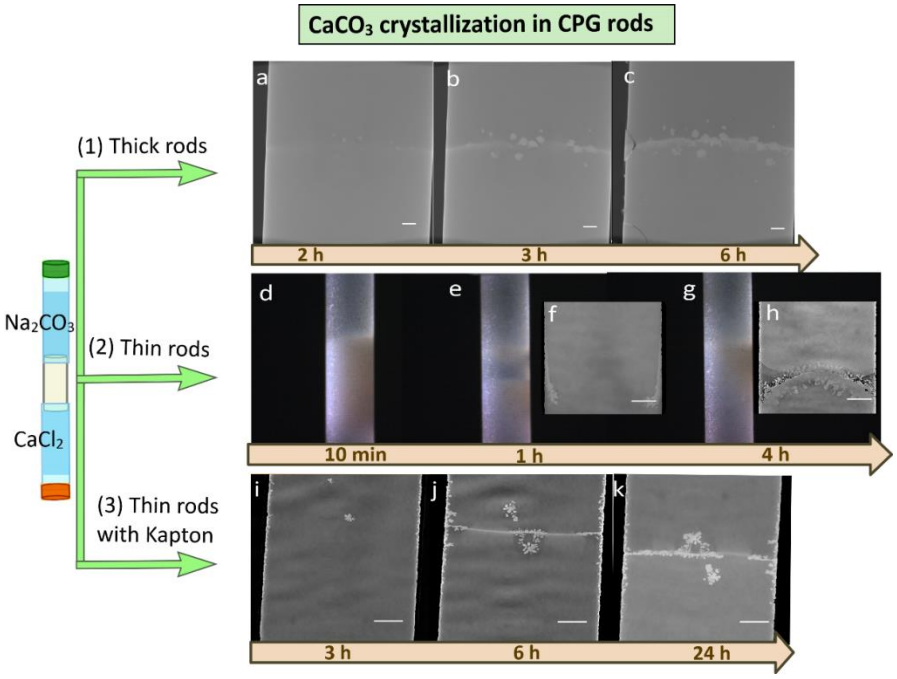

Figure 84. 1M $CaCO_3$ crystallization over time imaged optically and by µ-CT. (1) Crystallization in 1 mm rods where a thick ACC band is observed after 10 min and crystals form at the surfaces after 1 h. (2) Crystallization in 2.8 mm rods, where crystals in the rod are observed after 2 h together with a faint ACC band. (3) Crystallization in 1 mm rods wrapped with a Kapton film. ACC was not observed and crystals nucleated in the rod after 3 h. Scale bars = 200 µm. The reagent concentrations were 1 M in all 3 conditions.

$CaCO_3$ precipitation in 2.8 mm CPG rods at early stages (1-3 h) was followed over time with high resolution µ-CT (Figure 85). ACC precipitation was detected 1 h after injection of 1 M reagents. After 1 h 45 min, the band divided into two as previously observed in the thin rods (Figure 85 e). 15 min later, a few crystals were observed growing at the lower end of the upper band and the lower band started to dissolve (Figure 85 f). Further crystallization took place mainly at the upper band. The splitting of the bands within CPG rods can be explained by Ostwald ripening effects. The higher amount of ACC precipitating in the thin rods (due to evaporation effects) made it possible to observe the development of the amorphous phase by eye. In both 1 and 2.8 mm rods, the dense ACC band dissolved at the center, and then crystals started forming. The ACC at the lower band “moved” towards the crystals by a dissolution-reprecipitation process. As the crystals grow, ACC particles in their vicinity were consumed and the ACC further away from the band

dissolves to provide more ions to the growing crystals. This explains why the precipitation band becomes thinner when crystals grow, consuming the ACC.

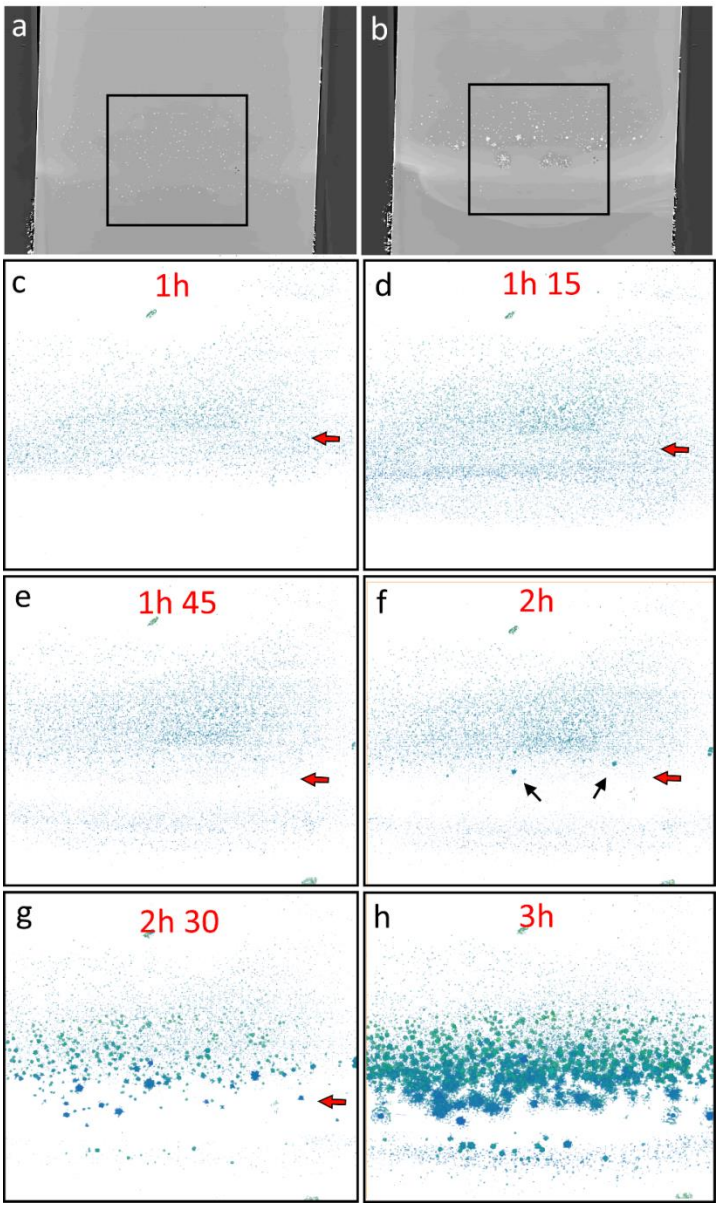

Figure 85. 2D (a,b) and 3D (c-h) tomograms of $CaCO_3$ precipitation in 2.8 mm CPG rods monitored over time. A precipitation band forms in the center of the rod 1 h after injection of 1 M reagents (a) and large crystals are observed by the band 3 h 30 after injection (b). The evolution over time was studied by high resolution µ-CT. The initial band grows until 1 h 15 (a,b) where red arrows indicate the center of the band. The precipitation front partially dissolves and the band splits into two (e). Crystals nucleate at the lower end of the upper band (indicated with black arrows) and the lower band slowly dissolves (f,g). Further nucleation and growth is mainly observed at the upper band after 3 h (h).

When the thin rods were wrapped with a Kapton film, the initial ACC band was not formed. Crystallization was observed 3 h after injection of 1 M reagents, 1 h later than within 2.8 mm rods. Although ACC was not observed at early stages, it was observed in the tomograms after 6 h as shown by µ-CT (Figure 86). Areas with a low amount of ACC presented lower contrast with respect to the glass framework than areas rich in ACC. The slower crystallization of $CaCO_3$ and the lack of ACC at early stages can be rationalized by the formation of a humid environment around the rod. As observed in 1 mm and 2.8 mm rods, the crystals usually grow at the expense of the ACC band by a dissolution-reprecipitation mechanism. Under humid conditions, the precipitation of ACC could be inhibited, therefore retarding $CaCO_3$ crystallization. An interesting observation was the presence of ACC in the pores for long periods of time (more than 21 h). In the previous study, the amorphous phase of calcium sulfate precipitated in CPG rods, dissolved when the crystals formed. Here, ACC remained stable and dissolution only happened near growing $CaCO_3$ crystals (Figure 86).

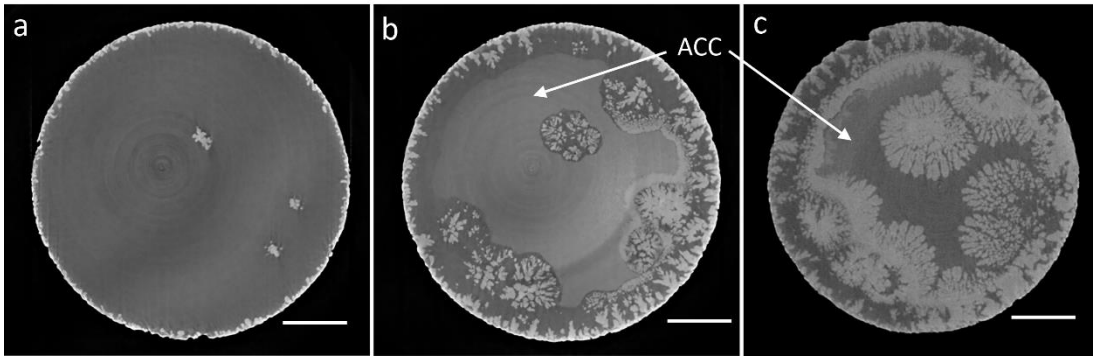

Figure 86. 2D tomograms of $CaCO_3$ precipitation in a 1 mm CPG rod wrapped with a Kapton film (a) 3 h, (b) 6 h and (c) 21 h after injection of 1M reagents.

$CaCO_3$ crystallization in 2.8 mm rods was also studied at low concentrations (250 mM), where similar results were obtained as compared with 1 M concentrations. After 3 h, crystals were observed growing from a very faint ACC band (Figure 87). Moreover, for both conditions, 1 M and 250 mM, three different regions could be differentiated in the CPG rods depending on their relative position to the reservoir. The first region of crystal formation is in the

center of the rod. Large dendritic crystals grow at the expense of the ACC at the center of the band. Smaller crystals also grow closer to the calcium and the carbonate reservoirs. The ratio of Ca^{2+}/CO_3^{2-} in these regions will not be equimolar and this caused changes in polymorphism along the rod (discussed below). Figure 87 and Figure 88 show the crystallization of $CaCO_3$ in 2.8 mm CPG rods over time at 250 mM and 1 M concentrations.

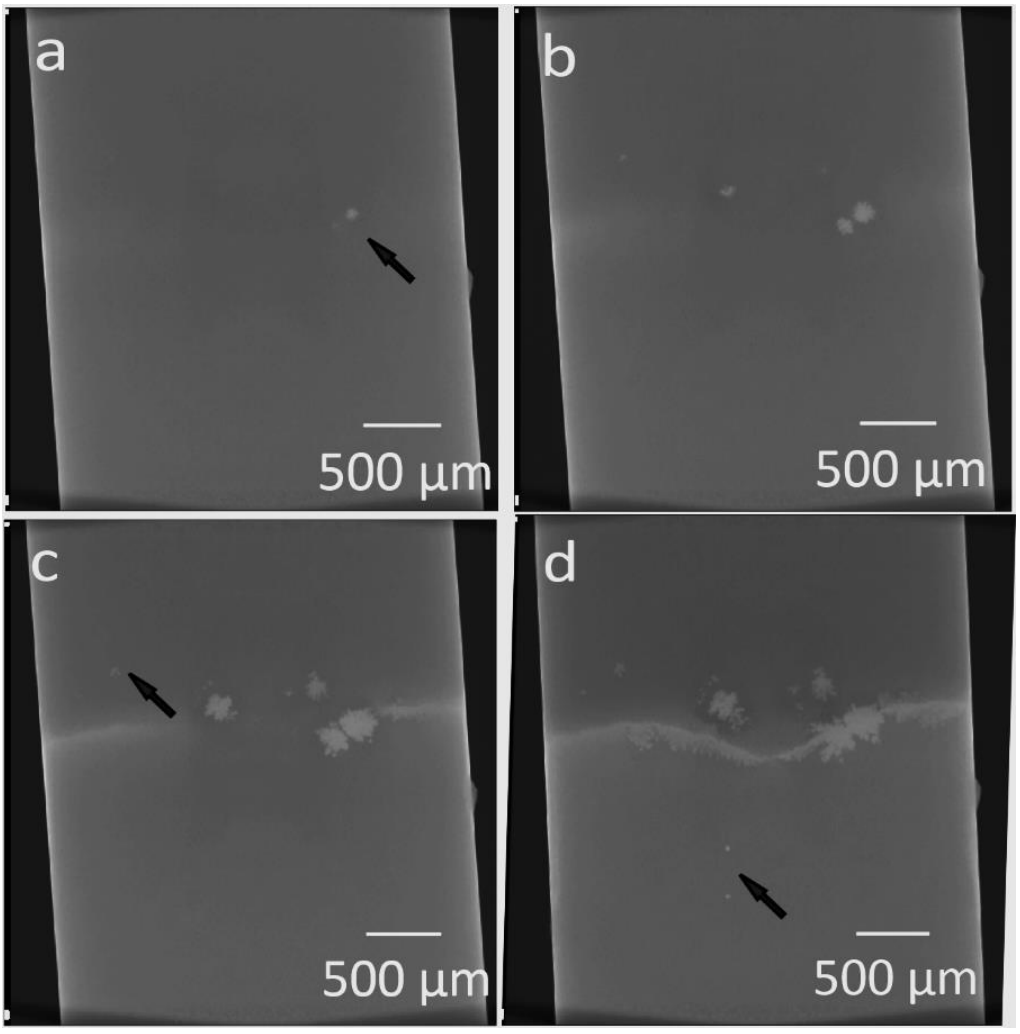

Figure 87. 2D images of $CaCO_3$ crystallization over time in a 2.8 mm rod. (a) 3 h after injection of 250mM M reagents, crystals start nucleating. (b) Crystals form around the faint band of precipitation after 4 h and smaller crystals also nucleate close to the calcium (c) and carbonate (d) reservoirs after 6h (indicated with arrows).

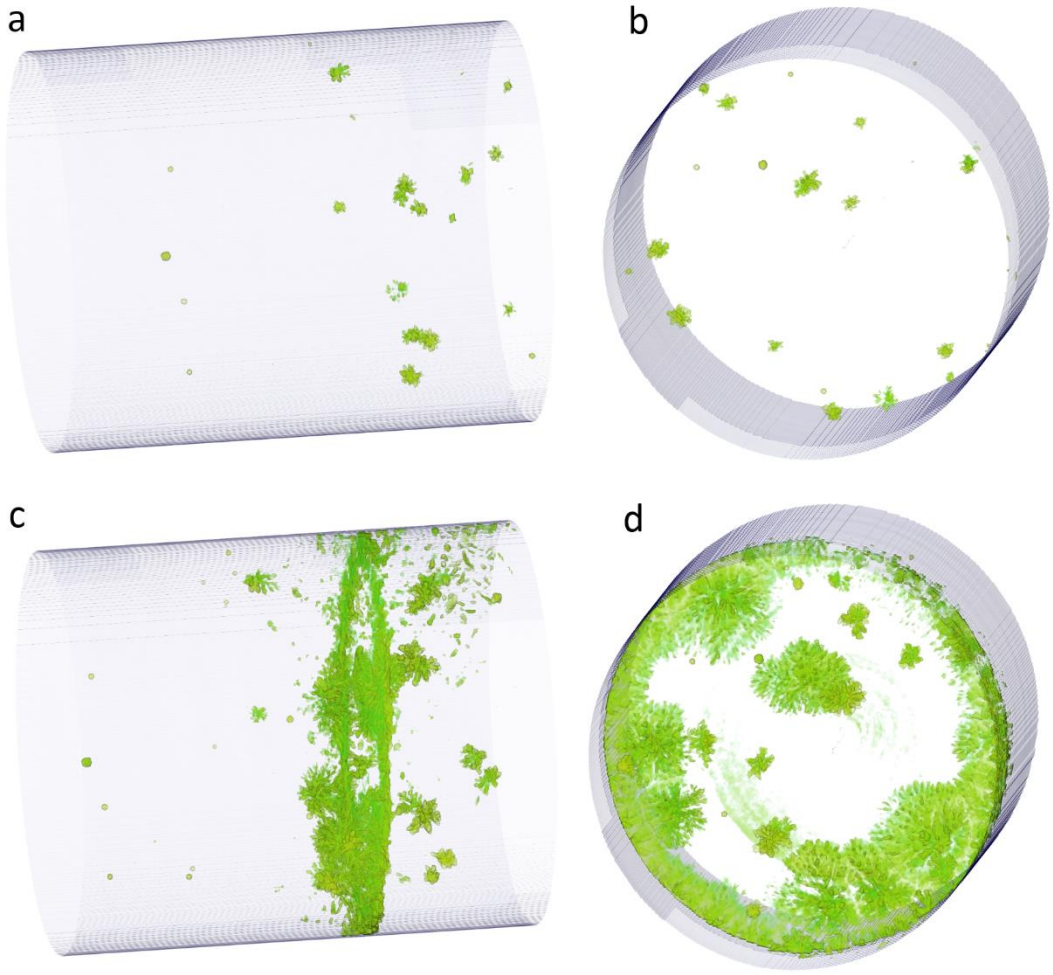

Figure 88. 3D images of $CaCO_3$ crystallization 3h (a,b) and 6h (c,d) after injection of 1 M reagents in 2.8 mm rods.

Ex situ characterization of crystals in CPG rods by Raman spectroscopy

Polymorph analysis was carried out by Raman spectroscopy of dry, fractured CPG rods. *In situ* Raman analysis of intact rods was only possible when the crystal sizes were relatively large (hundreds of microns). Many $CaCO_3$ crystallites in the rods were too small for *in situ* characterization by Raman spectroscopy and therefore the analysis was carried out *ex situ*. The reaction was quenched 4 and 24 h after injection of 1 M reagents, where similar results were obtained at both times. To stop the reaction, the 2.8 mm rods were first immersed in H_2O for 5 min, followed by ethanol for 30 min and then left to dry at ambient conditions. Once dry, the rods were broken in half and three different crystal morphologies were found by optical microscopy (Figure 89b). The crystals closer to the carbonate reservoir presented more globular

morphologies and were identified as aragonite by Raman (Figure 89c). Vaterite was found as large dendritic crystals at the center of the band (Figure 89d), while calcite crystallized closer to the calcium reservoir as dendritic crystals (Figure 89e).

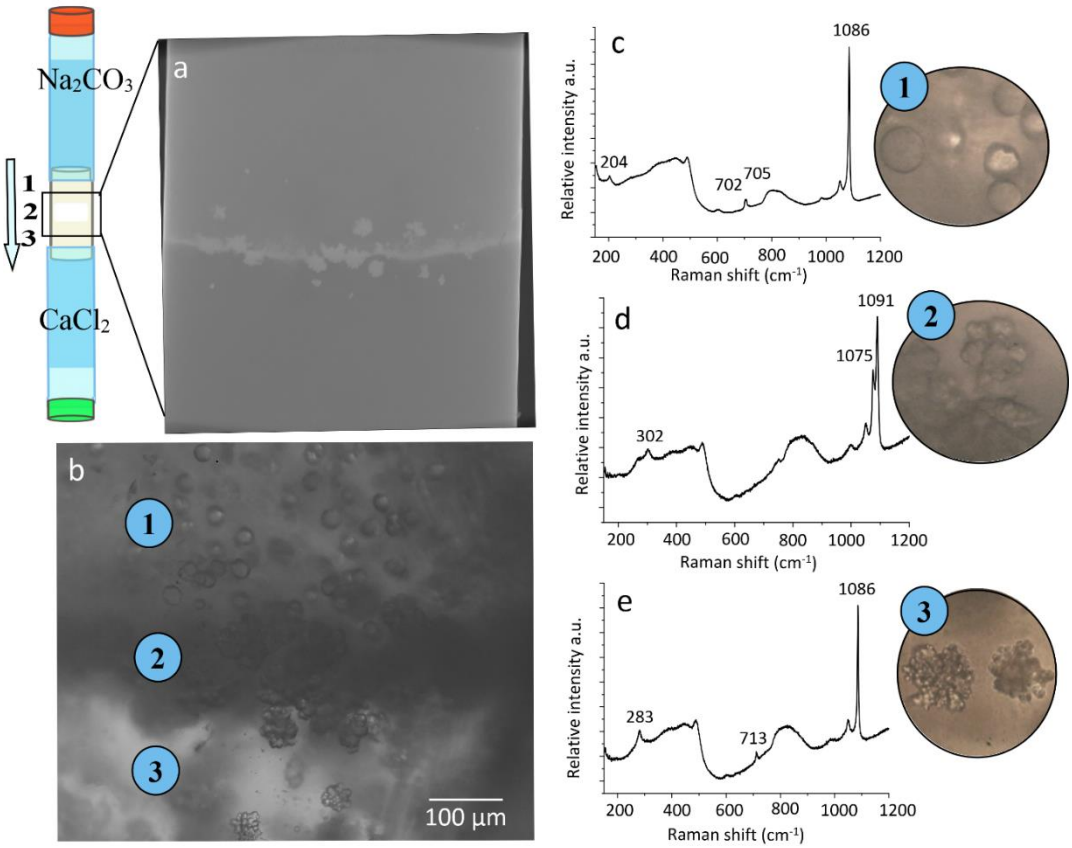

Figure 89. Ex-situ characterization of $CaCO_3$ crystals by Raman spectroscopy 4 h after injection of 1 M reagents. Three different regions were found by optical microscopy (b). Crystals growing in region 1, closer to the carbonate reservoir, were aragonite by Raman (c) while the crystals in the center of the band (region 2) were vaterite (d) and the crystals closer to the calcium reservoir (region 3) were calcite (e).

Crystal characterization in CPG rods by diffraction topography

The results were supported by *in situ* diffraction tomography (DCT) of the rods. Diffraction maps were first taken at three different positions along the length of the rod with a 100 x 100 μm^2 beam. Vaterite was the most abundant polymorph found at any position in the rod at any given time after 1 M solution injection. It usually precipitated both at the perimeters of the rod and inside (Figure 90). Calcite crystals were found close to the Ca^{2+} reservoir after 24 h.

Note that the diffraction maps are better resolved at longer times due to the larger amounts of solids in the pores. The fact that calcite was not found at earlier times, and the absence of aragonite might be due to the low resolution of the scans and/or the position of the scans. Each scan was separated from the other by a height of 200 μm, which might not have been sufficient separation to observe the polymorphs closer to the Ca^{2+}/CO_3^{2-} reservoirs.

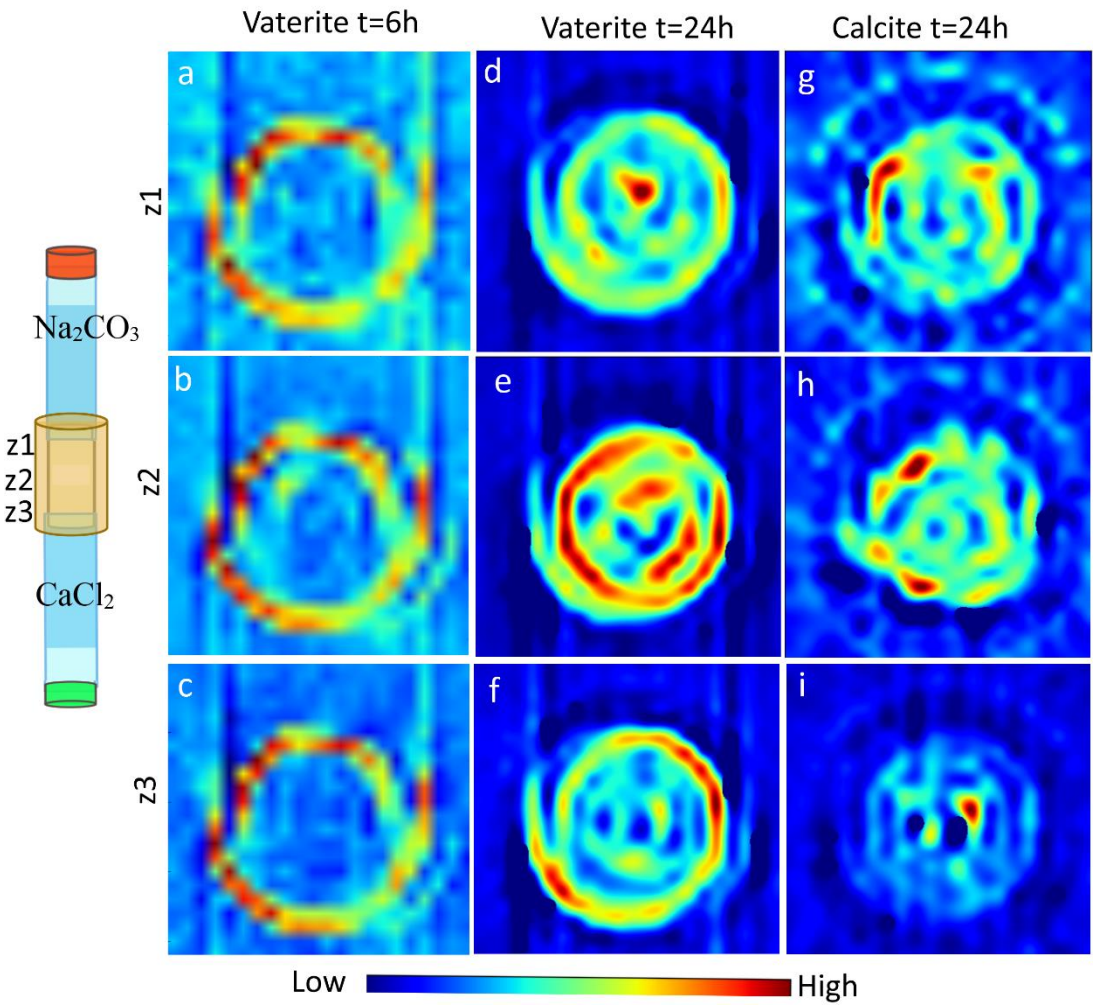

Figure 90. 2D diffraction maps with 100 μm resolution of $CaCO_3$ crystals at three different positions along the length of a CPG rod and separated by 200 μm 6h (a-c) and 24h (d-i) after injection of 1 M solutions. Vaterite was the main phase present at the scanned planes although calcite was also found at longer times.

The large beam size allowed a faster scan rate but poorer resolution. Scans with higher resolution were then obtained with a 50 x 50 μm^2 beam in order to obtain phase information about smaller crystals. The three polymorphs were

then found at different positions of the rod, where vaterite and calcite were the most abundant phases throughout the rod (Figure 91). Each scan took a total of 2h 30 min, which makes time-resolved experiments challenging. Moreover, aragonite crystals only grew to tens of microns in size (as observed optically) which presents difficulties for detecting them with a large X-ray beam size. Raman is in this sense a more useful technique since fast scans with up to 1 µm resolution can be obtained easily. However, fracture of the rods was required for Raman analysis of small crystals. The combination of different techniques was therefore necessary to understand $CaCO_3$ crystallization in nanopores.

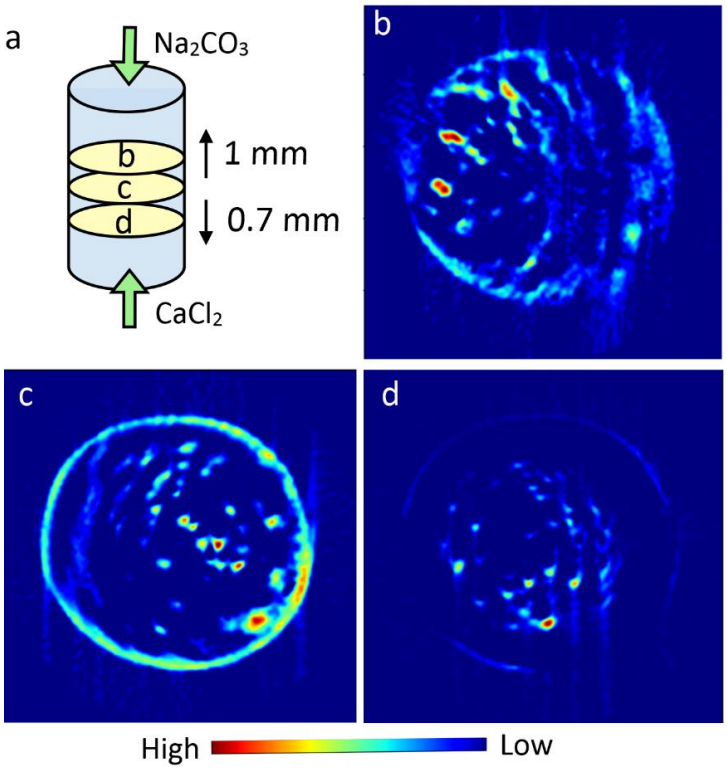

Figure 91. (a) Schematic and 2D spatial diffraction maps with 50 µm resolution of $CaCO_3$ crystals growing at different positions in a CPG rod 24h after injection of 1 M reagents. (b) Aragonite crystals were found in spatial maps recorded 1 mm towards the CO_3^{2-} reservoir from the center of the band. (c) Vaterite crystals were mainly present at the center of the rod. (d) Calcite crystals were found in maps recorded 0.7 mm below the band, towards the Ca^{2+} reservoir.

Additional challenges for aragonite characterization by DCT were that a mixture of vaterite and aragonite crystals was often found in the diffraction maps. The aragonite crystals also appeared to be oriented in the rods, such that, they only showed (012) and (021) reflections in the diffraction patterns. These peaks are found to be very close to (101) and (102) of vaterite and can be mistaken. Vaterite crystals show random orientations and therefore the diffraction patterns present other characteristic peaks such as (100) or (110). Diffraction maps plotted with various reflections are therefore essential for polymorph characterization. The diffraction patterns at various positions in a CPG rod are shown in Figure 92.

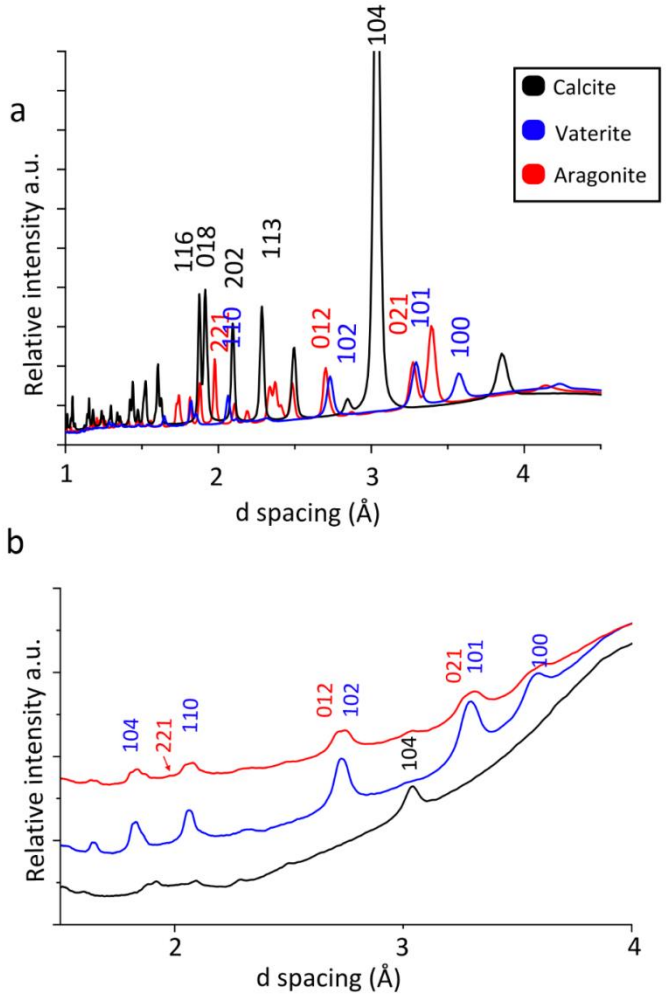

Figure 92. Diffraction data of $CaCO_3$ crystals from (a) reference samples where calcite in represented in black, vaterite in blue and aragonite in red and (b) inside CPG rods where the black pattern shows calcite crystals, the blue vaterite crystals and the red a mixture of vaterite and aragonite.

The effects of the surface chemistry of the pores on $CaCO_3$ crystallization in CPG rods was also explored. However, no noticeable differences were observed when the pores were coated with -COOH or -SO_3 groups. Vaterite and calcite were principally found at all positions of the rods.

The fact that aragonite precipitates in CPG rods is intriguing since this polymorph is very difficult to obtain synthetically at room temperature without the use of additives. The hypothesis presented here is that aragonite crystallization is promoted when the concentration of CO_3^{2-} is high with respect to the Ca^{2+} concentration in the pores. In order to verify this theory, $CaCO_3$ was precipitated in 2.8 mm CPG rods using reagents of concentration [Na_2CO_3] = 1M and [$CaCl_2$] = 50 mM. A defined band at the center of the rod was not observed in this case, and crystals with various morphologies precipitated along the length of the rod (Figure 93). After 24 h, the reaction was quenched and the crystals were characterized by a combination of Raman and optical microscopy. The three crystalline polymorphs of $CaCO_3$ were detected in the rods: vaterite crystals presented a dendritic flower-like morphology, calcite crystals showed dendritic irregular surfaces and aragonite crystals were more globular. Aragonite crystals were distributed along the length of the rod and not only close to the CO_3^{2-} reservoir. Vaterite crystals were also found at different positions along the rod and calcite crystals were less abundant and were found closer to the Ca^{2+} reservoir. The fact that aragonite crystals were now more heterogeneously distributed along the rod corroborated the hypothesis previously stated: a higher CO_3^{2-}/Ca^{2+} ratio in the pores promotes the precipitation of aragonite.

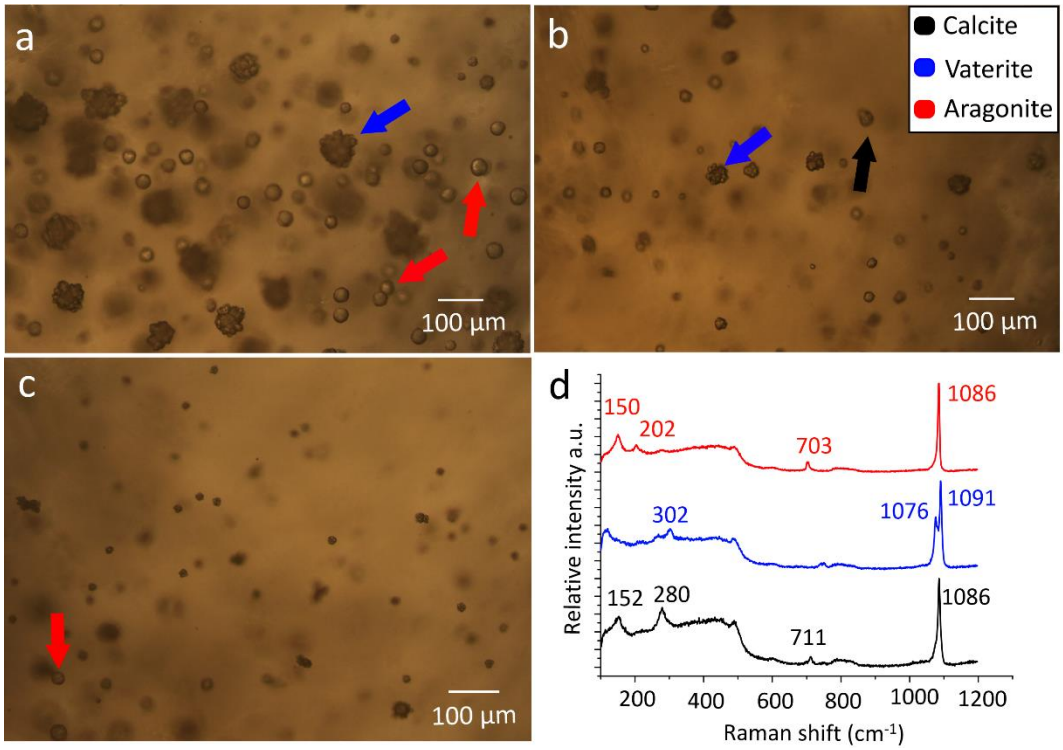

Figure 93. Micrographs (a-c) and Raman spectra (d) of $CaCO_3$ crystals inside a CPG rod 24 h after injection of the reagents: [Na_2CO_3] = 1M and [$CaCl_2$] = 50 mM. (a) Image of the crystals at the middle of the rod, (b) closer to the Ca^{2+} and (c) CO_3^{2-} reservoir. (d) Raman showing calcite crystals in black, vaterite crystals in blue and aragonite crystals in red. The different polymorphs are found along the length of the rod and some of them are pointed by arrows of the same color as their Raman spectra.

Crystal characterization in CPG rods by solid-state NMR

Although DCT allows the *in situ* characterization of $CaCO_3$ crystals in nanopores, the long scan times did not allow the collection of time-resolved information about the crystallization process. This can be achieved by fast, *in situ* solid-state NMR analysis of the crystals in the porous rods. ^{13}C NMR spectra of ACC, calcite, vaterite and aragonite were first recorded from bulk samples as references (Figure 94). Subsequently, $CaCO_3$ crystallization in the pores was carried out by first placing the ends of a wet CPG rod in between two tubes, one containing a $CaCl_2$ solution and the other a ^{13}C-labeled Na_2CO_3 solution, for 30 min (with 1 M reagent concentrations) and 2 h (with 250 mM reagent concentrations). The tubes were then removed and the CPG rod was inserted in a sealed 4 mm zirconia rotor, and NMR spectra were collected over time. A summary of the chemical shifts observed in bulk and in the CPG rods is presented in Table 8.

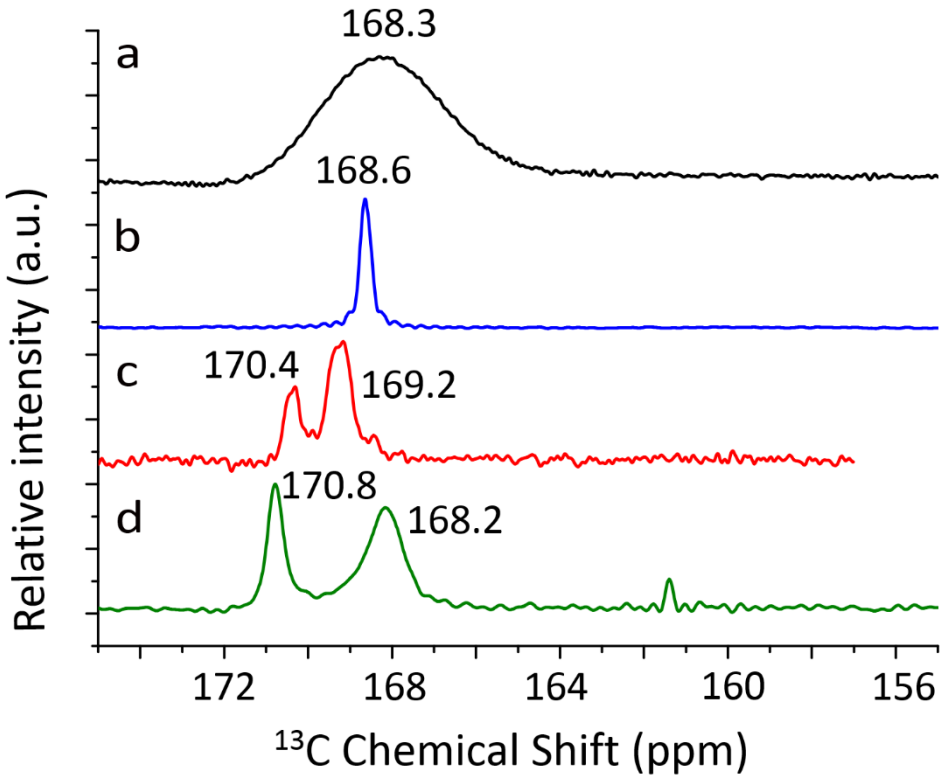

Figure 94. Solid-state NMR spectra of samples of (a) ACC, (b) calcite, (c) vaterite and (d) mixture of aragonite (170.8 ppm) and magnesian calcite (168.2 ppm).

The results confirmed that vaterite was the first crystalline phase to nucleate in the CPGs 1.5-2 h after injection of 1 M reagents (Figure 95a). Calcite nucleation in the pores was detected slightly later (<1h) and was significantly less abundant (Figure 95a). A broad hump underneath the calcite peak could also be observed in the NMR spectra, which corresponds to ACC (Figure 95a). Aragonite peaks were not observed probably due to the small size of the crystals or their low abundance in the pores.

At lower reagent concentrations (250mM), the most intense peak corresponded to calcite, although vaterite peaks were still present (Figure 95b). A small peak at 171 ppm could correspond to either vaterite or aragonite but the intensity of the peak was too low to confirm the phase. The small amount of material in the pores made it difficult to characterize the polymorphs, especially at low concentrations. Moreover, there was a slight

shift of the peaks of about 0.4 ppm with respect to the references, which was probably due to difficulties in spinning the CPG rod in the rotor.

At the two studied concentrations, a peak around 160 ppm was also observed in the NMR spectra. This peak did not correspond to solid $CaCO_3$ and it was observed to shift from 164 to 161 ppm over time (Figure 95). This peak was assigned to the CO_3^{2-}/HCO_3^- ions in solution. As the carbonate ions in the pores are being consumed by the crystals and converting into HCO_3^- their concentration changes, which is reflected in the NMR spectra.

	C.S. (ppm) Bulk	*C.S. CPG 1M (a)*	*C.S. (ppm) CPG 250 mM (b)*
ACC	168.3	-	-
Calcite	168.6	168.4	168.9
Vaterite	170.4	170.3	?171
	169.2	169.2	169.7
Aragonite	170.8	-	?171

Table 8. Chemical shift (C.S.) of $CaCO_3$ polymorphs in bulk and CPGs at two concentrations (1M and 250 mM).

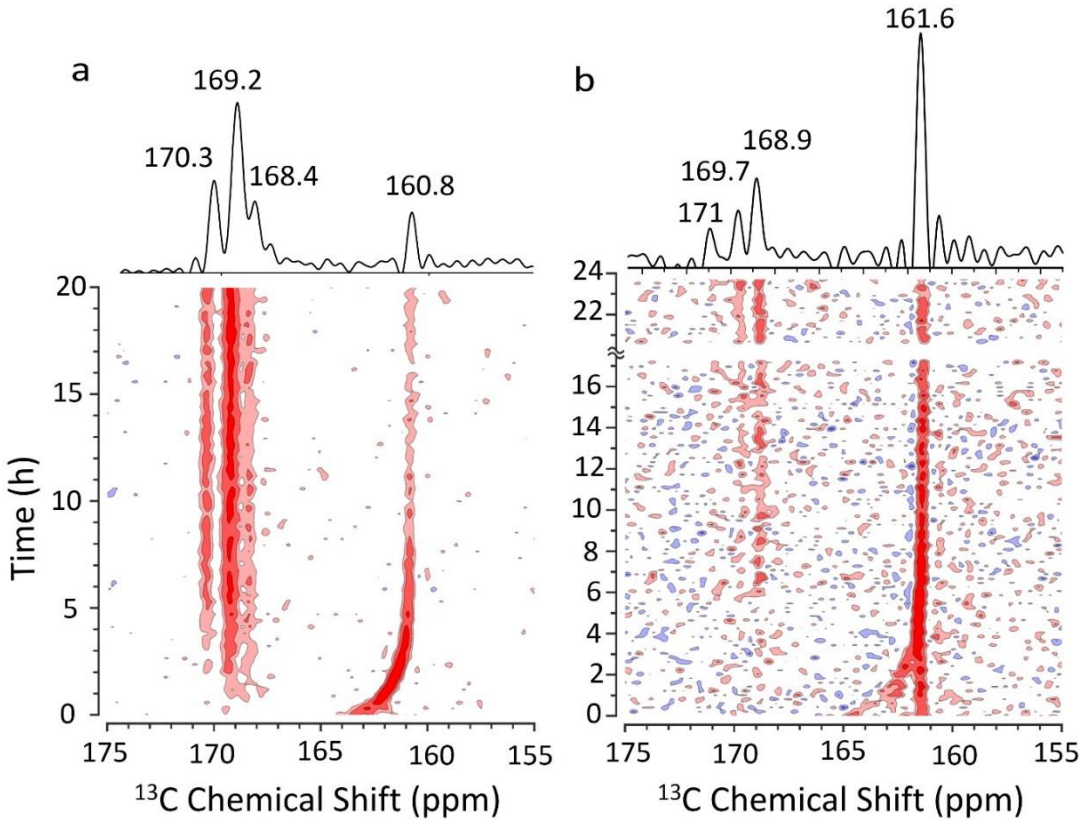

Figure 95. Solid-state NMR spectra of $CaCO_3$ crystals nucleating in CPG rods over time at initial conditions of (a) 1M and (b) 250 mM. In both cases peaks corresponding to vaterite and calcite can be observed, together with a strong peak around 161 from liquid CO_3^{2-}/HCO_3^-.

Electron microscopy analysis of $CaCO_3$ crystals within CPG rods

In order to confirm the integrity of the porous matrix after $CaCO_3$ crystallization, intentionally broken CPG rods were imaged by electron microscopy. 24 h after injection of 1 M reagents, the reaction was quenched and the rod was left to dry at ambient conditions. The CPG rod was then broken in half and imaged by SEM (Figure 96). A band of crystals was observed (Figure 96a), where the position of individual crystals was confirmed by EDAX (Figure 96b,d). High magnification images of the crystals did not show any apparent damage to the porous structure (Figure 96c).

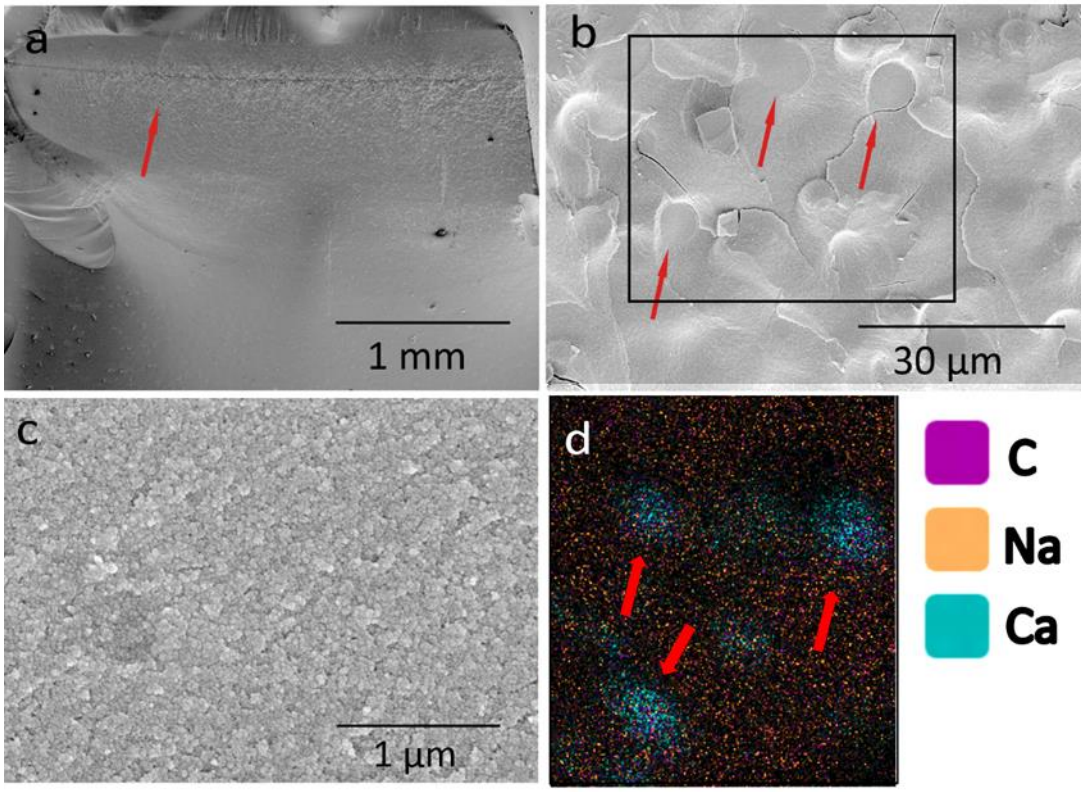

Figure 96. SEM images of a CPG rod broken in half 24h after $CaCO_3$ crystallization at 1 M reagent concentrations showing (a) the band of crystals and (b) individual crystals in the rod (indicated with red arrows), (c) high magnification image of one of the crystals, where the porous structure does not seem to be damaged and (d) EDAX mapping of the square area in (b) showing high amount of calcium at the three crystals indicated with the arrows.

Further information about the glass network after crystallization was obtained by dissolving the $CaCO_3$ with HCl. 24 h after injection of 1 M reagents, a CPG rod was immersed in a 0.1% HCl for 3 h. After crystal dissolution, the rod was broken in half and imaged by SEM (Figure 97 a,b). Cracks, cavities or other signs of major damage were not observed on the fracture surfaces of the broken rods. The integrity of the porous matrix on the mesoscale was also confirmed by µ-CT of a CPG rod after dissolving the crystals with HCl (Figure 97c). The data showed that the internal structure of the rod did not break during crystallization or dissolution.

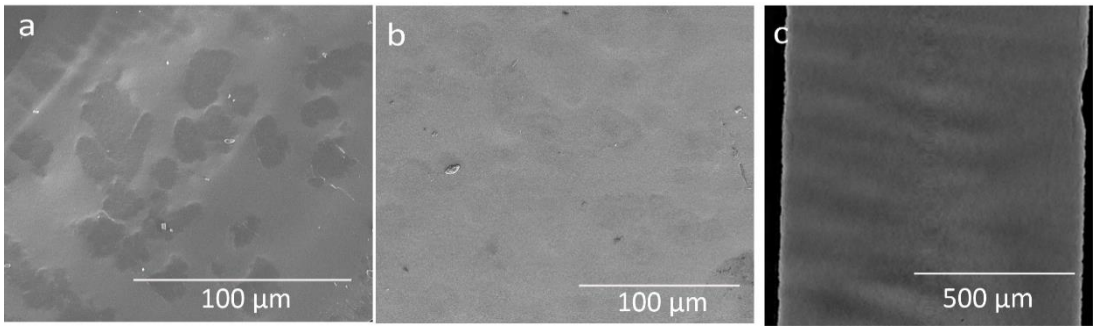

Figure 97. SEM images of a broken CPG rod after $CaCO_3$ crystallization (a) and after the dissolution of $CaCO_3$ crystals with HCl (b). (c) 2D tomogram of a CPG rod after dissolution of the $CaCO_3$ crystals. The internal porous glass matrix did not show damage on the mesoscale.

TEM was employed to characterize the crystals in the pores on the nanoscale. Thin sections of a CPG rod after 24 h crystallization using 1 M reagent concentrations were prepared by FIB milling (FIB was carried out by Dr. Alex Kulak). TEM images confirmed that the porous network remained intact after crystal growth (Figure 98 a-c). The crystals were templated by the porous structure as seen before with calcium sulfate crystals and in previous studies of $CaCO_3$ crystallization in larger porous media.[327, 328] Selected area electron diffraction confirmed the presence of vaterite in the thin section (Figure 98d).

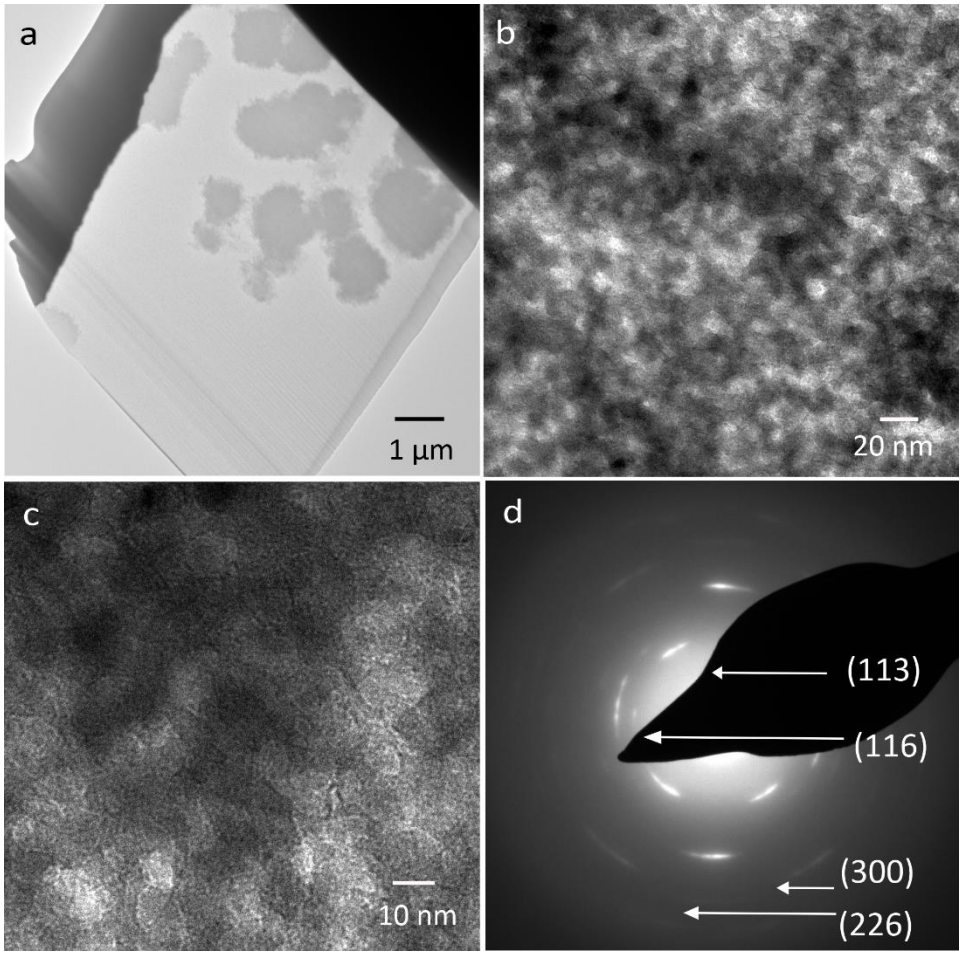

Figure 98. Thin section of a CPG rod after $CaCO_3$ crystallization analyzed by TEM, where $CaCO_3$ crystals present a darker contrast (a). (b,c) Higher magnification of an area containing a crystal, where the dark parts are the crystals and the lighter parts, the pores. (d) Electron diffraction of a crystal (c) in the CPG rod showed the phase present in this area to be vaterite.

4.4 Discussion

The results described in this chapter demonstrate the enormous effect that confinement has on the crystallization of inorganic solids and how they bring new insight into the mechanisms that govern these effects. By studying the crystallization of calcium sulfate and calcium carbonate in CPG rods, it was possible to track the early stages of crystallization of these solids and to follow their crystallization mechanisms *in situ*. These observations were possible since the crystallization of the solids in the pores was much slower than in bulk solution, due to confinement effects. These effects include slower ion diffusion and a decrease in convective transport of material through the pores,

restricted water availability and the lower likelihood of nucleation events occurring in a restricted environment.[117, 187, 299, 329] The results observed for calcium sulfate and calcium carbonate are discussed separately in this section.

4.4.1 Calcium sulfate in CPG rods

Over the last 6 years the mechanism of crystallization of calcium sulfate has been extensively discussed in the literature and a multi-step nucleation process with different precursors such as amorphous calcium sulfate (ACS) and bassanite was proposed.[118, 295-297] However, the nature of these precursors and the nucleation pathway of gypsum is still unclear due to the difficulties in tracking the early stages of crystallization of this solid in solution. Here, the existence of ACS was demonstrated, and the first diffraction pattern of this material was reported (Figure 62). The formation of a disordered, precursor phase in the pores was only observed at high concentrations and only for short periods of time (<30min). At low concentrations, the signal of the amorphous phase was probably too low to be detectable by X-ray diffraction or its life-time was too short. ACS rapidly redissolved in the pores to form bassanite which was stable in confinement for over 3 weeks. Confinement therefore acted to stabilize the metastable phases of calcium sulfate as observed previously for other solids in confinement.[114, 329, 330] The short lifetime of ACS in the pores explains the previous difficulties to observe and characterize it in bulk solution, where its stability must be much lower.

After ACS dissolution, significant stabilization of bassanite over gypsum at room temperature was observed in the nanopores, which can be explained by taking into account the differences in this restricted environments compared with bulk. While previous studies have achieved moderate stabilization of bassanite using additives[293] or confinement (using a crossed-cylinder apparatus),[118] bassanite was only stable for up to 24 h. In contrast, it reminded stable for at least 3 weeks in the nanoporous glass rods. Based on Classical Nucleation Theory it is evident that in the small volume of a nano-porous network, gypsum nucleation would be statistically more unlikely than in bulk.[331] This is due to the stochastic nature of nucleation, which requires the

random collision between ions to form clusters. In small volumes, the number of ions will be smaller and therefore the probability of collision and cluster formation will be lower.[177] This must be particularly relevant in the very small, tortuous pores of CPGs, where material-transport will be purely diffusion-driven (advection and convection are inhibited in small pores). Moreover, the overall ion diffusion is expected to be slower in nanopores.[274] Here, the ion diffusion coefficients of SO_4^{2-} and Ca^{2+} ions in the 7 nm pores suffered a decrease of 82% as modeled by computer simulations. This causes longer induction times and overall, slower crystallization processes in the nanopores.

That nucleation is suppressed in small volumes means that high values of supersaturations can be reached in the nanopores before crystallization.[176, 270] Indeed, according to the model, by the time precipitation is first observed (ACS or bassanite) in the pores, the system is supersaturated with respect to gypsum (S>4) based on published solubilities.[332] This is in agreement with previous studies of crystallization in gel media, where nucleation in the pores is observed at very high levels of supersaturation.[177, 270, 333] At these high supersaturations, kinetic factors are likely to control crystallization and the formation of intermediate phases such as ACS or bassanite is expected. Solubility data of ACS and bassanite in bulk are still under investigation, due to the low stability of these solids in water.[296] However, Wang et al. obtained ACS and bassanite in bulk at concentrations as low as 15 mM and therefore, the solution must already be supersaturated at these concentrations.[298] This means that the solution in the CPG pores must also be highly supersaturated with respect to ACS and bassanite when precipitation is first observed, although it is not possible at this stage to calculate the final supersaturation value. Furthermore, calcium sulfate crystallization in CPG rods with 50 mM reagent solutions was never observed. Under these conditions, the system would only reach maximum concentrations of 25 mM at the centre of the rod after around 15 h (Figure 60 d). The solution in the pores is now only slightly supersaturated with respect to gypsum and no nucleation could be detected. This again shows that nucleation in the nanopores requires higher supersaturations than in bulk to occur.

If kinetic factors control crystallization, lower energy barriers are expected for the nucleation of the possible intermediates, facilitating their precipitation in the pores (Figure 99). Thus, one can imagine that intermediate phases will be more stable in the nanopores than in bulk, since the activation energies necessary to obtain the thermodynamically stable phase are more difficult to overcome. Furthermore, according to Kröger *et al*. once a crystal is formed in a confined system, the ion concentration close to the precipitate suffers a significant decrease, increasing the stability of the precipitate.[334] Transformation from bassanite to gypsum is therefore expected to be inhibited in the nanopores, due to the large reduction of supersaturation in the areas surrounding the crystals. That bassanite remains stable even when it is located very close to gypsum particles further illustrates the reduced communication between crystallites in the porous environment. This means that an important difference between crystallization in bulk and confinement might be that while in bulk, every crystal is affected by the nucleation of other crystals in the same solution, a lower communication between crystals occurs in confinement.

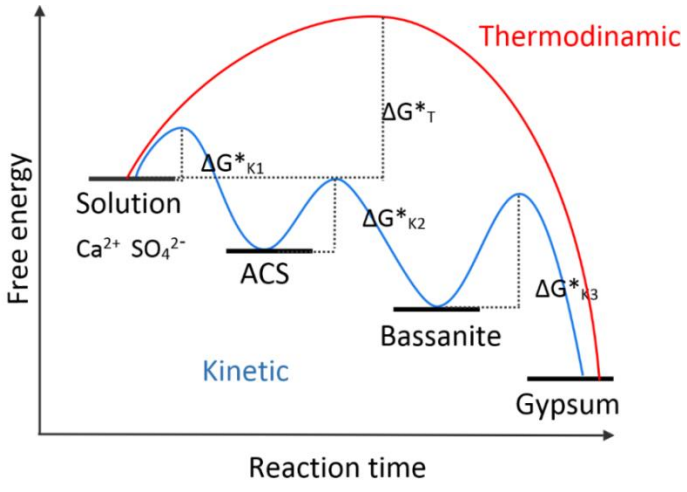

Figure 99. Calcium sulfate crystallization pathway under thermodynamic (in red) and kinetic (in blue) control, where gypsum nucleation proceeds by sequential precipitation of amorphous calcium sulfate (ACS) and bassanite.

Transformation from bassanite ($CaSO_4 \cdot 0.5H_2O$) to gypsum ($CaSO_4 \cdot 2H_2O$) also involves changes in the degree of hydration, which requires water

diffusion to the crystals. Water transport in the pores will be slower but additionally, there will be contact restrictions between the solution and the crystals in confinement as shown previously in other confinement systems such as the crossed-cylinder apparatus.[117, 118] For pores in the range 2-20 nm, we also need to consider possible layers of “surface water”, which have structures and dynamics different to bulk water. According to computer simulations of water behaviour in silica nanopores, there can be up to 3 monolayers of surface water (~0.9 nm)[335] in a 7 nm pore. This would leave around 40% of the water in the pores mobile (bulk water) with around 60% of the water attached to the surfaces.

Physical blockage effects due to crystal growth through the pores must also be taken into account, where this can cut off many diffusion paths and leave trapped water in between crystals. Recent studies of calcium sulfate crystallization have described the important role of available water.[295, 336] The stabilization of bassanite and anhydrite was possible by simply changing the crystallization solvent from water to ethanol or dry methanol. It was shown that conversion to gypsum only occurred at water contents higher than 50%.[291, 292] Here, if we consider that the surface water does not participate in crystallization processes, the amount of bulk water is calculated to be less than 50%. Nevertheles, previous studies have observed stabilization of metastable phases in confinement in systems with surface separations in the microscale range.[117, 118] These observations suggest that the presence of trapped H_2O on surface of the pores cannot be the decisive factor for confinement effects although it cannot be ruled out that it might have an impact in the results observed here.

How does bassanite convert?

The mechanism of transformation from bassanite to gypsum has also caused much debate, where two possible paths have been proposed. Originally, it was believed that gypsum precipitated after dissolution of basssanite due to its lower solubility, following a dissolution-reprecipitation mechanism. [287, 337] However, a new mechanism was observed later on by which bassanite

nanoparticles assembled into particles with morphologies similar to gypsum before their transformation into the most stable phase, following an aggregation-based process.[118, 296] The results described here allowed the observation of gypsum crstallization from ACS and bassanite precursors, prividing insight into the mechanisms that govern these transformations. The existence of several pathways of gypsum nucleation was demonstrated, where these can be selected according to subtle variations in the crystallization environment. Gypsum nucleation within CPGs was observed to precipitate *de novo*, but also from bassanite via a solid-state transformation, dissolution-reprecipitation and possible heterogeneous nucleation on bassanite surfaces. A schematic of the different calcium sulfate crystallizaiton pathways observed during this study is shown in Figure 100.

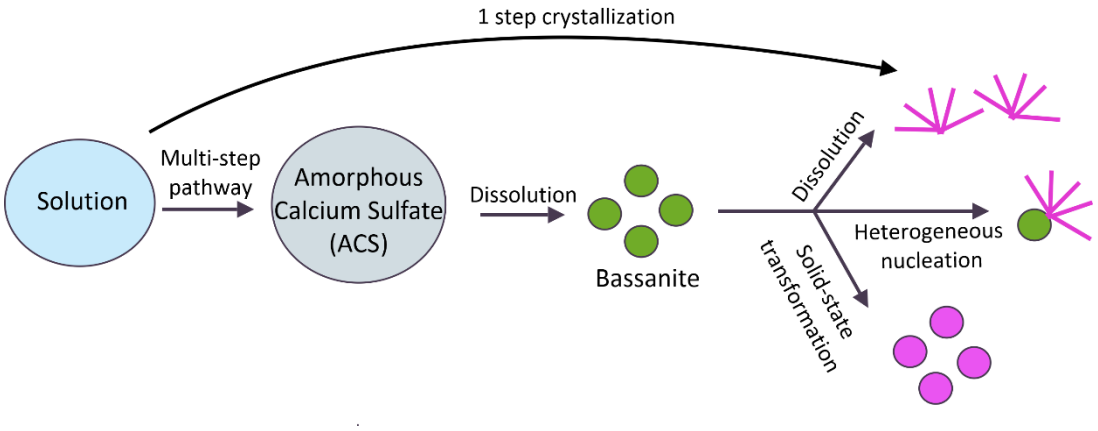

Figure 100. Diagram of the mechanisms of crystallization of gypsum observed in the CPG rods where these include a 1 step gypsum nucleation and a multi-step pathway with ACS and bassanite as precursors. Bassanite was seen to form after ACS dissolution and gypsum often nucleated very close to the surfaces of basanite crystals. Bassanite was also seen to convert into gypsum by solid-state transformation and dissolution-reprecipitation.

Firstly, analysis of precipitation within the uncoated CPG rods shows that calcium sulfate can precipitate via an X-ray amorphous phase that subsequently transforms to bassanite and ultimately gypsum. It was observed that when the CPG rods were broken or the rods were placed in humid conditions after crystallization, a complete change in morphologies from spherulite-like bassanite crystals to dendritic crystals or clusters of needles of

gypsum occurred (Figure 71). This is in agreement with a dissolution-reprecipitation mechanism. The transformation of bassanite to gypsum was also triggered by exchanging the solution reservoirs for water, where the transformation proceeded with retention of morphology. These observations are therefore consistent with the proposed aggregation-based mechanisms of calcium sulphate.[118, 298] In contrast, gypsum precipitated *de novo* within carboxylate-functionalized CPGs.

This study also demonstrates the importance of the surface chemistry of the host medium in directing the crystallization pathway. Functionalizing the pores with carboxyl terminated SAMs, promoted crystal nucleation, decreasing the nucleation time and increasing the density of crystals. Previous studies of crystallization on carboxyl functionalized surfaces in bulk also observed lower induction times and higher densities of crystals on the surfaces.[194] An increase in the heterogeneous nucleation rate on surfaces can be explained classically by the decrease in the interfacial free energy of the emergent nucleus, which causes a reduction in the thermodynamic energy barrier.[338] A higher crystal density on functionalized surfaces has been rationalized by a higher mass transport from the solution to the charged surfaces, thus promoting nucleation.[191] The pores of the CPG rods must be partially deprotonated in the pH regime of these experiments (5-6). [339] This must lead to an increase in the concentration of calcium ions at the pore surface and an enhanced concentration of sulfate towards the center of the pore. A faster transport of calcium and sulfate ions in the functionalized pores should enhance nucleation as previously suggested by Stack et al.[186]

The study of calcium sulfate crystallization in confinement not only provided information about the mechanism of crystallization of this solid, but also revealed the conditions under which it is possible to stabilize ACS and bassanite. Calcium sulfate deposits on Earth form due to water evaporation near sources of salt-water. Gypsum is the main phase present in these deposits and any bassanite forming in cracks must convert into gypsum in these humid environments. However, the surface of Mars is known to have a

low water content – especially at low lattitudes[340] were bassanite has been found.[281] It is possible that bassanite forms in cracks in this drier environment, where it would be more stable than on Earth. The stabilization of bassanite observed at lower Martian lattidudes may be affected by confinement effects analagous to the ones observed here, where low water transport in the pores prevents phase transformation. At higher lattitudes on Mars, the humidity increases, and gypsum is seen to be more abundant[341] possibly for the same reasons as seen on Earth and in the CPG rods at high humidities. Moreover, bassanite stabilization in confinement offers an explanation for the presence of this mineral in living organisms such as medusae,[342, 343] where calcium sulfate hemihydrate grows in confined structures (rhopalium) to fulfill the role of gravity sensors (statoliths).

Finally, the experiments described in this chapter provide insight into the fracture of porous materials due to crystallization. Crystals growing in a porous medium can exert crystallization pressure due to repulsive surface forces between the pore walls and the crystal.[103, 106] The generation of non-uniform crystallization pressures within a porous host can lead to local stresses, and ultimately fracture.[103] Here, it was shown that both bassanite and gypsum particles grow uniformly within the CPGs, and that this does not generate the local stresses that give rise to macroscopic fracture. No damage is observed even on the nanoscale level, where this can be rationalized by crystals exerting comparable pressures at both sides of a pore wall. It is important to highlight that CPGs are more fragile than most rocks. In contrast, gypsum precipitation from the surfaces of the rock, invariably leads to fracture. The crystals forming at the surfaces of the rods grow rapidly, at the expense of bassanite crystals confined in the pores, by a dissolution-reprecipitation mechanism.[287] The gypsum crystals forming at the surfaces grow within the pores adjacent to the surfaces since they are fed by ions from the interior of the rod. This causes local stress at the pores adjacent to the surfaces, causing fracture. CPG rods offer a model system with controlled pore size, porosity and surface chemistry which can be used in the future for other studies on breakage of porous materials during weathering.

4.4.2 Calcium carbonate in CPG rods

Inorganic and organic additives have been commonly used to obtain $CaCO_3$ crystals with specific morphologies, sizes and structures.[82, 90] However, over the last decade, confinement has been shown to be a tool that could potentially be as efficient as additives to control crystallization and to gain insight into the crystallization pathways of $CaCO_3$.[116, 156] Here, $CaCO_3$ crystallization in confinement was imaged by micro-computed tomography to reveal different crystal morphologies than those observed in bulk and Ostwald ripening effects never before seen in nanopores. Wide ACC bands were observed to form and "move" across the porous rods by dissolution-reprecipitation. This effect is similar to the appearance of Liesegang rings in convection-free systems such as gel media.[344] The formation of these "moving bands" is rationalized in the same way as the existence of Liesegang rings: CPG rods provide a diffusion-driven process within the nanopores with negligible advection. Fluctuations of the ion concentrations in the system promote the nucleation and dissolution of ACC until the system reaches equilibrium, giving birth to crystalline phases which consume ACC from the surroundings. This phenomenon is comparable to the formation of Liesegang rings in sandstones or other sedimentary rocks based on cycles of supersaturation-nucleation-depletion.[344]

Previous studies of $CaCO_3$ precipitation in nanopores were undertaken by Stack et al. who packed CPG beads in a capillary and followed the crystallization by small angle X-ray scattering (SAXS).[186] They suggested that $CaCO_3$ precipitation inside nanopores of native CPGs is not possible due to the limited transport of CO_3^{2-} ions through the SiO_2 nanopores. It was proven here that $CaCO_3$ can indeed form inside 7 nm pores and that the lack of precipitation within the porous beads was probably because of the competition between nano and macropores. Certainly, the macrochannels between CPG particles or even the surfaces of the beads offer an easier place for crystallization to take place, resulting in empty nanopores as observed in this study.

By using CPG rods and studying crystallization through a combination of diffraction and absorption tomography, it was possible to monitor $CaCO_3$ precipitation in glass nanopores *in situ* for the first time. The first phase to crystallize in the pores was ACC, which was stable in the pores for longer than 24h. In contrast, it dissolved within 2 h in a glass capillary at the same conditions. Stabilization of ACC in nanopores is in agreement with previous studies of $CaCO_3$ in porous membranes or crossed-cylinders.[156, 345] A proposed explanation for ACC stabilization in the crossed-cylinders was that ACC could be stabilized below its bulk solubility when it is confined between two surfaces.[156] This situation is similar to a liquid that condenses in between two surfaces from vapor. The liquid condensate in the pores would be stabilized since the interfacial free energy between the liquid and the solid is lower than the one between the vapor and the solid.[346] Considering ACC precipitated between two hydrophilic surfaces or in a hydrophilic pore, it could be metastable towards crystallization but stable towards dissolution. This condition, together with lower water availability in the pores than in bulk, might inhibit ACC dissolution. Moreover, it has been suggested that the degree of aggregation of ACC particles affects their stability.[156] In a 7 nm pore network, the amorphous particles must have a reduced freedom of movement. Therefore, limited aggregation of ACC is expected, which may retard transformation to the crystalline phase. The size of the ACC particles could be also affected by confinement, which would also have an effect on their stability and transformation. From the results described in this chapter, the conversion of ACC to crystalline polymorphs follows a dissolution-precipitation mechanism. This was observed by differences in phase contrast before and after crystallization by µ-CT. Crystals grew at the expense of ACC and no direct ACC-crystal transformation was observed under these conditions, in agreement with previous bulk studies.[310]

Both diffraction and *in situ* solid state NMR showed that vaterite was the first and most abundant crystalline polymorph to form in the nanopores at 1 M reagent concentrations. Vaterite is the least stable polymorph of $CaCO_3$, but

is often observed as a transient phase in highly supersaturated solutions and converts rapidly into calcite by a dissolution re-precipitation mechanism.[151] Thus, mixtures of calcite-vaterite are often obtained in solution after the dissolution of an ACC precursor, but pure vaterite is very difficult to obtain without the presence of additives.[347] Previous studies of $CaCO_3$ crystallization within the pores of a track-etch membrane showed that confinement can increase the stability of vaterite, making it possible to obtain pure single crystals of vaterite in the pores.[116] In CPG rods, dendritic vaterite crystals hundreds of microns in size formed within the pores and they remained stable for the whole period of study. Conversion from vaterite to calcite was never observed and calcite and aragonite crystals were usually seen to nucleate at other positions in the rod. The stabilization of vaterite in the pores can again be rationalized by the overall retardation of the crystallization pathways in confinement, due to slow transport of material in the pores and the possible deficiency of water available to dissolve one polymorph to form the most stable one.

ACC and large vaterite crystals form a band at the center of the rod which is likely to hinder the transit of ions through the pores, creating differences in ion concentration along the length of the rod. Further computer simulations will be necessary to calculate the exact concentrations at various positions along the rod after crystallization. A higher CO_3^{2-} concentration will occur at the side of the band closer to the Na_2CO_3 reservoir and a higher Ca^{2+} ion concentration at the other side of the band. The different ratio of CO_3^{2-}/ Ca^{2+} ions might cause the formation of different polymorphs in confinement, which was also observed when changing the initial concentration of the reagents. It was shown that an excess of calcium or carbonate ions in the nanopores induces the formation of calcite or aragonite, respectively. Fernandez-Diaz et al. also observed the formation of aragonite at high CO_3^{2-} in a gel medium.[348] This can be explained by the differences in supersaturation along the porous column or rod, which leads to different degrees of metastability. Indeed, in an evolving system such as the one presented here, the kinetics of nucleation will vary across the system according to the supersaturation rate (the rate at which the system moves from the equilibrium). At the same time, the supersaturation

rate will vary with the system, since the transport of the ions through the pores will depend on the porosity and internal structure.

The fact that aragonite precipitation is promoted at high CO_3^{2-} in nanopores might help explain the presence of this polymorph in biominerals, especially at high CO_2 concentrations. This was already suggested by Given *et al*., who investigated the precipitation of carbonates in seawater, concluding that the decisive factor on the precipitation of calcite or aragonite was the ratio of Ca^{2+} and CO_3^{2-} ions in the environment.[349] Nevertheless, the physical explanation for these observations is still unknown. This shows once again the complexity of controlling crystallization processes, since every parameter plays an essential role which will define the properties of the crystal.[350] Control over morphology, polymorphism and orientation of the crystals found in nature, must be due to a combination of different important parameters involving the physical and chemical environment of the growing crystals.

4.4.3 Controlled pore glass rods

Finally, the confinement system used in these experiments offers, for the first time, the possibility to study and characterize the crystallization of inorganic solids in nanopores *in situ* using synchrotron absorption and diffraction tomography. 3D diffraction tomography has been generally used to map the distribution of phases in dry minerals such as byssus,[247] teeth[351] and bones[352] and other materials such as carbon[351, 353] and cement.[354] Absorption or computed tomography is widely used *in-situ* for medical and industrial applications since it allows a fast, non-destructive investigation of the interior of many objects.[171] The study of crystallization in porous media by synchrotron absorption tomography is an area of increasing interest since this technique offers the possibility to observe and quantify mineral reactions and crystal growth in a non-invasive way.[355] The high energy and flux obtained with a synchrotron combined with a mapping, in-situ, non-intrusive technique makes it the ideal option to analyze the crystal phases forming in the CPG rods and also to obtain morphological information about the crystals in the pores.

The CPG rods are easily manipulated and their surface can be easily cleaned as compared with the CPG beads that have often been used in previous confinement experiments.[109, 186, 187] Avoiding cystal precipitation on the surfaces of the CPG beads is in many cases almost impossible, which makes characterization of crystals present in the pores challenging, especially for insoluble solids. Indeed, when crystallizing calcium sulfate and calcium carbonate in CPG beads with 8 nm pore sizes, bassanite could not be detected in the pores due to the amount of gypsum precipitating on the surfaces or in between the CPG particles (Figure 57). Moreover, possible breakage of the internal structure of the CPG beads due to crystals growing from the surfaces was not considered, which may be relevant to some of the previous studies using these. CPG rods therefore present a new, effective system for studying crystallization, and could be exceptionally useful in generating a new understanding of crystallization processes and confinement effects.

4.5 Conclusions

This chapter presented a novel system to study the crystallization of inorganic solids in confinement: nanoporous glass rods. This system allows the *in situ* visualization and characterization of crystals growing in nanopores, facilitating the study of crystallization pathways and stabilization of transient phases. The crystallization of calcium sulfate and calcium carbonate were studied in CPG rods and it was seen to occur significantly more slowly than in bulk solution. This allowed the observation and characterization of the amorphous precursor phases of both solids, which crystallized over time into metastable crystalline phases. The stabilization of metastable polymorphs inside the nanopores was such that their transformation into the thermodynamically stable phases was often completely impeded. The crystals grew within the nanopores, templated by the glass framework, reaching sizes of hundreds of microns without any conconmitant structural breakage. However, conditions that facilitated gypsum precipitation on and below the surface of the rod inevitably lead to catastrophic fracture. Moreover, the effect of the surface chemistry was shown to have a significant influence on crystallization at the nanoscale, since great

differences were observed when crystallizing calcium sulfate in carboxyl-functionalized pores. Finally, the results presented in this chapter bring new insight into the factors governing crystallization in confinement, which moves us towards understanding crystallization in natural environments.

Chapter 5: Protein crystallization in confinement: the inverted watch glass system

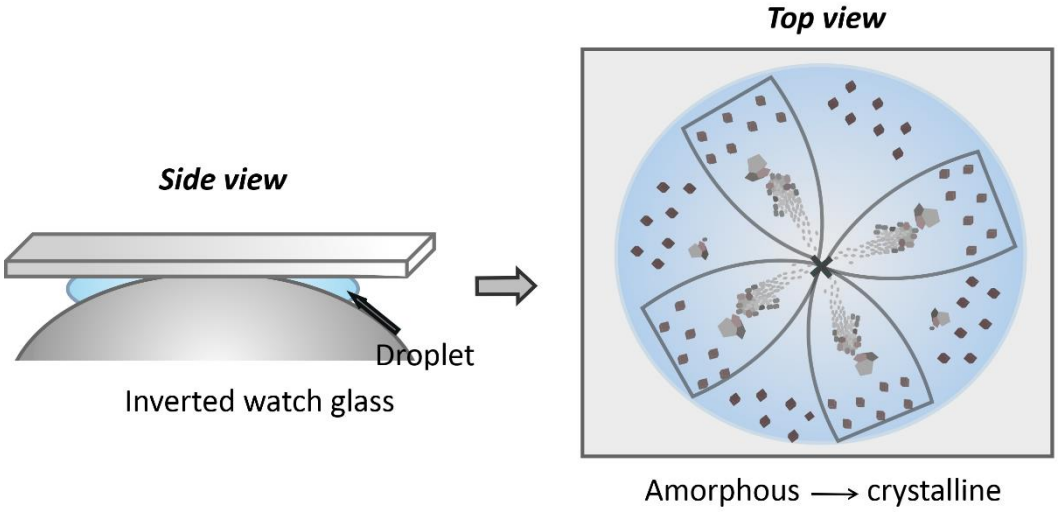

5.1 Introduction

5.1.1 Aims and overview

In prior chapters of this thesis it was shown that one of the main effects of confinement on the crystallization of inorganic solids is to retard this process, extending the lifetime of amorphous precursor phases and metastable crystalline polymorphs. These studies provided information about the early stages of crystallization that would otherwise be too fast to be studied. Confinement can therefore be used as a means to increase our understanding of crystallization mechanisms. A better comprehension of the mechanisms that govern protein crystallization is indispensable in order to gain control over this process, which is critical in areas such as medicine, pharmaceuticals and biological crystallography.

A crossed-cylinder apparatus has been used in previous work to study the crystallization mechanisms of calcium carbonate,[114, 156] calcium sulfate[118] and calcium phosphate.[89] In this apparatus, a drop of solution is located between two half cylinders in which the surface separation (SS) increases continuously from zero, where the cylinders are in contact, to millimeters at the perimeter of the cylinders. This offers the possibility to investigate the effects of confinement at varying degrees of confinement within the same experiment, and therefore, to observe different stages of crystal growth. Here, an improved crystallization system based on the same principle as the crossed-cylinder apparatus was developed: the inverted watch glass system. This allows *in situ* visualization of the particles forming at different degrees of confinement. The proteins lysozyme, catalase and trypsin were successfully crystallized using the inverted watch glass system with the aim of increasing our understanding of the early stages of their crystallization. The results described in this chapter bring new insights into protein nucleation pathways and provide a new method to stabilize intermediate phases of protein crystallization. The data collected during this study can also be used to predict the spatial conditions in which protein nucleation can be inhibited, and which should be avoided when developing new devices for protein crystallization.

5.1.2 Introduction to model proteins

More than 100,000 protein structures are currently available in the Protein Data Bank (PDB),[356] where most of them were resolved thanks to X-ray crystallography. Nevertheless, only a few proteins are regularly used for studies of crystal growth. These proteins are commonly named model proteins and they are usually selected for their relative ease of crystallization. The model proteins selected and studied in this thesis are presented below.

Lysozyme

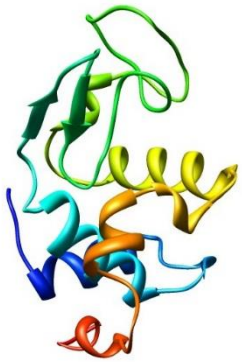

Lysozyme[357] is a globular enzyme found on the walls of some bacteria cells and is responsible for catalyzing the hydrolysis of polysaccharides and for the protection of the cell. Hen egg white lysozyme was the first protein studied by X-ray diffraction and it has been widely studied since then, being the preferred model protein for many fundamental studies of crystallization. It is composed of a single chain with a molecular weight of 14.3 KDa[37] which corresponds to a minimum diameter of around 3.2 nm.[358]

Trypsin

Trypsin is an enzyme found in many vertebrates and is produced by the pancreas. Its main purpose is to help break down other proteins in the digestive process.[359] Trypsin is also a small protein with molecular weight of 23.3 KDa and it has a minimum diameter of 3.8 nm.[360]

Catalase

Catalase[357] is an enzyme found in the liver, which is responsible for the catalysis of the decomposition of hydrogen peroxide without formation of free radicals.[37] It is a large protein containing 4 subunits, with a molecular weight of 250 KDa and has a diameter of around 8.1 nm.[361]

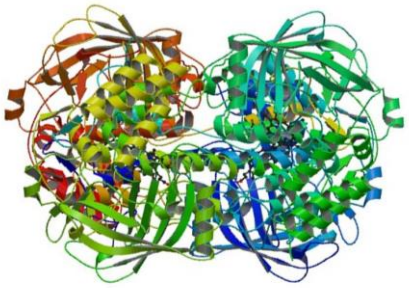

Thaumatin

Thaumatin is a plant protein usually found in African berries and is currently used as a low calorie sweetener and flavour modifier. Although thaumatin does not readily crystallize from solution, the addition of tartrate forces its precipitation into beautiful bipyramidal crystals.[362] It is a small protein of 22 KDa and 3.5 nm diameter.[363]

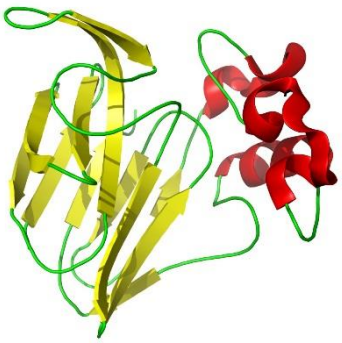

5.2 Experimental

5.2.1 Materials

Lysozyme (hen egg white), thaumatin (from Thaumatococcus danielli), trypsin (from bovine pancreatic), catalase (from bovine liver), glutaraldehyde, sodium acetate, $CaCl_2 \cdot 2H_2O$, bemzamidine, Hepes, NaCl, polyethylene glycol (PEG) (Mw=3350, 8000), Tris hydrochloride and tri-ammonium citrate were purchased from Sigma Aldrich and were used with no further purification. Silanes for surface coatings were purchased from Sigma Aldrich using 3-Aminopropyl-triethoxysilane for hydrophilic coatings and triethoxy(octyl)silane for hydrophobic coatings. Watch glasses 50 mm in diameter were used for protein crystallization and were obtained from VWR International Ltd.

5.2.2 The inverted watch glass system

The confinement system used in this chapter consisted of an inverted watch glass fastened to a glass slide with blue tack as shown in Figure 101a. The watch glass and the glass slide are pressed until they are in contact, and an annular wedge is formed between the two surfaces. This wedge provides surface separations (SS) that vary from 0 at the contact point to several millimeters.

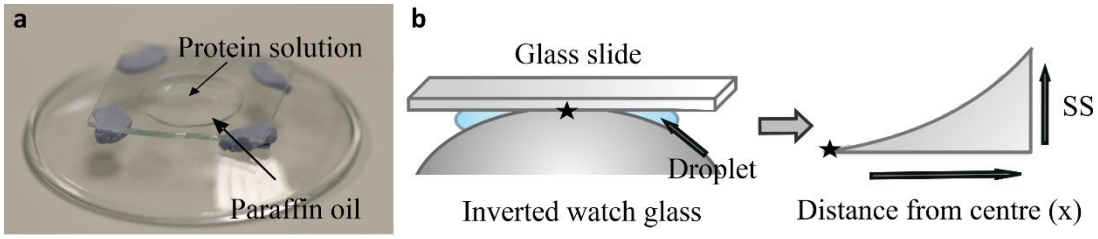

Figure 101. Protein crystallization set-up in the inverted watch glass system (a) and (b) schematic of the system showing the variation of surface separations (SS) with the distance from the center (represented with a star).

The surface separation between the watch glass and the glass slide (SS) at different positions from the center (x) can be calculated using the following equation, assuming that the distances are equal to those between a sphere and a flat surface.[114]

$$\boldsymbol{SS = R - \sqrt{R^2 - x^2}} \quad \text{(Equation 27)}$$

The radius of the sphere (R) was calculated by considering the watch glass as a spherical cap (Figure 102) and therefore:

$$\boldsymbol{R^2 = (R - h)^2 + (\frac{d}{2})^2} \quad \text{(Equation 28)}$$

where *h* is the height of the watch glass and *d* is its diameter. The height and diameter of the watch glasses used in this study were 5.2 and 50 mm respectively, such that the total radius of the sphere (R) is 62.7 mm.

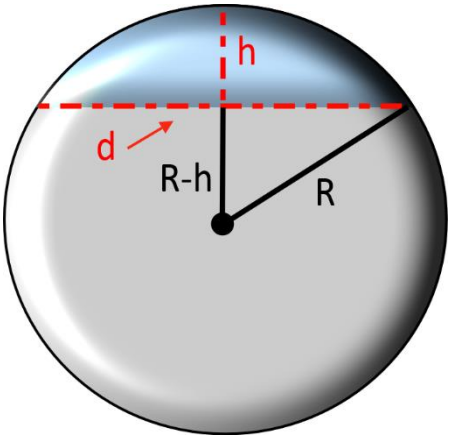

Figure 102. Schematic representing a watch glass as part of a sphere, where *h* is the height of the watch glass and *d* is its diameter.

The watch glasses and the cover slides were functionalized with silanes with different terminal groups using the chemical vapour deposition method described in chapter 2 (2.1.1.3). Static contact angle measurements of the coated samples were taken using a FTA 4000 (First Ten Angstroms, USA) by depositing droplets at three different areas of the same surface. The measurements are described in Table 9.

Sample	Functional group	Static contact angle (°)
Clean glass	-OH	10 ± 3
3-aminopropyl-triethoxysilane coated glass	$-NH_2$	31 ± 2
3-aminopropyl-triethoxysilane coated glass modified by succinamidation	-COOH	23 ± 2
Triethoxy(octyl)silane coated glass	$-CH_3$	46 ± 3

Table 9. Static contact angle of water on silane modified glass substrates

5.2.3 Systems with constant surface separation

The inverted watch glass system provides a unique way of studying crystallization at different degrees of confinement since it presents varying SS across the system. Nevertheless, studying the effects of confinement at one

specific SS is difficult, since crystals forming at different SS will always grow in competition. In order to study protein crystallization at specific SS, crystallization wells with constant SS were built. Two systems with SS = 5 µm and SS = 55 µm were created by firstly spin coating polydimethylsiloxane (PDMS) at 5000 and 1000 rpm for 5 min and 1 min, respectively, on two glass slides, where the thickness of the PDMS layer deposited decreases with spin speed and time.[364] After curing at 60 °C overnight, an approximately 8 mm x 10 mm rectangular area of PDMS was removed from the slides with a razor blade, creating a well for protein crystallization. These coated slides were then treated with oxygen plasma for 45 s to activate the PDMS surface for subsequent bonding. Immediately after plasma treatment, 2 µL of solution (1 µL of protein and 1 µL of precipitant) were deposited in the well, and a second (non-coated) glass slide (which was also plasma treated) was pressed against the first slide to seal the well. A schematic of this procedure is shown in Figure 103. The samples were then checked by optical microscopy after 1 and 2 days.

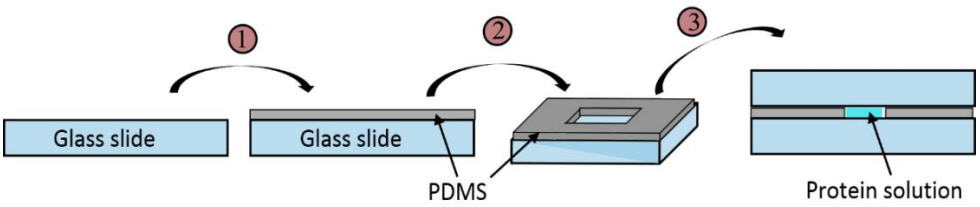

Figure 103. Diagram of the manufacturing process of confinement systems with regular surface separations for protein crystallization. (1) A PDMS layer is deposited on a glass slide by spin coating. (2) A well is created by cutting a rectangle of the PDMS layer. (3) The substrate and a clean glass slide are plasma treated and bonded together after placing a drop of solution in the well.

5.2.2 Crystallization methods

Protein crystallization was performed using the batch method.[72] The proteins were initially crystallized using microbatch 72 well plates in order to screen protein and precipitant concentrations. 1 µL of protein solution was mixed with 1 µL of precipitant in each well and the plate was then covered with paraffin oil and kept in an incubator at 20 °C. The precipitant, buffer solutions and

selected protein concentrations used in these experiments are summarized in Table 10.

Protein	Buffer solution (in water)	Protein concentration (in buffer) (mg/mL)	Precipitant solution (in water)
Lysozyme	0.1 M sodium acetate, pH 4.5	30	1.2 M NaCl
Trypsin	10 mM $CaCl_2$ 10 mg/mL Benzamidine 20 mM Hepes, pH 7	60	35% PEG 8000 0.1 M Tris, pH 7.5
Catalase	25 mM Hepes, pH 7	20	30% PEG 3350 0.2 M triammonium citrate 0.1 M Hepes, pH 7

Table 10. Selected solution conditions for crystallization using the batch method.

For confinement experiments in the inverted watch glass system, different solution volumes were tested in order to account for possible differences in protein precipitation depending on total volume. Volumes from 1 to 5 µL of protein solution with 1-5 µL of precipitant solution were injected between the glass surfaces, with 50 µL of paraffin oil being placed around the solution droplet to prevent evaporation (Figure 101). The samples were incubated at 20 °C and imaged by optical microscopy every 24 h for 2 weeks and then once again after 1 month.

5.2.3 Characterization methods

The samples were also imaged *ex situ* by SEM 24 h after solution injection. The protein crystals were crossed-linked with glutaraldehyde prior to SEM imaging in order to strengthen them and protect them against the mechanical stress produced by a vacuum. The glutaraldehyde was introduced into the protein solution by vapor diffusion following the mechanism described by Lusty.[365] This method provides a gentle way of cross-linking fragile proteins, and it consists of introducing the glutaraldehyde into the crystallization droplet by slow evaporation of a concentrated solution. As glutaraldehyde is volatile,

it is expected to travel from the concentrated solution to the protein droplet, to balance its concentration in both droplets. Here, the cross-linking was carried out by placing the inverted watch glass system next to a 5 µL drop of 25% glutaraldehyde in a sealed petri dish overnight. Subsequently, the system was opened by gently removing the glass slide from the watch glass. The surface of the glass watch was then rinsed with water and ethanol and carefully dried with a N_2 flow. The inverted watch glass was then mounted on an SEM stub using copper tape and coated with 2 nm of Ir prior to SEM imaging.

5.3 Results

5.3.1 Lysozyme crystallization

Lysozyme was first crystallized using the microbatch method, where single crystals of the protein were observed after 1 day at 30-40 mg/mL protein, with precipitant concentrations of 1-1.2 M (Figure 104). The morphologies of the crystals suggest that they possess a tetragonal structure, $P4_32_12$, which is commonly obtained when crystallizing lysozyme at room temperature with NaCl as precipitant.[366] The crystallization conditions used for lysozyme are described in Table 10.

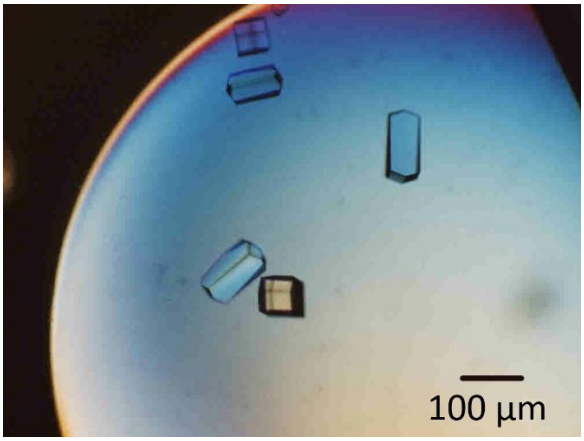

Figure 104. Optical microscope image of lysozyme crystals obtained by the microbatch method after 1 day at 30 mg/mL protein concentration with precipitant concentrations of 1.2 M.

Lysozyme was then crystallized at the same conditions in confinement, by injecting a droplet containing 5 µL of the protein solution with 5 µL of the precipitant solution between the surfaces of an inverted watch glass and a glass slide. The crystallization was monitored *in situ* for a period of 1 month by optical microscopy and *ex situ* by SEM after fixing the samples with glutaraldehyde. 24 h after solution injection, optical microscopy using crossed polarizers showed poorly crystalline particles close to the center, and more crystalline aggregates and single crystals at higher surface separations (Figure 105a). The drop can be separated into 4 different regions at different distances from the center, where particles and aggregates with increasing degrees of crystallinity were observed as the distance from the center increased (Figure 105b).

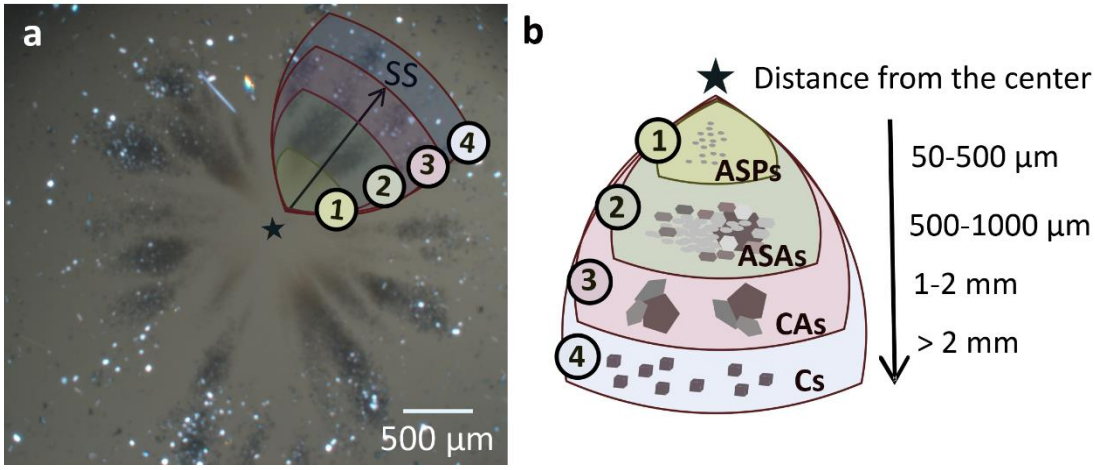

Figure 105. (a) Micrograph of lysozyme precipitation in the watch glass system obtained from imaging the solution drop under crossed polarizers 24 h after solution injection. The image shows the poorly crystalline character of the particles close to the centre and greater crystallinity at larger surface separations (SS). (b) Diagram of the 4 regions observed at different distances from the center (represented by a star). Amorphous solid particles (ASPs), amorphous solid aggregates (ASAs), crystalline aggregates (CAs) and lysozyme crystals (Cs) were observed at regions 1, 2 3 and 4 respectively (shown in more detail in Figure 106).

Further information about the particles that precipitated in each region was obtained by SEM. The first region covered distances from about 50 to 500 µm from the center, with surface separations (SS) of 20 nm to 2 µm. Particles of sizes between hundreds of nanometers to 1-2 µm were found in this zone (Figure 106 a,b). These particles did not have sharp edges and they did not show any birefringence under polarized light, which is indicative of a poorly-crystalline or non-crystalline character. Moreover, these particles tended to aggregate but they did not coalesce, suggesting the these amorphous particles had solid character. They were therefore referred as amorphous solid particles (ASPs). The second region was about 500 µm to 1 mm from the center (SS = 2-8 µm). Here, the ASPs aggregated into large amorphous solid aggregates (ASAs) (Figure 106 c) from which particles with sharp edges started to appear mainly at the perimeters of the aggregates (indicated by a red arrow in Figure 106 d). Polycrystalline aggregates (CAs) of irregular shape and flattened top surfaces were observed in the third region (at 1-2 mm from the center and SS =8-30 µm). The crystals had sizes > 100 µm and they grew sandwiched between the glass slide and the inverted watch glass (Figure 106 e). These crystals possessed rough surfaces comprising nano and micron sized particles, as observed in high magnification images (Figure 106 f). This suggests that crystal formation occurred through aggregation of the ASPs. At SS > 30 µm, fully faceted lysozyme crystals with similar morphologies to those observed in bulk were found (Figure 106 g,h). The dimensions of the crystals were similar to those observed at SS < 30 µm, but their crystal habit was significantly different. The differences in crystal habit are probably associated with an inhibition of crystal growth in confinement as previously reported for $CaCO_3$ in a crossed-cylinder apparatus.[114]

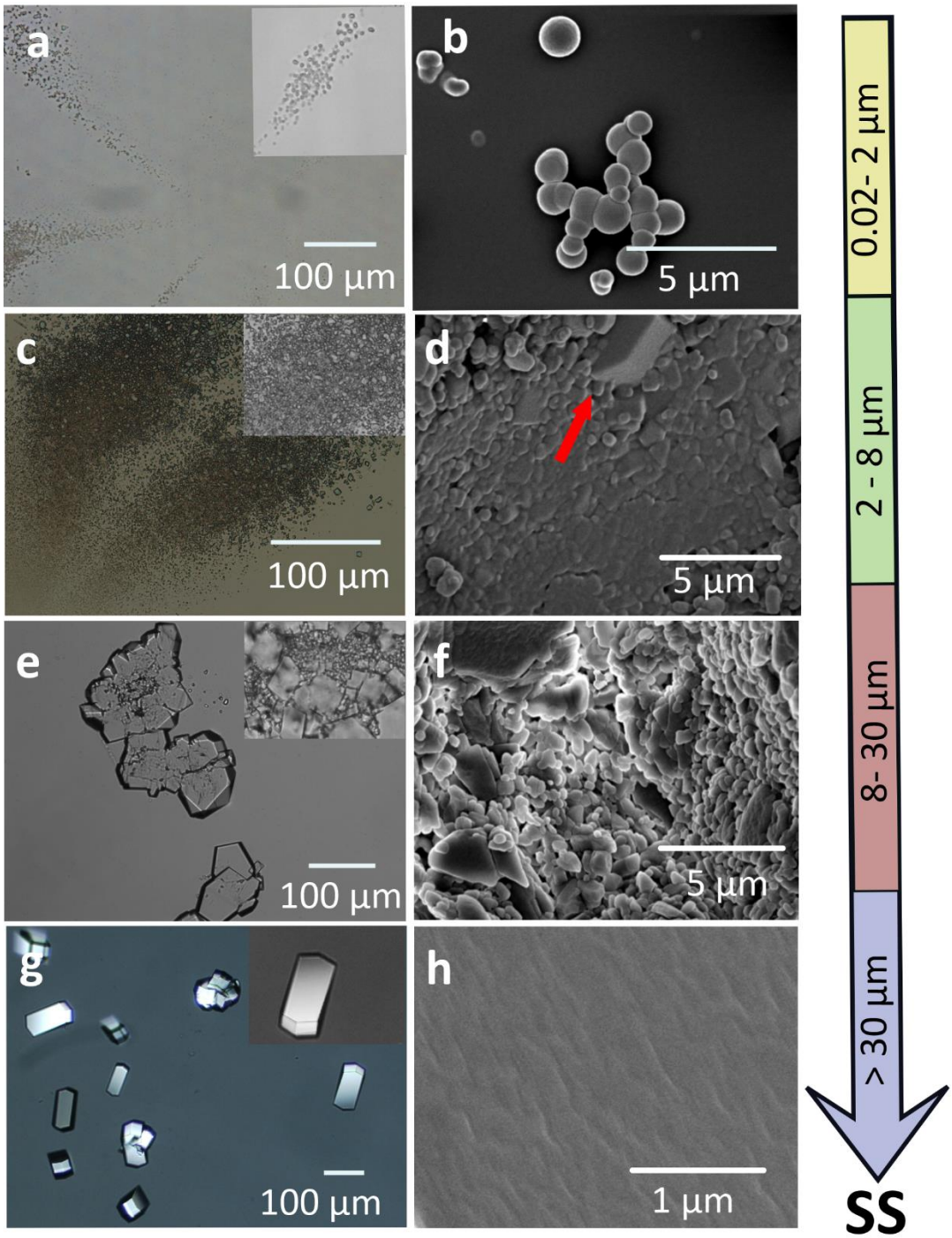

Figure 106. Optical microscope images (a, c, e, g) and SEM images (b, d, f, h) of particles in the different regions observed in the inverted watch glass system after 24 h of lysozyme crystallization. Amorphous solid particles (ASPs) were seen at low surface separations (SS= 20 nm - 2 µm) (a, b). Amorphous solid aggregates and a few crystallites (indicated with the red arrow) growing from the aggregates were observed at SS = 2-8 µm (c, d). Flattened crystalline aggregates were observed at higher SS (SS= 8-30 µm) (e, f). At SS>30 µm lysozyme crystals similar to those observed in bulk were present (g), whose surfaces were not completely smooth (h).

Varying the solution volume from 10 to 2 µL had no effect on crystallization in the inverted watch glass system. The total diameter of the droplet decreased when the total volume was decreased, but the different regions were found at the same SS regardless of the volume (Figure 107). Another interesting observation was that the precipitation at low SS was not uniform throughout the drop, but appeared to be divided into well-defined alternating sections with precipitation and precipitation-free areas (Figure 108).

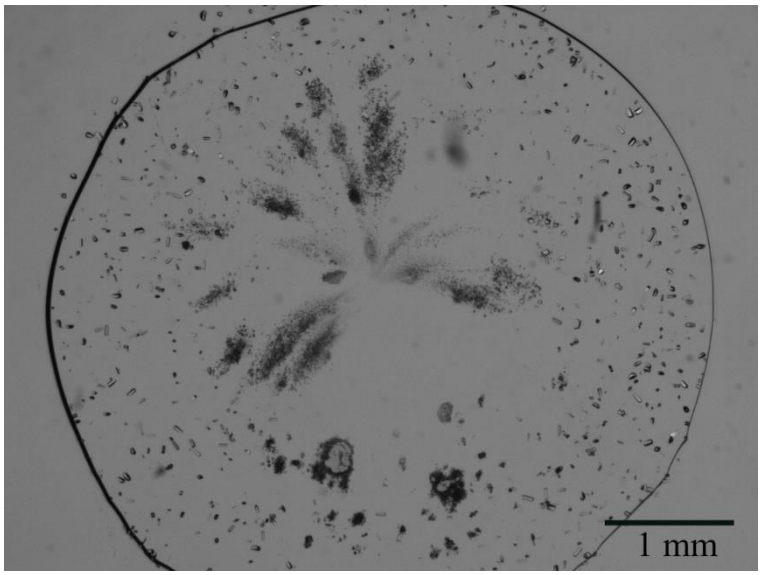

Figure 107. Lysozyme precipitation observed 24 h after injecting 1 µL of protein and 1 µL of precipitant into the inverted watch glass system. ASPs formed at SS = 20 nm-2 µm, amorphous aggregates and crystalline particles at SS = 2-8 µm, crystalline aggregates around SS = 8-30 µm and fully faceted lysozyme crystals at SS > 30 µm.

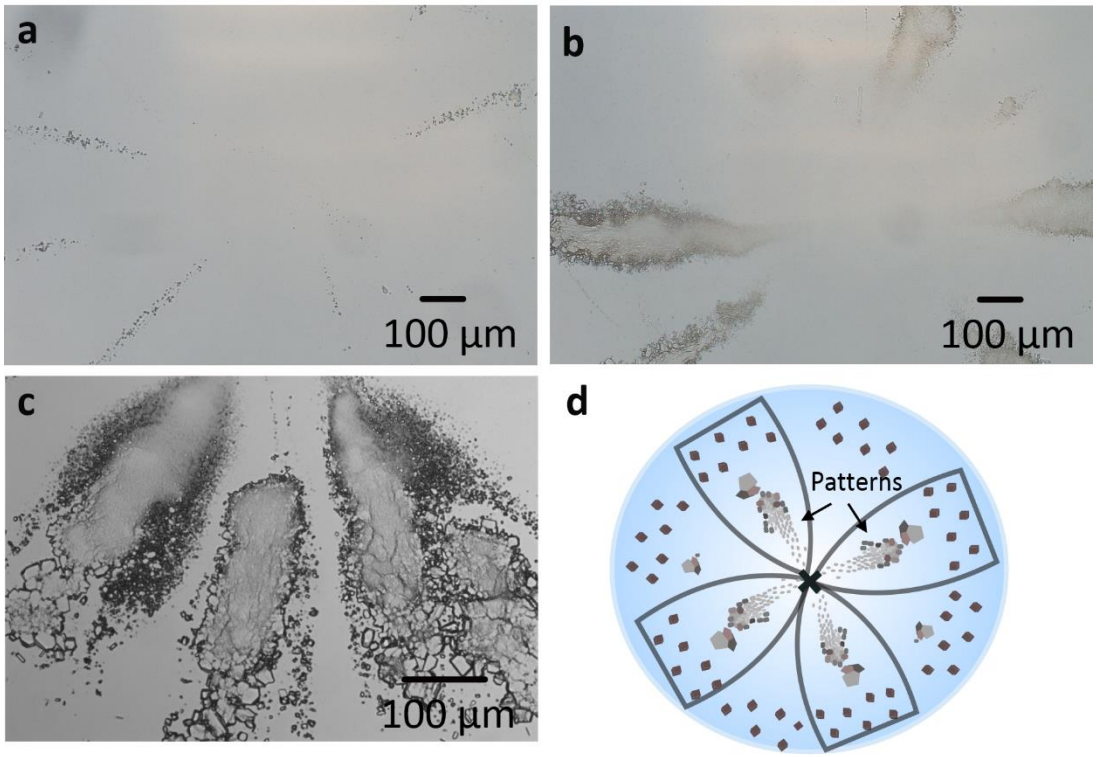

Figure 108. Micrographs (a-c) of lysozyme precipitation in the first two regions of the inverted watch glass system after 7 h (a), 24 h (b) and 48 h (c). The precipitation is not uniform across the surface but forms patterns as illustrated by the diagram in (d).

During protein crystallization, the inverted watch glass system was usually maintained in an incubator at 20 °C and was only removed for imaging once a day. In order to image the early stages of protein precipitation in the inverted watch glass system, the samples were placed under a microscope straight after solution injection and images were taken every 30 min at room temperature. The precipitation of ASPs at low SS was shown to take place after crystallization of lysozyme at high SS and interestingly, it was promoted by slight vibrations or disturbances of the system (Figure 109). The samples kept in an incubator were always imaged after movement since they needed to be transferred from the incubator to the microscope. Therefore, precipitation patterns were usually observed at low SS.

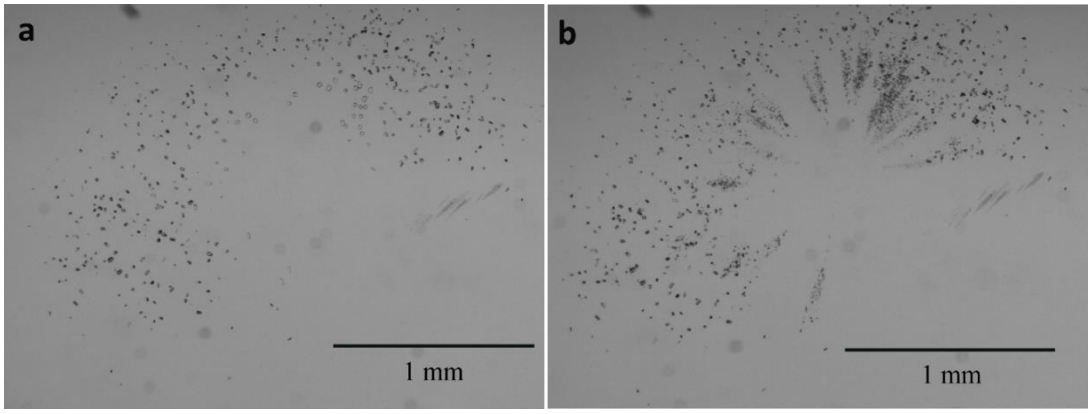

Figure 109. Lysozyme precipitation after 24 h in an inverted watch glass system before (a) and after (b) mechanical disturbance.

Lysozyme was also crystallized in wells of constant SS in order to compare these results with those obtained at different degrees of confinement in the inverted watch glass system. Two systems of SS ~ 5 and 55 μm were employed and lysozyme precipitation was examined by optical microscopy after 24 and 48 h. A large number of well-faceted lysozyme crystals were observed after 24 h in the system with high SS but no crystallization was observed in the system of low SS after 48 h (Figure 110). ASPs were not observed in any of the systems even after mechanical disturbance.

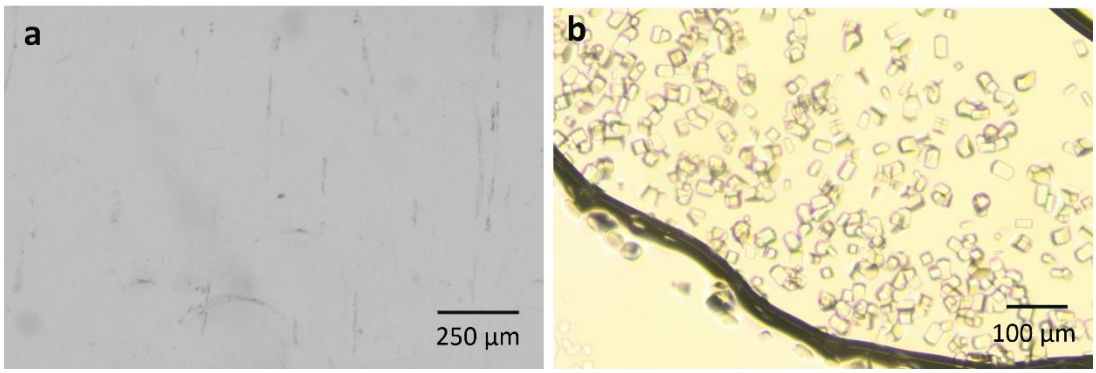

Figure 110. Lysozyme precipitation in wells of constant SS of 5 μm (a) and 55 μm (b) after 2 days. No precipitation was observed in the system of low SS (a) while many crystals formed in the system with larger SS (b). Note that the system of low SS contains some scratches due to the difficulty in removing PDMS from the glass substrate.

Time-resolved observations of phase transformations

Lysozyme crystallization in confinement was followed over one month using optical microscopy. No further transformations were detected after 2 weeks. At times up to 2 weeks, changes occurred mainly at low SS (0.02-8 µm). Individual ASPs that precipitated at low SS after 24 h either dissolved or aggregated over time, resulting in the formation of large amorphous aggregates (ASAs) at SS = 20 nm- 2 µm (Figure 111 b). At SS = 2-8 µm, many crystallites were now observed, where these mainly formed at the edges of the large amorphous aggregates (Figure 111c). A large number of crystalline aggregates were found in at SS = 8-30 µm (Figure 111 d) and large lysozyme crystals were observed at the edges of the droplet (Figure 111 e).

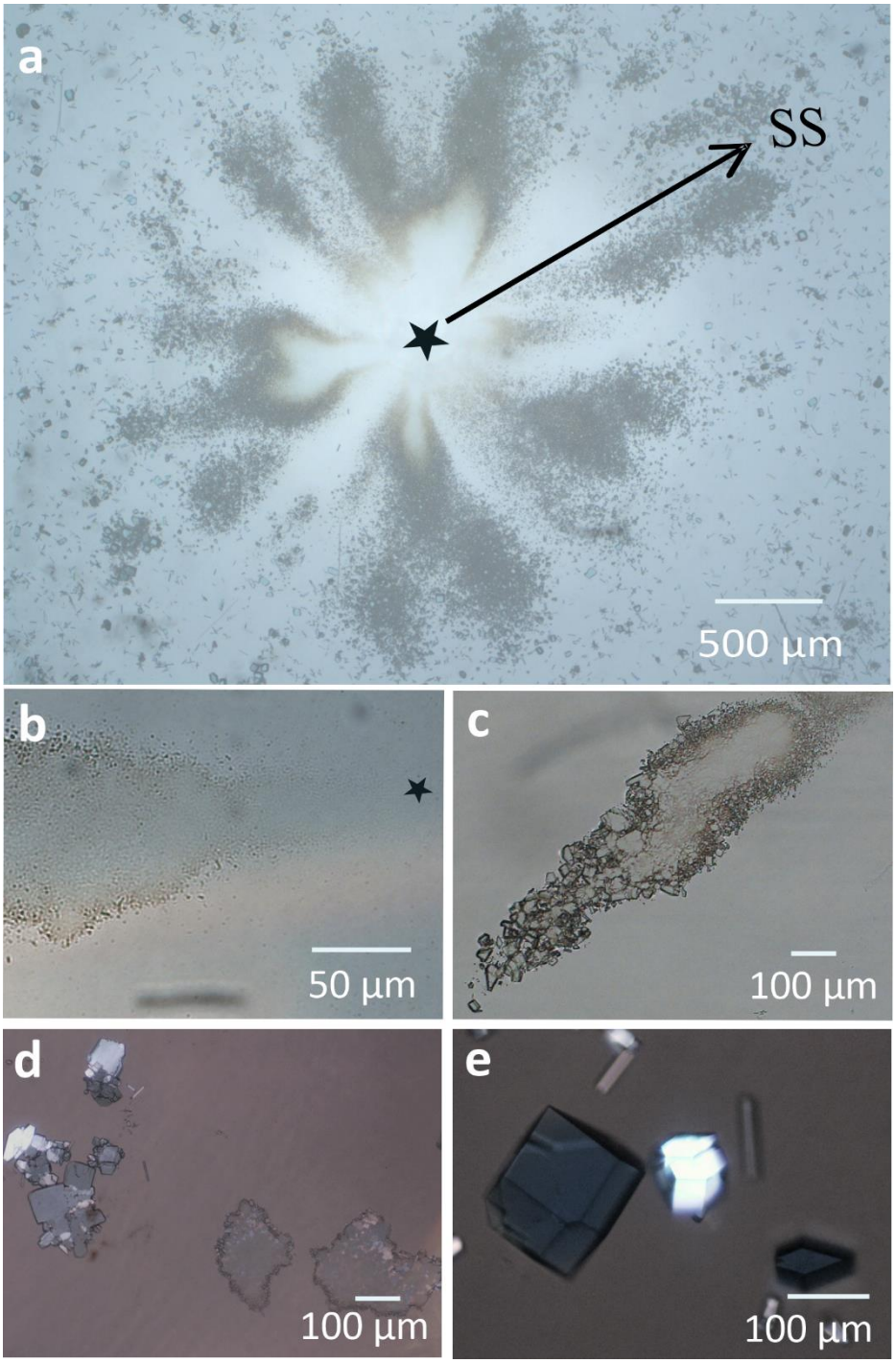

Figure 111. Overview of lysozyme crystallization imaged by optical microscopy in the inverted watch glass system after 2 weeks from solution injection (a). Amorphous particles observed close to the center, SS ~ 20 nm – 2 µm either dissolved or formed large amorphous aggregates (b). Many crystalline particles grew at the edges of amorphous aggregates at SS = 2-8 µm (c) and flattened crystalline aggregates were found in at SS = 8-30 µm (d). Large lysozyme single crystals and crystal clusters were observed at larger SS (e).

Surface chemistry modifications

The influence of the surface chemistry on crystallization in confinement was investigated by coating the glass surfaces with silanes with a range of terminal groups. Firstly, lysozyme was crystallized in an inverted watch glass system with carboxyl functionalized surfaces. After 24 h, no ASPs or amorphous aggregates were observed at any SS, and the first crystalline particles were found at SS > 8 µm. Aggregates of crystalline particles were found in the third region (SS ~ 20 µm) and in the fourth region, together with single crystals of lysozyme (Figure 112 a,b). No significant changes occurred over time, as no significant differences were observed after 1 month.

Coating the inverted watch glass system with methyl terminated silanes had similar effects on lysozyme crystallization. Precipitation of ASPs or amorphous aggregates was not observed at low or high SS, but single crystals and crystalline aggregates formed at SS > 8 µm (Figure 112 c,d). Thus, while we observed larger amounts of precipitation in the non-coated system, at the same times and concentrations, both coated systems promoted crystallization and inhibited ASP formation in confinement. If any ASPs formed between the inverted glass watch and the glass slide, they dissolved or became crystalline much faster than with the non-coated systems. Furthermore, crystalline aggregates of lysozyme in functionalized systems were shown to precipitate as individual patches and no well-defined precipitation patterns were observed as had been seen in the unfunctionalized systems.

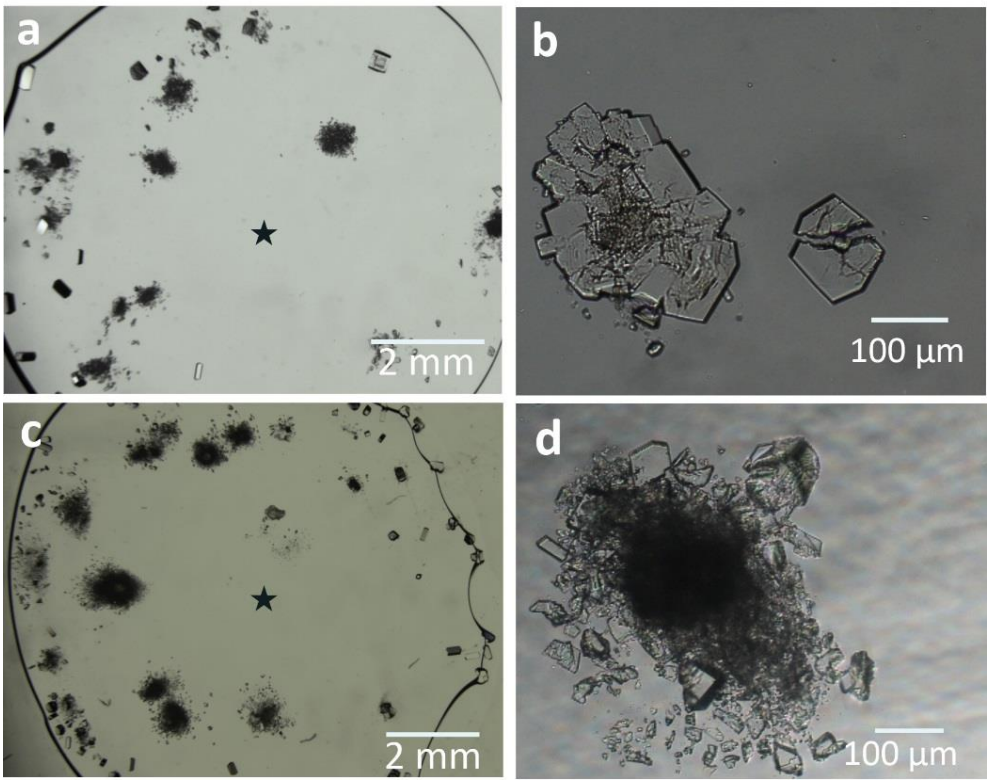

Figure 112. Optical micrographs of lysozyme crystallization in a -COO^- (a,b) and -CH_3 (c,d) coated inverted watch glass system. Neither ASPs nor amorphous aggregates were found at low SS, whereas single crystals and crystalline aggregates were observed at SS > 8 µm (b,d).

5.3.2 Catalase and trypsin crystallization in confinement

To explore the generality of these results, trypsin and catalase were also precipitated in the inverted watch glass system. Trypsin is similar to lysozyme in its small size and positive charge at a working pH of 7. However, catalase is a large and negatively charged protein at pH 7, and it tends to form amorphous precipitates even at low supersaturations in bulk solution (Figure 113b). The crystallization conditions for both proteins in confinement were chosen by prior screening of crystallization conditions in bulk, using the microbatch method. The final crystallization conditions selected in this study are summarized in Table 10.

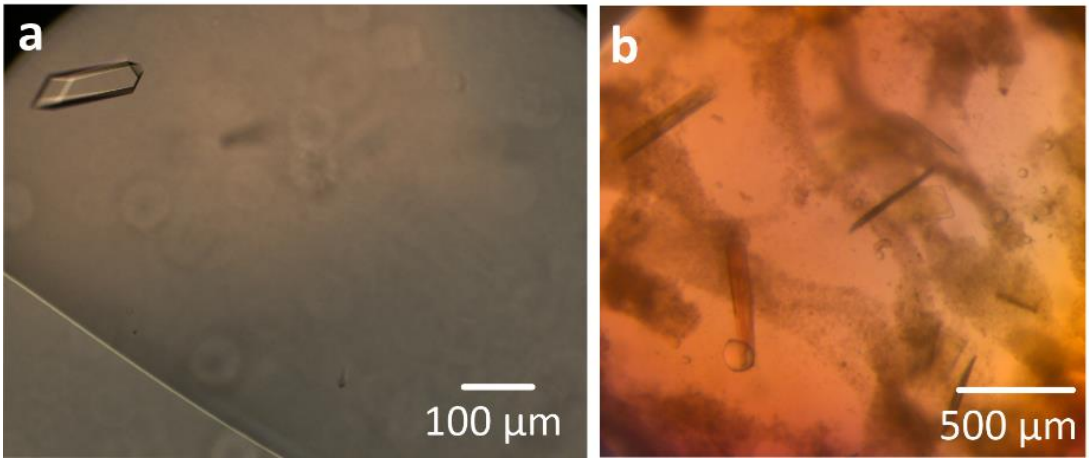

Figure 113. Optical microscopy images of (a) trypsin and (b) catalase in bulk by the microbatch method after 24 h.

The precipitation of trypsin and catalase in the inverted watch glass system were comparable to lysozyme crystallization using the same system, where again four different regions were observed around the contact point between the watch glass and the glass slide. ASPs were observed in region 1 for both proteins (Figure 114 a,b). Amorphous aggregates with a few crystalline particles were observed in region 2 (Figure 114 c,d) whereas more crystalline aggregates were observed in region 3 (Figure 114 e,f). Finally, at SS > 30 µm, crystals of trypsin and catalase were observed, although in the case of catalase, amorphous precipitation could still be observed at high SS as in the case of bulk solution. Precipitation patterns were again observed for both proteins in the inverted watch glass system although it was more obvious in the case of catalase (Figure 114 b,d).

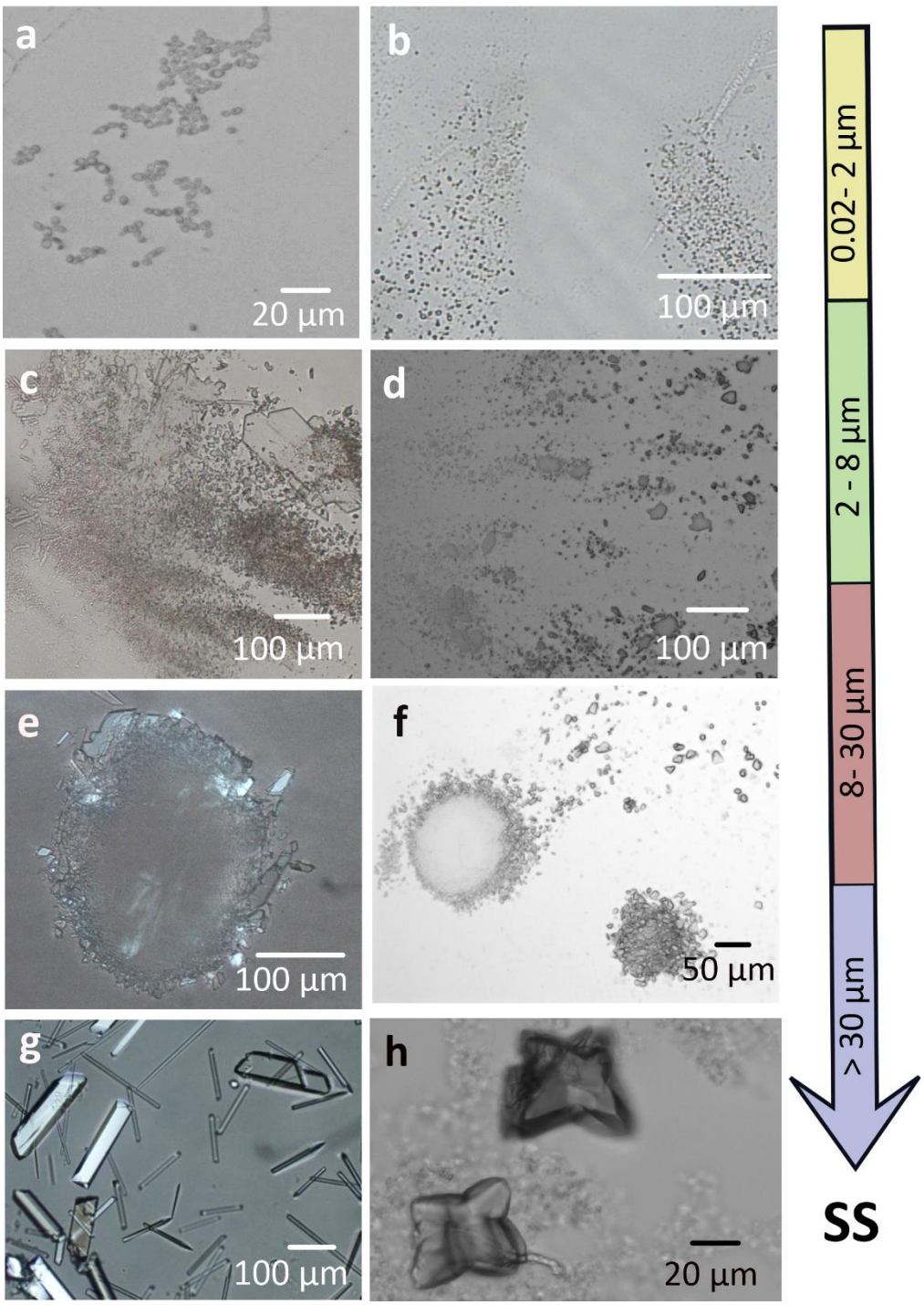

Figure 114. Trypsin (left column) and catalase (right column) crystals in an inverted watch glass system imaged by optical microscopy at different SS. ASPs were observed at low SS for both proteins (a, b). ASPs aggregates at SS = 2-8 µm from which crystalline material starts forming (c, d). Crystalline aggregates observed at higher SS (c, f) and single crystals of trypsin (g) and catalase (h) where amorphous precipitate were still present for catalase at SS > 30 µm (h).

5.4. Discussion

These results showed that confinement can have a large effect on protein crystallization and demonstrated how a simple system such as the inverted watch glass used here can help elucidate crystallization pathways and stabilize metastable phases. A two-step mechanism for protein crystallization has been previously reported for proteins such as lysozyme, hemoglobin and lumazine synthase, where metastable dense liquid clusters acted as precursors to crystal nucleation.[22] The liquid clusters showed different sizes, containing from 10 to as many as 106 molecules, and their lifetimes varied depending on the system.[53, 367] In addition, a study of lysozyme nucleation by liquid-cell TEM suggested an alternative pathway, where proteins could also nucleate from amorphous solid particles (ASPs), which acted as heterogeneous nucleation sites.[61] The experiments described here benefit from the fact that crystallization is slower in confinement than in bulk, which enables *in situ* investigation of the different stages of protein crystal growth.

The precipitation of the proteins lysozyme, trypsin and catalase in the inverted watch glass system revealed a two-step nucleation mechanism, where ASPs acted as precursors for protein crystallization.[61] Liquid phase separation was not observed for any of the proteins studied here, and no evidence was found for crystals nucleating within a single amorphous cluster. Instead, ASPs precipitated and aggregated at low SS (0.02-8 µm) and crystalline particles were usually seen to start forming after 24 h at the edges of the ASP aggregates. The mechanism of crystallization from the ASPs is, however, difficult to determine from these experiments. The crystals could have formed at the expense of the ASPs or they could have grown heterogeneously from the aggregates. Nevertheless, the faceting observed at the edges of the amorphous aggregates seems to be the result of an increase of crystallinity of the amorphous material in the areas in direct contact with the solution rather than a liquid-solid transition. This would explain why the aggregates maintain the same shape after 2 weeks, with many crystallites surrounding them (Figure 111c). If the crystals grew at the expense of the ASPs, one would expect that crystals would form at random locations and the aggregates would dissolve with time. A dissolution-reprecipitation mechanism from the ASPs to

crystals can therefore be discarded. However, it cannot be ruled out that the crystals nucleated directly from the solution and the amorphous aggregates simply acted as heterogeneous nucleation sites.

The crystalline particles observed at SS = 8-30 µm presented rough surfaces containing nano and micron size particles, which suggests that they also formed by the aggregation of ASPs. These crystalline particles were also characterized by their flat surfaces and irregular morphologies, which shows that crystal growth was significantly influenced by confinement. A similar situation was observed when crystallizing $CaCO_3$ in a crossed-cylinders apparatus, where flattened calcite crystals were obtained at low SS.[114] These observations can be due to the templating of crystal growth when the separation between two surfaces is very small. On the one hand, the crystals growing on the inverted watch glass towards the glass slide could find direct physical blockage by the second surface when they reach a certain size, which would prevent crystal growth in that direction. On the other hand, even if the crystals did not contact the second surface, the diffusion of proteins close to that surface would be expected to be very low as compared to the diffusion at edges of the crystals, therefore hindering growth in that direction. Finally, at SS > 30 µm, the solution is shown to behave like bulk, yielding fully faceted protein crystals after 1 day. A schematic representation of possible crystallization mechanisms is shown in Figure 115, where pathway c was observed in this study.

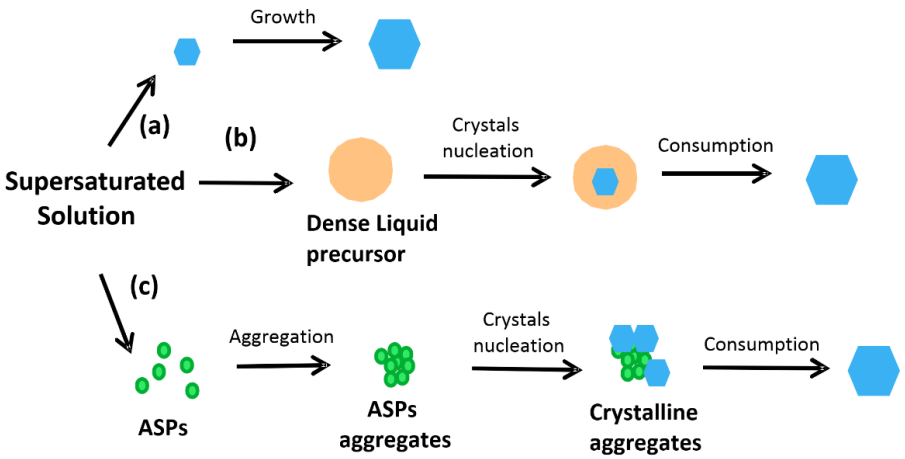

Figure 115. Diagram of three possible pathways for protein crystallization from a supersaturated solution. (a) Classical one-step crystallization where protein molecules in solution assemble into a crystal (observed in bulk). (b) Two-step mechanism of nucleation in which protein crystals nucleate within mesoscopic dense liquid precursors (not observed in this study). (c) Two-step mechanism observed in confinement, where crystals nucleated from ASP aggregates acting as heterogeneous nucleation sites.

One of the most interesting outcomes from the results described in this chapter is the stabilization of ASPs in confinement. Aggregates of ASPs could still be found at low SS (SS=2-8 µm) after one month, while they were not observed after 1 day in bulk. These observations are consistent with previous studies of inorganic solids precipitating in the crossed cylinder apparatus, where amorphous precursors were stabilized in confinement.[89, 114, 118] The stabilization of metastable phases in the inverted watch glass system can be attributed to a number of effects which influence the kinetics of precipitation of the solid.[89] Firstly, an increase of crystallinity of the amorphous material at the edges of the amorphous aggregates was observed, with no evidence for crystallization on single ASPs. This suggests that the aggregation of the ASPs is required for crystal nucleation. The aggregation of amorphous particles at low SS must be significantly lower than at high SS since the diffusion of these large particles in confinement will be limited.[118] Indeed, it has been shown that the diffusion coefficient of solid particles of few hundreds of nanometers in size, confined between two walls, is lower than in bulk.[368] A slower aggregation of ASP particles at low SS might result in the slower nucleation of the protein. Furthermore, it has been suggested that the contact between

particles precipitating at very low SS between two crossed cylinders and the solution is limited.[118] A limited contact between the amorphous aggregates with water would reduce their probability of crystallization since it has been shown that protein crystals contain large percentages of solvent in their structures.[369] This scenario must be especially relevant at the surfaces of the aggregates that are close to the glass surfaces. This could also explain why we observe crystal formation at the edges of the amorphous aggregates. Finally, the probability of crystal nucleation at high SS will be higher than in confined areas, and possible impurities acting as nucleants for protein crystallization, will be most likely found at high SS, thus increasing the chances of nucleation.

The relevance of these results to protein crystallization not only involves a fundamental mechanistic understanding but also has more practical applications. Protein crystallographers have over the years decreased the volume of the reaction wells where proteins crystallize, since proteins are on many occasions expensive and limited. However, decreasing the volume of solution also decreases the probability of nucleation as previously suggested by Ning *et al*.[23] and confinement effects might start having an influence on crystallization. The fact that crystals never nucleated at SS < 2 μm but they readily nucleated at higher SS shows that the probability of protein nucleation in confinement was significantly lower than in bulk, which was reaffirmed with the use of systems with constant SS. The results demonstrated once again the large influence of the crystallization environment on nucleation,[370] and showed that confinement effects must be taken into account when crystallizing proteins, especially in new systems involving very small volumes such as microfluidics.[143, 144, 371, 372] When crystallizing proteins in restricted volumes, it might be important to consider not only the total solution volume but also the spatial characteristics of the crystallization environment. For example, confinement effects started to be noticeable here at surface separations as large as 30 μm. Note that most microfluidic systems reported until now for protein crystallization contain droplets of > 100 μm in diameter, and therefore confinement effects may not be important in these systems.

In addition, protein crystallization in the inverted watch glass system revealed Ostwald ripening effects. As described in the previous chapter, transport in confined systems is generally driven by diffusion, since advection and convection are reduced in small volumes. Here, protein precipitation at low SS was seen to occur in well-defined patterns. The precipitation at low SS took place after the proteins crystallized at high SS, and it was induced by mechanical disturbances of the system (Figure 108). Preferred nucleation at higher SS is in agreement with the results discussed in the previous chapter: when there is a competition between confined and non-confined areas, crystallization usually takes place in the non-confined space. Furthermore, many studies have shown evidence that confined spaces can achieve high levels of supersaturation before nucleation.[177, 270] Thus, although nucleation first occurred at high SS in the inverted watch glass system, the supersaturation at low SS might have been very high. Slight vibrations of the system could therefore cause a further increase of the local concentration of the proteins at certain areas, triggering precipitation and depleting the areas next to the precipitation zones. This effect had never been seen before using the crossed cylinder apparatus with inorganic solids[114, 118] which might be due to the lower solubility of these solids. Lower supersaturations are needed for the precipitation of these solids and therefore, precipitation at low SS could potentially happen spontaneously, with no formation of precipitation patterns. These novel observations offer the possibility of building further understanding of how confinement affects ion/molecular diffusion, which is very important in many processes in nature.

Finally, the combined effect of confinement and surface chemistry on lysozyme crystallization was also investigated. Two surface chemistries were tested - carboxylate and methyl terminated surfaces and both were seen to prevent the stabilization of ASPs and amorphous aggregates in confinement. That ASPs were not detected in the coated systems could be attributed to a faster crystallization of the protein on the coated surfaces. Previous studies in bulk have shown that protein crystallization can be significantly promoted on functionalized surfaces due to fluctuations in the protein concentration when proteins interact with the functional groups of the coated surfaces.[204, 228]

Lysozyme molecules have been shown to readily adsorb to methyl terminated surfaces due to van der Waals interactions of their hydrophobic amino acids with the surfaces.[373] [204] In the experiments described here, lysozyme will be positively charged at the working pH, and therefore should be able to interact with the partially-deprotonated carboxylate surfaces.[374] If protein crystallization is enhanced on coated surfaces, large crystals might consume the protein molecules in the droplet faster than in the non-coated systems. This would reduce protein concentrations at lower SS, inhibiting lysozyme nucleation in confinement. Moreover, precipitation on coated surfaces did not show patterning but instead occurred as more localized precipitation at high surface separations (SS > 8 μm). This supports the idea that nucleation occurs more rapidly on the coated surfaces, where a large number of crystallites nucleated at random locations in the drop as observed in Figure 112. This causes protein molecules to be consumed and therefore the lack of precipitation at low SS.

5.5 Conclusions

This chapter described a study of the crystallization of the proteins lysozyme, catalase and trypsin in confinement using an inverted watch glass system. It was demonstrated that all three proteins precipitated as amorphous solid particles (ASPs) at low surface separations (SS). These aggregated, becoming precursors for protein crystallization, following a two-step nucleation mechanism. ASP aggregates were stabilized in confinement, although individual ASPs at SS < 2 μm dissolved or aggregated after 24 h. Moreover, it was observed for the first time that the proteins precipitated as well-distributed patterns across the crystallization droplet following the Ostwald principle. This precipitation process was avoided when the surface chemistry of the glass was modified with carboxyl or methyl terminated silanes. The coated systems promoted crystallization at high SS and the precipitation of ASPs in regular patterns in confinement was inhibited. The lack of precipitation in confinement in the functionalized system was linked to faster crystallization of the proteins at high SS, which consumed protein molecules, and prevented ASPs from being stabilized in confinement. These

results present a novel system for studying protein crystallization *in situ* at different degrees of confinement, which is important since crystallization in nature often occurs in restricted volumes. Moreover, in protein crystallization the reduction of the crystallization volume is in many cases required for crystallization screening, making the study of protein crystallization in limited spaces relevant. Finally, the fact that crystallization processes are slower in confinement than in bulk allowed us to gain insight into the mechanism of nucleation of proteins and to stabilize and analyze metastable phases.

Chapter 6: The effect of surface chemistry and topography on protein crystallization

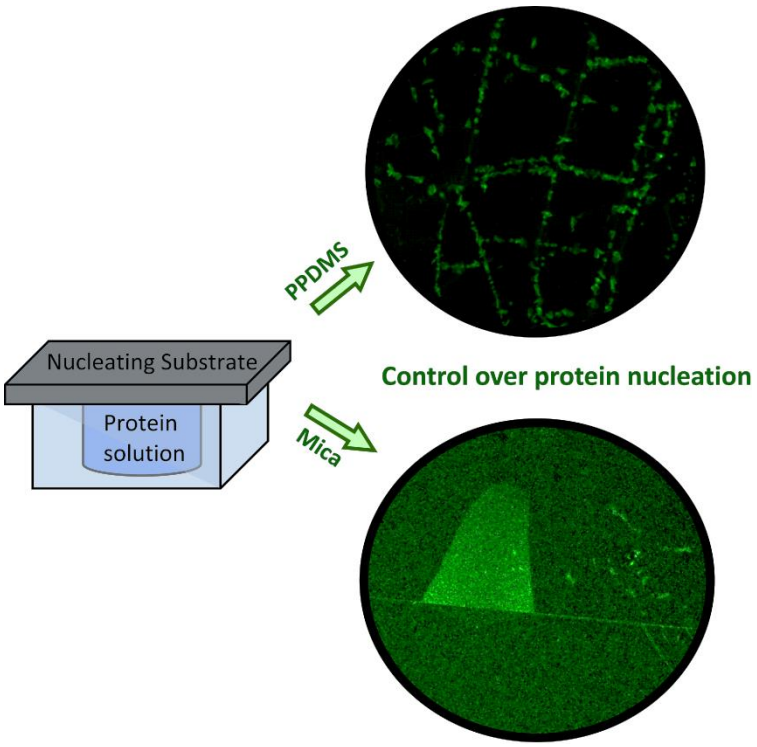

6.1 Introduction

6.1.1 Aims and overview

In the previous chapter, confinement was used as a tool to better understand the mechanism of crystallization of model proteins by retarding their crystallization. Nevertheless, the main problem with protein crystallization is the difficulty in inducing protein nucleation, which frequently requires the trial of hundreds of crystallization conditions, involving long times and high amounts of protein. In order to control and facilitate protein crystallization, recent studies have focused on the use of “nucleants” that promote the heterogeneous nucleation of proteins.[204, 222, 226] Substrates of different roughnesses (such as porous media) or surface chemistries have been commonly used as nucleating agents.[73, 222] However, the search for a “universal nucleant” capable of promoting the crystallization of both model and target proteins is still ongoing, where identifying the specific elements that are required to induce protein nucleation is essential for the optimal design of such a nucleant.[216]

This chapter presents two novel systems to control protein nucleation using a combination of topographic and chemical effects. The first system studied was plasma treated poly(dimethylsiloxane) substrates (PPDMS). PDMS substrates acquire fractured surfaces on exposure to air-plasma for sufficient time, where these act as topographic defects on which crystals preferentially nucleate. The second system consists of freshly-cleaved, chemically-modified mica. Silanized mica has already been shown to promote the crystallization of various proteins. However, surface chemistry effects were mainly associated with these observations.[228, 229] The effect of the natural defects present on cleaved mica on protein nucleation might have a large influence on their crystallization and has never been studied before. Three model (lysozyme, trypsin, thaumatin) and one target (crustacyanin, α-C) protein were crystallized on PPDMS and chemically modified mica with the objective of gaining insight into the effect of topography on crystallization and into what topographic defects are more favourable for protein nucleation.

The results demonstrate that the surface chemistry and the topography of a substrate play important roles in controlling protein crystallization and the combination of both effects is essential to promote protein nucleation. Indeed, while the cracks of uncoated PPDMS did not promote crystallization, crystals of the studied proteins showed a strong preference for the cracks of carboxyl-terminated PPDMS substrates. Moreover, methyl-terminated PPDMS surfaces often induced liquid-phase separation at the cracks of the substrate due to the high concentration of protein in the fractures. Preferential nucleation of the studied proteins was also observed at the step-edges and cave-like openings of carboxyl or methyl terminated cleaved mica, while no crystals were observed on uncoated mica surfaces under the same conditions. These results provide the first direct observations of protein nucleation within topographical features, demonstrating that the heterogeneous nucleation of the proteins in the features is due to an increase of the local concentration of the proteins in the defects by diffusion-adsorption effects.

6.1.2 Introduction to PDMS

Poly(dimethylsiloxane) is an organosilicone polymer with chemical structure –$((CH_3)_2SiO_2)_n$-. It has been widely used in industry due to its outstanding properties such as flexibility, gas permeability, optical transparency, biocompatibility and low surface tension.[375-377] In addition, its easy and cheap fabrication, low toxicity and inertness make PDMS an excellent material for the manufacture of microfluidic devices and molds.[378] One of the most important characteristics of PDMS is the ability to easily modify its wettability, which affects its adhesion, benefitting for example biomedical areas.[379] The hydrophobic surfaces of PDMS can be made hydrophilic by exposing it to an oxygen plasma for a period of time.[380] The plasma formed in a chamber at low pressures produces highly reactive species such as free radicals, ions, electrons and excited molecules.[381] During this process, oxygen radicals displace methyl groups on the surfaces of PDMS, which oxidize in the presence of air as shown in Figure 116.

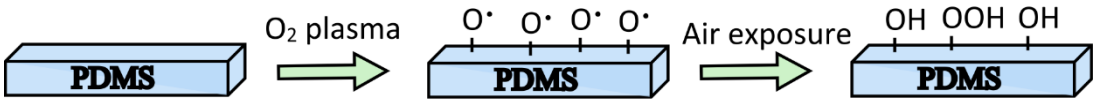

Figure 116. Diagram of the surface of a PDMS substrate during and after plasma treatment.

The exposure time of PDMS to plasma defines the thickness of the silica-like surface layer on the substrate. Short exposures to an oxygen plasma leads to surface layers thinner than 3 nm, while longer exposures generate surface layers of up to 10 nm that mainly consist of SiO_x, where each silicon bonds to three or four oxygen atoms.[382, 383] Interestingly, this process is reversible and the hydrophobicity of PDMS recovers with time.[378] When a PDMS substrate is heavily oxidized, waves or cracks on the surfaces are formed in order to facilitate the transport of low molar mass PDMS to the surface, promoting the hydrophobicity recovery.[380, 384, 385] Various studies have observed that wavy plasma treated PDMS (PPDMS) can induce the crystallization of a range of model proteins, although control over their nucleation was limited.[386, 387] PPDMS presents a system with controlled topographic defects which could be used to direct protein nucleation, as previously shown for $CaCO_3$.[193]

6.1.3 Introduction to target proteins

Over the last 20 years, researchers have determined the 3D molecular structure of thousands of proteins, using mainly X-ray crystallography and to a lesser extent, NMR spectroscopy. However, despite the large number of structurally-resolved proteins, many protein structures remain unsolved due to the difficulties in forming the large, high quality crystals necessary for X-ray characterization. These proteins of unknown structure are known as “target proteins”, as their crystallization is the main objective of most protein crystallographers and structural biologists.[388] The target protein alpha-crustacyanin (α-C) was selected and crystallized on the substrates presented in this chapter. A brief introduction to this protein is presented next.

Alpha-Crustacyanin (α-C)

α-C is a protein that is mainly found in the shells of lobsters. It belongs to the family of carotenoids and it is characterized by its bright blue color, which is responsible for the coloration of various crustacea.[389] Additionally, carotenoids are responsible for bringing vitamin A to the organism, participating in photosynthetic processes and acting as antioxidants. α-C has been crystallized before,[223] but the crystals obtained were usually too small or their quality was too low to obtain atomic-level crystal structure. Nevertheless, there have been a few studies where electron microscopy or small angle X-ray scattering techniques were used to estimate the shape and assembly of this protein.[390] Thus, α-C has been shown to comprise eight subunits of the protein β-crustacyanin,[391] forming a cylinder of about 9-10 nm and 22-25 nm in length.

6.2 Experimental

6.2.1 Plasma treated poly(dimethylsiloxane) (PPDMS)

A PDMS elastomer kit (Sylgard 184) was obtained from Dow Corning. The silicon base was thoroughly mixed with its curing agent in a 10:1 ratio and 13 g of the mixture was poured into a 100 x 100 mm square petri dish. The mixture was then degassed under vacuum until no more bubbles were observed and it was finally cured at 60 °C for 24 h. The cured PDMS was cut into rectangular sections of about 5 x 50 mm which were placed in a plasma cleaner (Harrick PDC-002) for 7 min. The PPDMS strips were then cut into smaller squares of about 5 x 5 mm, which were used within a day as a substrate for protein crystallization.

Surface modifications of the 5 x 5 mm PDMS and PPDMS sections were carried out by coating the substrates with a thin metal layer and then immersing them in a thiol solution. A more detailed description of the coating method can be found in the second chapter of this thesis (2.1.1.3). The substrates were used for crystallization experiments straight after the coating to avoid the accumulation of undesired impurities on their surfaces.

6.2.2 Mica substrates

Muscovite mica was obtained from Paramount Corp., New York and it will be referred to as “mica” throughout this thesis. The composition of this mineral is KAl_2- $(AlSi_3O_{10})(OH)_2$ and it exhibits a layered structure bonded through weak potassium ions which allows its easy cleavage. Here, large sheets of mica were first cleaved along their (001) plane. Squares of around 5 x 5 mm in size were selected from the cleaved mica and cut with scissors. The mica sheets and smaller substrates were handled under a laminar flow cabinet to prevent contamination. Before use, the substrates were rinsed with ethanol and dried under N_2 flow.

In order to modify the surface chemistry of the mica, the substrates were first exposed to air plasma for 2 min to induce the formation of hydroxyl groups on their surfaces.[392, 393] The substrates were then placed in a vacuum chamber in the presence of a liquid silane and the coating was performed by vapor deposition following standards methods,[229] as described in the general preparation methods of this thesis (2.1.1.3).

6.2.3 Crystallization methods

Thaumatin from Thaumatococcus danielii, 2-(N-morpholino)ethanesulfonic acid (MES), sodium potassium tartrate (NaKT) and polyethylene glycol (PEG) 5K were obtained from Sigma Aldrich and were used without further purification. The target protein alpha-crustacyanin (α-C) was provided by Professor Naomi Chayen of Imperial College of London. Table 11 summarizes the crystallization conditions used in this chapter.

Protein	Buffer solution (in water)	Protein concentration (in buffer) (mg/mL)	Precipitant solution (in water)
Lysozyme	0.1 M sodium acetate pH 4.5	20	0.8-1.2 M NaCl
Trypsin	10 mM $CaCl_2$ 10 mg/mL Benzamidine 20 mM Hepes pH 7	60	20-30% PEG 8K 0.1 M Tris pH 7.5
Thaumatin	H_2O	20	0.5 to 1 M NaKT
Alpha-C	0.1 MES pH 6.5	7	20 % PEG 5K 0.15 M $(NH_4)_2SO_4$, 0.07 M MES

Table 11. Crystallization conditions selected for protein crystallization on surfaces.

Previous studies of the effects of surface chemistry and topography on protein crystallization have used a vapor diffusion method, where protein droplets sat on the substrates until they crystallized.[204, 394] The ability of a surface to nucleate protein crystals was then measured by the presence and number of crystals in the droplet. Nevertheless, it is important to note that substrates with different surface chemistries have different wettability and therefore, the evaporation rate at different points of the rod is different. More crystals are then expected in droplets deposited on hydrophilic substrates since their evaporation rate will be higher (Figure 117). These observations have, however, little to do with the interaction of the proteins with the surfaces and their heterogeneous nucleation from the substrates.

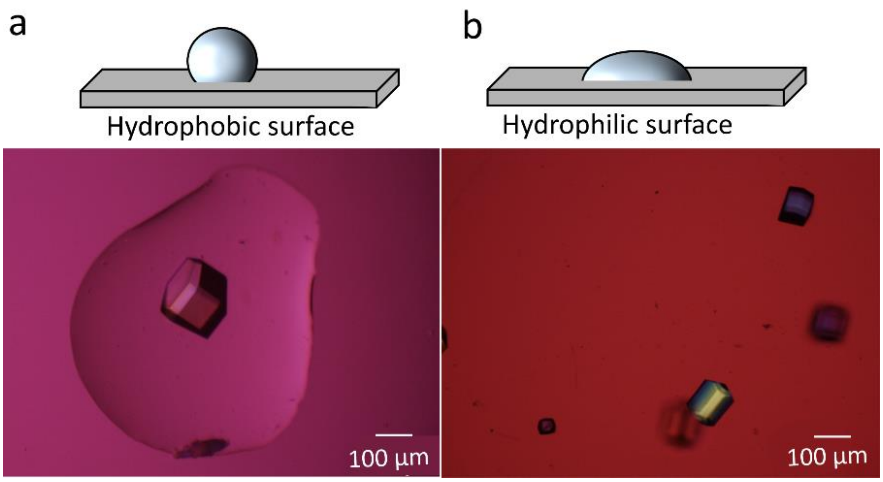

Figure 117. Differences in wettability and lysozyme crystallization on (a) hydrophobic and (b) hydrophilic surfaces.

Here, protein crystallization on different substrates was carried out by the batch method, where a mixture of protein and precipitant solutions is placed under paraffin oil to prevent evaporation. Moreover, in order to have a better idea of the real effect of the surfaces on crystallization, closed cells where the solution is in complete contact with the substrate regardless of its wettability, are necessary. With this purpose in mind, PDMS well plates were manufactured by the following process. Firstly, 20 g of pre-cured PDMS were poured into two 100 x 100 mm square petri dishes (10 g in each), generating 2 samples of around 1 mm thick PDMS. After degassing and curing the PDMS at 60 °C, 2 mm cylindrical holes were punched on one of the PDMS samples using a 2 mm diameter biopsy punch. The two PDMS samples where then plasma treated for 2 min to activate the PDMS substrates prior to bonding. The sample with voids was then bonded to the second PDMS sample, leading to a plate with cylindrical wells of 2 mm in diameter and 1 mm in height. The PDMS plate was then left in the oven at 60 °C for 5 min to ensure a strong bond. A schematic diagram of this procedure is shown in Figure 118.

Protein crystallization in the PDMS well plates was carried out by first dispensing 4 µL of solution into each well. Subsequently, the desired substrates (e.g. PPDMS or mica) were glued to the PDMS plates using EVO-STIK epoxy glue (Bostik, UK) and they were then left to dry at ambient

conditions for 5 min. Note that the substrates were always placed above the solution in order to avoid any crystals precipitating in bulk from settling onto the substrates (Figure 118). PDMS is gas-permeable and therefore, the PDMS well plates were kept under paraffin oil at all times after solution injection to prevent evaporation of the solution. As PDMS and mica are optically transparent, the crystals growing in the wells or on the substrates could be imaged by optical microscopy without opening the wells. Nevertheless, the wells can be easily opened by peeling the PDMS off the substrate in order to collect or further image the crystals with other techniques. Moreover, the volume of solution contained in the cells can be adjusted by simply increasing or decreasing the height or diameter of the wells.

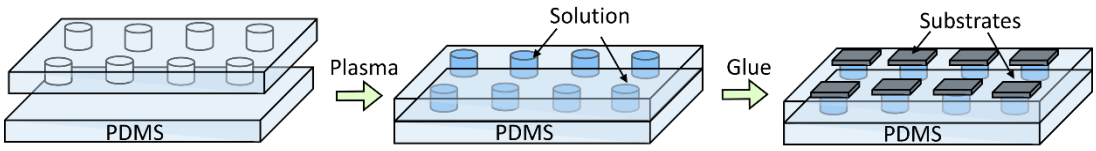

Figure 118. Diagram illustrating the manufacturing process of PDMS well plates for protein crystallization on different substrates.

6.2.4 Trace fluorescent labeling of protein molecules

In order to observe protein molecules in solution and to distinguish protein crystals from possible salt precipitates, the proteins were trace-labeled with the fluorescent dye fluorescein isothiocyanate (FITC). Although the crystallization of proteins might be affected by the presence of dyes or other additives, it has been demonstrated that by only labeling the protein with trace-levels of the dye, its crystallization remains unaffected.[395, 396] The method used for labeling the proteins was as follows; a concentrated protein solution of around 100 mg/mL (in buffer) was prepared in a centrifuge tube and 0.08 mL of this solution were transferred to another centrifuge tube. 1-20 µL (depending on the protein) of a 1mg/mL solution of FITC were added to the second tube where the mixture was left to react for 30 min. Subsequently, 50 µL of a solution of 0.1M glycine were added to react with any unreacted dye. This solution was then transferred to the first centrifuge tube with the initial unlabeled protein and the total solution was filtered with a Millipore 15000 MW

membrane. These membranes allowed the transit of molecules smaller than 15000 Da through them, but they retain the larger ones (protein and labelled protein). Thus, unreacted dye, glycine and labelled glycine should pass through the filter. Finally, the protein solution was washed 3 times with a buffer solution and the protein concentration was estimated by measuring the amount of solution left on the membrane.

Previous studies showed that the fluorescence intensity of the dye 1-anilino-8-naphthalenesulfonate (ANS) increases with the degree of unfolding of a protein. Here, ANS dye was used to test the folding integrity of lysozyme on methyl terminated substrates.[397, 398] Both ANS and lysozyme were dissolved in buffer solution (0.1 M sodium acetate pH 4.5) at 10 mM and 80 mg/mL respectively. 150 µL of the 10 mM ANS solution were then mixed with 150 µL of lysozyme 80 mg/mL and 255 µL of buffer solution and the final solution was used for crystallization experiments.

6.2.4 Patterning of PPDMS with TEM grids

Copper TEM grids were used as contact masks for the formation of controlled nucleation areas. On a PPDMS substrate, the cracks are randomly distributed across the surface. However, by patterning the substrates, it is possible to gain control over the distribution of the cracks on them. Here, TEM grids with various shapes were employed to cover parts of the PDMS substrates from being exposed to oxygen plasma. TEM grids were obtained from Agar scientific with 150 square mesh or 75 hexagonal mesh and they were 3.05 mm in diameter. They were carefully placed on PDMS stripes and exposed to 7 min of O_2 plasma. The substrates were then coated with 10 nm of iridium and the TEM grids were removed before immersing the substrates in thiol solution. For homogeneous coating of the PPDMS substrates, the TEM grids were removed straight after plasma treatment and the substrates were coated with 2 nm of chromium and 10 nm of gold before then forming the SAM.

6.2.4 Nanofabricated silicon substrates

Silicon substrates with topographic features of specifically designed sizes and shapes were also used to control protein crystallization. The nanofabricated substrates used in this thesis were manufactured in a cleanroom by Dr. Angela Bejarano-Villafuerte. The common procedure for the fabrication of the substrates is illustrated in Figure 119. First, a silicon substrate was coated with a layer of photoresist (ZEP520-A) and trenches of 100, 150 and 200 nm in width were obtained by electron beam lithography (EBL). Two different techniques were then used to obtain two types of trenches. The first one is reactive ion etching (RIE), which combines a plasma treatment of O_2 and SF_6 to produce a vertical etch on the silicon of approximately 500 nm. The second technique was a wet (or chemical) etch with a 40% KOH solution at 60 °C. This method produced inclined trenches that formed a wedge (Figure 120b), although the width of the final trenches was usually slightly larger than the ones obtained by RIE. After the etching processes, the substrates were immersed in piranha solution for 2 h to remove the photoresist and any remaining organic contamination. The substrates used in this thesis presented straight trenches across the surfaces with separations of 25 and 50 μm.

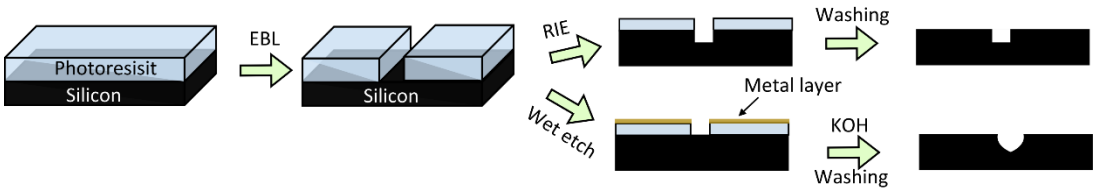

Figure 119. Nanofabrication process of silicon substrates with trenches of controlled size and shape.

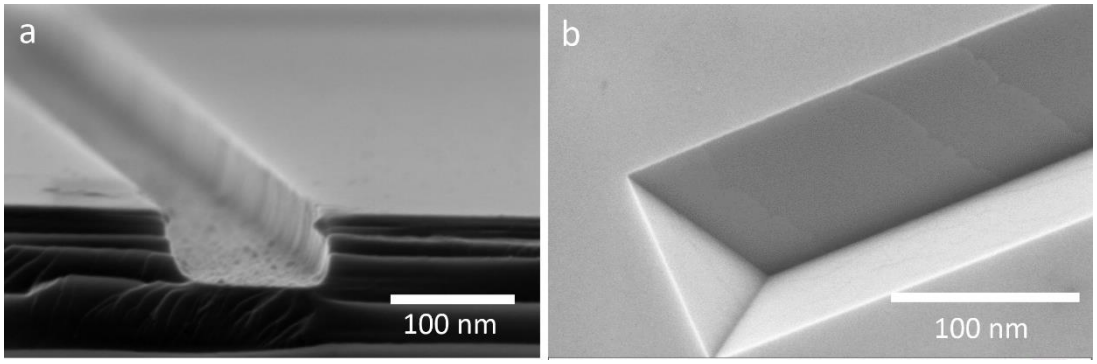

Figure 120. SEM micrographs of nanofabricated trenches on silicon substrates manufactured by reactive ion etching (a) and wet etch (b). Figures printed with the permission from Dr. Angela Bejarano-Villafuerte.

Surface modifications of the substrates were carried out by depositing a 10 nm layer of iridium on their surface before immersion in thiol solution. After coating, the substrates were placed in the precipitant solutions used for protein crystallization and they were degassed for 30 min. This step is important since any trapped air in the trenches would impede protein crystallization.

6.3 Results

6.3.1 Protein crystallization on PPDMS substrates

6.3.1.1 Characterization of PPDMS substrates

Cracks of hundreds of microns in length and 1-2 μm in width were typically observed by optical microscopy (Figure 121) after exposing the PDMS substrates to O_2 plasma for 7 min. The distribution of the cracks on the PPDMS substrates was however, reasonably diverse and difficult to predict. The most common layout was the rectangular grid-like distribution of cracks illustrated in Figure 121a. Nevertheless, more curved or irregular arrangements were also often observed using the same procedure (Figure 121 b,c). The density of the cracks can also vary from one substrate to another and even on the same substrate, where specific areas of the substrate might show higher crack densities than others (Figure 121d). The depth of the cracks is difficult to measure. However, previous characterization of cracks

obtained on PDMS using the same procedure as described here, showed that the depth of the tranches usually ranges from 80 to 260 nm.[193]

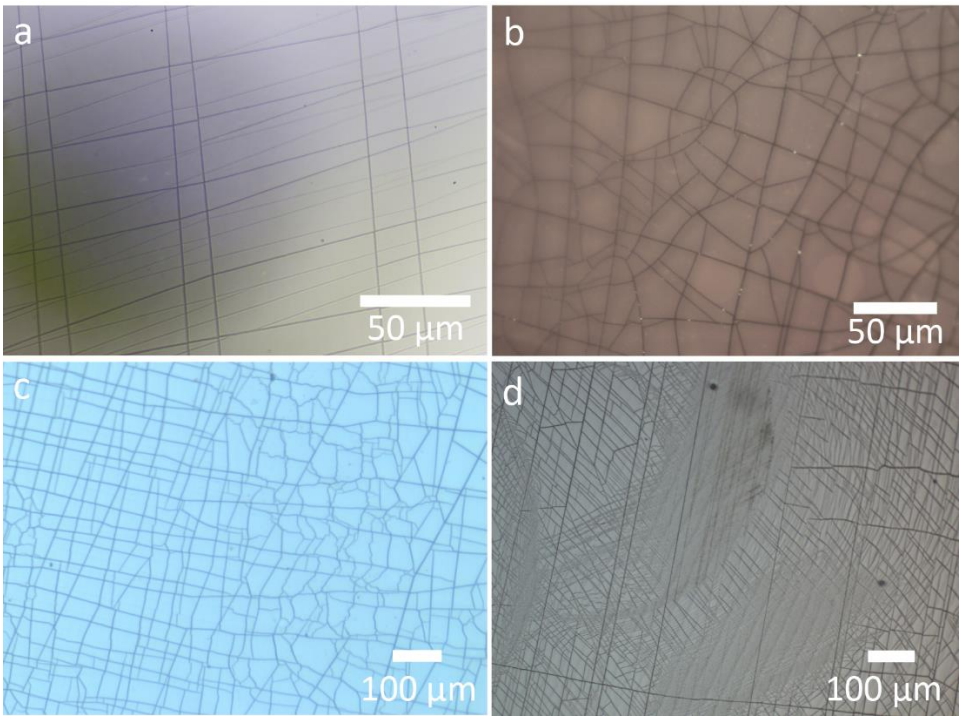

Figure 121. Optical micrographs of PPDMS substrates after iridium deposition showing different crack distributions.

Interestingly, although the width of the cracks was in the micron-range, internal nano-features are likely to form within the microcracks as shown by Lee.[193] The dimensions of the nanocracks observed by SEM ranged from <10 nm to around 90 nm (Figure 122) and their presence plays an important role in nucleation as will be discussed later in this chapter.

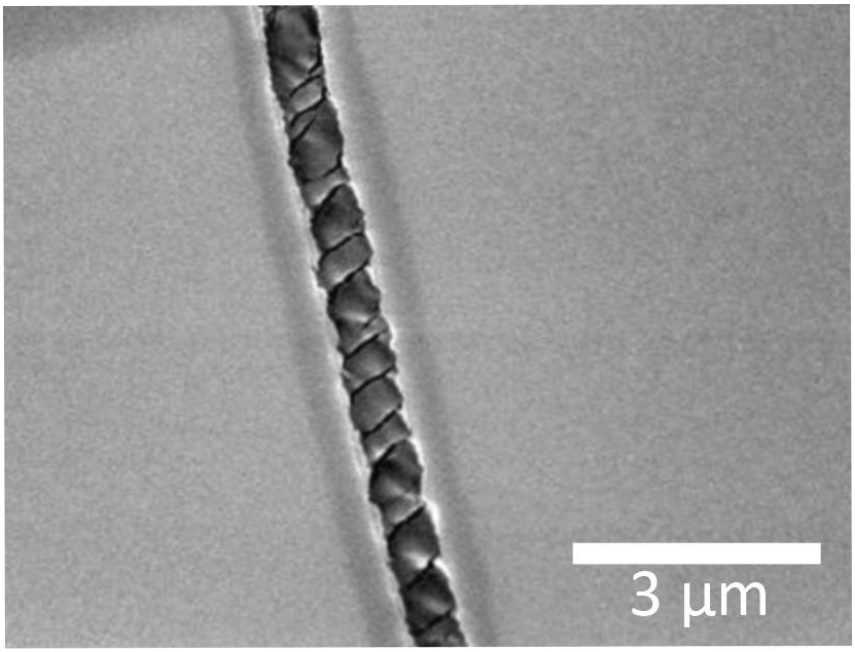

Figure 122. SEM image of nanofeatures formed within a microcrack on a PPDMS substrate. Figure shown with permission from Dr. Phillip Lee.[193]

In order to compare protein crystallization on substrates with different surface chemistries and topographies, substrates comprising cracked PPDMS, functionalized PPDMS, non-plasma treated PDMS and functionalized PDMS were investigated. Functionalized PDMS and PPDMS substrates were coated with a 10 nm layer of a metal before immersing them in thiol solution. Iridium and gold were tested as possible metals to coat the substrates. Iridium coatings generated flat and homogeneous films on the surfaces of the PPDMS as shown in Figure 121. However, when non-plasma treated PDMS substrates were coated with iridium and then immersed in thiol solution, the substrates presented both waves and cracks (Figure 123a). Although PDMS did not present cracks before coating, when it was immersed in a solution with ethanol as solvent, its surface compressed, disturbing the stability of the metal layer on the surface. This problem could be solved by changing the metal to coat the control PDMS substrates. PDMS surfaces coated with gold did not generate flat homogeneous surfaces due to the weaker attachment of Au to PDMS. However, when a 2 nm chromium layer was deposited in between PDMS and gold, a better adhesion was obtained. As gold is more ductile and less brittle than iridium,[399, 400] PDMS surfaces coated with Au did not crack after immersion in the thiol solution (Figure 123b). These surfaces showed

large differences with the cracked Au-PPDMS substrates (Figure 123c). Thus, the surface chemistry of PPDMS could be modified with self-assembly monolayers (SAMS) using either iridium or gold, but non-cracked surfaces of functionalized PDMS could only be achieved using gold as the coating metal.

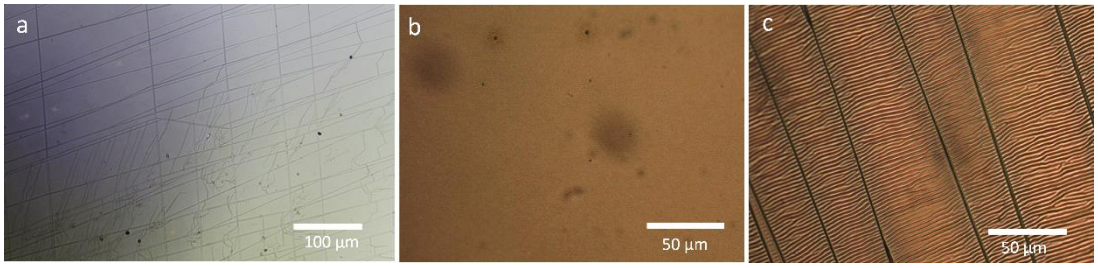

Figure 123. PDMS substrates after coating the substrates with 10 nm of (a) Ir and (b) Au (with a 2 nm Chromium layer) coating and immersion overnight in thiol solution. (c) PPDMS after Au and thiol coating.

6.3.1.2 Crystallization on PPDMS substrates

2 µL of protein and 2 µL of precipitant solutions were injected into PDMS wells which were then closed with a PPDMS or control PDMS substrate. The crystallization of the proteins was followed by optical microscopy every 48 h for 1 month. The results showed that protein nucleation was promoted on functionalized PDMS, PPDMS and functionalized PPDMS. Nucleation on these substrates was achieved at lower concentrations than on non-treated PDMS at the same conditions. A summary of the results observed for different proteins can be found in Table 12. In general, proteins on unfunctionalized or hydroxyl-functionalized PPDMS randomly nucleated on the substrates, showing no preference for the cracks. However, when PPDMS substrates were coated with carboxyl-terminated SAMs, protein crystals showed a remarkable preference for the cracks over the terraces, demonstrating the large effect of topography on crystallization. Moreover, methyl-terminated PPDMS often induced liquid phase separation of certain proteins such as lysozyme or thaumatin in the cracks. Crystals nucleating from the liquid droplets could be occasionally observed after times longer than 2 weeks. Figures 114, 115 and 116 show the precipitation of trypsin, lysozyme, thaumatin and alpha-crustacyanin on the different substrates.

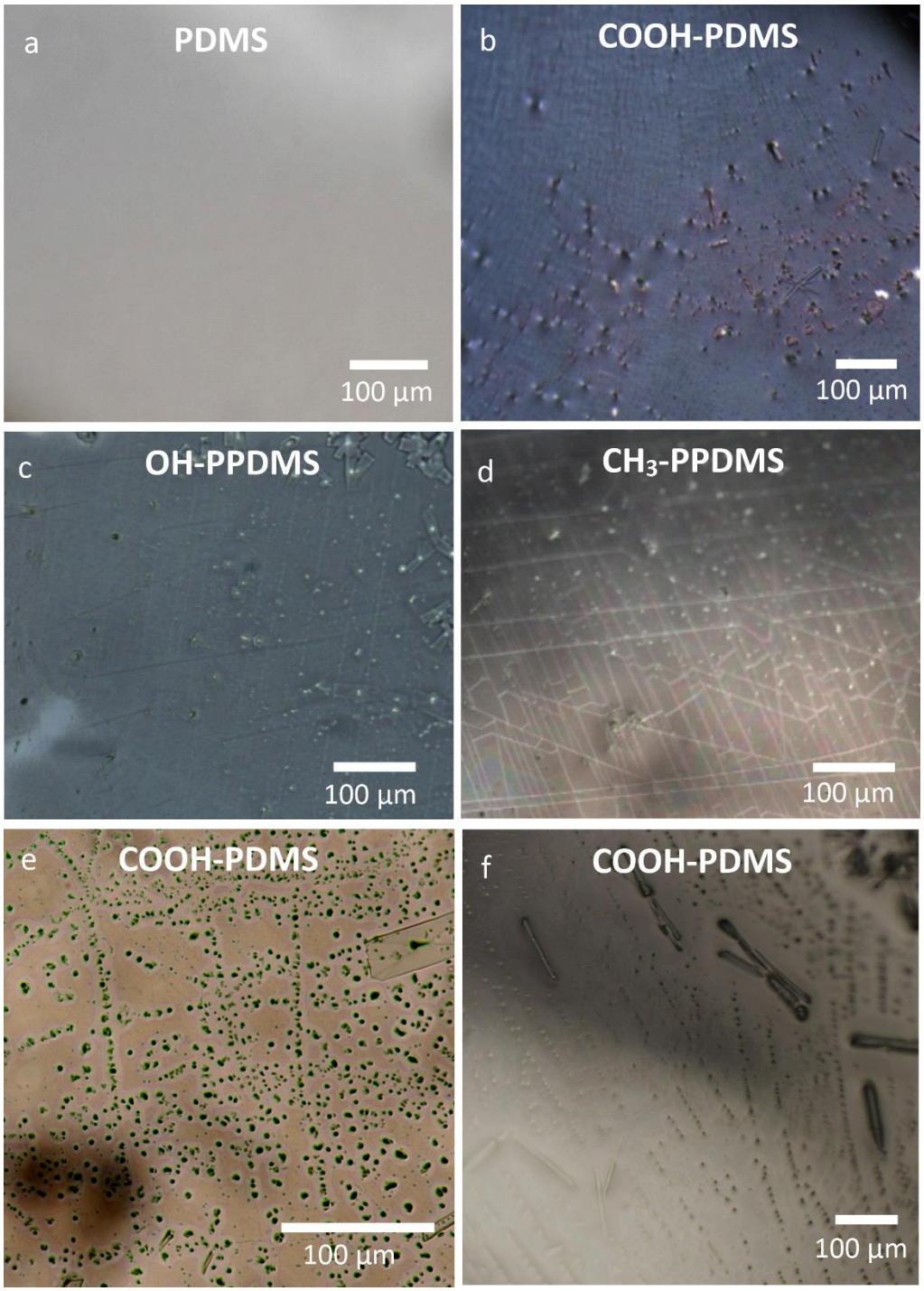

Figure 124. Optical micrographs showing the crystallization of trypsin after 48 h at precipitant concentrations of 25% on different substrates. Trypsin crystallization was promoted on every functionalized substrate but crystal alignment in the cracks was only achieved on carboxyl terminated PPDMS in both gold and iridium coated substrates (e,f).

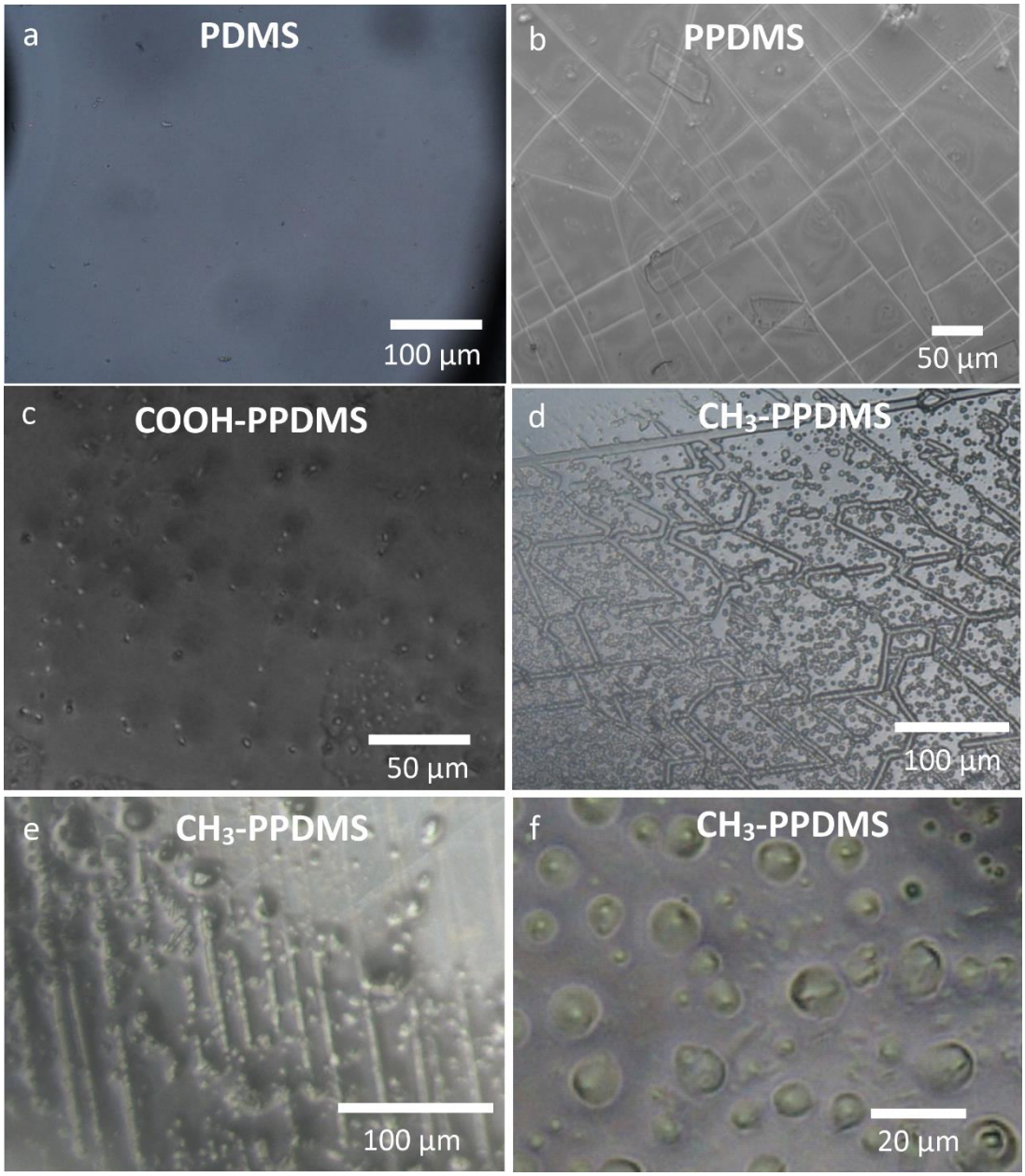

Figure 125. Optical micrographs of lysozyme precipitation at 1 M precipitant concentration on various substrates after 48 h. Lysozyme crystals nucleated inside the cracks of carboxyl terminated PPDMS (c) while liquid phase separation is observed in methyl terminated cracks (d) after 48 h. After 2 weeks, crystalline particles were observed in the CH_3- cracks forming from the cracks and the liquid droplets (e,f).

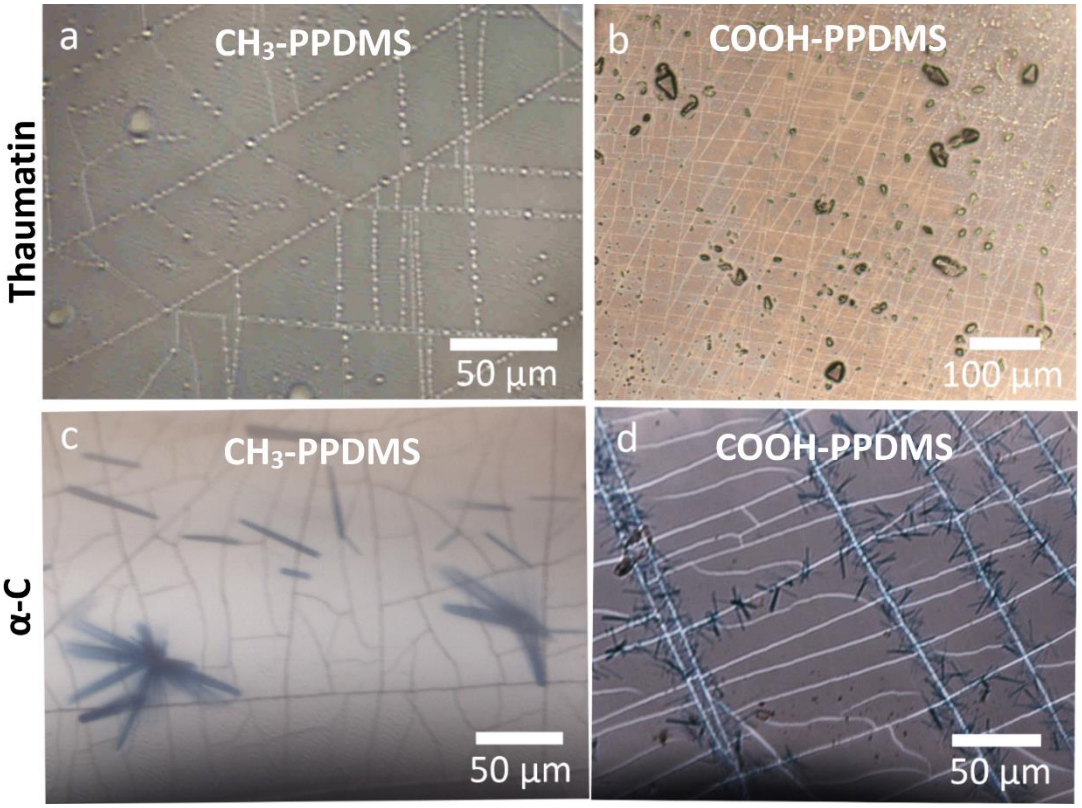

Figure 126. Optical micrographs of (a,b) thaumatin at 0.5 M precipitant concentration and (c,d) α-C at 20% precipitant on (a,c) CH_3-PPDMS and (b,d) COOH-PPDMS after 48 h. Thaumatin liquid phase is observed on methyl terminated PPDMS substrates (a) and random crystallization on carboxyl terminated PPDMS substrates (b) while α-C only showed preference for nucleating in the cracks of carboxyl terminated PPDMS (d).

	Tripsin (25% PEG)	**Lysozyme (1 M NaCl)**	**Thaumatin (0.5 M NaKT)**	**α-C (20% PEG)**
PDMS	No crystals	No crystals	No crystals	No crystals
PDMS –OH **PDMS –CH_3** **PDMS -COOH** **PPDMS** **PPDMS –OH**	Randomly distributed crystals	Randomly distributed crystals	Randomly distributed crystals	Randomly distributed crystals
PPDMS –CH_3	Randomly distributed crystals	Liquid phase separation in cracks	Liquid phase separation in cracks	Randomly distributed crystals
PPDMS –COOH	Crystals in cracks	Crystals in cracks	Randomly distributed crystals	Crystals in cracks

Table 12. Summary of protein crystallization on PDMS substrates at the indicated precipitant concentrations.

Trace-labelling of lysozyme and trypsin

The results described above were performed at relatively low protein and precipitant concentrations in order to pomote heterogeneous nucleation on the surfaces over homogeneous nucleation in bulk. Higher concentrations produce high levels of supersaturation in the solution, causing the nucleation of many crystallites in bulk with no evidence of crystals growing from the surfaces. Figure 127 shows the crystallization of trypsin and lysozyme on COOH-PPDMS at higher concentrations than before, which results in large crystals in bulk solution. When the solution is metastable, bulk crystallization is hindered and the cracks and surface chemistry are the driving forces for nucleation.

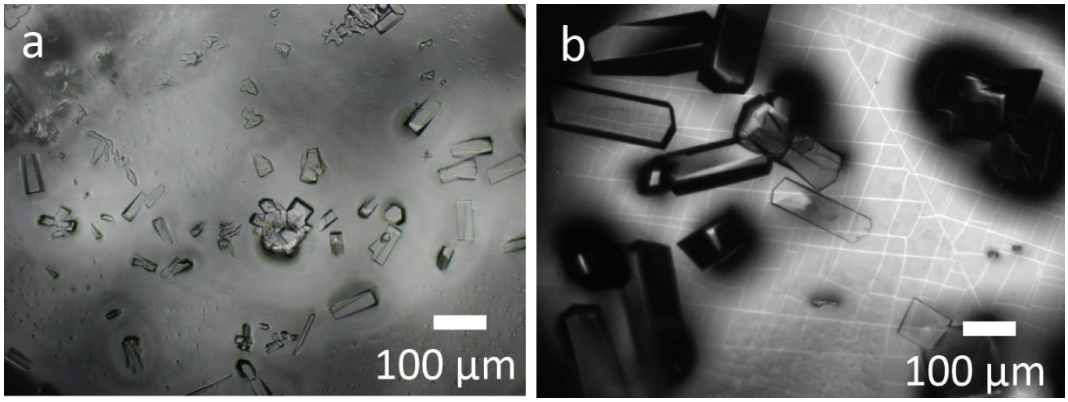

Figure 127. Optical micrographs of (a) trypsin and (b) lysozyme at concentrations of 60 mg/mL and 35% PEG for trypsin and 40 mg/mL and 1.2 M NaCl for lysozyme on COOH-PPDMS substrates.

In order to confirm that the crystals found in the cracks were indeed protein crystals, trypsin and lysozyme were labeled with a fluorescent dye (FITC) and the samples were imaged with a confocal microscope. The observations were carried out *in situ*, and the samples were imaged through the closed PDMS cells. Fluorescent trypsin crystals with two different morphologies were observed in the cracks of the COOH-PPDMS substrates: large flower-like and smaller crystals with irregular surfaces (Figure 128).

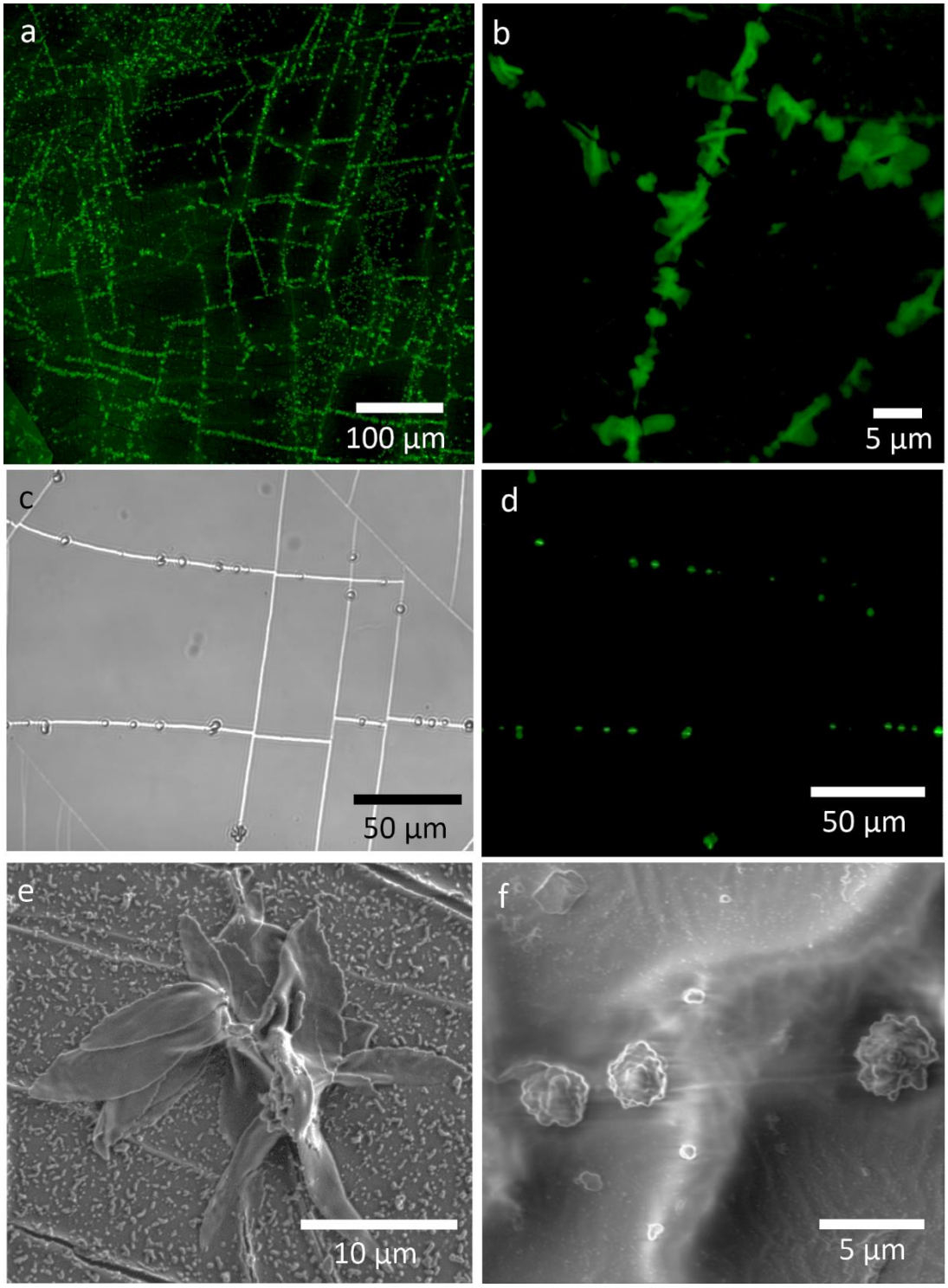

Figure 128. Confocal (a-d) and high magnification SEM (e,f) micrographs of FITC labelled trypsin crystals on COOH-PPDMS after 48 h from crystallization at precipitant concentrations of 25%. Two different crystal morphologies were observed in the cracks: large flower-like crystals (a,d,e) and smaller crystals with irregular surfaces (c,d,f).

A high concentration of adsorbed lysozyme molecules was observed along the cracks of both carboxyl- and methyl-terminated substrates (Figure 129). Whether the protein molecules formed any type of aggregate inside the cracks is difficult to tell from these observations. Lysozyme crystals growing from the cracks of COOH-PPDMS substrates could be distinguished by their higher fluorescent intensities as indicated by red arrows in Figure 129a. Fluorescent droplets of protein were often found on CH_3-PPDMS substrates (Figure 129 c,d). The droplets vary in size and shape and were often seen to coalesce, demonstrating their liquid-like nature (Figure 125d). The fluorescence intensity of lysozyme crystals was higher than the liquid droplets, allowing them to be detectable even at small sizes. However, the fluorescence intensity of small droplets of liquid-phase in the cracks was often too weak to be detectable by confocal microscopy through the PDMS cells (blue arrows in Figure 129d).

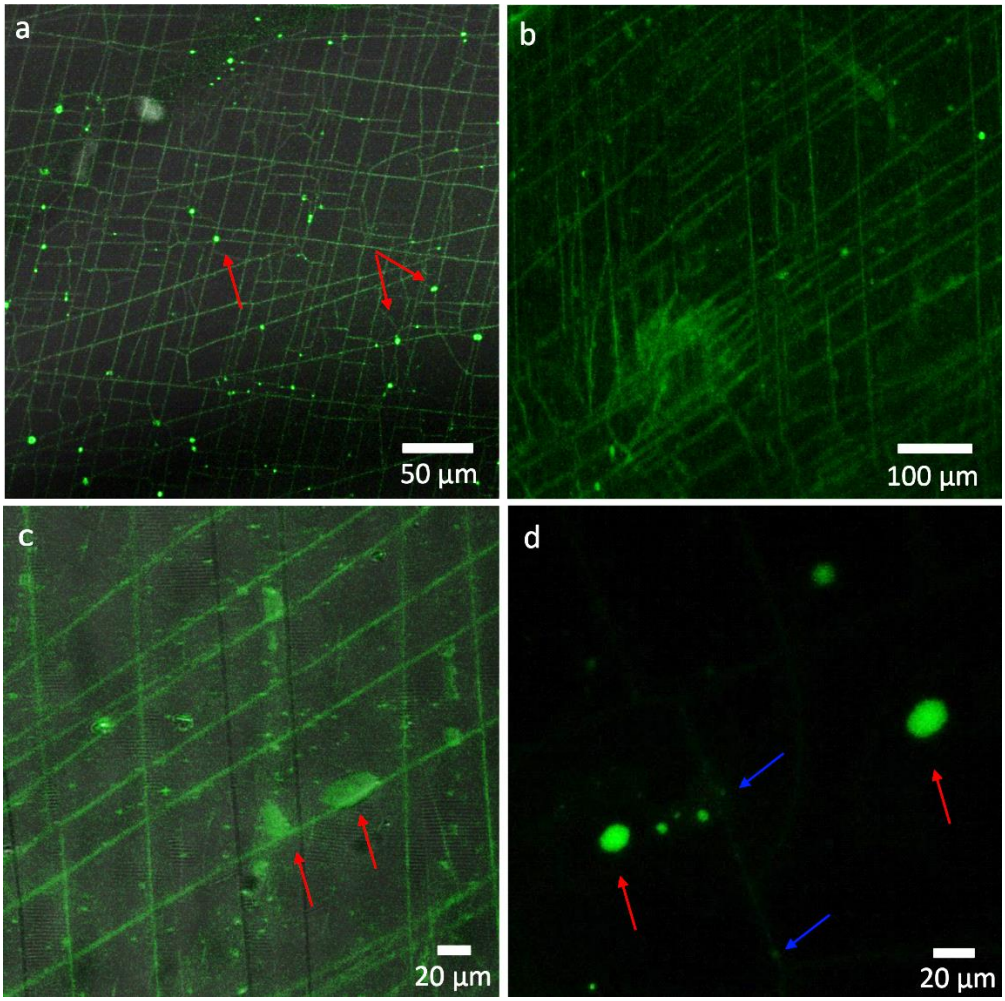

Figure 129. Confocal micrographs of labeled-lysozyme after 2 days from the start of the reaction at 1 M precipitant concentration on (a) COOH-PPDMS and (b-d) on CH_3-PPDMS. High protein concentrations are observed in the cracks, promoting crystal formation on carboxyl terminated substrates (a) and liquid phase separation on methyl terminated substrates (c,d). Observed crystals and liquid phase are indicated by red arrows. Small droplets of protein liquid phase in the cracks are indicated by blue arrows, showing their weak fluorescent intensity.

From the confocal microscopy observations, it was demonstrated that the liquid droplets present on methyl terminated PPDMS substrates were rich in lysozyme. The high local concentration of lysozyme in the hydrophobic cracks can be rationalized by van der Waal interactions between the hydrophobic amino acids of the proteins and the substrate. Such interactions might cause structural changes in the protein molecules or even denature them, affecting the ability of the protein to crystallize. In order to confirm the structural integrity of the macromolecule, lysozyme was labelled with the fluorescent dye 1-

anilino-8-naphthalenesulfonate (ANS). As demonstrated in previous studies, the fluorescence intensity of ANS increases with the degree of lysozyme unfolding.[397] Therefore, if lysozyme molecules are unfolded in the cracks of CH_3-PPDMS, the fluorescence of ANS in the CH_3-PPDMS cracks must be higher than on the terraces. Figure 130 compares the intensity of the ANS dye in a non-coated PDMS cell with the intensity of the dye on the surfaces of a methyl terminated PPDMS. Neither the surfaces nor the cracks in the PDMS showed high fluorescent signals, demonstrating that lysozyme proteins wereconformational stable on the hydrophobic surfaces.

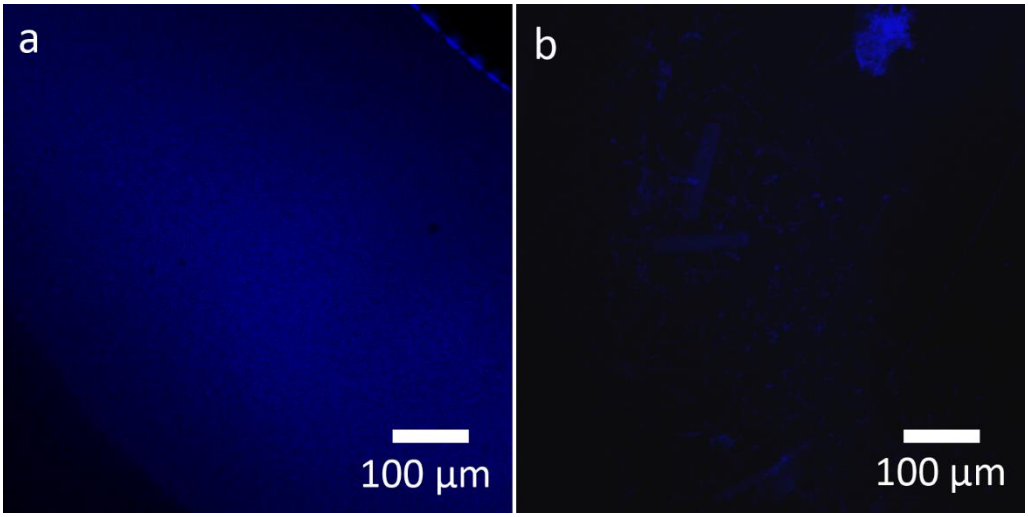

Figure 130. Confocal microscopy images of lysozyme labelled with ANS dye on (a) a PDMS cell and (b) on a CH_3-PPDMS substrate. Fluorescent signal in the cracks was not observed.

Formation of controlled nucleating areas on PPDMS substrates

Spatial control over crystal nucleation on PPDMS can be achieved by patterning the substrates. Previous work has shown that the nucleation of various solids can be directed to specific areas of a substrate where SAMs have been deposited.[129, 191, 207] The formation of such “islands” with a higher probability of nucleation has been previously carried out by a range of techniques including microcontact printing or the use of masks which direct metal deposition. Here, TEM grids were used as masks to direct the formation of both cracks and thiol coatings. To achieve this, a TEM grid was simply placed on the surface of a PDMS substrate which, after plasma treatment,

only presented cracks on the non-covered areas corresponding to the TEM windows as illustrated in Figure 131. After plasma treatment, the substrates were coated with iridium followed by SAMs, creating functionalized areas with cracks. Due to the large variety of commercially- available TEM grids, it is possible to easily modify the pattern of the substrates and select the preferred size and shape of the islands (Figure 132).

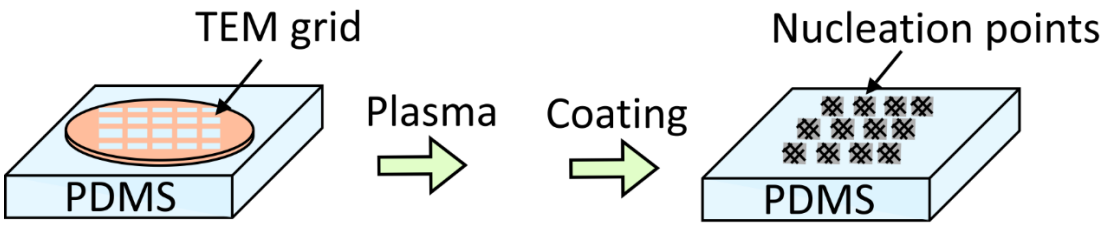

Figure 131. Diagram illustrating the procedure followed to pattern PDMS.

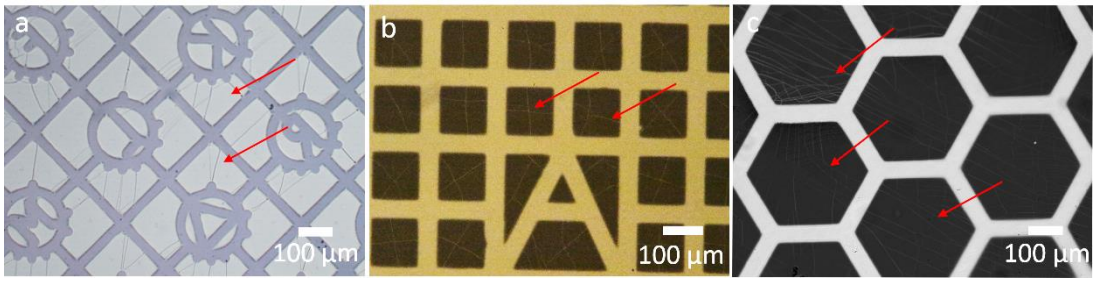

Figure 132. Micrographs of PPDMS substrates after patterning with different TEM grids. Nucleating areas have SAMs and cracks on them (indicated with red arrows).

Two days after solution injection in the PDMS cells, trypsin crystals started to form on the cracks of patterned COOH-PPDMS substrates (Figure 133). Interestingly, a film of liquid seemed to form on the nucleating areas. This liquid phase was rich in protein as observed by confocal microscopy of the labelled trypsin. Indeed, it often obscured the presence of crystals in the cracks, which were now difficult to detect by fluorescence microscopy. Moreover, it was noticed that the proteins preferentially accumulated and nucleated at the edges of the areas with cracks (the nucleating areas). A possible explanation for these observations might be the high amount of

waves and other surface defects at the interfaces between the nucleating areas and the rest of the substrates as observed by SEM (Figure 134).

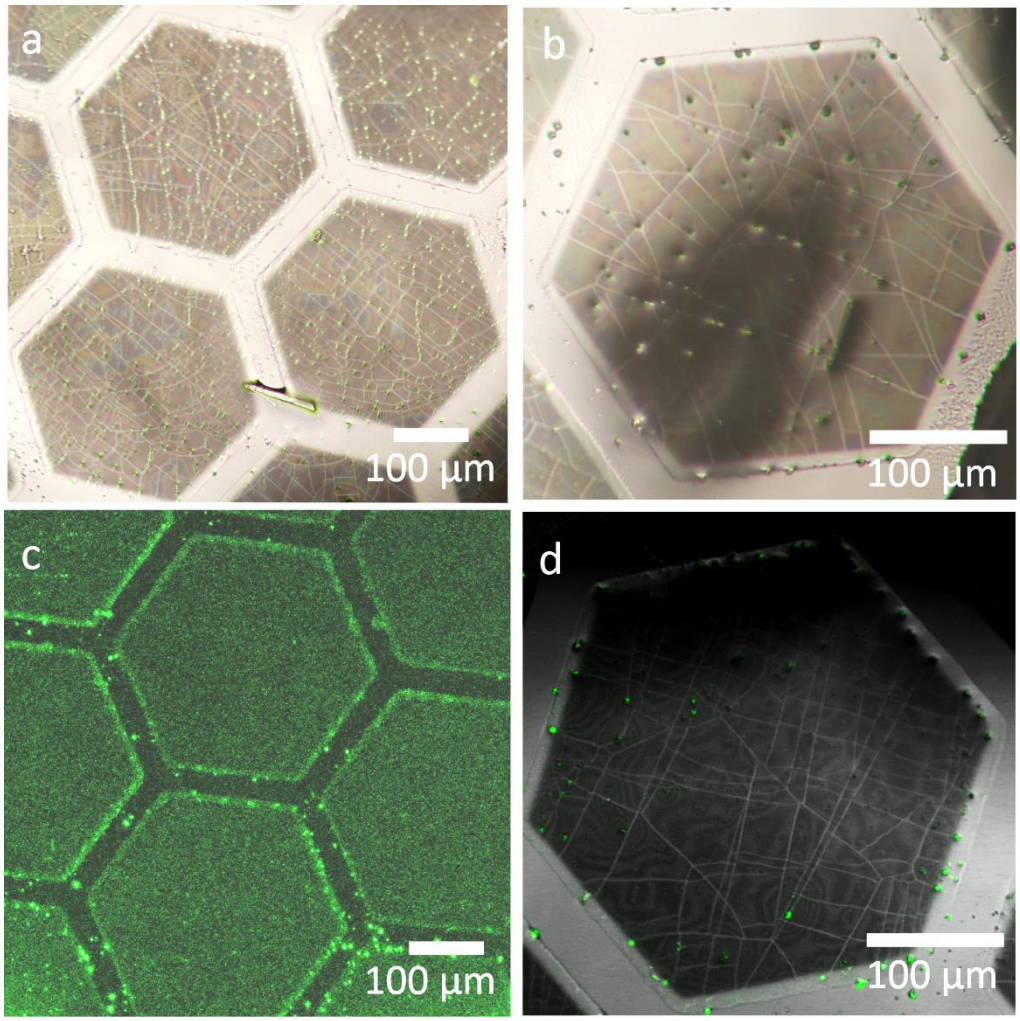

Figure 133. Optical (a,b) and confocal (c,d) micrographs of trypsin crystals on patterned COOH-PPDMS after 48 h at 25% PEG, where a protein layer forms on the nucleating areas and crystals form mainly at the edges of the nucleating areas and in the cracks.

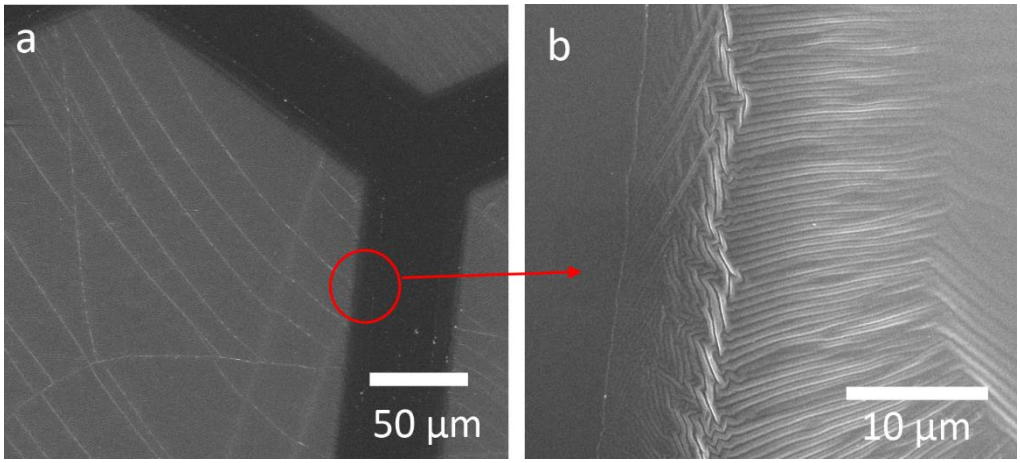

Figure 134. SEM images of patterned PPDMS. The edges of the nucleating areas present wavy and irregular surfaces.

Similar results were observed for lysozyme. A liquid layer of protein was observed on the nucleating areas of patterned COOH-PPDMS and CH_3-PPDMS. The protein concentration was also high in the cracks and the edges of the nucleation points (Figure 135). It is important to take into account that the nucleation areas have a layer of iridium, making them optically darker. This means that it is harder to observe the fluorescence protein in these islands than on the rest of the PDMS substrate.

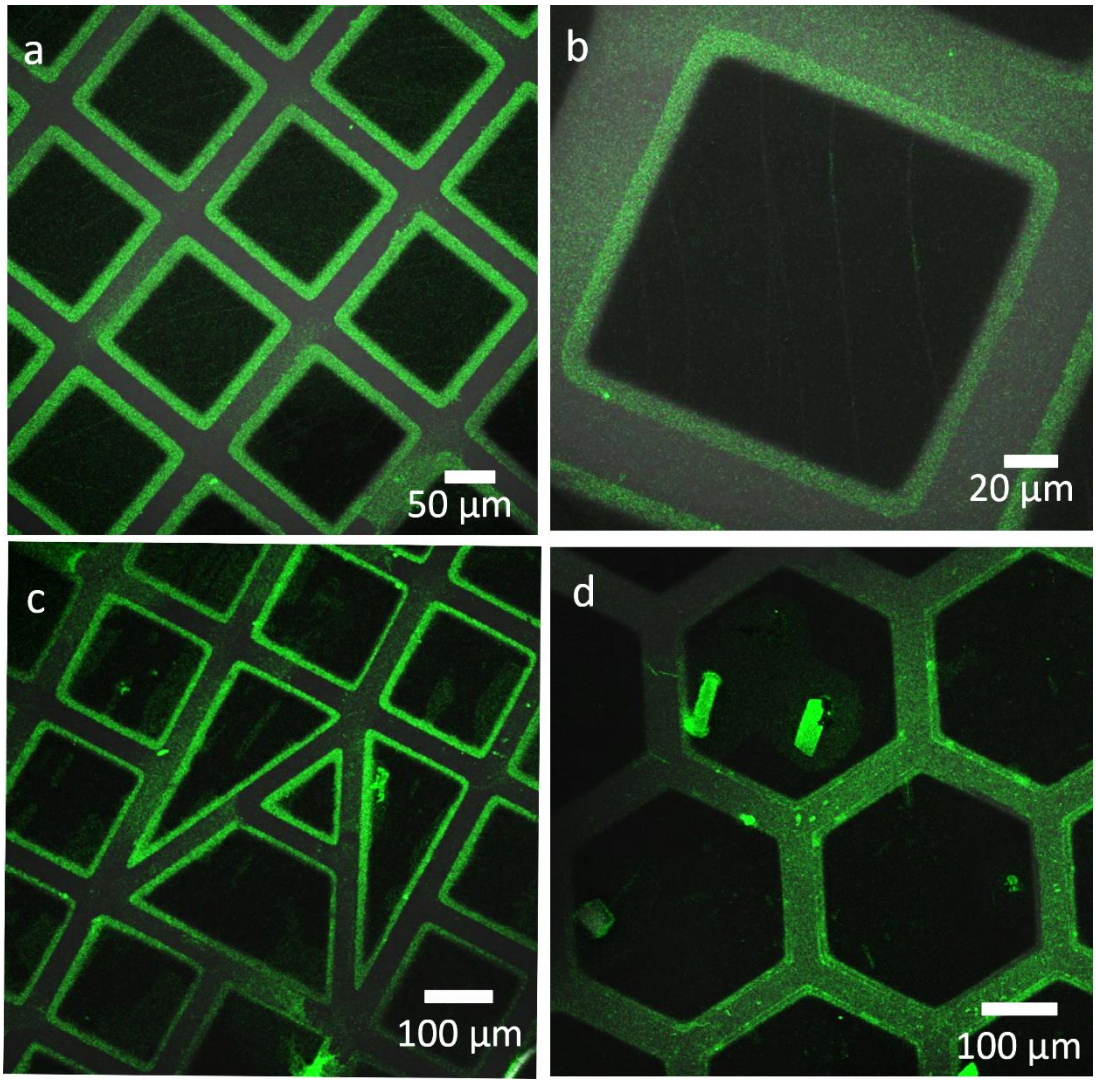

Figure 135. Confocal microscopy images of lysozyme precipitation on COOH-PPDMS (a,b) and CH_3-PPDMS (c,d) after 48 h at 1M NaCl.

Another important factor is that the 10 nm deposited iridium coating will create a step between the nucleating areas and the PDMS substrate. This step might also influence protein adsorption and precipitation. In an effort to create a homogeneous substrate, the whole substrate was gold-coated before forming the thiol coating (Figure 136). In this scenario, only specific areas contained cracks (the areas exposed to the plasma) but the whole substrate shared the same surface chemistry (Figure 137a).

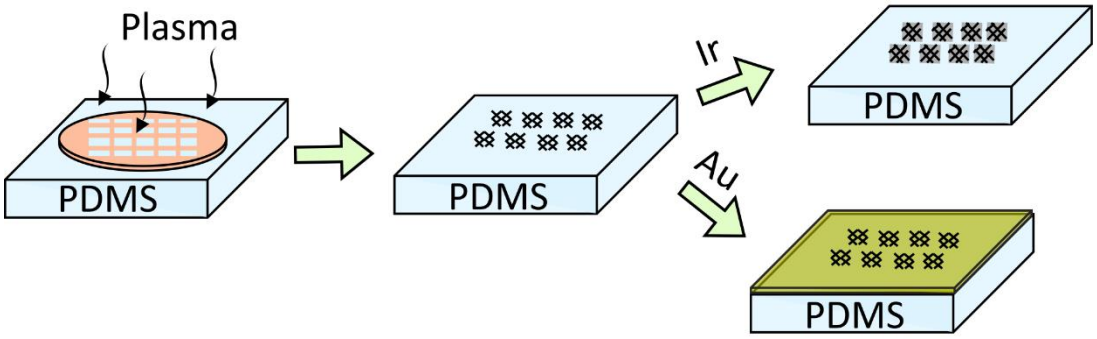

Figure 136. Diagram illustrating the two different procedures followed to pattern PDMS. After plasma treatment, areas with cracks were obtained on PDMS. Iridium coating on these areas created a substrate with different surface chemistries on the islands and on the rest of the substrate. In contrast, gold coating offers the possibility to obtain PDMS substrates with cracks in specific locations and the same surface chemistry over the whole substrate.

Trypsin was crystallized on carboxyl-terminated patterned substrates (with Au as bounding metal). It was observed that trypsin mainly adsorbed on the cracks and edges of the nucleation islands of gold patterned COOH-PPDMS, where crystallization took place (Figure 137b).

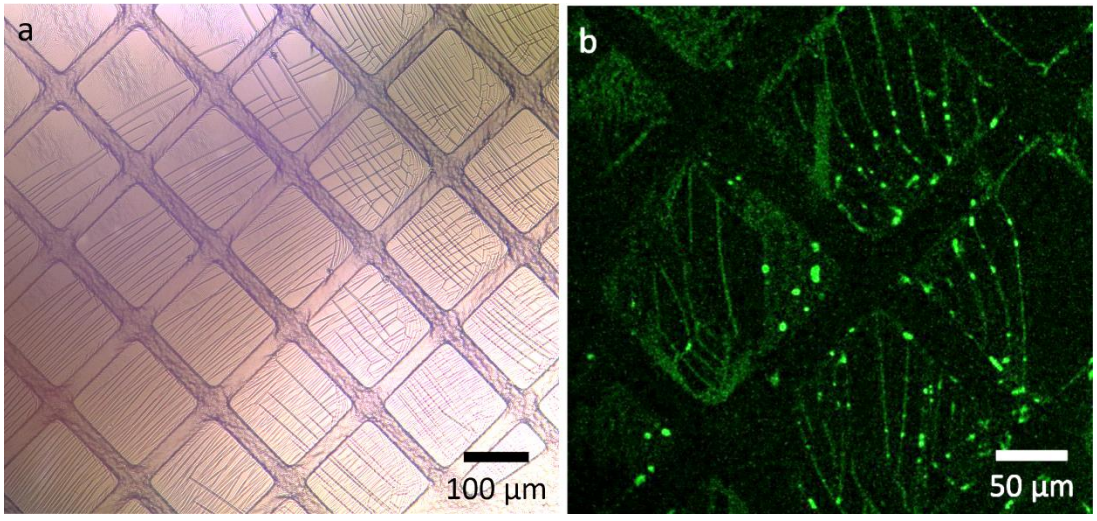

Figure 137. Micrographs of (a) patterned COOH-PPDMS on gold, where the surface chemistry is the same across the substrate and (b) trypsin crystallization of this substrate after 48 h at 25% precipitant.

6.3.2 Protein crystallization on mica substrates

6.3.2.1 Characterization of mica substrates

The surface of cleaved mica usually presents a range of topographic defects capable of inducing nucleation. For example, Campbell *et al*. observed the crystallization of various compounds from the vapor phase on specific surface features of mica.[220] The most observed recurrent features were step edges and cracks, overhanging flakes or loose fragments and cave-like openings where a pocket of trapped air is created in between step edges. Here, the features of a mica substrate were imaged before and after crystallization in order to determine the feature responsible for protein nucleation. Figure 138 shows an example of the most common topographic defects on mica that acted as nucleation sites for protein crystallization in the work presented here.

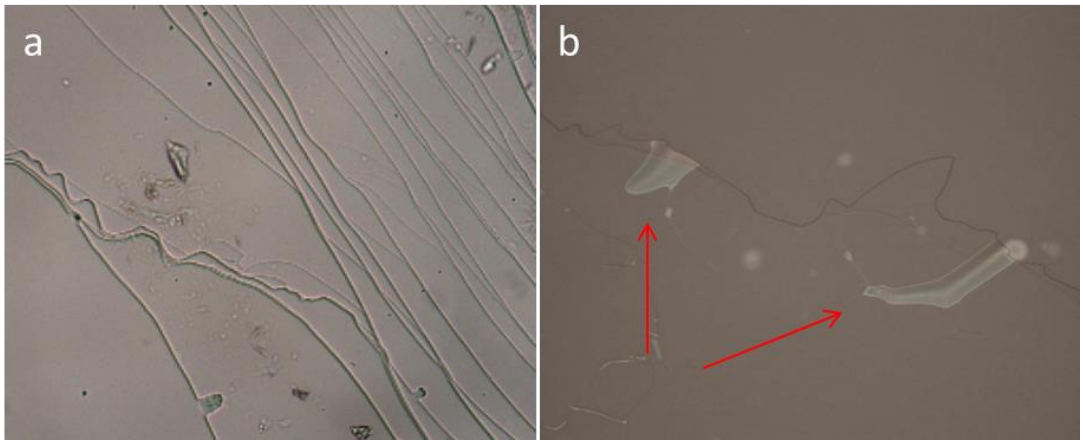

Figure 138. Micrographs of common features observed on the surfaces of cleavage mica showing (a) cracks and step edges and (b) cave-like openings on the step edges.

6.3.2.2 Crystallization on mica substrates

Protein crystallization on the surfaces of mica was carried out in PDMS well plates and observed *in situ* by optical and confocal microscopy over time. Protein crystals were not observed on the surfaces of unfunctionalized mica. However, SAMs-functionalized mica promoted protein crystallization mainly in cracks or steps and within cave-like openings. The nucleation of different proteins on the various topographical features of mica is described below.

Lysozyme crystals showed a preference to nucleate on the step edges and cave-like openings of methyl and carboxyl terminated mica. A liquid phase was frequently observed to form inside the pockets or on the steps, where it appeared that the crystals nucleated from the dense protein-rich liquid (Figure 139). As observed by confocal microscopy, protein adsorption was higher on the features than on the flat surfaces, generating a local increase of protein concentration and the formation of a liquid phase (Figure 140).

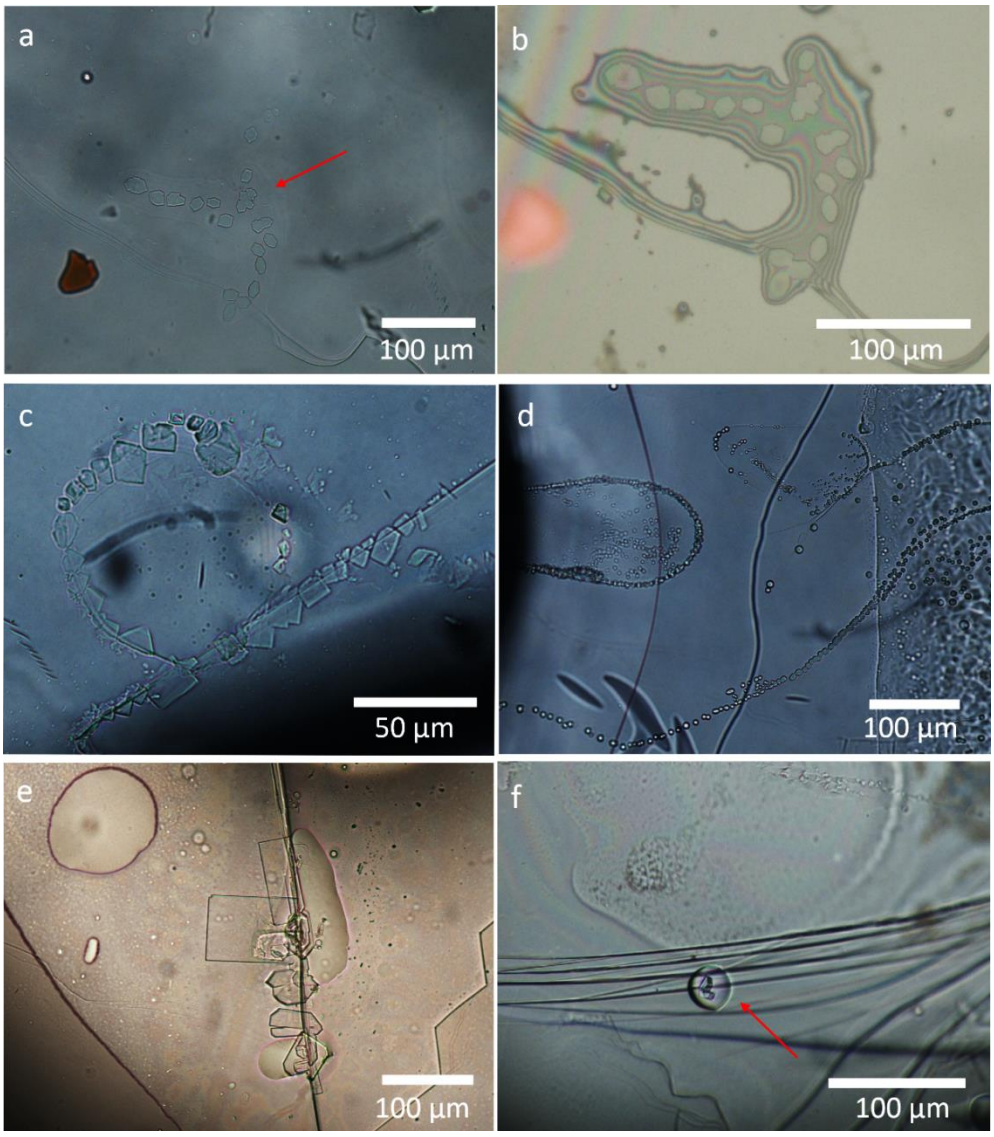

Figure 139. Optical microscopy images of lysozyme crystallization after 48 h at 1 M precipitant concentration on CH_3-mica (a-d) and COOH-mica (e,f). Crystals grew inside mica pockets as observed with transmission (a) and reflective (b) light but also surrounding the pockets and on cracks or steps on the surface (c,d). Liquid phase of lysozyme was also observed to form in the pockets (b) or step edges and crystals nucleated from it (e,f).

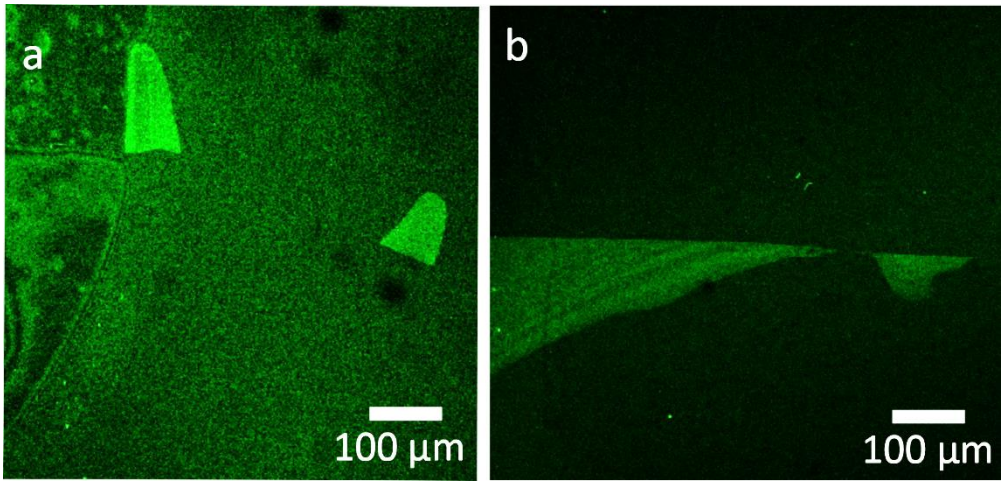

Figure 140. Confocal microscopy images of labelled lysozyme on (a) methyl and (b) carboxyl terminated mica, where a high protein concentration is located within the cave-like openings of the surfaces.

A similar situation was observed with the other proteins studied. Thaumatin also showed a preference to nucleate in the step edges and pockets of both carboxyl and methyl functionalized mica, while trypsin only crystallized on the features on COOH-mica. In contrast to the small trypsin crystals observed on COOH-PPDMS, large single crystals and clusters of trypsin often nucleated on the steps of functionalized mica (Figure 141). Moreover, as shown before, PPDMS did not promote the crystallization of thaumatin in the cracks; a liquid phase was frequently the only product observed in these sites. Nevertheless, thaumatin crystals were commonly observed in step edges and pockets of coated mica after 2 days (Figure 142). Thus, although the two studied systems allowed control over protein nucleation, the topographic defects of mica were shown to be more effective than the cracks of PPDMS for the growth of large protein crystals.

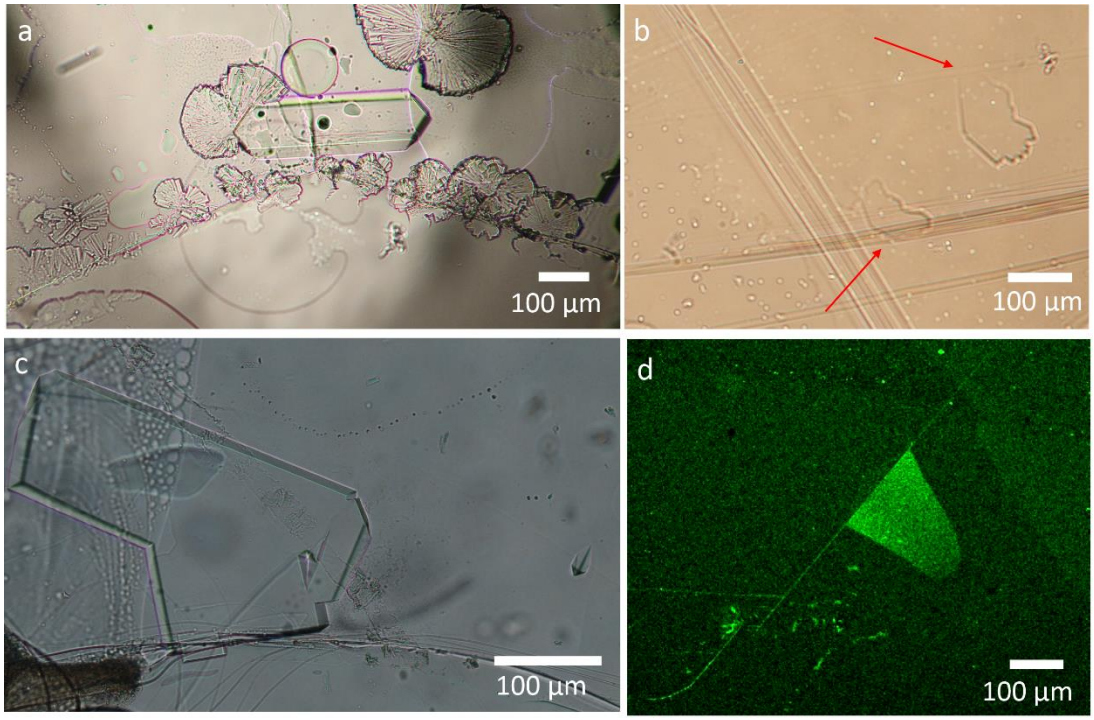

Figure 141. Optical (a-c) micrographs of trypsin crystals on COOH-mica after 48 h at 25% precipitant concentration. Large trypsin crystals grow on cracks and step edges of the mica surface. The protein adsorbs onto the steps and inside cave-like openings (d).

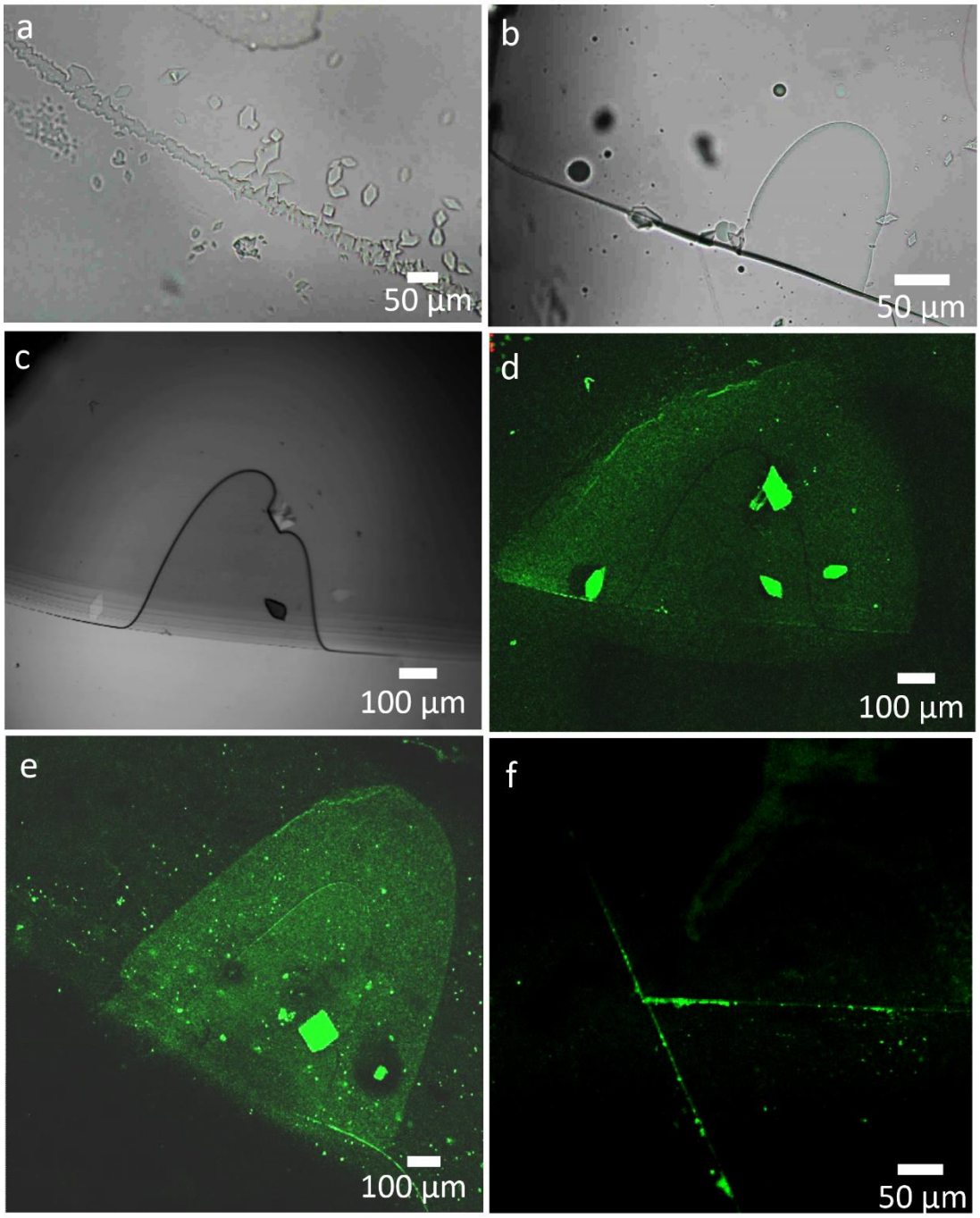

Figure 142. Optical (a-c) and confocal (d-f) micrographs of thaumatin crystallization on functionalized mica after 48 h at 0.7M. Crystals nucleated on step edges and inside cave-like openings on mica where a liquid phase often condenses (b). Air pockets are often present inside the cavities together with the protein as observed in c and d.

The different features on the surfaces on mica were also good nucleants for the target protein of study, alpha-crustacyanin (α-C). 48 h after solution injection, blue crystals grew along the steps and inside the pockets of carboxyl terminated mica (Figure 143). The blue color of the protein allowed its

observation even at low concentrations, with no need to label it with a fluorescent dye. The protein was seen to adsorb preferentially at the edges of the cave-like openings and on the steps and cracks of COOH-mica.

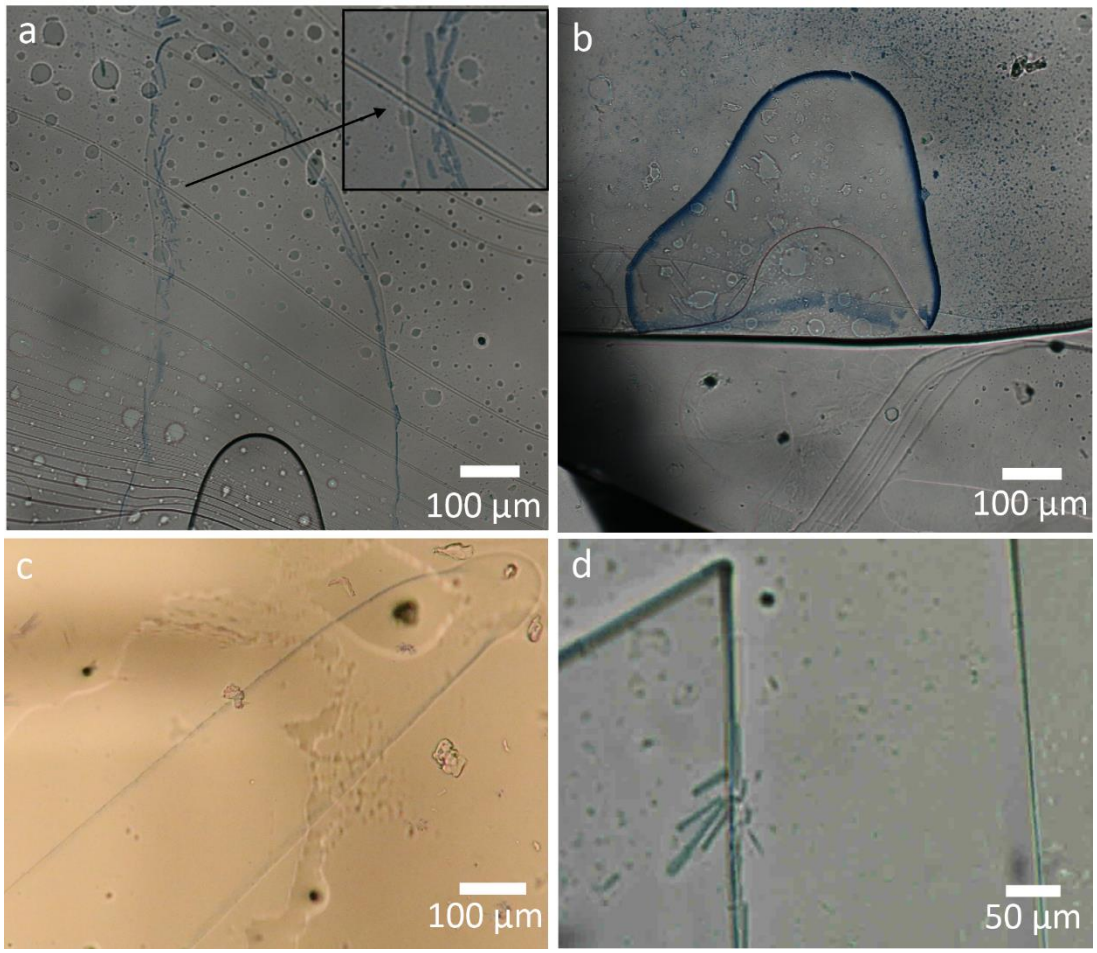

Figure 143. Micrographs of α-C precipitation on COOH-mica at 20% precipitant after 2 days, where the blue protein adsorbs at the edges of the mica pockets (a-c) and on the steps edges of the surface (d).

6.3.3 Protein crystallization on nanofabricated silicon substrates

Once the effectiveness of the combination of surface chemistry and topography to control protein crystallization was demonstrated, the next step was the fabrication of systems with controlled features. As discussed before, the size, density and distribution of the cracks formed on PPDMS substrates are difficult to predict. In addition, the steps and pockets on the surface of mica are naturally formed, and their sizes and shapes cannot be controlled in any

way. Thus, the creation of a substrate with control over the design of the topographic defects is the key to completely controlling crystal nucleation.

6.3.3.1 Crystallization on nanofabricated silicon substrates

Lysozyme and trypsin were crystallized on functionalized nanofabricated silicon substrates by injecting 4 µL of solution (protein and precipitant) in PDMS wells as in the previous experiments. Substrates with trenches of widths 100, 150 and 200 nm and around 500 nm in depth were tested. A range of precipitant concentrations was analysed as indicated in Table 11 and the substrates were imaged every two days for a month. However, protein crystals did not show any preference to nucleate in the trenches at any studied concentration and crystals were usually observed on random locations on the substrates (Figure 144).

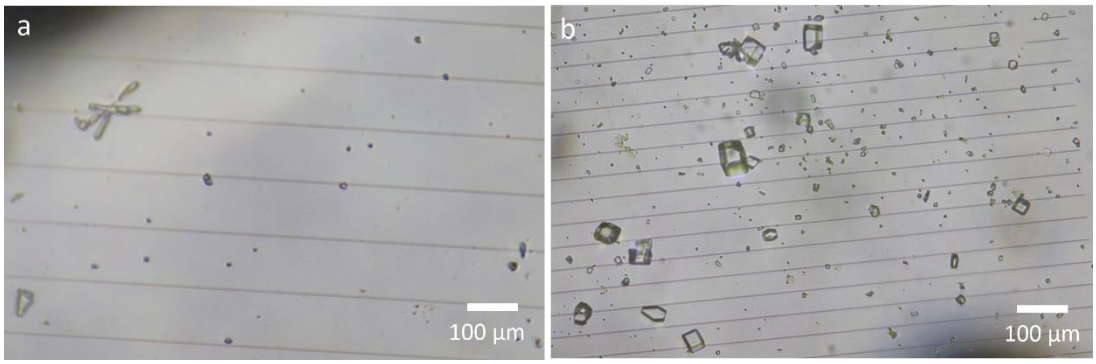

Figure 144. Lysozyme crystals on carboxyl coated nanofabricated silicon substrates after 48h at (a) 0.8 and (b) 1 M precipitant concentration. The crystals do not show any preference for the trenches.

6.4 Discussion

The results presented in this chapter provide direct observations of the heterogeneous nucleation of protein crystals in topographic defects. Indeed, while many systems such as mineral substrates, charged surfaces, porous materials or nanotemplates have been used as nucleants for protein crystallization,[221] the crystals always grew too large to detect the initial features that triggered nucleation. Figure 145 shows trypsin crystals nucleating from controlled pore glasses (CPGs) where, although it can be

speculated that the nucleation was initiated in a pore, no mechanistic information can be extracted from direct observations. Certainly, the nucleation could have been started at the macropores formed in between the CPGs or on the flat surfaces of the particles. Moreover, previous work of protein crystallization on surfaces simply evaluated the efficiency of a substrate to nucleate proteins by the reduction on their induction time, with no evaluation of which specific topographic defects were responsible for nucleation.[228, 394]

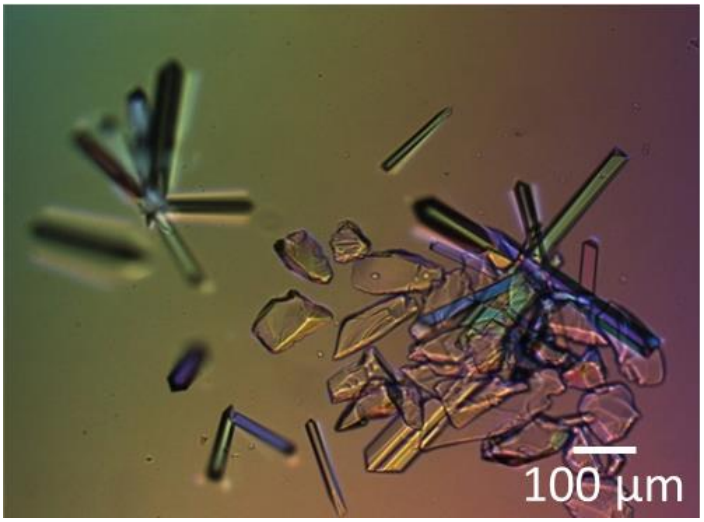

Figure 145. Trypsin crystals growing from controlled pore glass particles. Image from work undertaken at Leeds.

Here, preferential protein nucleation in the cracks of PPDMS or in the step edges or pockets on mica surfaces was observed. Nevertheless, it was found that coating of the surfaces was necessary to enhance protein nucleation. These observations are in agreement with previous work of protein nucleation on SAMS.[204] Crystallization of proteins is usually induced on functionalized surfaces due to fluctuations in the protein concentration when proteins adsorb onto the coated surfaces. Therefore, the degree of protein adsorption to the surface will be a determinant factor for their nucleation. In the case of hydrophilic surfaces, both protein and water molecules can adsorb onto the surface, creating a competition.[204] The adsorbed water layer makes it more difficult for the proteins to adsorb onto surfaces such as glass or mica (-OH terminated), therefore inhibiting protein crystallization.[373, 401, 402] On

hydrophobic surfaces (for example $–CH_3$ terminated), water adsorption onto the contact surface is much reduced, allowing protein interaction through Van der Waals forces with the surfaces.[403] Protein adsorption to the substrate produces a high local concentration which promotes crystallization. Nevertheless, not all hydrophilic surfaces inhibit protein nucleation since surface charge also plays an important role in protein adsorption. Cationic surfaces tend to strongly adsorb negatively charged proteins and vice-versa.[374] In addition, it was suggested that charged surfaces can cause changes in the molecular organization of proteins, enhancing their ordered packing, and thus inducing crystallization.[204] The proteins studied in this chapter, adsorbed and nucleated predominantly on features of methyl and carboxylate terminated surfaces. The relationship between the characteristics of the proteins studied with their ability to adsorb to different surface as observed here is summarized in Table 13. The fact that most proteins adsorbed in the features of $-CH_3$ surfaces was expected, according to the above explanations. The fact that carboxyl terminated surfaces promoted protein crystallization must be due to strong interactions between the partially deprotonated carboxylate groups and the positively charged proteins at the working pH.[374] Finally, the fact that small protein crystals could also be found at random locations of the non-coated substrates suggests that weak interactions probably exist between the proteins and the substrates. Chemical adsorption is therefore a critical first step to control protein nucleation.

	Lysozyme	Trypsin	Thaumatin	α-C
Diameter (nm)	3.2	3.8	3.5	9-10
Isoelectric point (pI)	11	10.5	12	?
Working pH	4.5	7	7	6.5
Protein overall charge	+ve	+ve	+ve	?
Surface chemistry binding	$-CH_3$ $-COO^-$	$-COO^-$	$-CH_3$ $-COO^-$	$-CH_3$ $-COO^-$

Table 13. Summary of the size and charge of the proteins investigated in this chapter and the observed binding of the proteins to a determinate surface chemistry.[360, 404]

Although the substrates presented homogeneous surface chemistries, proteins preferentially adsorbed and nucleated within the features of the substrates. Theoretical studies predict faster crystallization on surfaces with topographic defects such as grooves or pores due to a decrease of the energy nucleation barrier.[213] As described in the first chapter of this thesis, heterogeneous nucleation on a flat surface is more energetically favourable than homogeneous nucleation, due to the lower interfacial free energy of the nucleus in contact with the surface. Figure 146 compares the heterogeneous nucleation of a spherical critical nucleus on different substrates such as a flat surface, pore and wedge. In all three scenarios, the nucleus is partially in contact with a surface, resulting in a decrease of the surface area in contact with the solution.

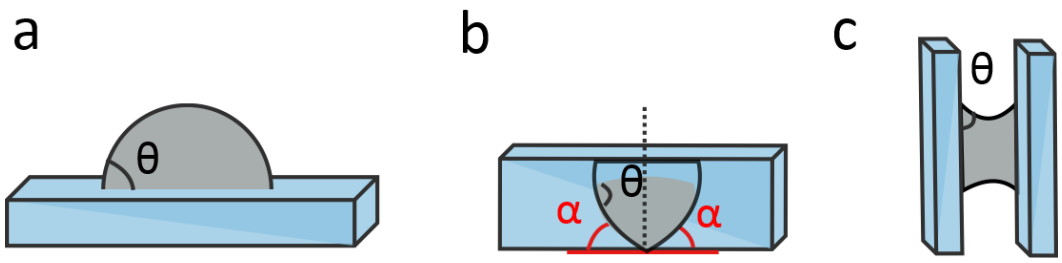

Figure 146. Schematic illustration of a critical nucleus (in grey) on a flat surface (a), in a wedge (b) and in a pore (c). Figure adapted from ref.[25]

The free-energy barrier for heterogeneous nucleation varies with supersaturation and interfacial free energy but also with the affinity of the solution for the substrate. Thus, the activation energy of nucleation on a flat surface depends on the contact angle between the solid and the solution according to: $\Delta G^*_{FLAT} = \Delta G^*_{HOMO} \cdot f(\theta)$ and in a wedge according to: $\Delta G^*_{WEDGE} = \Delta G^*_{HOMO} \cdot f(\theta,\alpha)$.[25] If $\alpha=0$, $\Delta G^*_{FLAT} = \Delta G^*_{WEDGE}$, but if $\alpha>0$, $f(\theta,\alpha)$ is always lower than $f(\theta)$ and therefore the nucleation in a wedge is always more favourable than on a flat surface. In the case of nucleation in pores, two different nucleation barriers are involved: the first one associated with nucleation inside the pore and the second one with the nucleation from the filled pore into the solution.[214] Both energy barriers have opposite directions when the pore size varies: the first barrier decreases with smaller pore sizes and the second decreases with larger pore sizes. As a consequence of this, there will be an ideal pore size with a minimum of activation energy and where the nucleation rate reaches its maximum. However, as the preferred pore diameter depends on the size of the critical nucleus, its size will vary with the nucleating material and also with the supersaturation of the solution. These parameters, together with the shape and surface chemistry of the pore, makes it difficult to predict what specific pore size will be favoured for each system. Thus, many experimental studies of protein crystallization on porous materials have suggested that systems with a wide distribution of pore sizes are more efficient at nucleating proteins than those containing one specific pore size.[215] This is rationalized by the fact that every protein has different dimensions, and therefore will nucleate preferentially in pores of different sizes.[227] Consequently, good protein nucleants will be those with pores or features that can match the sizes of the critical nuclei for a range of proteins, which are

estimated to vary from 5 to 50 nm.[216] In addition, a favourable interaction between the proteins and the surfaces of the pores will be essential for protein adsorption in the pores. This will increase the local concentration of proteins in the pores, promoting crystallization.

The nanofabricated silicon substrates used here presented uniform trenches with dimensions of ≥ 100 nm. These features were probably too large and too uniform in size to act as effective protein nucleants for the reasons stated above. The features observed on PPDMS or mica in this study are also larger than 50 nm. However, in the case of PPDMS, internal nano-features with a range of sizes (<10-90 nm) were observed inside cracks at high magnifications. These features could potentially act as nanopores, trapping the protein molecules inside the confined space to generate high local concentrations. Moreover, as the protein molecules have high affinities for the substrates, protein desorption is slow from sufficiently small cavities.[216] The high protein concentration in the cracks enhances protein nucleation and crystal formation for a range of different proteins since many features of different sizes are present on the substrate, matching different nucleus sizes. It is important to take into account that strong adsorption on the walls of the features could cause protein denaturation, which would inhibit crystal formation. However, protein denaturation was not observed in the systems studied. Here crystals were always present in the cracks of hydrophilic substrates and no lysozyme unfolding was detected when the protein was labelled with ANS dye.

In the case of functionalized mica substrates, steps and pockets on the surface of the substrates were the preferred nucleation features for all of the proteins studied. Campbell *et al.* suggested that the step edges observed on mica must present almost infinitely acute wedges due to delamination when two layers of the material have been separated.[220] This delamination must also be present at the edges of cave-like openings on mica, forming acute edges along the borders of the pocket. According to classical nucleation theory, a reduction in the activation energy of a nucleus is expected when

decreasing the angle of the wedge, making acute wedges more favourable for crystal nucleation.[25] The results presented here are in agreement with the observations described by Campbell *et al.*[220] and support the theory that acute wedges promote crystallization. Therefore, as in the case of PPDMS, the proteins will adsorb onto the acute wedges of coated mica, where the high local concentration and the lower energy barrier at these locations promotes crystallization.

Long-lifetime liquid protein droplets were also observed in the cracks of CH_3-PPDMS and on step edges of coated mica. High stability of the liquid phase in solution was detected for every system, where redissolution was never observed for at least 2 weeks. Crystals were often found growing from the liquid phase inside mica pockets and steps or in PPDMS cracks. Liquid intermediates such as the ones observed here have been widely studied for the last decade, and a two-step crystallization mechanism has now been accepted for many proteins.[3] The conformational flexibility of protein molecules allows them to bind to other proteins, forming mesoscopic clusters rich in disordered proteins, which might act as precursors for crystallization.[3] Thus, three different scenarios have been proposed (Figure 147): the first situation corresponds to a classical point of view, where protein crystals nucleate directly from solution (Figure 147 a-I). In the second scenario, metastable clusters are formed due to density fluctuations in the system (Figure 147 a-II). They have short lifetimes and sizes of several hundreds of nanometers. The third situation is the one observed here, where macroscopic dense liquid phases are formed when the system is located deep inside the liquid-liquid separation region. The liquid droplets are stable with respect to the solution but metastable with respect to the crystalline phase and their lifetimes can be very long (Figure 147 a-III).[405, 406] Possible crystal nucleation from these intermediates will depend on the system. Thus, while some studies have shown that dense macroscopic liquid droplets promote nucleation, other studies have observed very long stabilities of these droplets, without crystal formation, or even crystal nucleation in solution, rather than in the dense liquid droplets.[407] The observation of macroscopic liquid droplets in the topographical defects on the substrates studied here can be rationalized by

the great increase in local supersaturation within cracks, steps and pockets. As observed by confocal microscopy, a high concentration of protein adsorbs to these features, causing a liquid phase transition as the system is now highly supersaturated (Figure 147b). Finally, as protein is adsorbed in the cavities, a mass transport of proteins from the bulk to these features is expected, and crystallization will take place.

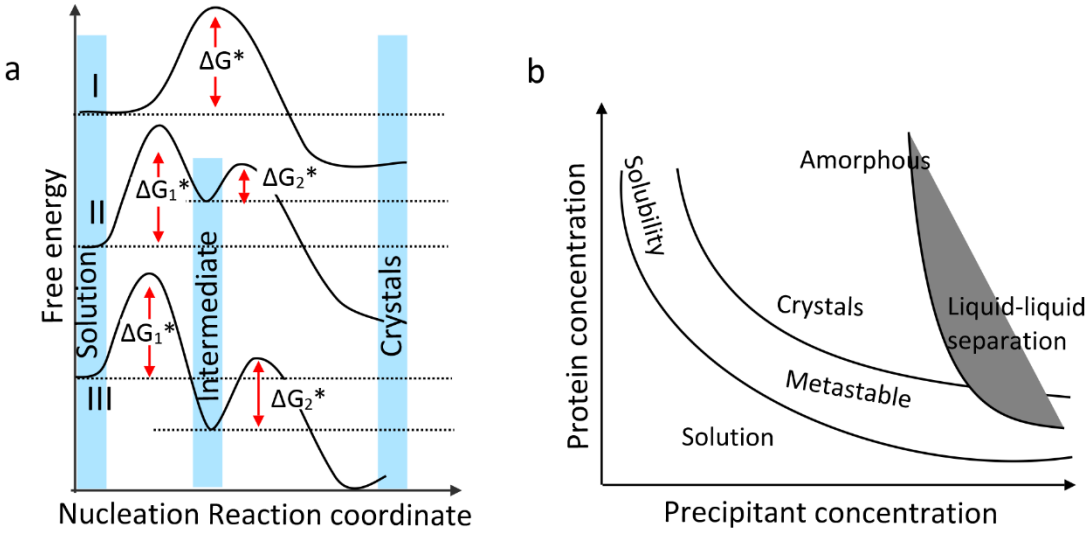

Figure 147. Schematic illustration of (a) free energy diagrams of 3 different pathways for protein crystallization where I corresponds to a classical view of nucleation from solution and II and III to non-classical points of view with unstable and stable intermediates. (b) Solubility diagram of a protein. Liquid-liquid separation is expected at high concentrations, although it varies with the protein and temperature. Figure adapted from ref.[3, 22]

6.5 Conclusions

This chapter demonstrated that surface topography can be used not only to enhance, but also to control the heterogeneous nucleation of proteins in a predictable way. Three model and one target protein were crystallized in the topographic defects of two different systems. The first system consisted of plasma-treated substrates of poly(dimethylsiloxane) (PPDMS) which contained microcracks with internal nano-features where protein crystals are likely to nucleate. The second system of study was Muscovite mica with characteristic features such as step edges and cave-like openings which were

shown to be effective nucleation sites for protein crystals. Importantly, modifying the surface chemistry of the substrates was critical in achieving attractive protein-substrate interactions and enhancing crystallization. Indeed, random nucleation was obtained when the proteins crystallized on non-coated substrates. Nevertheless, localized protein crystallization was achieved in the cracks of carboxyl terminated PPDMS, while dense, liquid droplets of proteins often precipitated in the cracks of methyl terminated PPDMS substrates. In both cases, amazing control over protein nucleation was achieved, such that protein nucleation only occurred in the topographical defects rather than on the terraces. A similar situation was observed on methyl and carboxyl terminated mica substrates, where crystals and dense liquid droplets were found inside step edges and cave-like openings on functionalized mica (CH_3- or COOH-). It was also demonstrated by confocal microscopy that adsorption of the proteins in the topographical defects is higher than anywhere else on the substrates and that this is essential for protein crystallization in these features. Site-specific protein adsorption causes an increase in the local concentration of the proteins, which gives rise to either protein crystals or/and dense liquid droplets. In conclusion, these results provide direct observation of proteins crystallizing within topographic defects, where this suggests a method to effectively control protein nucleation by manipulating the surface chemistry and topography of a substrate.

Chapter 7: conclusions and future work

The work presented in this thesis demonstrated that it is possible to better understand and control the crystallization of a solid by modifying the environment in which it precipitates. Crystallization in nature often occurs in small volumes rather than in bulk, where different surface chemistries are encountered. Inspired by crystallization in nature, the crystallization of various inorganic solids and proteins was studied *in situ,* using a range of substrates in order to further understand the role that the spatial environment where a solid form plays on its crystallization. It was shown that confinement, surface chemistry and topography have enormous effects on crystallization and new insights into the mechanisms that govern these effects were put forward.

The first two experimental chapters described the crystallization of potassium ferrocyanide trihydrate (KFCT), calcium sulfate and calcium carbonate in confinement. Controlled pore glass (CPG) particles with pore sizes from 8 to 362 nm were first used as a confinement system. It was shown that, while CPG beads were a viable tool for studying crystallization of very soluble solids in nanopores, pore filling was truly challenging for solids of lower solubility. Thus, a novel crystallization system was presented: macroscopic controlled pore glass (CPG) rods. CPG rods enabled the first study of the crystallization of poorly soluble solids in nanopores, and in particular the *in situ* imaging and characterization of the crystals. The crystallization of KFCT, calcium sulfate and $CaCO_3$ was significantly slower in confinement, such that metastable phases exhibited long lifetimes in the nanopores. Further, the fact that crystallization is retarded in small volumes means that confinement could be used as a tool for investigating crystallization pathways.

An exhaustive investigation of KFCT crystallization is presented in Chapter 3, where the crystallization of this solid in 8 nm pores was seen to be retarded by up to 5 orders of magnitude as compared with bulk. Anhydrous potassium ferrocyanide (KFC) was never detected in bulk aqueous solution, but it was the first phase to form in nanopores. KFC hydrated over time into the metastable tetragonal polymorph of KFCT and finally converted into the thermodynamically stable monoclinic polymorph. Moreover, it was demonstrated that polymorph stabilization increased with decreasing pore

size. In chapter 4 it was shown that both $CaCO_3$ and calcium sulfate crystallize through the precipitation and redissolution of amorphous precursors. The dissolution of the amorphous phases inside pores provided direct observations of Ostwald ripening effects in nanopores. Importantly, the significantly longer lifetime of amorphous calcium sulfate (ACS) in confinement, allowed its characterization by X-ray diffraction for the first time. After ACS dissolution, bassanite ($CaSO_4 \cdot 0.5H_2O$) crystals precipitated in the pores and they experienced the longest stabilization at room temperature observed to date, with no transformation of the crystals in the pores for at least 3 weeks. Finally, we demonstrated the existence of several coexisting mechanisms of gypsum nucleation including transformation from basanite and *de novo* nucleation of gypsum. Two different pathways of conversion from bassanite to gypsum were observed: a dissolution-precipitation mechanism on breaking the porous structure, and a solid-state transformation when the surface of the pores was modified. Stabilization of $CaCO_3$ polymorphs (vaterite and aragonite) was also achieved in the nanopores and their formation was seen to be very sensitive to the Ca^{2+}/CO_3^{2-} ratio in the pores.

The mechanisms that govern crystallization in confinement were also explored. The slower crystallization in the pores was explained by a combination of phenomena. First, ion diffusion was significantly slower in the nanopores than in bulk, as demonstrated by the modelling presented in this thesis. This caused longer induction times and overall, slower crystallization processes in the nanopores. Second, it was suggested that water availability in the pores must be restricted, due to the formation of layers of crystalline water trapped on the pore walls, plus a slower transport of water through the pores. Lastly, the crystals in the pores seemed to behave as isolated entities in the pores, showing reduced communication between crystallites in these environments. This, together with the lower probability of nucleation in confinement, must cause a significant retardation of crystallization in confinement.

Many experiments could be conducted as an extension of the work described in this thesis. It will be fascinating to investigate the crystallization of calcium

sulfate and $CaCO_3$ in CPG rods with different pore sizes in order to establish the pore range in which confinement effects become noticeable. The confinement methods developed here could also be used to crystallize a large range of different inorganic solids. Calcium phosphate and calcium oxalate would be particularly interesting as they are both highly important in healthcare issues. Their crystallization in nanopores could bring insight into bone formation mechanisms or kidney stones prevention. Finally, computer simulations of crystals growing in nanopores would be useful to have a comprehensive understanding of all of the chemical and physical factors affecting crystallization in confinement.

The final two experimental chapters of this thesis focused on providing a range of systems to further understand and control protein crystallization. Chapter 5 describes the crystallization of three different model proteins within an inverted watch glass system. This system offers the possibility to observe different stages of crystal growth *in situ* within the same experiment, since it presents continuously varying degrees of confinement. A two-step nucleation mechanism with solid amorphous intermediates was observed for all of the proteins studied. The amorphous precursors were stabilized in confinement and they acted as nucleation sites for protein crystallization. It was also shown that modifying the surface chemistry of the inverted watch glass system promoted protein crystallization and inhibited amorphous precipitation in confinement. This study not only revealed information about the mechanism of crystallization of proteins but also showed that protein nucleation can be dramatically reduced in confined spaces. This is important and needs to be taken into account, especially for crystallization screening within small volumes such as microfluidics or when using new techniques such as liquid-cell TEM.

Although the slower nucleation of proteins in confinement revealed important aspects of their crystallization pathways, systems that allow a controlled enhancement of protein nucleation are the final goal of any protein crystallographer. Chapter 6 describes the nucleation of three model and one target protein on various systems with topographic defects, namely

poly(dimethylsiloxane) (PPDMS), Muscovite mica and nanofabricated silicon substrates. PPDMS and mica substrates were demonstrated to be effective nucleants not only for the model proteins, but also for the studied target. The proteins selectively nucleated within the features of both systems after they were chemically modified, and showed a degree of localization never observed before. In addition, the formation of dense liquid droplets rich in protein was often promoted in the topographic defects of the functionalized substrates, due to the high concentration of adsorbed protein in these features. In contrast, the features on nanofabicated silicon substrates were too large and uniform in size and shape to induce protein nucleation, and therefore were not effective nucleants.

Further work could concentrate on the fabrication of designed substrates with smaller surface topographic features than the ones observed here. Indeed, the features where protein crystals nucleated have certain characteristics that could potentially be mimicked using current advances in nanofabrication techniques. The crystallization of new target proteins relevant to biological issues could also be tested in the systems presented here. The higher probability of nucleation in the topographic defects might induce the crystallization of proteins that have not yet been crystallized. Any crystals nucleating on the substrates could then be used to obtain structural information, or the substrates could be used for seeding experiments, to obtain larger and better quality crystals.

In conclusion, this thesis has demonstrated that confinement, surface chemistry, topography and a combination of these effects can be used as effective tools for understanding and controlling crystallization. The innovative systems and methods presented here open the door to further *in situ* studies of crystallization, to provide a complete understanding of the effects that rule crystallization in confinement or within topographic defects.

List of References

1. NISHINAGA, T. *Handbook of Crystal Growth: Fundamentals.* Elsevier, 2014.
2. SHAHIDZADEH-BONN, N., J. DESARNAUD, F. BERTRAND, X. CHATEAU and D. BONN. Damage in porous media due to salt crystallization. *Physical Review E*, 2010, **81**(6), p.066110.
3. VEKILOV, P.G. Nucleation of protein crystals. *Progress in Crystal Growth and Characterization of Materials*, 2016, **62**(2), pp.136-154.
4. VEKILOV, P.G. Nucleation. *Crystal Growth & Design*, 2010, **10**(12), p.5007.
5. SHAH, U.V., C. AMBERG, Y. DIAO, Z. YANG and J.Y. HENG. Heterogeneous nucleants for crystallogenesis and bioseparation. *Current Opinion in Chemical Engineering*, 2015, **8**, pp.69-75.
6. CALLISTER, W.D. and D.G. RETHWISCH. *Materials science and engineering.* John Wiley & Sons NY, 2011.
7. MELDRUM, F.C. and H. COELFEN. Controlling Mineral Morphologies and Structures in Biological and Synthetic Systems. *Chemical Reviews*, 2008, **108**(11), pp.4332-4432.
8. MULLIN, J.W. *Crystallization.* Butterworth-Heinemann, 2001.
9. STACHURSKI, Z.H. On Structure and Properties of Amorphous Materials. *Materials*, 2011, **4**(9), pp.1564-1598.
10. ADDADI, L., S. RAZ and S. WEINER. Taking advantage of disorder: Amorphous calcium carbonate and its roles in biomineralization. *Advanced Materials*, 2003, **15**(12), pp.959-970.
11. LOWENSTAM, H.A. and S. WEINER. Transformation of Amorphous Calcium-Phosphate to Crystalline Dahllite in the Radular Teeth of Chitons. *Science*, 1985, **227**(4682), pp.51-53.
12. TOWE, K.M. and H.A. LOWENSTAM. Ultrastructure and development of iron mineralization in the radular teeth of Cryptochiton stelleri (Mollusca). *Journal of ultrastructure research*, 1967, **17**(1-2), pp.1-13.
13. BRITTAIN, H.G. *Polymorphism in pharmaceutical solids.* CRC Press, 2016.
14. HILFIKER, R. *Polymorphism: in the pharmaceutical industry.* John Wiley & Sons, 2006.
15. BAUER, J., S. SPANTON, R. HENRY, J. QUICK, W. DZIKI, W. PORTER and J. MORRIS. Ritonavir: An extraordinary example of conformational polymorphism. *Pharmaceutical Research*, 2001, **18**(6), pp.859-866.
16. ANWAR, J. and D. ZAHN. Polymorphic phase transitions: Macroscopic theory and molecular simulation. *Advanced Drug Delivery Reviews*, 2017, **117**, pp.47-70.
17. DAVEY, R. and J. GARSIDE. *From molecules to crystallizers.* Oxford University Press, 2000.
18. BECKMANN, W. Crystallization of Pharmaceutical Compounds Polymorphs, Pseudo-Polymorphs and Particle Formation. *Engineering in Life Sciences*, 2003, **3**(3), pp.113-120.
19. POLTE, J. Fundamental growth principles of colloidal metal nanoparticles - a new perspective. *CrystEngComm*, 2015, **17**(36), pp.6809-6830.

20. KARTHIKA, S., T.K. RADHAKRISHNAN and P. KALAICHELVI. A Review of Classical and Nonclassical Nucleation Theories. *Crystal Growth & Design*, 2016, **16**(11), pp.6663-6681.
21. BOISTELLE, R. and J.P. ASTIER. Crystallization Mechanisms in Solution. *Journal of Crystal Growth*, 1988, **90**(1-3), pp.14-30.
22. GARCıA-RUIZ, J.M. Nucleation of protein crystals. *Journal of structural biology*, 2003, **142**(1), pp.22-31.
23. NING, D. and X.Y. LIU. Controlled ice nucleation in microsized water droplet. *Applied Physics Letters*, 2002, **81**(3), pp.445-447.
24. HAMILTON, B.D., J.-M. HA, M.A. HILLMYER and M.D. WARD. Manipulating Crystal Growth and Polymorphism by Confinement in Nanoscale Crystallization Chambers. *Accounts of Chemical Research*, 2012, **45**(3), pp.414-423.
25. SEAR, R.P. Nucleation: theory and applications to protein solutions and colloidal suspensions. *Journal of Physics-Condensed Matter*, 2007, **19**(3).
26. CUBILLAS, P. and M.W. ANDERSON. Synthesis mechanism: crystal growth and nucleation. *Zeolites and Catalysis: Synthesis, Reactions and Applications*, 2010, pp.1-55.
27. DE YOREO, J.J. and P.G. VEKILOV. Principles of crystal nucleation and growth. *Biomineralization*, 2003, **54**, pp.57-93.
28. DIRKSEN, J.A. and T.A. RING. Fundamentals of Crystallization - Kinetic Effects on Particle-Size Distributions and Morphology. *Chemical Engineering Science*, 1991, **46**(10), pp.2389-2427.
29. THRELFALL, T. Structural and thermodynamic explanations of Ostwald's rule. *Organic Process Research & Development*, 2003, **7**(6), pp.1017-1027.
30. MELDRUM, F. and R. SEAR. Now you see them. *Science*, 2008, **19**, pp.1802-1803.
31. GEBAUER, D., A. VOLKEL and H. COLFEN. Stable Prenucleation Calcium Carbonate Clusters. *Science*, 2008, **322**(5909), pp.1819-1822.
32. SETO, J., Y. MA, S.A. DAVIS, F. MELDRUM, A. GOURRIER, Y.-Y. KIM, U. SCHILDE, M. SZTUCKI, M. BURGHAMMER and S. MALTSEV. Structure-property relationships of a biological mesocrystal in the adult sea urchin spine. *Proceedings of the National Academy of Sciences*, 2012, **109**(10), pp.3699-3704.
33. WOLF, S.E., C.F. BOHM, J. HARRIS, B. DEMMERT, D.E. JACOB, M. MONDESHKI, E. RUIZ-AGUDO and C. RODRIGUEZ-NAVARRO. Nonclassical crystallization in vivo et in vitro (I): Process-structure-property relationships of nanogranular biominerals. *Journal of structural biology*, 2016, **196**(2), pp.244-259.
34. NIEDERBERGER, M. and H. CÖLFEN. Oriented attachment and mesocrystals: non-classical crystallization mechanisms based on nanoparticle assembly. *Physical Chemistry Chemical Physics*, 2006, **8**(28), pp.3271-3287.
35. STURM, E.V. and H. COLFEN. Mesocrystals: structural and morphogenetic aspects. *Chemical Society Reviews*, 2016, **45**(21), pp.5821-5833.
36. KIM, Y.Y., A.S. SCHENK, J. IHLI, A.N. KULAK, N.B.J. HETHERINGTON, C.C. TANG, W.W. SCHMAHL, E.

GRIESSHABER, G. HYETT and F.C. MELDRUM. A critical analysis of calcium carbonate mesocrystals. *Nature communications*, 2014, **5**.
37. LEUNISSEN, M. D.O.S.S. CHEMISTRY. *An essay on several aspects of protein crystallization research*. Radboud University Nijmegen, 2001.
38. PERTICAROLI, S., J.D. NICKELS, G. EHLERS, H. O'NEILL, Q. ZHANG and A.P. SOKOLOV. Secondary structure and rigidity in model proteins. *Soft Matter*, 2013, **9**(40), pp.9548-9556.
39. HUNEFELD. Die Chemismus in der Thierischen Organization. *Leipzig*, 1840, p.160.
40. HARTIG, T. Ueber das Klebermehl. *Botan Z*, 1855, **13**, p.881.
41. RITTHAUSEN, H. Ueber die Erwerskorper aus verschiedener Oelsamen. *Flugers Arch*, 1880, **21**, p.81.
42. SUMNER, J.B. The isolation and crystallization of the enzyme urease. Preliminary paper. *Journal of Biological Chemistry*, 1926, **69**(2), pp.435-441.
43. ABEL, J.J. Crystalline insulin. *Proceedings of the National Academy of Sciences*, 1926, **12**(2), pp.132-136.
44. ALDERTON, G. and H.L. FEVOLD. Direct Crystallization of Lysozyme from Egg White and Some Crystalline Salts of Lysozyme. *Journal of Biological Chemistry*, 1946, **164**(1), pp.1-5.
45. MCPHERSON, A. A brief history of protein crystal growth. *Journal of Crystal Growth*, 1991, **110**, pp.1-10.
46. MCPHERSON, A. *Crystallization of Biological Macromolecules.* New York, 1944.
47. VEKILOV, P.G., A.R. FEELING-TAYLOR, S.T. YAU and D. PETSEV. Solvent entropy contribution to the free energy of protein crystallization. *Acta Crystallographica Section D-Biological Crystallography*, 2002, **58**, pp.1611-1616.
48. GALKIN, O. and P.G. VEKILOV. Control of protein crystal nucleation around the metastable liquid–liquid phase boundary. *Proceedings of the National Academy of Sciences*, 2000, **97**(12), pp.6277-6281.
49. VEKILOV, P.G. Dense liquid precursor for the nucleation of ordered solid phases from solution. *Crystal Growth & Design*, 2004, **4**(4), pp.671-685.
50. TEN WOLDE, P.R. and D. FRENKEL. Enhancement of protein crystal nucleation by critical density fluctuations. *Science*, 1997, **277**(5334), pp.1975-1978.
51. SCHILLING, T., H.J. SCHÖPE, M. OETTEL, G. OPLETAL and I. SNOOK. Precursor-mediated crystallization process in suspensions of hard spheres. *Physical Review Letters*, 2010, **105**(2), p.025701.
52. SLEUTEL, M. and A.E. VAN DRIESSCHE. Role of clusters in nonclassical nucleation and growth of protein crystals. *Proceedings of the National Academy of Sciences*, 2014, **111**(5), pp.E546-E553.
53. PAN, W., P.G. VEKILOV and V. LUBCHENKO. Origin of anomalous mesoscopic phases in protein solutions. *The Journal of Physical Chemistry B*, 2010, **114**(22), pp.7620-7630.
54. VEKILOV, P.G. and M.A. VORONTSOVA. Nucleation precursors in protein crystallization. *Acta Crystallographica Section F: Structural Biology Communications*, 2014, **70**(3), pp.271-282.

55. PAN, W., O. GALKIN, L. FILOBELO, R.L. NAGEL and P.G. VEKILOV. Metastable mesoscopic clusters in solutions of sickle-cell hemoglobin. *Biophysical journal*, 2007, **92**(1), pp.267-277.
56. GLIKO, O., N. NEUMAIER, W. PAN, I. HAASE, M. FISCHER, A. BACHER, S. WEINKAUF and P.G. VEKILOV. A metastable prerequisite for the growth of lumazine synthase crystals. *Journal of the American Chemical Society*, 2005, **127**(10), pp.3433-3438.
57. MAES, D., M.A. VORONTSOVA, M.A. POTENZA, T. SANVITO, M. SLEUTEL, M. GIGLIO and P.G. VEKILOV. Do protein crystals nucleate within dense liquid clusters? *Acta Crystallographica Section F: Structural Biology Communications*, 2015, **71**(7), pp.815-822.
58. HARANO, K., T. HOMMA, Y. NIIMI, M. KOSHINO, K. SUENAGA, L. LEIBLER and E. NAKAMURA. Heterogeneous nucleation of organic crystals mediated by single-molecule templates. *Nature materials*, 2012, **11**(10), pp.877-881.
59. SAUTER, A., F. ROOSEN-RUNGE, F. ZHANG, G. LOTZE, R.M. JACOBS and F. SCHREIBER. Real-time observation of nonclassical protein crystallization kinetics. *Journal of the American Chemical Society*, 2015, **137**(4), pp.1485-1491.
60. SAUTER, A., F. ROOSEN-RUNGE, F. ZHANG, G. LOTZE, A. FEOKTYSTOV, R.M. JACOBS and F. SCHREIBER. On the question of two-step nucleation in protein crystallization. *Faraday Discussions*, 2015, **179**, pp.41-58.
61. YAMAZAKI, T., Y. KIMURA, P.G. VEKILOV, E. FURUKAWA, M. SHIRAI, H. MATSUMOTO, A.E. VAN DRIESSCHE and K. TSUKAMOTO. Two types of amorphous protein particles facilitate crystal nucleation. *Proceedings of the National Academy of Sciences*, 2017, p.201606948.
62. SALEMME, F.R., L. GENIESER, B.C. FINZEL, R.M. HILMER and J.J. WENDOLOWSKI. Molecular factors stabilizing protein crystals. *J. Crystal Growth*, 1988, **90**, p.273.
63. MALKIN, A.J., Y.G. KUZNETZOV, T.A. LAND and J.J. DEYOREO. Mechanisms of growth for protein and virus crystals. *Nat. Struct. Biol.*, 1995, **2**, p.956.
64. KUZNETSOV, Y.G., A.J. MALKIN, A. GREENWOOD and A. MCPHERSON. Michelson interferometric studies of protein and virus crystallization. *J. Crystal Growth*, 1996, **166**, p.913.
65. WIECHMANN, M., O. ENDERS, C. ZEILINGER and H.A. KOLB. Analysis of protein crystal growth at molecular resolution by atomic force microscopy. *Ultramicroscopy*, 2001, **86**(1-2), pp.159-166.
66. MUSCHOL, M. and F. ROSENBERGER. Lack of evidence for prenucleation aggregate formation in lysozyme crystal growth solutions. *Journal of Crystal Growth*, 1996, **167**(3-4), pp.738-747.
67. MUSCHOL, M. and F. ROSENBERGER. Interactions in undersaturated and supersaturated lysozyme solutions: Static and dynamic light scattering results. *Journal of Chemical Physics*, 1995, **103**(24), pp.10424-10432.
68. KOSZELAK and A. MCPHERSON. Time lapse microphotography of protein crystal growth using a color VCR. *J. Crystal Growth*, 1988, **90**, p.340.

69. KOSZELAK. Protein crystal growth rates determined by time lapse microphotography. *J. Crystal Growth*, 1991, **110**, p.177.
70. MCPHERSON, A., A.J. MALKIN, Y.G. KUZNETSOV and S. KOSZELAK. Incorporation of impurities into macromolecular crystals. *J. Crystal Growth*, 1996, **168**, p.74.
71. WEBER, P.C. Physical Principles of Protein Crystallization. *Advances in Protein Chemistry*, 1991, **41**, pp.1-36.
72. CHAYEN, N.E. Recent advances in methodology for the crystallization of biological macromolecules. *Journal of Crystal Growth*, 1999, **198**, pp.649-655.
73. SARIDAKIS, E. and N.E. CHAYEN. Towards a 'universal'nucleant for protein crystallization. *Trends in biotechnology*, 2009, **27**(2), pp.99-106.
74. NG, J.D., J.A. GAVIRA and J.M. GARCIA-RUIZ. Protein crystallization by capillary counterdiffusion for applied crystallographic structure determination. *Journal of structural biology*, 2003, **142**(1), pp.218-231.
75. GARCIA-RUIZ, J.M., F. OTALORA, M.L. NOVELLA, J.A. GAVIRA, C. SAUTER and O. VIDAL. A supersaturation wave of protein crystallization. *Journal of Crystal Growth*, 2001, **232**(1-4), pp.149-155.
76. GAVIRA GALLARDO, J.A. *Capillary counter-diffusion methods for protein crystallization* [online]. 2007. [Accessed]. Available from: http://www.chemie.uni-hamburg.de/bc/betzel/Gavira-Gallardo_1.pdf.
77. OTALORA, F., J.A. GAVIRA, J.D. NG and J.M. GARCIA-RUIZ. Counterdiffusion methods applied to protein crystallization. *Progress in Biophysics and Molecular Biology*, 2009, **101**(1-3), pp.26-37.
78. WU, Z.H., S.L. YANG and W. WU. Shape control of inorganic nanoparticles from solution. *Nanoscale*, 2016, **8**(3), pp.1237-1259.
79. SONG, R.Q. and H. COLFEN. Additive controlled crystallization. *CrystEngComm*, 2011, **13**(5), pp.1249-1276.
80. SCHENK, A.S., I. ZLOTNIKOV, B. POKROY, N. GIERLINGER, A. MASIC, P. ZASLANSKY, A.N. FITCH, O. PARIS, T.H. METZGER, H. COLFEN, P. FRATZL and B. AICHMAYER. Hierarchical Calcite Crystals with Occlusions of a Simple Polyelectrolyte Mimic Complex Biomineral Structures. *Advanced Functional Materials*, 2012, **22**(22), pp.4668-4676.
81. BORUKHIN, S., L. BLOCH, T. RADLAUER, A.H. HILL, A.N. FITCH and B. POKROY. Screening the Incorporation of Amino Acids into an Inorganic Crystalline Host: the Case of Calcite. *Advanced Functional Materials*, 2012, **22**(20), pp.4216-4224.
82. KIM, Y.Y., J.D. CARLONI, B. DEMARCHI, D. SPARKS, D.G. REID, M.E. KUNITAKE, C.C. TANG, M.J. DUER, C.L. FREEMAN, B. POKROY, K. PENKMAN, J.H. HARDING, L.A. ESTROFF, S.P. BAKER and F.C. MELDRUM. Tuning hardness in calcite by incorporation of amino acids. *Nature materials*, 2016, **15**(8), pp.903-+.
83. KIM, Y.Y., L. RIBEIRO, F. MAILLOT, O. WARD, S.J. EICHHORN and F.C. MELDRUM. Bio-Inspired Synthesis and Mechanical Properties of Calcite-Polymer Particle Composites. *Advanced Materials*, 2010, **22**(18), pp.2082-+.
84. KIM, Y.Y., K. GANESAN, P.C. YANG, A.N. KULAK, S. BORUKHIN, S. PECHOOK, L. RIBEIRO, R. KROGER, S.J. EICHHORN, S.P.

ARMES, B. POKROY and F.C. MELDRUM. An artificial biomineral formed by incorporation of copolymer micelles in calcite crystals. *Nature materials*, 2011, **10**(11), pp.890-896.

85. BRIF, A., G. ANKONINA, C. DRATHEN and B. POKROY. Bio-Inspired Band Gap Engineering of Zinc Oxide by Intracrystalline Incorporation of Amino Acids. *Advanced Materials*, 2014, **26**(3), pp.477-481.
86. KULAK, A.N., P.C. YANG, Y.Y. KIM, S.P. ARMES and F.C. MELDRUM. Colouring crystals with inorganic nanoparticles. *Chemical Communications*, 2014, **50**(1), pp.67-69.
87. GONG, X., Y.W. WANG, J. IHLI, Y.Y. KIM, S. LI, R. WALSHAW, L. CHEN and F.C. MELDRUM. The Crystal Hotel: A Microfluidic Approach to Biomimetic Crystallization. *Advanced Materials*, 2015, **27**(45), pp.7395-7400.
88. JIANG, Q. and M.D. WARD. Crystallization under nanoscale confinement. *Chem. Soc. Rev.*, 2014, **43**(7), pp.2066-2079.
89. WANG, Y.-W., H.K. CHRISTENSON and F.C. MELDRUM. Confinement increases the lifetimes of hydroxyapatite precursors. *Chemistry of Materials*, 2014, **26**(20), pp.5830-5838.
90. KIM, Y.-Y., C. FREEMAN, X. GONG, M.A. LEVENSTEIN, Y. WANG, A. KULAK, C. ANDUIX CANTO, S. LI, L. CHEN and P. LEE. The Effect of Additives on the Early Stages of Growth of Calcite Single Crystals. *Angewandte Chemie International Edition*, 2017.
91. LEVI-KALISMAN, Y., G. FALINI, L. ADDADI and S. WEINER. Structure of the nacreous organic matrix of a bivalve mollusk shell examined in the hydrated state using Cryo-TEM. *Journal of structural biology*, 2001, **135**(1), pp.8-17.
92. NUDELMAN, F., K. PIETERSE, A. GEORGE, P.H.H. BOMANS, H. FRIEDRICH, L.J. BRYLKA, P.A.J. HILBERS, G. DE WITH and N.A.J.M. SOMMERDIJK. The role of collagen in bone apatite formation in the presence of hydroxyapatite nucleation inhibitors. *Nature materials*, 2010, **9**(12), pp.1004-1009.
93. LI, Y., G.T. DUAN, G.Q. LIU and W.P. CAI. Physical processes-aided periodic micro/nanostructured arrays by colloidal template technique: fabrication and applications. *Chemical Society Reviews*, 2013, **42**(8), pp.3614-3627.
94. NUDELMAN, F. and N.A.J.M. SOMMERDIJK. Biomineralization as an Inspiration for Materials Chemistry. *Angewandte Chemie-International Edition*, 2012, **51**(27), pp.6582-6596.
95. FALINI, G. *Introduction to Biomineralization and Biominerals*. International School on Biological crystallization, 2015.
96. CANTAERT, B., Y.Y. KIM, H. LUDWIG, F. NUDELMAN, N.A.J.M. SOMMERDIJK and F.C. MELDRUM. Think Positive: Phase Separation Enables a Positively Charged Additive to Induce Dramatic Changes in Calcium Carbonate Morphology. *Advanced Functional Materials*, 2012, **22**(5), pp.907-915.
97. WEINER, S. and L. ADDADI. Crystallization Pathways in Biomineralization. *Annual Review of Materials Research, Vol 41*, 2011, **41**, pp.21-40.
98. TAYLOR, A.R., M.A. RUSSELL, G.M. HARPER, T.F.T. COLLINS and C. BROWNLEE. Dynamics of formation and secretion of

heterococcoliths by Coccolithus pelagicus ssp braarudii. *European Journal of Phycology*, 2007, **42**(2), pp.125-136.
99. BENIASH, E., J. AIZENBERG, L. ADDADI and S. WEINER. Amorphous calcium carbonate transforms into calcite during sea urchin larval spicule growth. *Proceedings of the Royal Society B-Biological Sciences*, 1997, **264**(1380), pp.461-465.
100. STEIGER, M. Crystal growth in porous materials—II: Influence of crystal size on the crystallization pressure. *Journal of Crystal Growth*, 2005, **282**(3), pp.470-481.
101. DESARNAUD, J., H. DERLUYN, L. MOLARI, S. DE MIRANDA, V. CNUDDE and N. SHAHIDZADEH. Drying of salt contaminated porous media: Effect of primary and secondary nucleation. *Journal of Applied Physics*, 2015, **118**(11), p.114901.
102. STACK, A.G. Precipitation in Pores: A Geochemical Frontier. *Pore-Scale Geochemical Processes*, 2015, **80**, pp.165-190.
103. DESARNAUD, J., D. BONN and N. SHAHIDZADEH. The Pressure induced by salt crystallization in confinement. *Scientific Reports*, 2016, **6**.
104. STEIGER, M. Crystal growth in porous materials—I: The crystallization pressure of large crystals. *Journal of Crystal Growth*, 2005, **282**(3), pp.455-469.
105. SCHERER, G.W. Crystallization in pores. *Cement and Concrete research*, 1999, **29**(8), pp.1347-1358.
106. HAMILTON, A., V. KOUTSOS and C. HALL. Direct measurement of salt-mineral repulsion using atomic force microscopy. *Chemical Communications*, 2010, **46**(29), pp.5235-5237.
107. SCHERER, G.W. Internal stress and cracking in stone and masonry. *Measuring, Monitoring and Modeling Concrete Properties*, 2006, pp.633-641.
108. NOIRIEL, C., F. RENARD, M.-L. DOAN and J.-P. GRATIER. Intense fracturing and fracture sealing induced by mineral growth in porous rocks. *Chemical Geology*, 2010, **269**(3), pp.197-209.
109. BONN, N.S., F. BERTRAND and D. BONN. Damage due to salt crystallization in porous media. *arXiv preprint arXiv:0906.2502*, 2009.
110. DOEHNE, E. Salt weathering: a selective review. *Geological society, London, special publications*, 2002, **205**(1), pp.51-64.
111. DERLUYN, H., J. DEWANCKELE, M.N. BOONE, V. CNUDDE, D. DEROME and J. CARMELIET. Crystallization of hydrated and anhydrous salts in porous limestone resolved by synchrotron X-ray microtomography. *Nuclear Instruments & Methods in Physics Research Section B-Beam Interactions with Materials and Atoms*, 2014, **324**, pp.102-112.
112. NOIRIEL, C., C.I. STEEFEL, L. YANG and D. BERNARD. Effects of pore-scale precipitation on permeability and flow. *Advances in Water Resources*, 2016, **95**, pp.125-137.
113. WHITTAKER, M.L., P.M. DOVE and D. JOESTER. Nucleation on surfaces and in confinement. *Mrs Bulletin*, 2016, **41**(5), pp.388-392.
114. STEPHENS, C.J., S.F. LADDEN, F.C. MELDRUM and H.K. CHRISTENSON. Amorphous Calcium Carbonate is Stabilized in Confinement. *Advanced Functional Materials*, 2010, **20**(13), pp.2108-2115.

115. CANTAERT, B., E. BENIASH and F.C. MELDRUM. Nanoscale Confinement Controls the Crystallization of Calcium Phosphate: Relevance to Bone Formation. *Chemistry-a European Journal*, 2013, **19**(44), pp.14918-14924.
116. SCHENK, A.S., E.J. ALBARRACIN, Y.-Y. KIM, J. IHLI and F.C. MELDRUM. Confinement stabilises single crystal vaterite rods. *Chemical Communications*, 2014, **50**(36), pp.4729-4732.
117. LOSTE, E., R.J. PARK, J. WARREN and F.C. MELDRUM. Precipitation of calcium carbonate in confinement. *Advanced Functional Materials*, 2004, **14**(12), pp.1211-1220.
118. WANG, Y.W., H.K. CHRISTENSON and F.C. MELDRUM. Confinement leads to control over calcium sulfate polymorph. *Advanced Functional Materials*, 2013, **23**(45), pp.5615-5623.
119. IHLI, J., Y.W. WANG, B. CANTAERT, Y.Y. KIM, D.C. GREEN, P.H.H. BOMANS, N.A.J.M. SOMMERDIJK and F.C. MELDRUM. Precipitation of Amorphous Calcium Oxalate in Aqueous Solution. *Chemistry of Materials*, 2015, **27**(11), pp.3999-4007.
120. MANN, S., J.P. HANNINGTON and R.J.P. WILLIAMS. Phospholipid-Vesicles as a Model System for Biomineralization. *Nature*, 1986, **324**(6097), pp.565-567.
121. EANES, E.D. and A.W. HAILER. Liposome-Mediated Calcium-Phosphate Formation in Metastable Solutions. *Calcified Tissue International*, 1985, **37**(4), pp.390-394.
122. EANES, E.D., A.W. HAILER, R.J. MIDURA and V.C. HASCALL. Proteoglycan Inhibition of Calcium-Phosphate Precipitation in Liposomal Suspensions. *Glycobiology*, 1992, **2**(6), pp.571-578.
123. HEYWOOD, B.R. and E.D. EANES. An Ultrastructural-Study of Calcium-Phosphate Formation in Multilamellar Liposome Suspensions. *Calcified Tissue International*, 1987, **41**(4), pp.192-201.
124. TESTER, C.C., M.L. WHITTAKER and D. JOESTER. Controlling nucleation in giant liposomes. *Chemical Communications*, 2014, **50**(42), pp.5619-5622.
125. REES, G.D., R. EVANS-GOWING, S.J. HAMMOND and B.H. ROBINSON. Formation and morphology of calcium sulfate nanoparticles and nanowires in water-in-oil microemulsions. *Langmuir*, 1999, **15**(6), pp.1993-2002.
126. LAI, C., S.Q. TANG, Y.J. WANG, K. WEI and S.Y. ZHANG. Insight into shape control mechanism of calcium phosphate nanoparticles in reverse micelles solution. *Synthesis and Reactivity in Inorganic Metal-Organic and Nano-Metal Chemistry*, 2005, **35**(9), pp.717-725.
127. KUANG, D.B., A.W. XU, Y.P. FANG, H.D. OU and H.Q. LIU. Preparation of inorganic salts (CaCO3, BaCO3, CaSO4) nanowires in the Triton X-100/cyclohexane/water reverse micelles. *Journal of Crystal Growth*, 2002, **244**(3-4), pp.379-383.
128. STEPHENS, C.J., Y.-Y. KIM, S.D. EVANS, F.C. MELDRUM and H.K. CHRISTENSON. Early Stages of Crystallization of Calcium Carbonate Revealed in Picoliter Droplets. *Journal of the American Chemical Society*, 2011, **133**(14), pp.5210-5213.
129. LEE, A.Y., I.S. LEE and A.S. MYERSON. Factors affecting the polymorphic outcome of glycine crystals constrained on patterned

substrates. *Chemical Engineering & Technology*, 2006, **29**(2), pp.281-285.
130. LEE, I.S., K.T. KIM, A.Y. LEE and A.S. MYERSON. Concomitant crystallization of glycine on patterned substrates: The effect of pH on the polymorphic outcome. *Crystal Growth & Design*, 2008, **8**(1), pp.108-113.
131. WU, Z.S., Y.Y. LIN, J.J. XING, M.Y. ZHANG and J.B. WU. Surface-tension-confined assembly of a metal-organic framework in femtoliter droplet arrays. *The Royal Society of Chemistry Advances*, 2018, **8**(7), pp.3680-3686.
132. SANANDAJI, N., A. OKO, D.B. HAVILAND, E.A. THOLEN, M.S. HEDENQVIST and U.W. GEDDE. Inkjet printing as a possible route to study confined crystal structures. *European Polymer Journal*, 2013, **49**(1), pp.203-208.
133. BUANZ, A.B.M. and S. GAISFORD. Formation of Highly Metastable beta Glycine by Confinement in Inkjet Printed Droplets. *Crystal Growth & Design*, 2017, **17**(3), pp.1245-1250.
134. GU, Z.K., K. WANG, H.Z. LI, M. GAO, L.H. LI, M.X. KUANG, Y.S. ZHAO, M.Z. LI and Y.L. SONG. Direct-Writing Multifunctional Perovskite Single Crystal Arrays by Inkjet Printing. *Small*, 2017, **13**(8), p.1603217.
135. WOLF, S.E., J. LEITERER, M. KAPPL, F. EMMERLING and W. TREMEL. Early homogenous amorphous precursor stages of calcium carbonate and subsequent crystal growth in levitated droplets. *Journal of the American Chemical Society*, 2008, **130**(37), pp.12342-12347.
136. TSUJINO, S. and T. TOMIZAKI. Ultrasonic acoustic levitation for fast frame rate X-ray protein crystallography at room temperature. *Scientific Reports*, 2016, **6**, p.25558.
137. NGUYEN, T.Y., E.A. ROESSLER, K. RADEMANN and F. EMMERLING. Control of organic polymorph formation: crystallization pathways in acoustically levitated droplets. *Zeitschrift Fur Kristallographie-Crystalline Materials*, 2017, **232**(1-3), pp.15-24.
138. LEE, S., H.S. WI, W. JO, Y.C. CHO, H.H. LEE, S.Y. JEONG, Y.I. KIM and G.W. LEE. Multiple pathways of crystal nucleation in an extremely supersaturated aqueous potassium dihydrogen phosphate (KDP) solution droplet. *Proceedings of the National Academy of Sciences of the United States of America*, 2016, **113**(48), pp.13618-13623.
139. NEBEL, H., M. NEUMANN, C. MAYER and M. EPPLE. On the structure of amorphous calcium carbonate - A detailed study by solid-state NMR spectroscopy. *Inorganic Chemistry*, 2008, **47**(17), pp.7874-7879.
140. SEEMANN, R., M. BRINKMANN, T. PFOHL and S. HERMINGHAUS. Droplet based microfluidics. *Reports on progress in physics*, 2012, **75**(1), p.016601.
141. SHI, H.H., Y. XIAO, S. FERGUSON, X. HUANG, N. WANG and H.X. HAO. Progress of crystallization in microfluidic devices. *Lab on a Chip*, 2017, **17**(13), pp.2167-2185.
142. LONGUET, C., A. YAMADA, Y. CHEN, D. BAIGL and J. FATTACCIOLI. Spatially-controlled protein crystallization in

microfluidic chambers. *Journal of Crystal Growth*, 2014, **386**, pp.179-182.
143. LI, L. and R.F. ISMAGILOV. Protein Crystallization Using Microfluidic Technologies Based on Valves, Droplets and SlipChip. *Annual Review of Biophysics, Vol 39*, 2010, **39**, pp.139-158.
144. ABDALLAH, B.G., S. ROY-CHOWDHURY, R. FROMME, P. FROMME and A. ROS. Protein Crystallization in an Actuated Microfluidic Nanowell Device. *Crystal Growth & Design*, 2016, **16**(4), pp.2074-2082.
145. LOUNACI, M., Y. CHEN and P. RIGOLET. Channel height dependent protein nucleation and crystal growth in microfluidic devices. *Microelectronic Engineering*, 2010, **87**(5-8), pp.750-752.
146. HANSEN, C.L., E. SKORDALAKES, J.M. BERGER and S.R. QUAKE. A robust and scalable microfluidic metering method that allows protein crystal growth by free interface diffusion. *PNAS*, 2002, **99**(26), pp.16531–16536.
147. SAUTER, C. *Microfluidics, crystallization and crystallography* [online]. 2011. [Accessed]. Available from: http://hamptonresearch.com/documents/ramc/RAMC2011_T3_Sauter.pdf.
148. ZHENG, B., J.D. TICE, L.S. ROACH and R.F. ISMAGILOV. A droplet-based, composite PDMS/glass capillary microfluidic system for evaluating protein crystallization conditions by microbatch and vapor-diffusion methods with on-chip X-ray diffraction. *Angewandte Chemie-International Edition*, 2004, **43**(19), pp.2508-2511.
149. LENG, J. and J.B. SALMON. Microfluidic crystallization. *Lab on a Chip*, 2009, **9**(1), pp.24-34.
150. ZHANG, S.H., C.J.J. GERARD, A. IKNI, G. FERRY, L.M. VUILLARD, J.A. BOUTIN, N. FERTE, R. GROSSIER, N. CANDONI and S. VEESLER. Microfluidic platform for optimization of crystallization conditions. *Journal of Crystal Growth*, 2017, **472**, pp.18-28.
151. YASHINA, A., F. MELDRUM and A. DEMELLO. Calcium carbonate polymorph control using droplet-based microfluidics. *Biomicrofluidics*, 2012, **6**.
152. ILDEFONSO, M., E. REVALOR, P. PUNNIAM, J.B. SALMON, N. CANDONI and S. VEESLER. Nucleation and polymorphism explored via an easy-to-use microfluidic tool. *Journal of Crystal Growth*, 2012, **342**(1), pp.9-12.
153. MIJATOVIC, D., J.C.T. EIJKEL and A. VAN DEN BERG. Technologies for nanofluidic systems: top-down vs. bottom-up - a review. *Lab on a Chip*, 2005, **5**(5), pp.492-500.
154. GHAZAL, A., J.P. LAFLEUR, K. MORTENSEN, J.P. KUTTER, L. ARLETH and G.V. JENSEN. Recent advances in X-ray compatible microfluidics for applications in soft materials and life sciences. *Lab on a Chip*, 2016, **16**(22), pp.4263-4295.
155. GOYAL, S., A.E. ECONOMOU, T. PAPADOPOULOS, E.M. HORSTMAN, G.G.Z. ZHANG, Y.C. GONG and P.J.A. KENIS. Solvent compatible microfluidic platforms for pharmaceutical solid form screening. *The Royal Society of Chemistry Advances*, 2016, **6**(16), pp.13286-13296.

156. WANG, Y., M. ZENG, F.C. MELDRUM and H.K. CHRISTENSON. Using Confinement To Study the Crystallization Pathway of Calcium Carbonate. *Crystal Growth & Design*, 2017.
157. DEVOL, R.T., C.Y. SUN, M.A. MARCUS, S.N. COPPERSMITH, S.C.B. MYNENI and P.U.P.A. GILBERT. Nanoscale Transforming Mineral Phases in Fresh Nacre. *Journal of the American Chemical Society*, 2015, **137**(41), pp.13325-13333.
158. FALINI, G. Crystallization of calcium carbonates in biologically inspired collagenous matrices. *International Journal of Inorganic Materials*, 2000, **2**(5), pp.455-461.
159. SHAHIDZADEH-BONN, N., J. DESARNAUD, F. BERTRAND, X. CHATEAU and D. BONN. Damage in porous media due to salt crystallization. *Physical Review E*, 2010, **81**(6), p.066110
160. YANG, X.Y., L.H. CHEN, Y. LI, J.C. ROOKE, C. SANCHEZ and B.L. SU. Hierarchically porous materials: synthesis strategies and structure design. *Chemical Society Reviews*, 2017, **46**(2), pp.481-558.
161. MENG, L.L., X.F. ZHANG, Y.S. TANG, K.H. SU and J. KONG. Hierarchically porous silicon-carbon-nitrogen hybrid materials towards highly efficient and selective adsorption of organic dyes. *Scientific Reports*, 2015, **5**, p.7910
162. KONISHI, J., K. FUJITA, S. OIWA, K. NAKANISHI and K. HIRAO. Crystalline ZrO2 monoliths with well-defined macropores and mesostructured skeletons prepared by combining the alkoxy-derived sol-gel process accompanied by phase separation and the solvothermal process. *Chemistry of Materials*, 2008, **20**(6), pp.2165-2173.
163. CHAKRABORTY, S., Y.J. COLON, R.Q. SNURR and S.T. NGUYEN. Hierarchically porous organic polymers: highly enhanced gas uptake and transport through templated synthesis. *Chemical Science*, 2015, **6**(1), pp.384-389.
164. PARK, R.J. and F.C. MELDRUM. Shape-constraint as a route to calcite single crystals with complex morphologies. *Journal of Materials Chemistry*, 2004, **14**(14), pp.2291-2296.
165. PARK, R.J. and F.C. MELDRUM. Synthesis of single crystals of calcite with complex morphologies. *Advanced Materials*, 2002, **14**(16), pp.1167-1169.
166. LOSTE, E. and F.C. MELDRUM. Control of calcium carbonate morphology by transformation of an amorphous precursor in a constrained volume. *Chemical Communications*, 2001, (10), pp.901-902.
167. AIZENBERG, J., D.A. MULLER, J.L. GRAZUL and D.R. HAMANN. Direct fabrication of large micropatterned single crystals. *Science*, 2003, **299**(5610), pp.1205-1208.
168. MARTIN, C.R. Membrane-based synthesis of nanomaterials. *Chemistry of Materials*, 1996, **8**(8), pp.1739-1746.
169. IMAI, H., Y. TAKEI, K. SHIMIZU, M. MATSUDA and H. HIRASHIMA. Direct preparation of anatase TiO2 nanotubes in porous alumina membranes. *Journal of Materials Chemistry*, 1999, **9**(12), pp.2971-2972.

170. ASENATH-SMITH, E., J.M. NOBLE, R. HOVDEN, A.M. UHL, A. DICORATO, Y.Y. KIM, A.N. KULAK, F.C. MELDRUM, L.F. KOURKOUTIS and L.A. ESTROFF. Physical Confinement Promoting Formation of Cu_2O-Au Heterostructures with Au Nanoparticles Entrapped within Crystalline Cu_2O Nanorods. *Chemistry of Materials*, 2017, **29**(2), pp.555-563.
171. CNUDDE, V. and M.N. BOONE. High-resolution X-ray computed tomography in geosciences: A review of the current technology and applications. *Earth-Science Reviews*, 2013, **123**, pp.1-17.
172. GODINHO, J.R. and P.J. WITHERS. Time-lapse 3D imaging of calcite precipitation in a microporous column. *Geochimica et Cosmochimica Acta*, 2018, **222**, pp.156-170.
173. ANOVITZ, L.M. and D.R. COLE. Characterization and Analysis of Porosity and Pore Structures. *Pore-Scale Geochemical Processes*, 2015, **80**, pp.61-164.
174. ANOVITZ, L.M., D.R. COLE, G. ROTHER, L.F. ALLARD, A.J. JACKSON and K.C. LITTRELL. Diagenetic changes in macro- to nano-scale porosity in the St. Peter Sandstone: An (ultra) small angle neutron scattering and backscattered electron imaging analysis. *Geochimica et Cosmochimica Acta*, 2013, **102**, pp.280-305.
175. WANG, H.W., L.M. ANOVITZ, A. BURG, D.R. COLE, L.F. ALLARD, A.J. JACKSON, A.G. STACK and G. ROTHER. Multi-scale characterization of pore evolution in a combustion metamorphic complex, Hatrurim basin, Israel: Combining (ultra) small-angle neutron scattering and image analysis. *Geochimica et Cosmochimica Acta*, 2013, **121**, pp.339-362.
176. PRIETO, M. Nucleation and supersaturation in porous media (revisited). *Mineralogical Magazine*, 2014, **78**(6), pp.1437-1447.
177. PUTNIS, A. Transient Porosity Resulting from Fluid-Mineral Interaction and its Consequences. *Pore-Scale Geochemical Processes*, 2015, **80**, pp.1-23.
178. ENKE, D., F. JANOWSKI and W. SCHWIEGER. Porous glasses in the 21st century—a short review. *Microporous and mesoporous materials*, 2003, **60**(1), pp.19-30.
179. SUZUKI, M. and T. TANAKA. Prediction of phase separation in multi-component oxide glass for the fabrication of porous glass materials from waste slag. *In: Journal of Physics: Conference Series*: IOP Publishing, 2009, p.012078.
180. SHAFER, M.W., D.D. AWSCHALOM, J. WARNOCK and G. RUBEN. The Chemistry of and Physics with Porous Sol-Gel Glasses. *Journal of Applied Physics*, 1987, **61**(12), pp.5438-5446.
181. WOIGNIER, T., A.H. ALAOUI, J. PRIMERA and J. PHALIPPOU. Properties and applications of porous glasses from foamed glasses and gel-derived glasses to allophanes. *Revista Mexicana De Fisica*, 2006, **52**(3), pp.190-194.
182. XU, B., X. DI and G.B. MCKENNA. Melting of pentaerythritol tetranitrate (PETN) nanoconfined in controlled pore glasses (CPG). *Journal of Thermal Analysis and Calorimetry*, 2013, **113**(2), pp.539-543.
183. CHRISTENSON, H.K. Confinement effects on freezing and melting. *Journal of Physics-Condensed Matter*, 2001, **13**(11), pp.R95-R133.

184. HA, J.M., J.H. WOLF, M.A. HILLMYER and M.D. WARD. Polymorph selectivity under nanoscopic confinement. *Journal of the American Chemical Society*, 2004, **126**(11), pp.3382-3383.
185. HA, J.-M., B.D. HAMILTON, M.A. HILLMYER and M.D. WARD. Phase Behavior and Polymorphism of Organic Crystals Confined within Nanoscale Chambers. *Crystal Growth & Design*, 2009, **9**(11), pp.4766-4777.
186. STACK, A.G., A. FERNANDEZ-MARTINEZ, L.F. ALLARD, J.L. BANUELOS, G. ROTHER, L.M. ANOVITZ, D.R. COLE and G.A. WAYCHUNAS. Pore-Size-Dependent Calcium Carbonate Precipitation Controlled by Surface Chemistry. *Environmental Science & Technology*, 2014, **48**(11), pp.6177-6183.
187. ANDUIX-CANTO, C., Y.-Y. KIM, Y.-W. WANG, A. KULAK, F.C. MELDRUM and H.K. CHRISTENSON. Effect of Nanoscale Confinement on the Crystallization of Potassium Ferrocyanide. *Crystal Growth & Design*, 2016, **16**(9), pp.5403-5411.
188. RZAYEV, J. and M.A. HILLMYER. Nanochannel array plastics with tailored surface chemistry. *Journal of the American Chemical Society*, 2005, **127**(38), pp.13373-13379.
189. HAMILTON, B.D., M.A. HILLMYER and M.D. WARD. Glycine polymorphism in nanoscale crystallization chambers. *Crystal Growth & Design*, 2008, **8**(9), pp.3368-3375.
190. RENGARAJAN, G.T., D. ENKE, M. STEINHART and M. BEINER. Stabilization of the amorphous state of pharmaceuticals in nanopores. *Journal of Materials Chemistry*, 2008, **18**(22), pp.2537-2539.
191. AIZENBERG, J., A.J. BLACK and G.M. WHITESIDES. Control of crystal nucleation by patterned self-assembled monolayers. *Nature*, 1999, **398**(6727), pp.495-498.
192. HOLBROUGH, J.L., J.M. CAMPBELL, F.C. MELDRUM and H.K. CHRISTENSON. Topographical Control of Crystal Nucleation. *Crystal Growth & Design*, 2012, **12**(2), pp.750-755.
193. LEE, P.A. *Control of crystallisation using surface topography*. thesis, University of Leeds, 2017.
194. EJGENBERG, M. and Y. MASTAI. *Crystallization on Self Assembled Monolayers" in Advances in Crystallization Processes,.* Advances in Crystallization Processes. 2012.
195. CASALINI, S., C.A. BORTOLOTTI, F. LEONARDI and F. BISCARINI. Self-assembled monolayers in organic electronics. *Chemical Society Reviews*, 2017, **46**(1), pp.40-71.
196. ULMAN, A. Formation and structure of Self-Assembled monolayers. *Chem. Rev.*, 1996, **96**, pp.1533-1554.
197. LOVE, J.C., L.A. ESTROFF, J.K. KRIEBEL, R.G. NUZZO and G.M. WHITESIDES. Self-assembled monolayers of thiolates on metals as a form of nanotechnology. *Chemical Reviews*, 2005, **105**(4), pp.1103-1169.
198. AIZENBERG, J., G. LAMBERT, S. WEINER and L. ADDADI. Factors involved in the formation of amorphous and crystalline calcium carbonate: A study of an ascidian skeleton. *Journal of the American Chemical Society*, 2002, **124**(1), pp.32-39.
199. ADDADI, L. and S. WEINER. Interactions between Acidic Proteins and Crystals - Stereochemical Requirements in Biomineralization.

Proceedings of the National Academy of Sciences of the United States of America, 1985, **82**(12), pp.4110-4114.
200. BERMAN, A., L. ADDADI and S. WEINER. Interactions of Sea-Urchin Skeleton Macromolecules with Growing Calcite Crystals - a Study of Intracrystalline Proteins. *Nature*, 1988, **331**(6156), pp.546-548.
201. MANN, S. *Handbook of Biomineralization: Biomimetic and bioinspired chemistry.* John Wiley & Sons, 2009.
202. AIZENBERG, J., A.J. BLACK and G.H. WHITESIDES. Oriented growth of calcite controlled by self-assembled monolayers of functionalized alkanethiols supported on gold and silver. *Journal of the American Chemical Society*, 1999, **121**(18), pp.4500-4509.
203. LEE, A.Y., A. ULMAN and A.S. MYERSON. Crystallization of amino acids on self-assembled monolayers of rigid thiols on gold. *Langmuir*, 2002, **18**(15), pp.5886-5898.
204. ZHANG, C.-Y., H.-F. SHEN, Q.-J. WANG, Y.-Z. GUO, J. HE, H.-L. CAO, Y.-M. LIU, P. SHANG and D.-C. YIN. An investigation of the effects of self-assembled monolayers on protein crystallisation. *International journal of molecular sciences*, 2013, **14**(6), pp.12329-12345.
205. JIANG, P., Z.F. LIU and S.M. CAI. Growing monodispersed PbS nanoparticles on self-assembled monolayers of 11-mercaptoundecanoic acid on Au(111) substrate. *Langmuir*, 2002, **18**(11), pp.4495-4499.
206. TARASEVICH, B.J., C.C. CHUSUEI and D.L. ALLARA. Nucleation and growth of calcium phosphate from physiological solutions onto self-assembled templates by a solution-formed nucleus mechanism. *Journal of Physical Chemistry B*, 2003, **107**(38), pp.10367-10377.
207. AIZENBERG, J. Crystallization in patterns: A bio-inspired approach. *Advanced Materials*, 2004, **16**(15), pp.1295-1302.
208. HIREMATH, R., J.A. BASILE, S.W. VARNEY and J.A. SWIFT. Controlling molecular crystal polymorphism with self-assembled monolayer templates. *Journal of the American Chemical Society*, 2005, **127**(51), pp.18321-18327.
209. DRESSLER, D.H. and Y. MASTAI. Controlling polymorphism by crystallization on self-assembled multilayers. *Crystal Growth & Design*, 2007, **7**(5), pp.847-850.
210. GEORGIEVA, D.G., M.E. KUIL, T.H. OOSTERKAMP, H.W. ZANDBERGEN and J.P. ABRAHAMS. Heterogeneous nucleation of three-dimensional protein nanocrystals. *Acta Crystallographica Section D-Biological Crystallography*, 2007, **63**, pp.564-570.
211. DEAN, J.R. *Practical skills in chemistry.* Pearson Education, 2002.
212. SHOLL, C. and N. FLETCHER. Decoration criteria for surface steps. *Acta Metallurgica*, 1970, **18**(10), pp.1083-1086.
213. PAGE, A.J. and R.P. SEAR. Crystallization controlled by the geometry of a surface. *Journal of the American Chemical Society*, 2009, **131**(48), pp.17550-17551.
214. HEDGES, L.O. and S. WHITELAM. Selective nucleation in porous media. *Soft Matter*, 2013, **9**(41), pp.9763-9766.
215. CHAYEN, N.E., E. SARIDAKIS and R.P. SEAR. Experiment and theory for heterogeneous nucleation of protein crystals in a porous

medium. *Proceedings of the National Academy of Sciences of the United States of America*, 2006, **103**(3), pp.597-601.
216. NANEV, C.N., E. SARIDAKIS and N.E. CHAYEN. Protein crystal nucleation in pores. *Scientific Reports*, 2017, **7**.
217. KEYSAR, S., R. SEMIAT, D. HASSON and J. YAHALOM. Effect of surface roughness on the morphology of calcite crystallizing on mild steel. *Journal of Colloid and Interface Science*, 1994, **162**(2), pp.311-319.
218. MACADAM, J. and S.A. PARSONS. Calcium carbonate scale control, effect of material and inhibitors. *Water Science and Technology*, 2004, **49**(2), pp.153-159.
219. DENNIG, P.A. and D.A. STEVENSON. Influence of Substrate Topography on the Nucleation of Diamond Thin-Films. *Applied Physics Letters*, 1991, **59**(13), pp.1562-1564.
220. CAMPBELL, J.M., F.C. MELDRUM and H.K. CHRISTENSON. Characterization of Preferred Crystal Nucleation Sites on Mica Surfaces. *Crystal Growth & Design*, 2013, **13**(5), pp.1915-1925.
221. ZHOU, R.B., H.L. CAO, C.Y. ZHANG and D.C. YIN. A review on recent advances for nucleants and nucleation in protein crystallization. *CrystEngComm*, 2017, **19**(8), pp.1143-1155.
222. KHURSHID, S., E. SARIDAKIS, L. GOVADA and N.E. CHAYEN. Porous nucleating agents for protein crystallization. *Nat. Protocols*, 2014, **9**(7), pp.1621-1633.
223. SARIDAKIS, E., S. KHURSHID, L. GOVADA, Q. PHAN, D. HAWKINS, G.V. CRICHLOW, E. LOLIS, S.M. REDDY and N.E. CHAYEN. Protein crystallization facilitated by molecularly imprinted polymers (vol 108, pg 11081, 2011). *Proceedings of the National Academy of Sciences of the United States of America*, 2011, **108**(45), pp.18566-18566.
224. KHURSHID, S., L. GOVADA, H.F. EL-SHARIF, S.M. REDDY and N.E. CHAYEN. Automating the application of smart materials for protein crystallization. *Acta Crystallographica Section D-Structural Biology*, 2015, **71**, pp.534-540.
225. CHAYEN, N., E. SARIDAKIS, R. EL-BAHAR and Y. NEMIROVSKY. Porous silicon: an effective nucleation-inducing material for protein crystallization. *Journal of Molecular Biology*, 2001, **312**(4), pp.591-595.
226. GOVADA, L., H.S. LEESE, E. SARIDAKIS, S. KASSEN, B. CHAIN, S. KHURSHID, R. MENZEL, S. HU, M.S.P. SHAFFER and N.E. CHAYEN. Exploring Carbon Nanomaterial Diversity for Nucleation of Protein Crystals. *Scientific Reports*, 2016, **6**.
227. SHAH, U.V., M.C. ALLENBY, D.R. WILLIAMS and J.Y.Y. HENG. Crystallization of Proteins at Ultralow Supersaturations Using Novel Three-Dimensional Nanotemplates. *Crystal Growth & Design*, 2012, **12**(4), pp.1772-1777.
228. TANG, L., Y. HUANG, D. LIU, J. LI, K. MAO, L. LIU, Z. CHENG, W. GONG, J. HU and J. HE. Effects of the silanized mica surface on protein crystallization. *Acta Crystallographica Section D: Biological Crystallography*, 2005, **61**(1), pp.53-59.
229. FALINI, G., S. FERMANI, G. CONFORTI and A. RIPAMONTI. Protein crystallisation on chemically modified mica surfaces. *Acta*

Crystallographica Section D: Biological Crystallography, 2002, **58**(10), pp.1649-1652.

230. DE POEL, W., J.A. MÜNNINGHOFF, J.A. ELEMANS, W.J. VAN ENCKEVORT, A.E. ROWAN and E. VLIEG. Surfaces with Controllable Topography and Chemistry used as a Template for Protein Crystallization. *Crystal Growth & Design*, 2018, **18**(2), pp.763-769.
231. LE CAER, S., F. BRUNET, C. CHATELAIN, D. DURAND, V. DAUVOIS, T. CHARPENTIER and J. PH. RENAULT. Modifications under irradiation of a self-assembled monolayer grafted on a nanoporous silica glass: a solid-state NMR characterization. *The Journal of Physical Chemistry C*, 2012, **116**(7), pp.4748-4759.
232. ZHANG, H., C.-Y. LIN and S.J. HOLLISTER. The interaction between bone marrow stromal cells and RGD-modified three-dimensional porous polycaprolactone scaffolds. *Biomaterials*, 2009, **30**(25), pp.4063-4069.
233. ARCHIBALD, D., S. QADRI and B. GABER. Modified calcite deposition due to ultrathin organic films on silicon substrates. *Langmuir*, 1996, **12**(2), pp.538-546.
234. SEMWOGERERE, D. and E.R. WEEKS. Confocal microscopy. *Encyclopedia of Biomaterials and Biomedical Engineering*, 2005, **23**, pp.1-10.
235. NELLIST, P.D., M.F. CHISHOLM, N. DELLBY, O.L. KRIVANEK, M.F. MURFITT, Z.S. SZILAGYI, A.R. LUPINI, A. BORISEVICH, W.H. SIDES and S.J. PENNYCOOK. Direct sub-angstrom imaging of a crystal lattice. *Science*, 2004, **305**(5691), pp.1741-1741.
236. KANTOR, M.M. Physical Principles of High-Voltage Electron-Microscopy and Possibilities of Its Application in the Study of Materials (Review). *Industrial Laboratory*, 1981, **47**(11), pp.1148-1159.
237. LIAO, H.G. and H.M. ZHENG. Liquid Cell Transmission Electron Microscopy. *Annual Review of Physical Chemistry, Vol 67*, 2016, **67**, pp.719-+.
238. NOGALES, E. The development of cryo-EM into a mainstream structural biology technique. *Nature Methods*, 2016, **13**(1), pp.24-27.
239. CHRISTENSON, H.K. Contact angles and wetting. *In: module PHYS5320M*, Leeds University. 2011.
240. BRUNAUER, S., P.H. EMMETT and E. TELLER. Adsorption of gases in multimolecular layers. *Journal of the American Chemical Society*, 1938, **60**, pp.309-319.
241. SING, K. The use of nitrogen adsorption for the characterisation of porous materials. *Colloids and Surfaces a-Physicochemical and Engineering Aspects*, 2001, **187**, pp.3-9.
242. MICROMERITICS. *ASAP 2020 accelerated surface area and porosimetry system.* Apendix C-13. 2010.
243. PANCHBHAI, A.S. Wilhelm Conrad Röntgen and the discovery of X-rays: Revisited after centennial. *Journal of Indian Academy of Oral Medicine and Radiology*, 2015, **27**(1), p.90.
244. WILLMOTT, P. *An introduction to synchrotron radiation: techniques and applications.* John Wiley & Sons, 2011.

245. FACILITY, E.S.R.F. [online]. [Accessed]. Available from: http://www.esrf.eu/about/synchrotron-science/synchrotron.
246. BIRKBAK, M.E., H. LEEMREIZE, S. FROLICH, S.R. STOCK and H. BIRKEDAL. Diffraction scattering computed tomography: a window into the structures of complex nanomaterials. *Nanoscale*, 2015, **7**(44), pp.18402-18410.
247. LEEMREIZE, H., J.D. ALMER, S.R. STOCK and H. BIRKEDAL. Three-dimensional distribution of polymorphs and magnesium in a calcified underwater attachment system by diffraction tomography. *Journal of The Royal Society Interface*, 2013, **10**(86), p.20130319.
248. GÜNTHER, H. *NMR spectroscopy: basic principles, concepts and applications in chemistry.* John Wiley & Sons, 2013.
249. KUHN, L.T. and J. BARGON. Exploiting nuclear spin polarization to investigate free radical reactions via in situ NMR. *In Situ Nmr Methods in Catalysis*, 2007, **276**, pp.125-154.
250. HAN, X.W., Z.M. YAN, W.P. ZHANG and X.H. BAO. Applications of in situ NMR in catalytic processes of organic reactions. *Current Organic Chemistry*, 2001, **5**(10), pp.1017-1037.
251. LADIZHANSKY, V. Recent Advances in Magic-Angle Spinning Solid-State NMR of Proteins. *Israel Journal of Chemistry*, 2014, **54**(1-2), pp.86-103.
252. POENOVA, T., R. GUPTA and A. GOLDBOURT. Magic Angle Spinning NMR Spectroscopy: A Versatile Technique for Structural and Dynamic Analysis of Solid-Phase Systems. *Analytical chemistry*, 2015, **87**(11), pp.5458-5469.
253. HUGHES, C.E. and K.D.M. HARRIS. A technique for in situ monitoring of crystallization from solution by solid-state C-13 CPMAS NMR spectroscopy. *Journal of Physical Chemistry A*, 2008, **112**(30), pp.6808-6810.
254. HUGHES, C.E. and K.D.M. HARRIS. Direct observation of a transient polymorph during crystallization. *Chemical Communications*, 2010, **46**(27), pp.4982-4984.
255. HUGHES, C.E., P.A. WILLIAMS, T.R. PESKETT and K.D.M. HARRIS. Exploiting In Situ Solid-State NMR for the Discovery of New Polymorphs during Crystallization Processes. *Journal of Physical Chemistry Letters*, 2012, **3**(21), pp.3176-3181.
256. HUGHES, C.E., P.A. WILLIAMS and K.D.M. HARRIS. "CLASSIC NMR": An In-Situ NMR Strategy for Mapping the Time-Evolution of Crystallization Processes by Combined Liquid-State and Solid-State Measurements. *Angewandte Chemie-International Edition*, 2014, **53**(34), pp.8939-8943.
257. WILLANS, M.J., R.E. WASYLISHEN and R. MCDONALD. Polymorphism of Potassium Ferrocyanide Trihydrate as Studied by Solid- State Multinuclear NMR Spectroscopy and X-ray Diffraction. *Inorganic Chemistry*, 2009, **48**(10), pp.4342-4353.
258. GAFFAR, M.A. and M.H. OMAR. Thermal analytical study of different phases of potassium hexacyanoferrate(II) crystal - Effects of growth conditions, heat treatment and gamma-irradiation on the unit cell parameters. *Journal of Thermal Analysis and Calorimetry*, 2005, **81**(2), pp.477-487.

259. GAIL, E., S. GOS, R. KULZER, J. LORÖSCH, A. RUBO, M. SAUER, R. KELLENS, J. REDDY, N. STEIER and W. HASENPUSCH. Cyano Compounds, Inorganic. *In: Ullmann's Encyclopedia of Industrial Chemistry*. Wiley-VCH Verlag GmbH & Co. KGaA, 2000.
260. BERNHARDT, P.V., F. BOZOGLIÁN, B.P. MACPHERSON and M. MARTÍNEZ. Molecular mixed-valence cyanide bridged Co III–Fe II complexes. *Coordination chemistry reviews*, 2005, **249**(17), pp.1902-1916.
261. LESCOUËZEC, R., L.M. TOMA, J. VAISSERMANN, M. VERDAGUER, F.S. DELGADO, C. RUIZ-PÉREZ, F. LLORET and M. JULVE. Design of single chain magnets through cyanide-bearing six-coordinate complexes. *Coordination chemistry reviews*, 2005, **249**(23), pp.2691-2729.
262. KIRIYAMA, R., N. NIIZEKI, H. HIRABAYASHI, T. WADA and H. KIRIYAMA. NUCLEAR MAGNETIC RESONANCE + X-RAY STUDIES OF POTASSIUM FERROCYANIDE TRIHYDRATE CRYSTAL. *Journal of the Physical Society of Japan*, 1964, **19**(4), pp.540-&.
263. BLINC, R., J.S. WAUGH and M. BRENMAN. PROTON MAGNETIC RESONANCE STUDY OF FERROELECTRIC POTASSIUM FERROCYANIDE TRIHYDRATE. *Journal of Chemical Physics*, 1961, **35**(5), pp.1770-&.
264. TOYODA, H., N. NIIZEKI and S. WAKU. OPTICAL AND STRUCTURAL ANOMALIES IN POTASSIUM FERROCYANIDE TRIHYDRATE CRYSTALS. *Journal of the Physical Society of Japan*, 1960, **15**(10), pp.1831-1841.
265. WYROUBOFF. Ferrocyanure de Potassium. *Annales de Chimie et Physique*, 1869, pp.293-301.
266. BRIGGS, S.H.C. The isomerism of ferrocyanides. *Journal of the Chemical Society*, 1911, **99**, pp.1019-1035.
267. BRIGGS, S.H.C. The nature of the beta-ferricyanides and the beta-ferrocyanides. *Journal of the Chemical Society*, 1920, **117**, pp.1026-1034.
268. KANAGADURAI, R., R. SANKAR, G. SIVANESAN, S. SRINIVASAN and R. JAYAVEL. Growth and properties of ferroelectric potassium ferrocyanide trihydrate single crystals. *Crystal Research and Technology*, 2006, **41**(9), pp.853-858.
269. GENEVICIUTE, L., N. FLORIO and S. LEE. Toward Polymorph Control in an Inorganic Crystal System by Templated Nucleation at a Microdroplet Liquid Interface: Potassium Hexacyanoferrate(II) Trihydrate. *Crystal Growth & Design*, 2011, **11**(10), pp.4440-4448.
270. PUTNIS, A., M. PRIETO and L. FERNANDEZDIAZ. Fluid Supersaturation and Crystallization in Porous-Media. *Geological Magazine*, 1995, **132**(1), pp.1-13.
271. FLURY, M. and T. GIMMI. Solute diffusion *In: Methods of Soil Analysis*. Madison: Soil Science Society of Ameica, 2002.
272. BOUFADEL, M.C., M.T. SUIDAN and A.D. VENOSA. A numerical model for density-and-viscosity-dependent flows in two-dimensional variably saturated porous media. *Journal of Contaminant Hydrology*, 1999, **37**(1), pp.1-20.

273. MILLINGTON, R. and J. QUIRK. Permeability of porous solids. *Transactions of the Faraday Society*, 1961, **57**, pp.1200-1207.
274. CHOU, H.Y., L.S. WU, L.Z. ZENG and A. CHANG. Evaluation of solute diffusion tortuosity factor models for variously saturated soils. *Water Resources Research*, 2012, **48**.
275. MITZITHRAS, A., F.M. COVENEY and J.H. STRANGE. Nmr-Studies of the Diffusion of Cyclohexane in Porous Silica. *Journal of Molecular Liquids*, 1992, **54**(4), pp.273-281.
276. MESSAGER, R., D. CHATENAY, W. URBACH, J.P. BOUCHAUD and D. LANGEVIN. Tracer Self-Diffusion in Porous Silica - a Dynamical Probe of the Structure. *Europhysics Letters*, 1989, **10**(1), pp.61-66.
277. SHEN, L. and Z.X. CHEN. Critical review of the impact of tortuosity on diffusion. *Chemical Engineering Science*, 2007, **62**(14), pp.3748-3755.
278. HA, J.-M., B.D. HAMILTON, M.A. HILLMYER and M.D. WARD. Alignment of Organic Crystals under Nanoscale Confinement. *Crystal Growth & Design*, 2012, **12**(9), pp.4494-4504.
279. WARREN, J.K. *Evaporites: sediments, resources and hydrocarbons.* Springer Science & Business Media, 2006.
280. GENDRIN, A., N. MANGOLD, J.-P. BIBRING, Y. LANGEVIN, B. GONDET, F. POULET, G. BONELLO, C. QUANTIN, J. MUSTARD and R. ARVIDSON. Sulfates in Martian layered terrains: the OMEGA/Mars Express view. *Science*, 2005, **307**(5715), pp.1587-1591.
281. WRAY, J.J., S.W. SQUYRES, L.H. ROACH, J.L. BISHOP, J.F. MUSTARD and E.Z.N. DOBREA. Identification of the Ca-sulfate bassanite in Mawrth Vallis, Mars. *Icarus*, 2010, **209**(2), pp.416-421.
282. CHAROLA, A.E., J. PÜHRINGER and M. STEIGER. Gypsum: a review of its role in the deterioration of building materials. *Environmental geology*, 2007, **52**(2), pp.339-352.
283. AHMED, S.B., M. TLILI, M.B. AMOR, H.B. BACHA and B. ELLEUCH. Calcium sulphate scale prevention in a desalination unit using the SMCEC technique. *Desalination*, 2004, **167**, pp.311-318.
284. WEISS, H. and M.F. BRÄU. How much water does calcined gypsum contain? *Angewandte Chemie International Edition*, 2009, **48**(19), pp.3520-3524.
285. LANGEVIN, Y., F. POULET, J.-P. BIBRING and B. GONDET. Sulfates in the north polar region of Mars detected by OMEGA/Mars Express. *Science*, 2005, **307**(5715), pp.1584-1586.
286. THOMAS, M.V., D.A. PULEO and M. AL-SABBAGH. Calcium sulfate: a review. *Journal of long-term effects of medical implants*, 2005, **15**(6).
287. SINGH, N. and B. MIDDENDORF. Calcium sulphate hemihydrate hydration leading to gypsum crystallization. *Progress in Crystal Growth and Characterization of Materials*, 2007, **53**(1), pp.57-77.
288. VAN DRIESSCHE, A.E., T.M. STAWSKI, L.G. BENNING and M. KELLERMEIER. Calcium sulfate precipitation throughout its phase diagram. *In: New Perspectives on Mineral Nucleation and Growth*. Springer, 2017, pp.227-256.

289. *Ullmann's Encyclopedia of Industrial Chemistry*. s.v. Calcium Sulfate, 2000.
290. PRIETO-TABOADA, N., O. GOMEZ-LASERNA, I. MARTINEZ-ARKARAZO, M.A. OLAZABAL and J.M. MADARIAGA. Raman Spectra of the Different Phases in the CaSO4-H2O System. *Analytical chemistry*, 2014, **86**(20), pp.10131-10137.
291. TRITSCHLER, U., M. KELLERMEIER, C. DEBUS, A. KEMPTER and H. CÖLFEN. A simple strategy for the synthesis of well-defined bassanite nanorods. *CrystEngComm*, 2015, **17**(20), pp.3772-3776.
292. TRITSCHLER, U., A.E. VAN DRIESSCHE, A. KEMPTER, M. KELLERMEIER and H. CÖLFEN. Controlling the selective formation of calcium sulfate polymorphs at room temperature. *Angewandte Chemie International Edition*, 2015, **54**(13), pp.4083-4086.
293. WANG, Y.-W. and F.C. MELDRUM. Additives stabilize calcium sulfate hemihydrate (bassanite) in solution. *Journal of Materials Chemistry*, 2012, **22**(41), pp.22055-22062.
294. PACKTER, A. The precipitation of calcium sulphate dihydrate from aqueous solution: Induction periods, crystal numbers and final size. *Journal of Crystal Growth*, 1974, **21**(2), pp.191-194.
295. STAWSKI, T.M., A.E. VAN DRIESSCHE, M. OSSORIO, J.D. RODRIGUEZ-BLANCO, R. BESSELINK and L.G. BENNING. Formation of calcium sulfate through the aggregation of sub-3 [thinsp] nanometre primary species. *Nature communications*, 2016, **7**.
296. VAN DRIESSCHE, A., L. BENNING, J. RODRIGUEZ-BLANCO, M. OSSORIO, P. BOTS and J. GARCÍA-RUIZ. The role and implications of bassanite as a stable precursor phase to gypsum precipitation. *Science*, 2012, **336**(6077), pp.69-72.
297. JONES, F. Infrared investigation of barite and gypsum crystallization: Evidence for an amorphous to crystalline transition. *CrystEngComm*, 2012, **14**(24), pp.8374-8381.
298. WANG, Y.-W., Y.-Y. KIM, H.K. CHRISTENSON and F.C. MELDRUM. A new precipitation pathway for calcium sulfate dihydrate (gypsum) via amorphous and hemihydrate intermediates. *Chemical Communications*, 2012, **48**(4), pp.504-506.
299. WANG, Y.-W., H.K. CHRISTENSON and F.C. MELDRUM. Confinement Leads to Control over Calcium Sulfate Polymorph. *Advanced Functional Materials*, 2013, **23**(45), pp.5615-5623.
300. SAHA, A., J. LEE, S.M. PANCERA, M.F. BRAEU, A. KEMPTER, A. TRIPATHI and A. BOSE. New Insights into the Transformation of Calcium Sulfate Hemihydrate to Gypsum Using Time-Resolved Cryogenic Transmission Electron Microscopy. *Langmuir*, 2012, **28**(30), pp.11182-11187.
301. OSSORIO, M., T.M. STAWSKI, J.D. RODRIGUEZ-BLANCO, M. SLEUTEL, J.M. GARCIA-RUIZ, L.G. BENNING and A.E.S. VAN DRIESSCHE. Physicochemical and Additive Controls on the Multistep Precipitation Pathway of Gypsum. *Minerals*, 2017, **7**(8).
302. GOWER, L.B. Biomimetic Model Systems for Investigating the Amorphous Precursor Pathway and Its Role in Biomineralization. *Chemical Reviews*, 2008, **108**(11), pp.4551-4627.
303. DUNSMORE, H.E. A Geological Perspective on Global Warming and the Possibility of Carbon-Dioxide Removal as Calcium-Carbonate

Mineral. *Energy Conversion and Management*, 1992, **33**(5-8), pp.565-572.
304. LIPPMANN, F. *Sedimentary carbonate minerals.* Springer-Verlag, 1973.
305. TUCKER, M.E. and V.P. WRIGHT. Carbonate mineralogy and chemistry. *Carbonate Sedimentology*, 1990, pp.284-313.
306. DE LEEUW, N.H. and S.C. PARKER. Surface structure and morphology of calcium carbonate polymorphs calcite, aragonite, and vaterite: An atomistic approach. *Journal of Physical Chemistry B*, 1998, **102**(16), pp.2914-2922.
307. QIAO, L., Q.L. FENG and Z. LI. Special vaterite found in freshwater lackluster pearls. *Crystal Growth & Design*, 2007, **7**(2), pp.275-279.
308. MICHEL, F.M., J. MACDONALD, J. FENG, B.L. PHILLIPS, L. EHM, C. TARABRELLA, J.B. PARISE and R.J. REEDER. Structural characteristics of synthetic amorphous calcium carbonate. *Chemistry of Materials*, 2008, **20**(14), pp.4720-4728.
309. TITILOYE, J.O., S.C. PARKER, D.J. OSGUTHORPE and S. MANN. Predicting the influence of growth additives on the morphology of ionic-crystals. *Journal of the Chemical Society-Chemical Communications*, 1991, (20), pp.1494-1496.
310. NIELSEN, M.H., S. ALONI and J.J. DE YOREO. In situ TEM imaging of CaCO3 nucleation reveals coexistence of direct and indirect pathways. *Science*, 2014, **345**(6201), pp.1158-1162.
311. RADHA, A.V., T.Z. FORBES, C.E. KILLIAN, P.U.P.A. GILBERT and A. NAVROTSKY. Transformation and crystallization energetics of synthetic and biogenic amorphous calcium carbonate. *Proceedings of the National Academy of Sciences of the United States of America*, 2010, **107**(38), pp.16438-16443.
312. MASS, T., A.J. GIUFFRE, C.Y. SUN, C.A. STIFLER, M.J. FRAZIER, M. NEDER, N. TAMURA, C.V. STAN, M.A. MARCUS and P.U.P.A. GILBERT. Amorphous calcium carbonate particles form coral skeletons. *Proceedings of the National Academy of Sciences of the United States of America*, 2017, **114**(37), pp.E7670-E7678.
313. GEBAUER, D., P.N. GUNAWIDJAJA, J.Y.P. KO, Z. BACSIK, B. AZIZ, L.J. LIU, Y.F. HU, L. BERGSTROM, C.W. TAI, T.K. SHAM, M. EDEN and N. HEDIN. Proto-Calcite and Proto-Vaterite in Amorphous Calcium Carbonates. *Angewandte Chemie-International Edition*, 2010, **49**(47), pp.8889-8891.
314. AZAIS, T., C. TOURNE-PETEILH, F. AUSSENAC, N. BACCILE, C. COELHO, J.-M. DEVOISSELLE and F. BABONNEAU. Solid-state NMR study of ibuprofen confined in MCM-41 material. *Chemistry of Materials*, 2006, **18**(26), pp.6382-6390.
315. HAYNES, W.M. *CRC handbook of chemistry and physics.* CRC press, 2014.
316. SANTOS, A.M.M. and W.L. VASCONCELOS. Properties of porous silica glasses prepared via sol-gel process. *Journal of Non-Crystalline Solids*, 2000, **273**(1-3), pp.145-149.
317. VERAN-TISSOIRES, S., M. MARCOUX and M. PRAT. Salt crystallisation at the surface of a heterogeneous porous medium. *EPL (Europhysics Letters)*, 2012, **98**(3), p.34005.

318. HUININK, H., L. PEL and M.V.A. MICHELS. How ions distribute in a drying porous medium: A simple model. *Physics of Fluids*, 2002, **14**(4), pp.1389-1395.
319. MATYKA, M., Z. KOZA and K. VAFAI. How to calculate tortuosity easily? *In: AIP Conference Proceedings 4*: AIP, 2012, pp.17-22.
320. SCHMIDT, H., I. PASCHKE, D. FREYER and W. VOIGT. Water channel structure of bassanite at high air humidity: crystal structure of CaSO4 center dot 0.625H(2)O. *Acta Crystallographica Section B-Structural Science Crystal Engineering and Materials*, 2011, **67**, pp.467-475.
321. BALLIRANO, P., A. MARAS, S. MELONI and R. CAMINITI. The monoclinic I2 structure of bassanite, calcium sulphate hemihydrate (CaSO4· 0.5 H2O). *European Journal of Mineralogy*, 2001, **13**(5), pp.985-993.
322. COMODI, P., S. NAZZARENI, P.F. ZANAZZI and S. SPEZIALE. High-pressure behavior of gypsum: A single-crystal X-ray study. *American Mineralogist*, 2008, **93**(10), pp.1530-1537.
323. SEUFERT, S., C. HESSE, F. GOETZ-NEUNHOEFFER and J. NEUBAUER. Quantitative determination of anhydrite III from dehydrated gypsum by XRD. *Cement and Concrete research*, 2009, **39**(10), pp.936-941.
324. CHAROLA, A.E., J. PUHRINGER and M. STEIGER. Gypsum: a review of its role in the deterioration of building materials. *Environmental geology*, 2007, **52**(2), pp.207-220.
325. FAATZ, M., F. GROHN and G. WEGNER. Amorphous calcium carbonate: Synthesis and potential intermediate in biomineralization. *Advanced Materials*, 2004, **16**(12), pp.996-1000.
326. RODRIGUEZ-BLANCO, J.D., S. SHAW and L.G. BENNING. How to make 'stable' ACC: protocol and preliminary structural characterization. *Mineralogical Magazine*, 2008, **72**(1), pp.283-286.
327. MELDRUM, F.C. and S. LUDWIGS. Template-Directed Control of Crystal Morphologies. *Macromolecular bioscience*, 2007, **7**(2), pp.152-162.
328. YUE, W., A.N. KULAK and F.C. MELDRUM. Growth of single crystals in structured templates. *Journal of Materials Chemistry*, 2006, **16**(4), pp.408-416.
329. WANG, Y.W., H.K. CHRISTENSON and F.C. MELDRUM. Confinement Increases the Lifetimes of Hydroxyapatite Precursors. *Chemistry of Materials*, 2014, **26**(20), pp.5830-5838.
330. TESTER, C.C., R.E. BROCK, C.-H. WU, M.R. KREJCI, S. WEIGAND and D. JOESTER. In vitro synthesis and stabilization of amorphous calcium carbonate (ACC) nanoparticles within liposomes. *CrystEngComm*, 2011, **13**(12), pp.3975-3978.
331. DUBROVSKII, V. Fundamentals of Nucleation Theory. *In: Nucleation Theory and Growth of Nanostructures*. Springer, 2014, pp.1-73.
332. FREYER, D. and W. VOIGT. Crystallization and phase stability of CaSO4 and CaSO4–based salts. *Monatshefte für Chemie/Chemical Monthly*, 2003, **134**(5), pp.693-719.
333. PRIETO, M., A. PUTNIS and L. FERNANDEZDIAZ. Factors Controlling the Kinetics of Crystallization - Supersaturation Evolution

in a Porous-Medium - Application to Barite Crystallization. *Geological Magazine*, 1990, **127**(6), pp.485-495.
334. KRÖGER, R. and A. VERCH. Liquid Cell Transmission Electron Microscopy and the Impact of Confinement on the Precipitation from Supersaturated Solutions. *Minerals*, 2018, **8**(1), p.21.
335. BOURG, I.C. and C.I. STEEFEL. Molecular dynamics simulations of water structure and diffusion in silica nanopores. *The Journal of Physical Chemistry C*, 2012, **116**(21), pp.11556-11564.
336. OSSORIO, M., A. VAN DRIESSCHE, P. PÉREZ and J. GARCÍA-RUIZ. The gypsum–anhydrite paradox revisited. *Chemical Geology*, 2014, **386**, pp.16-21.
337. SOLBERG, C. and S. HANSEN. Dissolution of CaSO 4· 1/2H 2 O and precipitation of CaSO 4· 2H 2 O: a kinetic study by synchrotron X-ray powder diffraction. *Cement and Concrete research*, 2001, **31**(4), pp.641-646.
338. HU, Q., M.H. NIELSEN, C. FREEMAN, L. HAMM, J. TAO, J. LEE, T.Y.-J. HAN, U. BECKER, J. HARDING and P. DOVE. The thermodynamics of calcite nucleation at organic interfaces: Classical vs. non-classical pathways. *Faraday Discussions*, 2012, **159**(1), pp.509-523.
339. BALA, T., B. PRASAD, M. SASTRY, M.U. KAHALY and U.V. WAGHMARE. Interaction of different metal ions with carboxylic acid group: a quantitative study. *The Journal of Physical Chemistry A*, 2007, **111**(28), pp.6183-6190.
340. TOSCA, N.J., A.H. KNOLL and S.M. MCLENNAN. Water activity and the challenge for life on early Mars. *Science*, 2008, **320**(5880), pp.1204-1207.
341. VANIMAN, D., D. BISH and S. CHIPERA. Bassanite on Mars. *In: Lunar and Planetary Science Conference*, 2009, p.1654.
342. BECKER, A., I. SÖTJE, C. PAULMANN, F. BECKMANN, T. DONATH, R. BOESE, O. PRYMAK, H. TIEMANN and M. EPPLE. Calcium sulfate hemihydrate is the inorganic mineral in statoliths of scyphozoan medusae (cnidaria). *Dalton Transactions*, 2005, (8), pp.1545-1550.
343. TIEMANN, H., I. SÖTJE, A. BECKER, G. JARMS and M. EPPLE. Calcium sulfate hemihydrate (bassanite) statoliths in the cubozoan Carybdea sp. *Zoologischer Anzeiger-A Journal of Comparative Zoology*, 2006, **245**(1), pp.13-17.
344. HENISCH, H.K. *Crystals in gels and Liesegang rings.* Cambridge University Press, 2005.
345. KIM, Y.Y., N.B.J. HETHERINGTON, E.H. NOEL, R. KROGER, J.M. CHARNOCK, H.K. CHRISTENSON and F.C. MELDRUM. Capillarity Creates Single-Crystal Calcite Nanowires from Amorphous Calcium Carbonate. *Angewandte Chemie-International Edition*, 2011, **50**(52), pp.12572-12577.
346. NOWAK, D., M. HEUBERGER, M. ZACH and H.K. CHRISTENSON. Thermodynamic and kinetic supercooling of liquid in a wedge pore. *Journal of Chemical Physics*, 2008, **129**(15).
347. KRALJ, D., L. BRECEVIC and A.E. NIELSEN. Vaterite Growth and Dissolution in Aqueous-Solution .1. Kinetics of Crystal-Growth. *Journal of Crystal Growth*, 1990, **104**(4), pp.793-800.

348. FERNANDEZDIAZ, L., A. PUTNIS, M. PRIETO and C.V. PUTNIS. The role of magnesium in the crystallization of calcite and aragonite in a porous medium. *Journal of Sedimentary Research*, 1996, **66**(3), pp.482-491.
349. GIVEN, R.K. and B.H. WILKINSON. Kinetic Control of Morphology, Composition, and Mineralogy of Abiotic Sedimentary Carbonates - Reply. *Journal of Sedimentary Petrology*, 1985, **55**(6), pp.921-926.
350. TAI, C.Y. and F.B. CHEN. Polymorphism of CaCO3 precipitated in a constant-composition environment. *Aiche Journal*, 1998, **44**(8), pp.1790-1798.
351. BLEUET, P., E. WELCOMME, E. DOORYHÉE, J. SUSINI, J.-L. HODEAU and P. WALTER. Probing the structure of heterogeneous diluted materials by diffraction tomography. *Nature materials*, 2008, **7**(6), pp.468-472.
352. BARROSO, R., R. LOPES, E. DE JESUS and L. DE OLIVEIRA. Synchrotron biomedical applications using X-ray diffraction tomography. *In: Nuclear Science Symposium, 1999. Conference Record. 1999 IEEE*: IEEE, 1999, pp.855-859.
353. ALVAREZ-MURGA, M., P. BLEUET, L. MARQUES, C. LEPOITTEVIN, N. BOUDET, G. GABARINO, M. MEZOUAR and J.-L. HODEAU. Microstructural mapping of C60 phase transformation into disordered graphite at high pressure, using X-ray diffraction microtomography. *Journal of Applied Crystallography*, 2011, **44**(1), pp.163-171.
354. VOLTOLINI, M., M.C. DALCONI, G. ARTIOLI, M. PARISATTO, L. VALENTINI, V. RUSSO, A. BONNIN and R. TUCOULOU. Understanding cement hydration at the microscale: new opportunities frompencil-beam'synchrotron X-ray diffraction tomography. *Journal of Applied Crystallography*, 2013, **46**(1), pp.142-152.
355. GODINHO, J.R., K.M. GERKE, A.G. STACK and P.D. LEE. The dynamic nature of crystal growth in pores. *Scientific Reports*, 2016, **6**.
356. BERNSTEIN, F.C., T.F. KOETZLE, G.J. WILLIAMS, E.F. MEYER, M.D. BRICE, J.R. RODGERS, O. KENNARD, T. SHIMANOUCHI and M. TASUMI. The protein data bank. *The FEBS Journal*, 1977, **80**(2), pp.319-324.
357. GÓMEZ-MORALES, J., G. FALINI and J.M. GARCÍA-RUIZ. 20 - Biological Crystallization. *In:* T. NISHINAGA, ed. *Handbook of Crystal Growth (Second Edition)*. Boston: Elsevier, 2015, pp.873-913.
358. DA SILVA, M.A., R. ITRI and E.P.G. AREAS. Lysozyme viscoelastic matrices in tetramethylurea/water media: a small angle X-ray scattering study. *Biophysical Chemistry*, 2002, **99**(2), pp.169-179.
359. RINCON BONILLA, M. and S.K. BHATIA. Diffusion in pore networks: effective self-diffusivity and the concept of tortuosity. *The Journal of Physical Chemistry C*, 2013, **117**(7), pp.3343-3357.
360. ERICKSON, H.P. Size and shape of protein molecules at the nanometer level determined by sedimentation, gel filtration, and electron microscopy. *Biol Proced Online*, 2009, **11**(1), pp.32-51.
361. MALMON, A.G. Small Angle X-Ray Scattering Studies of the Size, Shape, and Hydration of Catalase. *Biochimica Et Biophysica Acta*, 1957, **26**(2), pp.233-240.

362. MCPHERSON, A. and J. WEICKMANN. X-Ray-Analysis of New Crystal Forms of the Sweet Protein Thaumatin. *Journal of Biomolecular Structure & Dynamics*, 1990, **7**(5), pp.1053-1060.
363. KUZNETSOV, Y.G., J. KONNERT, A.J. MALKIN and A. MCPHERSON. The advancement and structure of growth steps on thaumatin crystals visualized by atomic force microscopy at molecular resolution. *Surface Science*, 1999, **440**(1-2), pp.69-80.
364. KOSCHWANEZ, J.H., R.H. CARLSON and D.R. MELDRUM. Thin PDMS Films Using Long Spin Times or Tert-Butyl Alcohol as a Solvent. *Plos One*, 2009, **4**(2).
365. LUSTY, C.J. A gentle vapor-diffusion technique for cross-linking of protein crystals for cryocrystallography. *Journal of Applied Crystallography*, 1999, **32**(1), pp.106-112.
366. HEIJNA, M.C.R., W.J.P. VAN ENCKEVORT and E. VLIEG. Growth inhibition of protein crystals: A study of lysozyme polymorphs. *Crystal Growth & Design*, 2008, **8**(1), pp.270-274.
367. VEKILOV, P.G. Metastable mesoscopic phases in concentrated protein solutions. *Annals of the New York Academy of Sciences*, 2009, **1161**(1), pp.377-386.
368. BELONGIA, B.M. and J.C. BAYGENTS. Measurements on the diffusion coefficient of colloidal particles by Taylor-Aris dispersion. *Journal of Colloid and Interface Science*, 1997, **195**(1), pp.19-31.
369. FREY, M. Water-Structure Associated with Proteins and Its Role in Crystallization. *Acta Crystallographica Section D-Biological Crystallography*, 1994, **50**, pp.663-666.
370. TANAKA, S., S. EGELHAAF and W. POON. Protein crystallization in confined geometries. *arXiv preprint cond-mat/0309373*, 2003.
371. HAEBERLE, S. and R. ZENGERLE. Microfluidic platforms for lab-on-a-chip applications. *Lab on a Chip*, 2007, **7**(9), pp.1094-1110.
372. LI, L., D. MUSTAFI, Q. FU, V. TERESHKO, D.L.L. CHEN, J.D. TICE and R.F. ISMAGILOV. Nanoliter microfluidic hybrid method for simultaneous screening and optimization validated with crystallization of membrane proteins. *Proceedings of the National Academy of Sciences of the United States of America*, 2006, **103**(51), pp.19243-19248.
373. GLASSFORD, S., K.A. CHAN, B. BYRNE and S.G. KAZARIAN. Chemical imaging of protein adsorption and crystallization on a wettability gradient surface. *Langmuir*, 2012, **28**(6), pp.3174-3179.
374. SAHA, B., J. SAIKIA and G. DAS. Tuning the selective interaction of lysozyme and serum albumin on a carboxylate modified surface. *RSC Advances*, 2013, **3**(21), pp.7867-7879.
375. MORRA, M., E. OCCHIELLO, R. MAROLA, F. GARBASSI, P. HUMPHREY and D. JOHNSON. On the aging of oxygen plasma-treated polydimethylsiloxane surfaces. *Journal of Colloid and Interface Science*, 1990, **137**(1), pp.11-24.
376. CHUA, D.B., H. NG and S.F. LI. Spontaneous formation of complex and ordered structures on oxygen-plasma-treated elastomeric polydimethylsiloxane. *Applied Physics Letters*, 2000, **76**(6), pp.721-723.
377. TSOUGENI, K., A. TSEREPI, G. BOULOUSIS, V. CONSTANTOUDIS and E. GOGOLIDES. Control of Nanotexture and Wetting Properties

of Polydimethylsiloxane from Very Hydrophobic to Super-Hydrophobic by Plasma Processing. *Plasma Processes and Polymers*, 2007, **4**(4), pp.398-405.

378. LI, S.B., X.Q. GONG, C.S. MC NALLY, M.L. ZENG, T. GAULE, C. ANDUIX-CANTO, A.N. KULAK, L.A. BAWAZER, M.J. MCPHERSON and F.C. MELDRUM. Rapid preparation of highly reliable PDMS double emulsion microfluidic devices. *RSC Advances*, 2016, **6**(31), pp.25927-25933.
379. BOXSHALL, K., M.H. WU, Z. CUI, Z.F. CUI, J.F. WATTS and M.A. BAKER. Simple surface treatments to modify protein adsorption and cell attachment properties within a poly(dimethylsiloxane) micro-bioreactor. *Surface and Interface Analysis*, 2006, **38**(4), pp.198-201.
380. BODAS, D. and C. KHAN-MALEK. Hydrophilization and hydrophobic recovery of PDMS by oxygen plasma and chemical treatment—An SEM investigation. *Sensors and Actuators B: Chemical*, 2007, **123**(1), pp.368-373.
381. RICCARDI, C., R. BARNI, E. SELLI, G. MAZZONE, M.R. MASSAFRA, B. MARCANDALLI and G. POLETTI. Surface modification of poly(ethylene terephthalate) fibers induced by radio frequency air plasma treatment. *Applied Surface Science*, 2003, **211**(1-4), pp.386-397.
382. HILLBORG, H. and U. GEDDE. Hydrophobicity recovery of polydimethylsiloxane after exposure to corona discharges. *Polymer*, 1998, **39**(10), pp.1991-1998.
383. HILLBORG, H., J. ANKNER, U.W. GEDDE, G. SMITH, H. YASUDA and K. WIKSTRÖM. Crosslinked polydimethylsiloxane exposed to oxygen plasma studied by neutron reflectometry and other surface specific techniques. *Polymer*, 2000, **41**(18), pp.6851-6863.
384. MANCA, M., B. CORTESE, I. VIOLA, A.S. ARICÒ, R. CINGOLANI and G. GIGLI. Influence of chemistry and topology effects on superhydrophobic CF4-plasma-treated poly (dimethylsiloxane)(PDMS). *Langmuir*, 2008, **24**(5), pp.1833-1843.
385. HUCK, W.T., N. BOWDEN, P. ONCK, T. PARDOEN, J.W. HUTCHINSON and G.M. WHITESIDES. Ordering of spontaneously formed buckles on planar surfaces. *Langmuir*, 2000, **16**(7), pp.3497-3501.
386. GHATAK, A.S. and A. GHATAK. Disordered Nanowrinkle Substrates for Inducing Crystallization over a Wide Range of Concentration of Protein and Precipitant. *Langmuir*, 2013, **29**(13), pp.4373-4380.
387. GHATAK, A.S., G. RAWAL and A. GHATAK. Precipitant-Free Crystallization of Protein Molecules Induced by Incision on Substrate. *Crystals*, 2017, **7**(8).
388. TAYLOR, J.B., D.J. TRIGGLE and P.D. KENNEWELL. *Comprehensive Medicinal Chemistry II.: Global perspective.* Elsevier, 2007.
389. RHYS, N.H., M.C. WANG, T.A. JOWITT, J.R. HELLIWELL, J.G. GROSSMANN and C. BALDOCK. Deriving the ultrastructure of alpha-crustacyanin using lower-resolution structural and biophysical methods. *Journal of Synchrotron Radiation*, 2011, **18**, pp.79-83.
390. DELLISANTIA, C.D., S. SPINELLI, C. CAMBILLAU, J.B.C. FINDLAY, P.F. ZAGALSKY, S. FINET and V. RECEVEUR-BRECHOT.

Quaternary structure of alpha-crustacyanin from lobster as seen by small-angle X-ray scattering. *Febs Letters*, 2003, **544**(1-3), pp.189-193.

391. CIANCI, M., P.J. RIZKALLAH, A. OLCZAK, J. RAFTERY, N.E. CHAYEN, P.F. ZAGALSKY and J.R. HELLIWELL. The molecular basis of the coloration mechanism in lobster shell: beta-crustacyanin at 3.2-angstrom resolution. *Proceedings of the National Academy of Sciences of the United States of America*, 2002, **99**(15), pp.9795-9800.
392. CAMPBELL, J.M., F.C. MELDRUM and H.K. CHRISTENSON. Is ice nucleation from supercooled water insensitive to surface roughness? *The Journal of Physical Chemistry C*, 2015, **119**(2), pp.1164-1169.
393. PARKER, J.L., D.L. CHO and P.M. CLAESSON. Plasma Modification of Mica - Forces between Fluorocarbon Surfaces in Water and a Nonpolar Liquid. *Journal of Physical Chemistry*, 1989, **93**(16), pp.6121-6125.
394. LIU, Y.-X., X.-J. WANG, J. LU and C.-B. CHING. Influence of the roughness, topography, and physicochemical properties of chemically modified surfaces on the heterogeneous nucleation of protein crystals. *The Journal of Physical Chemistry B*, 2007, **111**(50), pp.13971-13978.
395. PUSEY, M., J. BARCENA, M. MORRIS, A. SINGHAL, Q.Y. YUAN and J. NG. Trace fluorescent labeling for protein crystallization. *Acta Crystallographica Section F-Structural Biology Communications*, 2015, **71**, pp.806-814.
396. FORSYTHE, E., A. ACHARI and M.L. PUSEY. Trace fluorescent labeling for high-throughput crystallography. *Acta Crystallographica Section D-Biological Crystallography*, 2006, **62**, pp.339-346.
397. BYINGTON, M.C., M.S. SAFARI, J.C. CONRAD and P.G. VEKILOV. Shear flow suppresses the volume of the nucleation precursor clusters in lysozyme solutions. *Journal of Crystal Growth*, 2017, **468**, pp.493-501.
398. FRARE, E., M.F. MOSSUTO, P.P. DE LAURETO, S. TOLIN, L. MENZER, M. DUMOULIN, C.M. DOBSON and A. FONTANA. Characterization of Oligomeric Species on the Aggregation Pathway of Human Lysozyme. *Journal of Molecular Biology*, 2009, **387**(1), pp.17-27.
399. GORNOSTYREV, Y.N., M.I. KATSNELSON, N.I. MEDVEDEVA, O.N. MRYASOV, A.J. FREEMAN and A.V. TREFILOV. Peculiarities of defect structure and mechanical properties of iridium: Results of ab initio electronic structure calculations. *Physical Review B*, 2000, **62**(12), pp.7802-7808.
400. HECKER, S.S., D.L. ROHR and D.F. STEIN. Brittle-Fracture in Iridium. *Metallurgical Transactions a-Physical Metallurgy and Materials Science*, 1978, **9**(4), pp.481-488.
401. GENZER, J. *Soft Matter Gradient Surfaces: Methods and Applications.* John Wiley & Sons, 2012.
402. OSTUNI, E., B.A. GRZYBOWSKI, M. MRKSICH, C.S. ROBERTS and G.M. WHITESIDES. Adsorption of proteins to hydrophobic sites on mixed self-assembled monolayers. *Langmuir*, 2003, **19**(5), pp.1861-1872.

403. XIE, Y., M.F. LIU and J. ZHOU. Molecular dynamics simulations of peptide adsorption on self-assembled monolayers. *Applied Surface Science*, 2012, **258**(20), pp.8153-8159.
404. NORD, F.F. and M. BIER. On the Mechanism of Enzyme Action .55. A Study of the Interaction between Calcium and Trypsin. *Biochimica Et Biophysica Acta*, 1953, **12**(1), pp.56-66.
405. SAUTER, A., M. OELKER, G. ZOCHER, F.J. ZHANG, T. STEHLE and F. SCHREIBER. Nonclassical Pathways of Protein Crystallization in the Presence of Multivalent Metal Ions. *Crystal Growth & Design*, 2014, **14**(12), pp.6357-6366.
406. PETSEV, D.N., X.X. WU, O. GALKIN and P.G. VEKILOV. Thermodynamic functions of concentrated protein solutions from phase equilibria. *Journal of Physical Chemistry B*, 2003, **107**(16), pp.3921-3926.
407. KUZNETSOV, Y.G., A.J. MALKIN and A. MCPHERSON. The liquid protein phase in crystallization: a case study - intact immunoglobulins. *Journal of Crystal Growth*, 2001, **232**(1-4), pp.30-39.